



NATIONAL TECHNICAL UNIVERSITY OF ATHENS
SCHOOL OF APPLIED MATHEMATICAL AND PHYSICAL SCIENCES
DEPARTMENT OF PHYSICS

Development of the Detector Control System for the Muon Spectrometer of the ATLAS Experiment and the Z boson Mass measurement

A dissertation presented by

Ioannis Drivas-Koulouris

The Department of Physics
National Technical University of Athens

Athens, November 2025

Development of the Detector Control System for the Muon Spectrometer of the ATLAS Experiment and the Z boson Mass measurement

Ph.D Thesis

Ioannis Drivas-Koulouris

Advisor: Theodoros Alexopoulos
Professor NTUA Greece

Exam comittee:

.....	
Theodoros Alexopoulos	Theodoros Geralis	Michael Kokkoris	
Professor,	Director of Research, NCSR,	Professor,	
N.T.U.A., Greece	Demokritos, Greece	N.T.U.A., Greece	
.....
Stavros Maltezos	Ioannis Kopsalis	Georgios Stavropoulos	Dimitrios Sampsonidis
Professor Emeritus,	Assistant Professor,	Director of Research, NCSR,	Professor,
N.T.U.A., Greece	N.T.U.A., Greece	"Demokritos", Greece	AUTh, Greece

Athens, November 2025

.....
Ioannis Drivas-Koulouris



ΕΘΝΙΚΟ ΜΕΤΣΟΒΙΟ ΠΟΛΥΤΕΧΝΕΙΟ
ΣΧΟΛΗ ΕΦΑΡΜΟΣΜΕΝΩΝ ΜΑΘΗΜΑΤΙΚΩΝ ΚΑΙ ΦΥΣΙΚΩΝ
ΕΠΙΣΤΗΜΩΝ
ΤΟΜΕΑΣ ΦΥΣΙΚΗΣ

Ανάπτυξη των συστημάτων αυτομάτου
ελέγχου για το φασματομέτρο μιονίων
του πειράματος του ATLAS και μέτρηση
της μάζα του μποζονίου Z

Διδακτορική Διατριβή του

Ιωάννη Δρίβα-Κουλούρη

Διπλωματούχου Φυσικού Πανεπιστημίου Πατρών, κάτοχος Μάστερ
Εθνικού Μετσόβιου Πολυτεχνείου

Επιβλέπων: Θεόδωρος Αλεξόπουλος
Καθηγητής Εθνικού Μετσόβιου Πολυτεχνείου

Αθήνα, Νοέμβριος 2025



ΕΘΝΙΚΟ ΜΕΤΣΟΒΙΟ ΠΟΛΥΤΕΧΝΕΙΟ
ΣΧΟΛΗ ΕΦΑΡΜΟΣΜΕΝΩΝ ΜΑΘΗΜΑΤΙΚΩΝ ΚΑΙ ΦΥΣΙΚΩΝ
ΕΠΙΣΤΗΜΩΝ
ΤΟΜΕΑΣ ΦΥΣΙΚΗΣ

Ανάπτυξη των συστημάτων αυτομάτου ελέγχου
για το φασματόμετρο μιονίων του πειράματος
του ΑΤΛΑΣ και μέτρηση της μάζα του
μποζονίου Z

Διδακτορική Διατριβή του

Ιωάννη Δρίβα-Κουλούρη

Διπλωματούχου Φυσικού Πανεπιστημίου Πατρών, κάτοχος Μάστερ
Εθνικού Μετσόβιου Πολυτεχνείου

**ΤΡΙΜΕΛΗΣ ΣΥΜΒΟΥΛΕΥΤΙΚΗ Ε-
ΠΙΤΡΟΠΗ:**

1. Θεόδωρος Αλεξόπουλος, Καθ. Ε.Μ.Π.
2. Θεόδωρος Γέραλης, Διευθ. Ερευνών,
Ε.Κ.Ε.Φ.Ε. 'Δ.'
3. Μιχαήλ Κόκκορης, Καθ. Ε.Μ.Π.

ΕΠΤΑΜΕΛΗΣ ΕΞΕΤΑΣΤΙΚΗ ΕΠΙΤΡΟΠΗ:

1. Θεόδωρος Αλεξόπουλος, Καθ. Ε.Μ.Π.
2. Θεόδωρος Γέραλης, Διευθ. Ερευνών, Ε.Κ.Ε.Φ.Ε.
'Δ.'
3. Μιχαήλ Κόκκορης, Καθ. Ε.Μ.Π.
4. Σταύρος Μαλτέζος, Ομότιμος Καθηγητής Ε.Μ.Π.
5. Ιωάννης Κοψαλής, Επίκουρος Καθηγητής Ε.Μ.Π.
6. Γεώργιος Σταυρόπουλος, Διευθ. Ερευνών,
Ε.Κ.Ε.Φ.Ε. 'Δ.'
7. Δημήτριος Σαμψωνίδης, Καθηγητής Α.Π.Θ.

Αθήνα, Νοέμβριος 2025

.....
Ιωάννης Δρίβας-Κουλούρης

© 2025 Εθνικό Μετσόβιο Πολυτεχνείο. Με επιφύλαξη παντός δικαιώματος.

Ελληνική Περίληψη

Το πείραμα ATLAS, εγκατεστημένο στον Μεγάλο Επιταχυντή Αδρονίων (LHC) του CERN, αποτελεί ένα από τα σημαντικότερα ερευνητικά έργα της φυσικής υψηλών ενεργειών. Σκοπός του είναι η διερεύνηση θεμελιωδών ερωτημάτων για το Σύμπαν, όπως η προέλευση της μάζας, η φύση της σκοτεινής ύλης και η ύπαρξη νέας φυσικής πέραν του Καθιερωμένου Προτύπου. Η παρούσα διδακτορική διατριβή αφορά στην ανάπτυξη και ενσωμάτωση του Συστήματος Αυτομάτου Ελέγχου (Detector Control System - DCS) για τα υποσυστήματα του φασματόμετρου μιονίων του πειράματος ATLAS στον Μεγάλο Επιταχυντή Αδρονίων (LHC) του CERN. Το DCS αποτελεί κρίσιμο στοιχείο για την ασφαλή και αξιόπιστη λειτουργία του ανιχνευτή, επιτρέποντας την απομακρυσμένη παρακολούθηση, διάγνωση και διαχείριση παραμέτρων όπως τάσεις, θερμοκρασίες, κατάσταση συστημάτων ψύξης και παροχή αερίων. Υλοποιήθηκε με την πλατφόρμα SCADA WinCC OA και το πλαίσιο JCOP, και εφαρμόστηκε επιτυχώς σε παλαιά και νέα υποσυστήματα (MDT, Micromegas, sTGC).

Επιπρόσθετα, η παρούσα διδακτορική διατριβή, είχε ως στόχο την ακριβέστερη μέτρηση της μάζας του μποζονίου Z μέσω ανασύνθεσης γεγονότων $Z \rightarrow \mu^+ \mu^-$. Η ανάλυση περιλαμβάνει στατιστική επεξεργασία δεδομένων με χρήση της πλατφόρμας Histmaker και προσομοιώσεων Monte Carlo, με ιδιαίτερη έμφαση στη διόρθωση συστηματικών σφαλμάτων όπως το sagitta bias. Εφαρμόστηκαν προηγμένες τεχνικές προσαρμογής κατανομών, όπως η μέθοδος ψευδομάζας και πιθανότητες μέγιστης αξιοπιστίας, οδηγώντας σε ακριβή εκτίμηση της μάζας, συμβατή με τη διεθνώς αποδεκτή τιμή. Τέλος η εργασία συμβάλλει στην αξιοπιστία του πειράματος ATLAS και στη θεωρητική ισχύ του Καθιερωμένου Προτύπου.

Abstract

The ATLAS experiment, located at the Large Hadron Collider (LHC) at CERN, is one of the flagship projects of high-energy physics. Its mission is to investigate fundamental questions about the Universe, such as the origin of mass, the nature of dark matter, and potential new physics beyond the Standard Model.

This doctoral dissertation presents the development and integration of the Detector Control System (DCS) for the muon spectrometer subsystems of the ATLAS experiment at the Large Hadron Collider (LHC) at CERN. The DCS is a crucial component for ensuring the safe and efficient operation of the detector infrastructure, enabling real-time monitoring, diagnostics, and control of high- and low-voltage systems, cooling stations, and gas modules. Implemented through the WinCC OA SCADA platform within the JCOP framework, the system was successfully extended to legacy and upgraded components, including the MDT, Micromegas, and sTGC technologies.

In parallel, the thesis focuses on the precision measurement of the Z boson mass using reconstructed $Z \rightarrow \mu^+ \mu^-$ events. A dedicated data analysis pipeline was developed using Histmaker and Monte Carlo simulations, with careful attention to systematic uncertainties such as sagitta bias. Corrective strategies and advanced fitting techniques (e.g., pseudo-mass asymmetry and likelihood fits) were applied to obtain an accurate estimation of the Z boson mass, yielding results compatible with the world average. The study not only validates the robustness of the ATLAS detector systems but also contributes to the ongoing verification of

the Standard Model.

Preface

This dissertation presents the development of the Detector Control System (DCS) for the Muon Spectrometer of the ATLAS experiment at CERN, as well as the methodology and results of the Z boson mass measurement. The structure of the thesis is organized in a way that gradually introduces the reader to the necessary theoretical background, the experimental infrastructure, the technical implementations of the control system, and the data analysis involved in precision measurements.

Chapter 1 – Theoretical Part:

This chapter provides the theoretical foundation necessary for understanding the field of particle physics. It covers the Standard Model, the role of CERN, and the infrastructure of the LHC and its associated experiments. A general overview of particle interactions, detector technologies, and the physics motivation behind the ATLAS experiment is provided.

Chapter 2 – The ATLAS Experiment:

A detailed description of the ATLAS detector and its subsystems is given here, with particular focus on the Muon Spectrometer. The technologies involved in muon detection, such as MDTs, RPCs, TGCs, CSCs, sTGCs, and Micromegas, are presented, along with recent upgrade projects like BIS78.

Chapter 3 – Development of the Detector Control System:

This core chapter outlines the implementation of the Detector Control System for the muon subdetectors. It introduces the architecture of the

DCS based on the WinCC OA platform and describes in detail the functionalities of its components such as FSMs, high-voltage systems, gas systems, alignment monitoring, and integration with DAQ systems. Various subprojects, including those related to the BIS78 and MDT chambers, are also covered extensively.

Chapter 4 – Z Boson Mass Measurement:

The final chapter presents the analysis performed to measure the mass of the Z boson. It details the datasets used, simulation tools, muon selection criteria, background estimation methods, and the systematic uncertainties considered. Particular attention is given to the radial bias analysis and sagitta distortions, as well as fitting techniques like the Likelihood and Trex Fit approaches.

This thesis aims to contribute both to the technical advancement of the ATLAS experiment's infrastructure and to the precision measurements that deepen our understanding of fundamental physics.

Acknowledgments

This will take long...

To begin with, I would like to express my sincere gratitude to my supervisor, Theodoros Alexopoulos, who has supported and guided me throughout all these years since 2018, when I first joined the High Energy Physics group of NTUA. He was always available to assist me and offered me the opportunity to pursue my doctoral research at CERN.

I would also like to thank Theodoros Gerasis for his continuous advice and suggestions throughout the years of my doctoral studies. In addition, I would like to express my gratitude to Stavros Maltezos for his comments and guidance during this time. Lastly, I would like to thank Michael Kokkoris, Ioannis Kopsalis, Georgios Stavropoulos, and Dimos Sampsonidis for their help and for kindly agreeing to serve as members of my examination committee.

Regarding CERN, I would first like to express my gratitude to Stephanie Zimmerman, my first supervisor in the MDT DCS project. She guided and supported me, and I learned a great deal from her during my first months at CERN. Her dedication to her work was a great source of inspiration and motivation for me to pursue this PhD. Her loss is deeply felt. I would also like to thank Gregor Herten for his support and assistance during the early years of my doctoral studies, as well as in the years that followed.

I would also like to thank the postdoctoral researcher Efstathios Karentzos. Stathis has been my supervisor for the MDT DCS since 2020, and I have learned a great deal working alongside him. His guidance has helped me understand many aspects of the DCS and reach the level at which I stand today. At the same time, he has been one of the people who have supported, advised, and helped me extensively — almost like an older brother and a close friend.

Regarding the muon community, I would like to thank Philipp Fleischmann and Paolo Iengo, the two Muon Project Leaders during my PhD, for their support and assistance throughout these years of my doctoral research. On the MDT side, I would like to thank Tiesheng Dai and Zhen Yan for their continuous support regarding the MDT detectors, for the knowledge they shared with me, and for their constant willingness to be actively involved and helpful.

Regarding the DCS team, I had the opportunity to work with many people from all the sub-detectors. In particular, I would like to thank Efstathios Karentzos, Christos Paraskevopoulos, Pollyneikis Tzanis, Henso Abreu, and Karol Poplawski for our collaboration and for the knowledge we exchanged while working on the DCS, as well as for our weekly meetings. I would also like to express my gratitude to Stefan Schlenker and Paris Moschovakos from the Central DCS for their continuous support and assistance.

My collaboration with the Z mass analysis group lasted for only three years, but it gave me the opportunity to work with some truly brilliant people. I would like to thank Emilien Chapon, Stefano Camarda, and Johannes Junggeburth for their help and guidance throughout this period.

Lastly, I would like to express my gratitude to my colleague and friend since my Master's studies, Olga Zormpa, for her support and collaboration on this project.

I would also like to express my heartfelt gratitude to the many friends I made at CERN, for their support, their companionship, and all the pleasant moments we shared together. In particular, I would like to thank Andreas, Despoina, Dimitra, Emanuele, Euripidis, Kostas, Magda, Panagiotis, Thanasis, Vangelis, and Zeta.

I would also like to thank my friends back in Greece, who have always stood by my side and supported me through difficult moments: Charis, Dimitris, Giorgos, Kostas, Kostis, Thodoris, and Vasiliki.

Finally, I would like to express my deepest gratitude to my family, and especially to my parents, Konstantinos and Konstantina, who are always by my side — supporting, loving, and helping me through every challenging moment I face.

Tomorrow Comes

Contents

Abstract	11
Preface	1
Acknowledgments	5
List of Figures	15
List of Tables	27
1 High Energy Physics and CERN	37
1.1 The Standard Model	37
1.2 The Standard Model and Particle Physics	39
1.3 CERN	44
1.4 The Large Hadron Collider and the ATLAS experiment	45
1.5 The High Luminosity LHC	47
1.6 The experiments of LHC	50
1.6.1 The CMS Experiment	51
1.6.2 The Alice Experiment	51
1.6.3 The LHCb Experiment	53
Bibliography	55
2 The ATLAS Experiment	57
2.0.1 The ATLAS Detector	57

2.0.2	The Magnet system	59
2.0.3	The Inner Detector	60
2.0.4	The ATLAS Calorimeters	62
2.0.5	Trigger and Data Acquisition System (TDAQ) . .	64
2.0.6	The Muon Spectrometer	65
2.0.6.1	The Resistive plate chambers: RPCs . . .	67
2.0.6.2	The Thin Gap Chambers (TGCs): TGCs	68
2.0.6.3	The Cathode Strip Chambers: CSCs . . .	68
2.0.6.4	The Monitored Drift Tubes: MDTs . . .	69
2.0.7	Atlas Phase-I Upgrades	71
2.0.8	The BIS78 Project	72
2.0.9	Micromegas Detectors	76
2.1	STG Detectors	79
Bibliography		81
 3 The Development of the Detector Control System of the		
Muon Subdetectors of ATLAS Experiment		85
3.1	The ATLAS Detector Control System	86
3.1.1	The DCS Building Blocks	87
3.2	The WinCC OA Framework	90
3.2.1	Process interface	91
3.2.2	Project Administrator panel	91
3.2.3	Console	92
3.2.4	Log Viewer	92
3.2.5	Event Manager	93
3.2.6	Database Manager	94
3.2.7	Control Manager	95
3.2.8	Archive Managers	96

3.2.9	API Managers	96
3.2.10	The WinCC OA User Interface	97
3.2.11	The Graphics Editor (GEDI)	97
3.2.12	The PARA module of WinCC OA	98
3.2.13	The WinCC OA Alarm Screen	99
3.2.14	The JOint Control Project Framework	100
3.2.15	The WinCC OA Communication Protocols	103
	3.2.15.1 The OPC UA Servers	103
	3.2.15.2 The Distributed Information Management Sys- tem	104
	3.2.15.3 The Data Interchange Protocol	105
3.3	The Finite State Machine	106
3.3.1	Control Unit	107
3.3.2	Device Unit	107
3.3.3	Logical Unit	108
3.3.4	FSM States	108
3.4	The Muon Cooling Station	112
3.5	The High Voltage Power Systems	117
3.5.1	High Voltage Mapping	119
	3.5.1.1 sTGC	119
	3.5.1.2 The NSW Mapping scheme	120
	3.5.1.3 Micromegas	124
	3.5.1.4 Mapping scheme	125
3.6	NSW Caen Easy System DCS	130
3.7	NSW (STG) Caen 48 V Generators	132
3.8	NSW Reset Network	134
3.9	MM HV Validation Test	138
3.10	HV Operation Panel	143

3.11 BIS78 DCS Project	144
3.11.1 BIS78A DCS Power Supply	145
3.11.2 BIS78A DCS JTAG/ELTX Project	148
3.11.3 BIS78A DCS GAS Project	151
3.11.4 BIS78A DCS P2C Project	153
3.11.5 DAQ to DCS Communication	154
3.11.6 Advanced Panels	158
3.12 The group Operation sMDT chambers panel	159
3.13 The MDT Small Wheel Removal	160
3.13.1 MDT High Voltage project	163
3.13.2 MDT MDM project	164
3.13.3 MDT ELTX project	165
3.13.4 EI DCS P2C Project	166
3.13.5 EI DCS GAS Project	167
3.14 MDT DSS Revival	169
3.15 MDT GAS Developments	172
3.15.1 The Mixer Module	174
3.15.2 The Gas Humidifier	177
3.15.3 The MDT Gas Pump	178
3.16 The MDT Endcap Alignment System	179
3.16.1 Process Heartbeat Monitoring	182
3.16.1.1 Process Checker Monitoring	182
3.16.1.2 CycleLogic Monitoring	183
3.16.1.3 Database Monitoring	183
3.16.1.4 Crate Communication Monitoring	184
3.16.1.5 Automatic Crate-Off Mechanism	184
3.16.1.6 The EndCap Alignment DCS	185
Bibliography	187

4	Z boson mass measurement	193
4.1	The origin of weak bosons	193
4.2	ElectroWeak Fit	196
4.3	Motivation	198
4.4	Datasets and Monte Carlo Simulations	199
4.4.1	Datasets for Z Mass Analysis	199
4.5	Monte Carlo Simulated Samples	200
4.6	Muon Selections	201
4.7	Selection Criteria	203
4.8	Histmaker Plots	203
4.9	Multijet background Estimation	211
4.10	Radial Bias Analysis	214
4.10.1	Distortions of the inner detector: sagitta bias	214
4.10.2	The Pseudo-mass method	215
4.10.3	Sagitta and background	222
4.11	Likelihood Fit	226
4.12	TRExFitter	228
4.13	Trex Fit Results	234
	Bibliography	236
A	MDT Configuration Database	241

List of Figures

1.1	The elementary particles of the Standard Model.	41
1.2	CERN's main site in Meyrin, Switzerland, looking towards the French border.	45
1.3	The schematic representation of the accelerators-injectors of LHC.	47
1.4	HL-LHC plan with last update January 2025.	48
1.5	LHC Page on April 2024 on stable beams.	50
1.6	The CMS Experiment	52
1.7	The Alice experiment structure	53
1.8	The LHCb experiment structure	54
2.1	An illustration of the ATLAS Magnet System.	58
2.2	The ATLAS Magnets	60
2.3	The ATLAS Inner Detector	62
2.4	The ATLAS Calorimeters	63
2.5	The ATLAS Muon Spectrometer	66
2.6	The Mechanical structure of an RPC chamber	67
2.7	The Thin Gap Chambers	69
2.8	The Cathode Strip Chambers	70
2.9	The Monitored Drift Tubes	72
2.10	The BIS78A chambers as they are positioned into the AT- LAS MS	73

2.11 The BIS78A chambers as they are positioned into the ATLAS MS.	74
2.12 General characteristics and properties of the BIS78A chambers.	75
2.13 The drift time spectrum of the BIS78A chambers.	76
2.14 The position of the BIS78A chambers into the MS at the UX15 cavern	76
2.15 Micromegas Detector Structure	78
2.16 The sTGC Detector Structure	80
3.1 The basic architecture of ATLAS Detector Control System.	87
3.2 Project Administrator panel	92
3.3 WinCC OA Console	93
3.4 WinCC OA log viewer	94
3.5 The WinCC OA architecture	95
3.6 The Graphics Editor (GEDI) of WinCC OA	98
3.7 The PARA module of WinCC OA	100
3.8 The WinCC OA alarm Screen	101
3.9 The Installation panel of JCOP Components	102
3.10 The OPC Communication Chain	104
3.11 The Distributed Information Management System	105
3.12 The FSM hierarchy with control units and device units	108
3.13 The Distributed Information Management System	110
3.14 The MDT Infrastructure FSM Tree	111
3.15 The New Datapoints structure of Muon Cooling	112
3.16 The service panel for the creation of Muon Cooling system	114
3.17 The DU structure of Muon Cooling FSM	114
3.18 The Alarm limits of Muon Cooling	115
3.19 The Main FSM Panel of Muon Cooling	115

3.20 The Main FSM Panel that gives information for every loop	116
3.21 CAEN's A3540 and A3535 boards	120
3.22 Arrangement of HV units for sTGC in the cavern. A graphical illustration of the arrangement of HV units for sTGC in the cavern is presented. The HV supplies (left) and arrangement of the HV boards in the crates (right) are shown.	123
3.23 Arrangement of HV units for micromegas in the cavern. A graphical illustration of the arrangement of HV units for micromegas in the cavern is presented. The HV supplies (left) and arrangement of the HV boards in the mainframes (right) are shown.	124
3.24 CAEN's A7038AP and A7038ST(N/P) boards	125
3.25 The MMG patch panel at the ATLAS UX15 Cavern. . .	127
3.26 A schematic of the high voltage cable connections from the racks to the detectors	128
3.27 The HV units and racks at different stages of HV connections are shown.	129
3.28 Main FSM MMG panel for the Mainframes	131
3.29 On the left is Main FSM STG panel for the Mainframes. On the right the Main FSM panel for STG crates. . . .	132
3.30 On the left is Main FSM STG panel for the Mainframes. On the right the Main FSM panel for STG crates. . . .	133
3.31 Main panel for MMG Reset Network FSM.	135
3.32 The Agilent lines of Reset Network of the Muon Systems	136
3.33 Main panel for STG Reset Network FSM, for controlling the branches.	137
3.34 Main panel for STG Reset Network FSM, for controlling the Mainframes.	138

3.35 Test setup at BB5 laboratory.	140
3.36 Data points and low level structure of the test parameters	140
3.37 Main test visualization panel.	141
3.38 Monitoring Voltage (V) and Current (μ A) of the boards, during a cycle.	142
3.39 The NSW Operation panels	144
3.40 The crate at rack Y6004X1, hosts the LV boards, that sup- ply the front-end electronics of the chambers.	146
3.41 A typical RackBuilder file contains all the necessary infor- mation of the hardware mapping.	146
3.42 Advanced expert panels facilitating the configuration and the handling of all the vital parameters (mapping, archive, alarm, description). Typical examples can be seen for the archive handling (top), and the description handling (bot- tom).	147
3.43 On the left the main channel panel have been modified to include all the shared channels wherever applicable. On the right, the associated for the shared LV channel panel. .	148
3.44 The main FSM panel of the JTAG along with all the main configuration parameters.	150
3.45 The main FSM panel of the ELTX along with all the main configuration parameters.	151
3.46 The main FSM panel of the GAS project along with all the gas parameters. Chambers have been grouped based on the associated gas line.	152
3.47 The Advanced Expert panel for the mapping and the HV in- terlock handling. A direct synchronisation with the ConfDB is established during the start up of the panel.	152

3.48 The main Conditional DB panel. The main MDT folders (HV,LV,JTAG) can be seen and selected for editing and viewing.	153
3.49 Parameters and configs inside CoolDB channels	154
3.50 DAQ Run Status Panel	156
3.51 mdtDDCchamber DPT	156
3.52 mdtDDCMrod DPT	156
3.53 Dropped Recovery panel	157
3.54 The mdmNodeBrowser Panel	158
3.55 MDT ELTX and Temperature Colormap	159
3.56 The BMG chambers installed in the feet of the ATLAS detector, at the middle layer of the barrel	160
3.57 the sMDT Operational Panel	161
3.58 SW electronics decommissioning on both sides of ATLAS.	162
3.59 New mapping provided for the new scheme	162
3.60 The FSM main panels of the ATLMDTPS3 project after the removal of the SW. (a) Main panel associated with the partition node. (b) Main panel associated with the inner layer node. (c) Main panel associated with a sector node.	164
((a))	164
((b))	164
((c))	164
3.61 The FSM main panel associated to the partition node of the ATLMDTMDM4 project after the removal of the SW. It is evident on the top left the missing even sectors.	165

3.62	The FSM main panels of the ATLMDTELTx project after the removal of the SW. Figure (a) shows the main panel associated to the partition node, figure (b) shows the main panel associated to the inner layer node and figure (c) shows the main panel associated to one sector node.	166
	((a))	166
	((b))	166
	((c))	166
3.63	The main Conditional DB panel. The three collection MDT folders (HV, LV, JTAG) can be seen and selected for editing and viewing, based on the expert's needs.	167
3.64	Parameters and configs inside ConditionDB collection folder. On the left, the folder's payload where the main configs declared. This defines the amount of data per channel pushed into the CondDB. The middle area is the channel definition where the expert can add or import via file new channels or to edit existing ones. Last, the rightmost part holds the mapping of each selected channels.	168
3.65	The main FSM panel of the GAS project along with all the gas parameters. Chambers have been grouped based on the associated gas line.	169
3.66	The Advanced Expert panel for the mapping and the hv interlock handling. A direct synchronisation with the ConfDB is establish during the start up of the panel.	169
3.67	A service panel has been created for the restoration of the MDT DSS System.	172
3.68	The main DSS Expert panel with alarms and actions for the MDT System.	173

3.69	The main FSM panel Gas Panel for the Gas Mixer . . .	175
3.70	The FSM Panel of Primary Supply for the Gas Mixer .	176
3.71	The FSM Panel of Analyser for the Gas Mixer	176
3.72	A datapoint that checks if the Gas Mixer has higher value than the primary gas	177
3.73	The main FSM panel for Gas Humidifier	178
3.74	The main FSM panel for Gas Pumps	179
3.75	The layout of the end-cap alignment system. The various colored lines indicate the end-cap alignment sensor lines. With green are the polar BCAMs, blue the azimuthal BCAMs, orange the RASNIK proximity sensors, red the in-plane RASNIKS and in yellow the chamber temperature sensors. Right: Schematic representation of the in-plane RASNIK layout for an MDT chamber installed in the internal spacer frame.	181
3.76	Left: Graphical representation of the LWDAQ system ca- bling scheme. A single LWDAQ device may be connected directly to the driver via a root cable or alternatively mul- tiple devices can be connected through branch cables to the multiplexers. Right: A block diagram representing the flow of the End-cap Alignment data through the various pro- cesses and the DCS.	181
3.77	The MDT DCS Alignment	186
3.78	The control managers 93,97 that help the operation of the EndCap alignment DCS System.	186

4.1	(a) Summary of measurements performed by the LEP collaborations (ALEPH, L3, DELPHI, and OPAL), along with their combined result. (b) Evolution of the world average value of m_Z and its associated uncertainties from 1990 to 2004.	197
	((a)) m_Z	197
	((b)) m_Z per year	197
4.2	(a) Overview of the measurements of m_W by the LEP, Tevatron and LHC collaborations. (b) Overview of world average of m_W and its uncertainties versus Year from 1998 to 2016.	198
	((a)) m_W	198
	((b)) m_W per year	198
4.3	Cuts applied for Data of years 2015-16.	203
	((a)) cuts for 2015 Data	203
	((b)) cuts for 2016 Data	203
4.4	Cuts applied for Data of years 2017-18.	204
	((a)) cuts for 2017 Data	204
	((b)) cuts for 2018 Data	204
4.5	p_T of leading muon	205
	((a)) 2015	205
	((b)) 2016	205
4.6	p_T of leading muon	206
	((a)) 2017	206
	((b)) 2018	206
4.7	p_T of sub-leading muon	206
	((a)) 2015	206
	((b)) 2016	206
4.8	p_T of sub-leading muon	207
	((a)) 2017	207

((b))2018	207
4.9 p_T for di-muon	207
((a))2015	207
((b))2016	207
4.10 p_T for di-muon	208
((a))2017	208
((b))2018	208
4.11 η_μ leading muon	208
((a))2015	208
((b))2016	208
4.12 η_μ of leading muon	209
((a))2017	209
((b))2018	209
4.13 η_μ of sub-leading muon	209
((a))2015	209
((b))2016	209
4.14 η_μ of sub-leading muon	210
((a))2017	210
((b))2018	210
4.15 $Y_{\mu\mu}$ for two muons	210
((a))2015	210
((b))2016	210
4.16 $Y_{\mu\mu}$ for two muons	211
((a))2017	211
((b))2018	211
4.17 Z mass distributions for 2015 and 2016 data	212
((a))2015	212
((b))2016	212

4.18 Z mass distributions for 2017 and 2018 data	212
((a))2017	212
((b))2018	212
(a) 2015	213
(b) 2016	213
(c) 2017	213
(d) 2018	213
4.19 same sign muons on datasets 2015-18.	213
4.20 Schematic illustration of the sagitta bias in charged particle tracks, arising from geometrical deformations in the bending plane.	214
4.21 Z mass distribution for 2015 data. On the left is the dis- tribution for sagitta bias $\delta_s = 0 \text{ TeV}^{-1}$ and on the right for $\delta_s = -0.1 \text{ TeV}^{-1}$	217
4.22 Z mass distribution for 2016 data. On the left is the dis- tribution for sagitta bias $\delta_s = 0 \text{ TeV}^{-1}$ and on the right for $\delta_s = -0.1 \text{ TeV}^{-1}$	217
4.23 Z mass distribution for 2017 data. On the left is the dis- tribution for sagitta bias $\delta_s = 0 \text{ TeV}^{-1}$ and on the right for $\delta_s = -0.1 \text{ TeV}^{-1}$	218
4.24 Z mass distribution for 2018 data. On the left is the dis- tribution for sagitta bias $\delta_s = 0 \text{ TeV}^{-1}$ and on the right for $\delta_s = -0.1 \text{ TeV}^{-1}$	218
4.25 Pseudomass asymmetry distribution for simulated $Z \rightarrow \mu^+ \mu^-$ events generated with Powheg, shown for the case without any sagitta bias (red) and after introducing a sagitta bias of $\delta_s = 0.2 \text{ TeV}^{-1}$ (blue).	219

4.26 The Pseudomass distribution for 2015 data (left) and the pseudomass asymmetry (right).	220
4.27 The Pseudomass distribution for 2016 data (left) and the pseudomass asymmetry (right).	220
4.28 The Pseudomass distribution for 2017 data (left) and the pseudomass asymmetry (right).	221
4.29 The Pseudomass distribution for 2018 data (left) and the pseudomass asymmetry (right).	221
4.30 Normalized backgrounds and signal for year's 2018 luminosity.	223
4.31 On the left is the initial asymmetry and on the right the sagitta from extracted backgrounds.	223
((a)) asymmetry of 2015	223
((b)) extracted from data asymmetry of 2015	223
4.32 On the left is the initial asymmetry and on the right the sagitta from extracted backgrounds.	224
((a)) asymmetry of 2016	224
((b)) extracted from data asymmetry of 2016	224
4.33 On the left is the initial asymmetry and on the right the sagitta from extracted backgrounds.	224
((a)) asymmetry of 2017	224
((b)) extracted from data asymmetry of 2017	224
4.34 On the left is the initial asymmetry and on the right the sagitta from extracted backgrounds.	225
((a)) extracted from data asymmetry of 2018	225
((b)) extracted from data asymmetry of 2018	225
4.35 Pre-fit (left) and post-fit (right) distributions for the 2015 dataset.	230

((a))2015 pre-fit plot	230
((b))2015 post-fit plot	230
4.36 Pre-fit (left) and post-fit (right) distributions for the 2016 dataset.	231
((a))2016 pre-fit plot	231
((b))2016 post-fit plot	231
4.37 Pre-fit (left) and post-fit (right) distributions for the 2017 dataset.	232
((a))2017 pre-fit plot	232
((b))2017 post-fit plot	232
4.38 Pre-fit (left) and post-fit (right) distributions for the 2018 dataset.	233
((a))2018 pre-fit plot	233
((b))2018 post-fit plot	233
4.39 Pre-fit and post-fit plots for the full Run-2 dataset. . .	233
((a))Pre-fit for all Run-2 data	233
((b))Post-fit for all Run-2 data	233
A.1 MDM Browser details from MDT configuration database.	242
A.2 Number of chamber Mezzs filled by MDT configuration database.	242

List of Tables

3.1	The requirements of the high voltage power supply in sTGC and MM detectors	118
3.2	The arrangement of crate and HV boards for sTGC detectors in the cavern for NSW-A and NSW-C	121
3.3	The arrangement of mainframe and HV boards for micromegas in the cavern	127
4.1	Selections on analysis data	201
4.2	Luminosity per year for the entire Run-2	222
A.1	Information stored into the configuration database for the BIS78 chambers.	242

Εκτεταμένη Ελληνική Περίληψη

Το Καθιερωμένο Πρότυπο

Το Καθιερωμένο Πρότυπο της σωματιδιακής φυσικής είναι το θεωρητικό πλαίσιο που περιγράφει τις θεμελιώδεις αλληλεπιδράσεις —ηλεκτρομαγνητική, ασθενή και ισχυρή— καθώς και των σωματιδίων - φορέων τους. Οι φορείς της ασθενούς αλληλεπίδρασης είναι τα μποζόνια W^+ , W^- και Z , τα οποία μεταδίδουν την ασθενή πυρηνική δύναμη, υπεύθυνη για φαινόμενα όπως οι β -διασπάσεις.

Η ενοποίηση της ηλεκτρομαγνητικής και ασθενούς δύναμης μέσω της θεωρίας της ηλεκτρασθενούς σύζευξης (Glashow-Weinberg-Salam) προβλέπει την ύπαρξη των βαρέων μποζονίων. Ο μηχανισμός Higgs προσφέρει τη δυναμική εξήγηση για τη μάζα τους μέσω της αυθόρμητης παραβίασης της συμμετρίας. Το μποζόνιο higgs, το οποίο ανακαλύφθηκε πειραματικά το 2012, είναι θεμελιώδες σε αυτό το θεωρητικό πλαίσιο.

Το Z είναι ηλεκτρικά ουδέτερο και αλληλεπιδρά με όλα τα φορτισμένα λεπτόνια και κουάρκ. Τα ουδέτερα ρεύματα της ασθενούς αλληλεπίδρασης που προκύπτουν από την αλληλεπίδραση του Z επιβεβαιώθηκαν πειραματικά το 1973 (πείραμα Gargamelle), και αποτέλεσαν ισχυρό θεμέλιο του Καθιερωμένου Προτύπου.

Η σύγχρονη ανάλυση των ιδιοτήτων του Z από πειράματα όπως το ATLAS αυξάνει την ακρίβεια της θεωρίας και περιορίζει τις πιθανότητες απόκλισης, θέτοντας αυστηρούς περιορισμούς σε νέα φυσική πέραν του Καθιερωμένου

Προτύπου.

Εισαγωγή στο Πείραμα ATLAS

Το ATLAS (A Toroidal LHC ApparatuS) είναι ένα από τα πιο εμβληματικά πειράματα στον χώρο της φυσικής υψηλών ενεργειών. Είναι εγκατεστημένο στο CERN, στον Μεγάλο Επιταχυντή Αδρονίων (LHC), και έχει ως αποστολή να απαντήσει σε θεμελιώδη ερωτήματα για τη δομή του Σύμπαντος. Με στόχο την κατανόηση της προέλευσης της μάζας, τη φύση της σκοτεινής ύλης, τη δυνατότητα ύπαρξης υπερσυμμετρίας και πρόσθετων διαστάσεων, το ATLAS συμβάλλει αποφασιστικά στη διαμόρφωση της σύγχρονης θεωρητικής και πειραματικής φυσικής.

Το πείραμα σχεδιάστηκε για να καταγράφει τα προϊόντα των συγκρούσεων πρωτονίων σε ενεργειακά επίπεδα που προσομοιώνουν τις συνθήκες αμέσως μετά τη Μεγάλη Έκρηξη. Από την αρχή της λειτουργίας του, το 2009, και ιδιαίτερα μετά την ανακάλυψη του μποζονίου higgs το 2012, το ATLAS αποτέλεσε σημείο αναφοράς για την επιβεβαίωση και πιθανή επέκταση του Καθιερωμένου Προτύπου.

Δομή και Υποσυστήματα του Ανιχνευτή

Ο ανιχνευτής ATLAS έχει κυλινδρική γεωμετρία, μήκους 46 m και διαμέτρου περίπου 25 m, με βάρος περίπου 7000 τόνους. Οργανώνεται σε τέσσερα βασικά υποσυστήματα:

- ο Inner Detector (ID): Εντοπίζεται πλησιέστερα στο σημείο σύγκρουσης και περιλαμβάνει τα συστήματα pixel, silicon microstrips (SCT) και το Transition Radiation Tracker (TRT). Καταγράφει τις τροχιές των φορτισμένων σωματιδίων.
- ο Calorimeters: Περιλαμβάνει ηλεκτρομαγνητικά και αδρονικά θερμιδόμετρα για τη μέτρηση της ενέργειας των ηλεκτρονίων, φωτονίων και αδρονίων.
- ο Muon Spectrometer: Καταλαμβάνει την εξωτερική κυλινδρική περιοχή του ανιχνευτή και χρησιμοποιεί θαλάμους ανίχνευσης για την ανίχνευση των μιονίων.
- ο Magnet System: Αποτελείται από σωληνοειδείς και τοροειδείς μαγνήτες, απαραίτητους για την καμπύλωση των τροχιών και τον υπολογισμό της ορμής των σωματιδίων.

Το σύστημα συντεταγμένων είναι δεξιόστροφο με τον άξονα των z εφαπτομενικό στη δέσμη, τον άξονα των x προς το κέντρο του επιταχυντή και τον άξονα των y κατακόρυφο, ενώ χρησιμοποιούνται οι μεταβλητές ϕ (αζιμουθιακή γωνία), θ (πολική γωνία) και η ψευδοωκύτητα η για την περιγραφή των κατευθύνσεων.

Επιστημονική Συνεισφορά και Συνεργασία

Το ATLAS δεν αποτελεί μόνο ένα τεράστιο επιστημονικό και τεχνολογικό επίτευγμα, αλλά και ένα υπόδειγμα παγκόσμιας συνεργασίας. Περισσότεροι από 3000 φυσικοί, μηχανικοί και φοιτητές από 38 χώρες συμβάλλουν σε αυτό. Οι ομάδες ασχολούνται με την κατασκευή, συντήρηση, λειτουργία

του ανιχνευτή και ανάλυση των δεδομένων.

Η ανακάλυψη του μποζονίου higgs, με ταυτόχρονη παρατήρηση από τα πειράματα ATLAS και CMS, επιβεβαίωσε τον μηχανισμό Higgs ως μέθοδο απόδοσης μάζας στα στοιχειώδη σωματίδια. Πέρα από αυτό, το ATLAS συνεχίζει να διερευνά νέα φυσικά φαινόμενα, πραγματοποιώντας αναζητήσεις για υπερσυμμετρία, σκοτεινή ύλη και βαριά σωματίδια.

Το Σύστημα Ελέγχου Ανιχνευτών (DCS)

Το Detector Control System (DCS) αποτελεί ένα κρίσιμο υποσύστημα που εξασφαλίζει την ασφαλή λειτουργία των υποανιχνευτών. Αναπτύχθηκε με βάση το Joint Controls Project (JCOP), και υλοποιήθηκε σε πλατφόρμα SCADA (WinCC OA). Το DCS παρέχει:

- ο Συνεχή παρακολούθηση λειτουργικών παραμέτρων (τάσεις, θερμοκρασίες κ.ά.).
- ο Μηχανισμούς αυτοπροστασίας και συναγερμών.
- ο Απομακρυσμένο και ιεραρχικό έλεγχο μέσω διεπαφών χρήστη.

Η ύπαρξη ενός τέτοιου συστήματος εγγυάται όχι μόνο την προστασία του εξοπλισμού αλλά και την αξιοπιστία των δεδομένων που συλλέγονται.

Δομή του DCS

Το DCS διαχωρίζεται λειτουργικά σε δύο βασικά μέρη: το Front-End και το Back-End. Το Front-End περιλαμβάνει τις φυσικές μονάδες υλικού, όπως τροφοδοσίες υψηλής και χαμηλής τάσης, ψύκτες, αισθητήρες και ελεγκτές. Αυτά επικοινωνούν με το Back-End, το οποίο βασίζεται σε SCADA λογισμικό (WinCC OA) και παρέχει διεπαφές χρήστη, συστήματα ειδοποίησης, καταγραφή δεδομένων και απομακρυσμένη εποπτεία. Η δομή του DCS είναι ιεραρχική και παραμετροποιήσιμη, με δυνατότητα προσαρμογής ανά υποσύστημα. Παρέχει υποστήριξη για μηχανές καταστάσεων, οπτικοποίηση παραμέτρων σε πραγματικό χρόνο, καθώς και διαγνωστικά σφάλματος. Επιπλέον, η υποστήριξη ιστορικών δεδομένων επιτρέπει την επαναφορά συνθηκών ή την ανασκόπηση λειτουργίας για επίλυση προβλημάτων. Το DCS ενσωματώνει τεχνολογίες Ethernet, fieldbus και OPC για τη διασύνδεση των φυσικών στοιχείων με τα κεντρικά πληροφοριακά συστήματα. Μέσω αυτής της αρχιτεκτονικής, το σύστημα εξασφαλίζει ασφάλεια, επεκτασιμότητα και αδιάλειπτη λειτουργία ακόμη και σε δύσκολες συνθήκες λειτουργίας.

Υλοποίηση για Υποσυστήματα Μιονίων

Η επέκταση του DCS στα υποσυστήματα μιονίων έγινε σταδιακά και περιελάμβανε τόσο υλικοτεχνικές παρεμβάσεις όσο και αναβαθμίσεις λογισμικού. Το υποσύστημα Monitored Drift Tubes (MDT), που αποτελεί την παραδοσιακή τεχνολογία για την ανίχνευση μιονίων, απέκτησε ενσωμάτωση με νέους ελεγκτές και αναθεωρημένα διαγνωστικά.

Παράλληλα, τα νέα υποσυστήματα των Νέων Μικρών Τροχών (New Small Wheel, NSW), δηλαδή τα Micromegas και τα small-strip Thin Gap Chambers (sTGC), εξοπλίστηκαν με μονάδες DCS για τη διαρκή παρακολούθηση τάσεων, ρευμάτων, θερμοκρασιών και λειτουργικών καταστάσεων. Επιπλέον, αναπτύχθηκαν διασυνδέσεις με συστήματα δοκιμών και αυτοδιάγνωσης.

Η εγκατάσταση περιλάμβανε χιλιάδες καλώδια, ηλεκτρονικά εξαρτήματα και προγραμματιζόμενες μονάδες ελέγχου. Όλα αυτά ενοποιήθηκαν μέσα σε ένα αξιόπιστο σύστημα διαχείρισης που δοκιμάστηκε εκτενώς σε εγκαταστάσεις όπως το SR1 (Surface Hall) και το υπόγειο Point-1 του LHC.

Μέτρηση Μάζας του Μποζονίου Z

Η όσο το δυνατό ακριβέστερη μέτρηση της μάζας του ουδέτερου μποζονίου Z αποτελεί κρίσιμο τεστ εγκυρότητας του Καθιερωμένου Προτύπου. Το πείραμα ATLAS παρέχει μεγάλο όγκο δεδομένων από συγκρούσεις πρωτονίων και επιτρέπει την ανακατασκευή γεγονότων τύπου $Z \rightarrow \mu^+ \mu^-$. Τα δύο παρατηρούμενα μίονια επιτρέπουν τον υπολογισμό της μάζας του Z μέσω της συνολικής ενέργειας και ορμής τους.

Η πλατφόρμα Histmaker, που αναπτύχθηκε για στατιστική ανάλυση δεδομένων ανιχνευτών, χρησιμοποιείται για την παραγωγή κατανομών ενέργειας, γωνιακής διασποράς και αθροιστικής ορμής των μιονίων. Αυτές οι κατανομές συγκρίνονται με θεωρητικές προβλέψεις και προσομοιώσεις Monte Carlo, παρέχοντας μια μεθοδολογία υψηλής ακρίβειας για τον προσδιορισμό της μάζας.

Επιπλέον, η σύγκριση των πειραματικών δεδομένων με τις αναμενόμενες θεωρητικές κατανομές αποκαλύπτει τυχόν συστηματικές μετατοπίσεις που θα μπορούσαν να επηρεάσουν την τελική εκτίμηση.

Συστηματικά Σφάλματα και Διορθώσεις

Μία από τις μεγαλύτερες προκλήσεις στη μέτρηση της μάζας του μποζονίου Z είναι η αντιμετώπιση των συστηματικών σφαλμάτων που προκύπτουν από ατέλειες στον ανιχνευτή και στα μαγνητικά πεδία. Ένα από τα σημαντικότερα σφάλματα αυτού του είδους είναι το sagitta bias – δηλαδή η συστηματική μετατόπιση στην ανακατασκευή της καμπυλότητας της τροχιάς των φορτισμένων σωματιδίων.

Το sagitta bias εμφανίζεται όταν υπάρχει ασυμφωνία ανάμεσα στο πραγματικό και στο μοντελοποιημένο μαγνητικό πεδίο, ή σε περίπτωση που δεν έχουν βαθμονομηθεί σωστά οι θέσεις των ανιχνευτικών στοιχείων. Το αποτέλεσμα είναι η αλλοίωση της της εκτιμώμενης ορμής των σωματιδίων και, κατά συνέπεια, της υπολογιζόμενης μάζας του Z .

Στην ανάλυση των δεδομένων του πειράματος ATLAS εφαρμόστηκαν στρατηγικές διόρθωσης που περιλάμβαναν:

- ο Χρήση ελεγχόμενων δειγμάτων δεδομένων για εκτίμηση του σφάλματος.
- ο Παραμετρική προσαρμογή της μεροληψίας ανάλογα με την γωνιακή κατανομή των μιονίων.
- ο Εφαρμογή διορθώσεων βάσει δεδομένων προσομοίωσης Monte Carlo.

Αυτές οι διορθώσεις επέτρεψαν τη σημαντική μείωση της συστηματικής αβεβαιότητας, καθιστώντας την τελική εκτίμηση της μάζας αρκετά ακριβέστερη.

Προσεγγίσεις Προσαρμογής Καμπυλών

Η τελική φάση της ανάλυσης για τη μέτρηση της μάζας του μποζονίου Z περιλαμβάνει τη χρήση τεχνικών fitting στις κατανομές της αθροιστικής ορμής των μιονίων. Η διαδικασία fitting στοχεύει στην ακριβή προσέγγιση του μέγιστου της κατανομής μάζας και βασίζεται στην παραδοχή συγκεκριμένων στατιστικών μοντέλων, όπως η κατανομή Breit-Wigner ή η Gaussian με τροποποιήσεις.

Οι τεχνικές fitting που εφαρμόστηκαν:

- ο Περιλάμβαναν πολυπαραμετρικά μοντέλα που λαμβάνουν υπόψη την ενεργειακή ανάλυση του ανιχνευτή.
- ο Συγκρίθηκαν με δεδομένα Monte Carlo για επικύρωση της ακρίβειας.
- ο Ενσωμάτωσαν τις διορθώσεις sagitta bias για να μειώσουν τις μετατοπίσεις.

Τα αποτελέσματα για τη μέτρηση της μάζας του μποζονίου Z συγκρίθηκαν με την αναφορά των πειραμάτων LEP-DELPHI, $91.1876 \pm 0.0021 \text{ GeV}/c^2$, και παρουσίασαν εξαιρετική συμφωνία. Η διαδικασία fitting επιβεβαίωσε πως, με τις σωστές παραμέτρους, η μέτρηση από το πείραμα ATLAS μπορεί να είναι συμβατή εντός πολύ μικρής αβεβαιότητας με τα ιστορικά δεδομένα,

ενισχύοντας τη θέση του πειράματος ως πρότυπο ακρίβειας στη σωματιδιακή φυσική.

Chapter 1

High Energy Physics and CERN

This chapter will give an overview for the core of the particles physics, the standard model and the existence of the experiments of CERN.

1.1 The Standard Model

The Standard Model (SM) is a quantum field theory that unifies special relativity and quantum mechanics to describe the fundamental particles and their interactions. The interactions are encoded in the SM Lagrangian, which is a non-Abelian gauge theory characterized by the symmetry group shown in Equation 1.1:

$$G_{SM} = SU(3)_C \times SU(2)_L \times U(1)_Y \quad (1.1)$$

where:

- $SU(3)_C$ is the non-Abelian gauge group associated with the strong interaction in Quantum Chromodynamics (QCD). It corresponds to a special unitary group in three dimensions and is often referred to as the color group. The $SU(3)_C$ group has $3^2 - 1 = 8$ generators, corresponding to eight gluons—vector bosons that mediate the strong force between quarks inside hadrons.
- $SU(2)_L \times U(1)_Y$ represents the electroweak sector of the Standard Model. $SU(2)_L$ governs the weak isospin symmetry and mediates interactions between particles of different flavors, such as those involved in beta decay. $U(1)_Y$ corresponds to the hypercharge symmetry and governs the electromagnetic interaction through the conservation of electric charge, mediated by the photon.

The full dynamics of the Standard Model are described by the Lagrangian in Equation 1.2:

$$\mathcal{L}_{SM} = \mathcal{L}_{EW} + \mathcal{L}_{QCD} + \mathcal{L}_{Higgs} + \mathcal{L}_{Yukawa} \quad (1.2)$$

where:

- \mathcal{L}_{EW} : Describes the electroweak interactions, unifying electromagnetism and the weak force under a common framework.
- \mathcal{L}_{QCD} : Encodes the strong interaction described by Quantum Chromodynamics, including gluon self-interactions and their couplings to quarks.
- \mathcal{L}_{higgs} : Represents the dynamics of the Higgs field and includes the

Higgs boson, which is responsible for spontaneous symmetry breaking and mass generation.

- \mathcal{L}_{Yukawa} : Describes Yukawa interactions between the Higgs field and fermions (quarks and leptons), enabling the generation of fermion masses.

1.2 The Standard Model and Particle Physics

The field of particle physics is dedicated to studying particles and their interactions. The first elementary particle discovered was the electron, identified by J. J. Thomson in 1897. Subsequently, the treatment of electromagnetic radiation as a particle and the discovery of the atomic nucleus became two pivotal moments that transformed modern physics. These breakthroughs led to the discovery of numerous new particles and further exploration of matter's structure. The significant advancements in the field culminated in the creation of a theoretical framework known as the Standard Model of particle physics. This model categorizes fundamental particles based on their spin properties and explains their interactions. The Standard Model divides these particles into two groups: fermions, which have a half-integer spin, and bosons, which have an integer spin.

The Standard Model includes 12 elementary particles of spin $1/2$, known as fermions. Fermions respect the Pauli exclusion principle, meaning that two identical fermions cannot simultaneously occupy the same quantum state. Each fermion has a corresponding antiparticle, which are particles that have corresponding properties with the exception of opposite

charges. Fermions are classified based on how they interact, which is determined by the charges they carry, into two groups: quarks and leptons. Within each group, pairs of particles that exhibit similar physical behaviors are then grouped into generations. Each member of a generation has a greater mass than the corresponding particle of prior generations. Thus, there are three generations of quarks and leptons. First-generation particles do not decay, they comprise all of ordinary (baryonic) matter. Specifically, all atoms consist of electrons orbiting around the atomic nucleus, ultimately constituted of up and down quarks. On the other hand, second- and third-generation charged particles decay with very short half-lives and can only be observed in high-energy environments. Neutrinos of all generations also do not decay, and pervade the universe, but rarely interact with baryonic matter, only via the weak interactions.

There are six quarks: up, down, charm, strange, top, and bottom. Quarks carry color charge, and hence interact via the strong interaction. The color confinement phenomenon results in quarks being strongly bound together such that they form color-neutral composite particles called hadrons; quarks cannot individually exist and must always bind with other quarks. Hadrons can contain either a quark-antiquark pair (mesons) or three quarks (baryons). The lightest baryons are the nucleons: the proton and neutron. Quarks also carry electric charge and weak isospin, and thus interact with other fermions through electromagnetism and weak interaction. The six leptons consist of the electron, electron neutrino, muon, muon neutrino, tau, and tau neutrino. The leptons do not carry color charge, and do not respond to strong interaction. The charged leptons carry an electric charge of $-1e$, while the three neutrinos carry zero electric charge. Thus, the neutrinos' motions are influenced by only the weak interaction and gravity, making them difficult to observe.

The Standard Model includes four kinds of gauge bosons of spin 1, with bosons being quantum particles containing an integer spin. The gauge bosons are defined as force carriers, as they are responsible for mediating the fundamental interactions. The interaction between the fermions is expressed as an exchange of gauge bosons, as shown in Fig. 1.1, which are the mediators of the four fundamental forces of nature, in relative strength order:

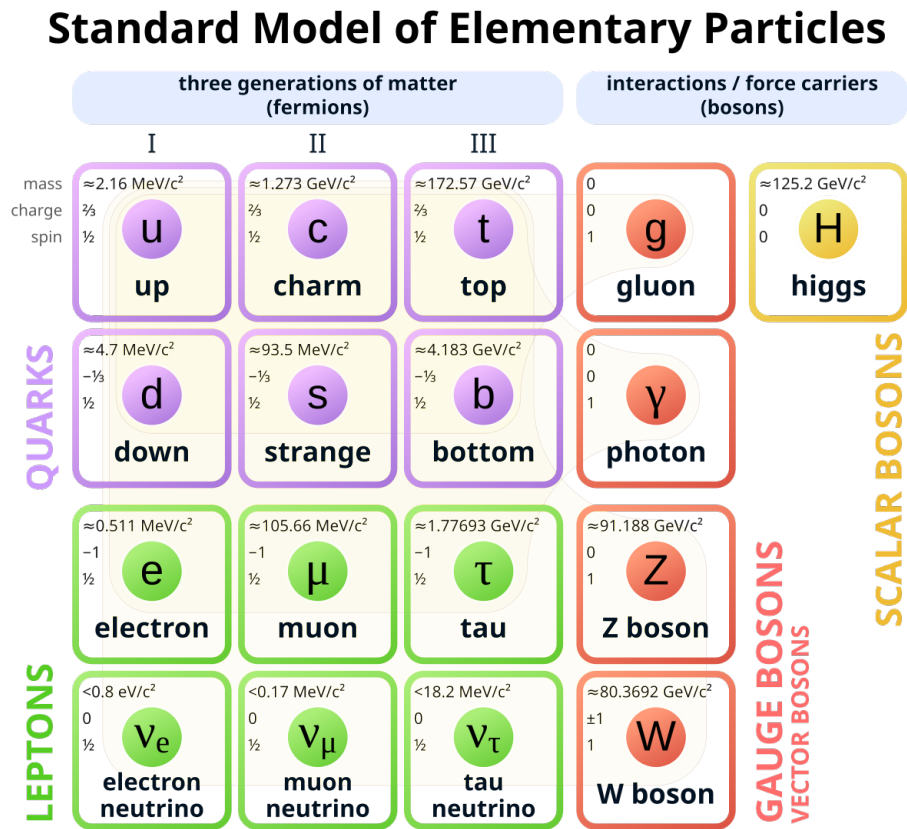


Figure 1.1: The elementary particles of the Standard Model.

- Strong interaction : In nature, in addition to elementary particles, we also observe another category of composite particles called hadrons. Hadrons are divided into two families: mesons, which consist of a quark-antiquark pair, and baryons, which are made up of

three quarks. A well-known example of mesons is the pion triplet (π^+ , π^0 , π^-), where the superscript represents the charge. Conversely, prominent baryons include the neutron (n) and the proton (p), which make up atomic nuclei. The quarks in these particles are bound together by the strong interaction, mediated by massless gluons. This fundamental force operates over a typical range of approximately 10^{-15} m.

- Weak Interaction :

The weak interaction is a short-range fundamental force that acts on the fermions of the Standard Model. It is termed "weak" because its field strength is several orders of magnitude lower than that of the electromagnetic and strong interactions at a given range. However, at extremely small distances, the weak force becomes stronger than the electromagnetic interaction. This interaction is mediated by the exchange of massive gauge bosons, specifically the W^+ , W^- , and Z bosons. In nuclear physics, the weak interaction is responsible for beta decay (β^-). Additionally, the weak and electromagnetic interactions are unified under a single framework known as electroweak theory.

- Electromagnetic Interaction :

The electromagnetic interaction is the second strongest fundamental force in nature and is mediated by the photon (γ). It acts on charged leptons and quarks, with its strength varying significantly with distance. Unlike the strong and weak interactions, the electromagnetic force has an infinite range, playing a crucial role in binding electrons to atoms and explaining numerous everyday phenomena.

- Gravitational force:

Gravity is the fourth and weakest fundamental force of nature. While its range is infinite, its strength is many orders of magnitude weaker than the other three fundamental forces, making its influence on elementary particles negligible. Gravity is described by Einstein's general theory of relativity as a classical field theory, with no established quantum counterpart. As a result, particle physicists often focus primarily on the other three fundamental forces.

The higgs particle is a massive scalar elementary particle proposed by Peter W. Higgs, Robert Brout and François Englert, in 1964. Higgs demonstrated that Goldstone's 1962 theorem, which addresses the spontaneous breaking of continuous symmetry, predicts a third polarization of a massive vector field. This led to the suggestion of the Higgs boson as the massive spin-zero particle, originating from Goldstone's original scalar doublet. The higgs boson is a crucial component of the Standard Model, possessing no intrinsic spin and thus classified as a spin-0 boson. In the Standard Model, the higgs boson plays a vital role by explaining why most elementary particles, except for the photon and gluon, have mass. It specifically accounts for why the photon remains massless, while the W and Z bosons are heavy. The differences in mass between particles like the photon and the W/Z bosons, as well as the distinction between electromagnetism (mediated by the photon) and the weak force (mediated by the W and Z bosons), are essential to understanding the structure of both microscopic and macroscopic matter. In electroweak theory, the higgs boson is responsible for giving mass to leptons (electron, muon, and tau) and quarks. Since the higgs boson is massive, it must interact with itself. Due to its large mass and its tendency to decay almost instantly after being created, the higgs boson can only be detected using

high-energy particle accelerators. Experiments to detect and study the higgs boson began at CERN's Large Hadron Collider (LHC) in early 2010, and similar experiments were conducted at Fermilab's Tevatron until its closure in late 2011. The Standard Model's mathematical consistency requires that any mechanism generating the masses of elementary particles must become visible at energies above 1.4 TeV. Thus, the LHC, designed to collide two 7 TeV proton beams, was built to answer the question of whether the higgs boson exists. On July 4, 2012, two experiments at the LHC, ATLAS and CMS, independently announced the discovery of a new particle with a mass of approximately 125 GeV/c² (about 133 proton masses or 10⁻²⁵ kg), which was "consistent with the higgs boson". On March 13, 2013, this particle was officially confirmed as the long-sought higgs boson.

1.3 CERN

CERN[1], the European Organization for Nuclear Research, is an inter-governmental institution that operates the largest particle physics laboratory in the world and comprising over 20 Member States. Headquartered in Geneva, its facilities span both sides of the French-Swiss border. CERN's[2] primary mission is to foster global collaboration in high-energy particle physics research. To achieve this, it designs, constructs, and operates particle accelerators and related experimental facilities. Currently, more than 11,000 scientists from research institutes worldwide utilize CERN's infrastructure for their experiments. The organization's accelerator complex consists of a series of machines that progressively boost particle beam energy. Each accelerator transfers the beam to the

next, raising its energy further. The centerpiece of this system is the Large Hadron Collider (LHC), CERN's most advanced accelerator.



Figure 1.2: CERN's main site in Meyrin, Switzerland, looking towards the French border.

1.4 The Large Hadron Collider and the ATLAS experiment

The Large Hadron Collider (LHC)[3] is the greatest and most famous accelerator in the world, operated by the European Organisation of Particle Physics (CERN). It is installed in a circular tunnel, that initially housed the Large Electron-Positron accelerator (LEP)[4], on average 100 m below the the earth's surface with a circumference of 26.7 Km. The LHC machine is designed to accelerate counter-rotating proton beams up to an energy of 7 TeV and collide them at the nominal centre-of- mass energy of 14 TeV, with the aim to reveal the physics at higgs sector and beyond the SM. Before the injection in the LHC ring, the beams are accelerated in several steps.

The accelerated beams at the LHC collide every 25 ns at four primary interaction points (IPs), where the main experiments ATLAS (A Toroidal LHC Apparatus)[5], CMS (Compact Muon Solenoid) [6], and ALICE (A Large Ion Collider Experiment)[7] are located. Additionally, LHCb (Large Hadron Collider beauty)[8], a forward spectrometer experiment, serves as the fourth largest experiment. It exploits p-p collisions as all the other 3 experiments but detects only the forward particles on one side of the beam. ATLAS and CMS are versatile, general-purpose experiments designed to precisely measure Standard Model (SM) processes and search for signs of new physics. A milestone achievement of these experiments was the discovery of the higgs boson, using data collected in 2011 and 2012, which opened new avenues for exploring physics beyond the SM. In contrast, LHCb and ALICE specialize in specific phenomena. LHCb focuses on studying decay products of charm and beauty hadrons, while ALICE investigates quark-gluon plasma in heavy-ion collisions using lead (Pb) ion beams provided by the LHC.

Several smaller, specialized experiments complement the primary ones. TOTEM (TOTAl Elastic and diffractive cross-section Measurement)[9], located near the CMS IP, examines total proton-proton cross-sections and the detailed structure of protons. LHCf (Large Hadron Collider forward)[10], positioned near the ATLAS IP, studies processes in the "forward" region close to the particle beam, including extremely high-energy cosmic rays. MoEDAL (Monopole and Exotics Detector At the LHC)[11], situated near LHCb, searches for magnetic monopoles and other exotic particles that could point to new physics beyond the SM. Lastly, FASER (Forward Search Experiment)[12], the newest addition to the LHC, is located 480 m from the ATLAS IP. It focuses on detecting light, weakly interacting particles and studying neutrino interactions.

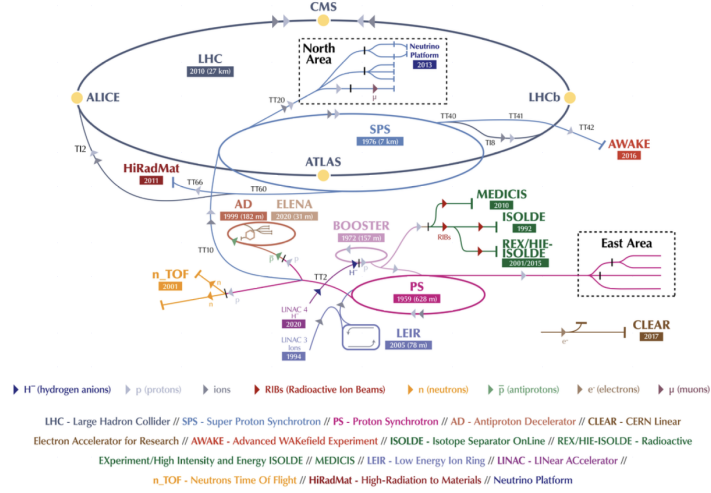


Figure 1.3: The schematic representation of the accelerators-injectors of LHC.

1.5 The High Luminosity LHC

The High-Luminosity Large Hadron Collider (HL-LHC) project is designed to enhance the performance of the LHC, significantly increasing the potential for groundbreaking discoveries beyond 2030. Its primary goal is to boost the integrated luminosity to ten times the original design value of the LHC. Luminosity is a key measure of an accelerator's performance, directly related to the number of collisions occurring over time. A higher luminosity allows experiments to collect more data, improving the chances of detecting rare processes. Expected to be operational by mid-2030, the HL-LHC will enable physicists to explore established phenomena, such as the higgs boson, with greater precision and potentially uncover new, rare processes. For instance, it is projected to produce at least 15 million higgs bosons annually, compared to approximately three million in 2017. The HL-LHC project was identified as the top priority

in the 2013 European Strategy for Particle Physics. Its development relies on advanced technological innovations. The initial phase, launched in 2011, was partially funded by the European Commission's Seventh Framework Programme (FP7) and involved multiple laboratories from CERN's Member States, as well as contributions from the United States, Japan, and Russia. The design phase concluded in October 2015 with the release of a Preliminary Design Report (PDR), marking the transition to the construction phase at CERN and within industry. The Technical Design Report (TDR), first published in 2017 based on pre-2016 modifications, was finalized in 2020. Civil engineering work commenced in April 2018. Led by CERN, the HL-LHC project is supported by an international collaboration of 44 institutions across 20 countries. Most participating institutions are from European nations, including Italy, Spain, Sweden, and the United Kingdom, alongside contributions from CERN's non-Member States such as the United States, Japan, and Canada.

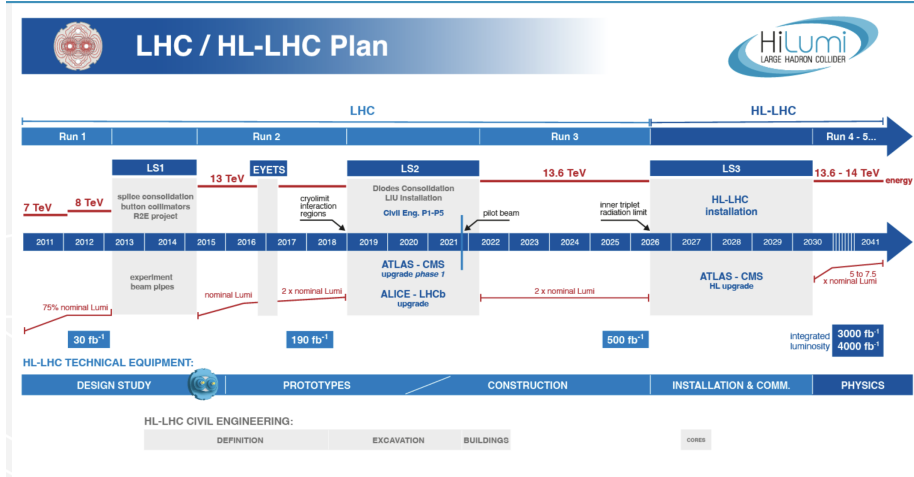


Figure 1.4: HL-LHC plan with last update January 2025.

Luminosity is not a fixed value but degrades over time due to various factors. Reasons like collisions, scattering of particles or beam-beam interactions, contribute to the gradual reduction of luminosity during data

taking.

During Run-1 (2010–2012), the LHC delivered a total integrated luminosity of $\int L dt = 28.26 \text{ fb}^{-1}$ at a center-of-mass energy of 14 TeV from proton–proton (p – p) collisions. This dataset enabled significant experimental achievements, most notably the discovery of the higgs boson.

The highly successful first run of the LHC concluded in December 2012, followed by Long Shutdown 1 (LS1)—a major two-year maintenance and upgrade period for both the accelerator and its experiments. This work was essential to advancing the LHC program. Run-2, which began in early 2015, was designed to operate at twice the center-of-mass energy (14 TeV) with a smaller bunch crossing (BC) interval of approximately 25 ns. As a result, luminosity was expected to increase to $L \approx 1 \times 10^{34} \text{ cm}^{-2} \text{ s}^{-1}$.

According to the current LHC schedule (Fig. 1.4), two additional shutdown periods were planned: Long Shutdown 2 (LS2) in 2019 and Long Shutdown 3 (LS3) in 2024. Following LS2, upgrades to the injector chain and the LHC itself would further increase luminosity to approximately $L = 2 \times 10^{34} \text{ cm}^{-2} \text{ s}^{-1}$. The transition from the LHC to the High-Luminosity LHC (HL-LHC) is set to occur during LS3, with over 3000 fb^{-1} of data expected to be delivered during Run-3. The HL-LHC will present a particularly challenging environment for experiments, as the predicted peak luminosity for ATLAS and CMS could reach $L = 7.5 \times 10^{34} \text{ cm}^{-2} \text{ s}^{-1}$. To handle the significantly higher particle rates, a series of upgrades has been proposed for the LHC experiments, ensuring their continued operation during the HL-LHC era.

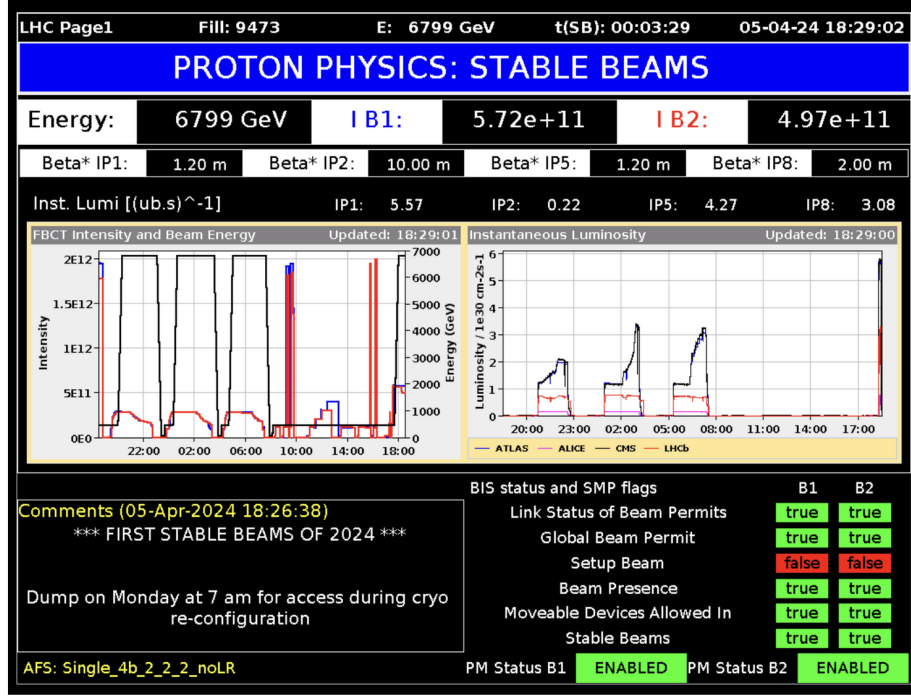


Figure 1.5: LHC Page on April 2024 on stable beams.

1.6 The experiments of LHC

Data collection from accelerator experiments is carried out using particle detectors. These detectors are arranged with cylindrical symmetry around the interaction points (IPs) to directly or indirectly capture the collision products. Typically, a detector consists of tracking systems within a solenoidal magnetic field, surrounded by calorimeters and particle identification detectors. The solenoid field, aligned parallel to the colliding beams, causes the particles' trajectories to bend. In most detectors, the outermost layer features a muon spectrometer. In the following sections, we will introduce the three main experiments—CMS, ALICE, and LHCb while in the next chapter will be given a more detailed discussion for the ATLAS detector.

1.6.1 The CMS Experiment

The Compact Muon Solenoid (CMS) is a general-purpose detector at the Large Hadron Collider (LHC). It has a broad physics programme ranging from studying the Standard Model (including the higgs boson) to searching for extra dimensions and particles that could make up dark matter. Although it has the same scientific goals as the ATLAS experiment, it uses different technical solutions and a different magnet-system design.

The CMS detector is built around a huge solenoid magnet. This takes the form of a cylindrical coil of superconducting cable that generates a field of 4 T, about 100,000 times the magnetic field of the Earth. The field is confined by a steel “yoke” that forms the bulk of the detector’s 14,000-tonne weight.

An unusual feature of the CMS detector is that instead of being built in-situ like the other giant detectors of the LHC experiments, it was constructed in 15 sections at ground level before being lowered into an underground cavern near Cessy in France and reassembled. The complete detector is 21 m long, 15 m wide and 15 m high.

1.6.2 The Alice Experiment

ALICE (A Large Ion Collider Experiment) is a specialized detector at the Large Hadron Collider (LHC) designed for heavy-ion physics. Its primary goal is to explore the properties of strongly interacting matter at extreme energy densities, where a unique state of matter known as quark-gluon

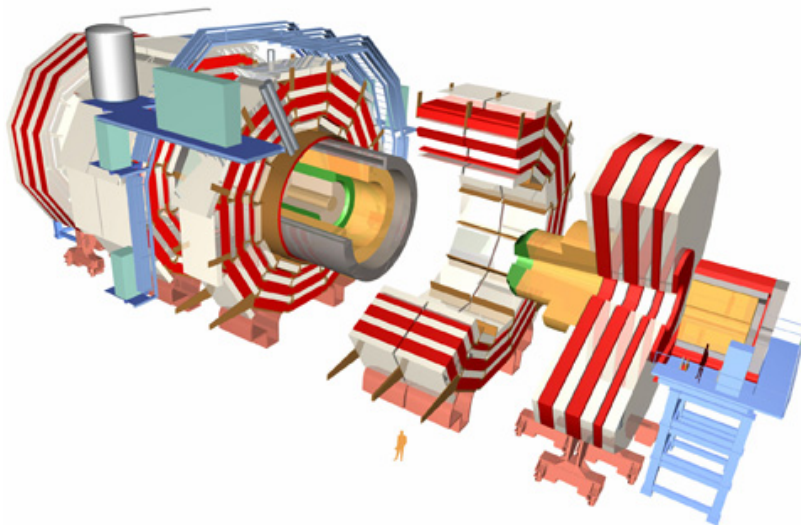


Figure 1.6: The CMS Experiment

plasma emerges.

In the present-day universe, all ordinary matter is composed of atoms. Each atom consists of a nucleus made up of protons and neutrons (except hydrogen, which has no neutrons), surrounded by a cloud of electrons. Protons and neutrons themselves are composed of quarks, which are held together by force-carrying particles called gluons. However, quarks have never been observed in isolation, as they are permanently confined within composite particles like protons and neutrons. This phenomenon is known as confinement.

Collisions at the LHC generate temperatures exceeding 100,000 times those at the Sun's core. During specific periods each year, the LHC collides lead ions, recreating conditions similar to those moments after the Big Bang. Under such extreme circumstances, protons and neutrons disintegrate, allowing quarks to break free from their gluon bonds, forming quark-gluon plasma. Understanding this phase is crucial for quantum chromodynamics (QCD), particularly in studying confinement and

a phenomenon known as chiral symmetry restoration. The ALICE collaboration investigates the quark-gluon plasma as it expands and cools, analyzing how it transitions into the particles that make up the matter of our universe today.

To conduct these studies, the ALICE collaboration utilizes the massive 10,000-tonne ALICE detector, measuring 26 m in length, 16 m in both height and width. Positioned in an underground cavern 56 m beneath the surface near St Genis-Pouilly, France, it receives particle beams from the LHC.

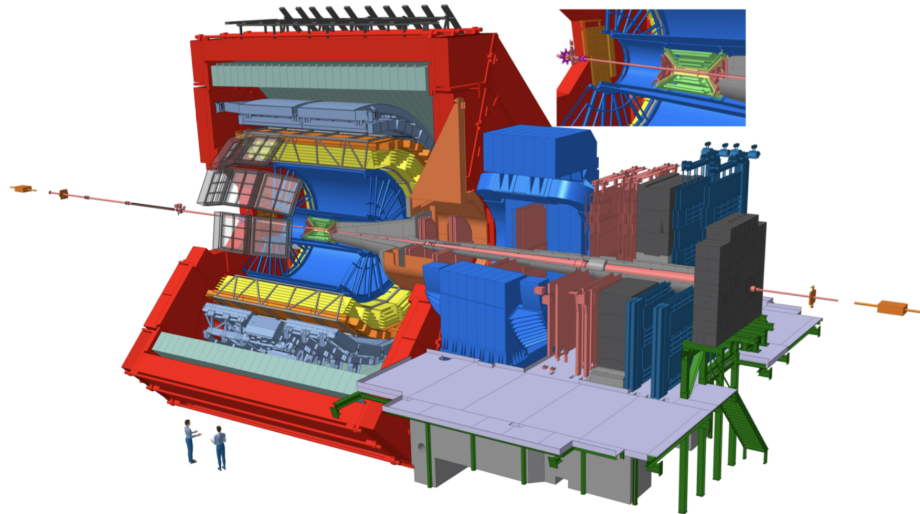


Figure 1.7: The Alice experiment structure

1.6.3 The LHCb Experiment

The Large Hadron Collider beauty (LHCb) experiment focuses on studying the subtle differences between matter and antimatter by analyzing a specific type of particle known as the "beauty quark" or "b quark."

Unlike the ATLAS and CMS experiments, which enclose the entire collision point with a detector, LHCb employs a sequence of subdetectors designed to capture mainly forward-moving particles—those propelled in a single direction by the collision. The first subdetector is positioned near the collision point, while the others are arranged in succession over a span of 20 m.

The LHC produces a variety of quark types, which rapidly decay into other forms. To detect b quarks, LHCb utilizes advanced, movable tracking detectors placed close to the beams circulating within the collider.

The LHCb detector, weighing 5,600 tonnes, consists of a forward spectrometer and planar detectors. It measures 21 m in length, 10 m in height, and 13 m in width, and is located 100 m underground near Ferney-Voltaire, France.

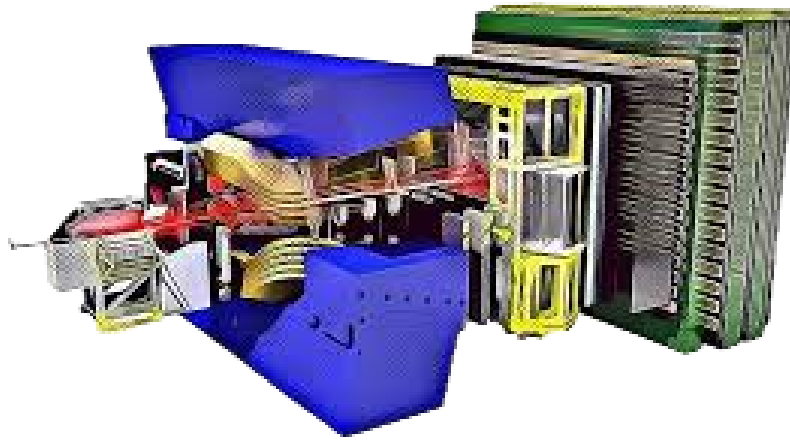


Figure 1.8: The LHCb experiment structure

Bibliography

- [1] J. Krige, "Studies in CERN history", CHS-32, June 1991. <https://cds.cern.ch/record/232756/files/CERN-CH-32.pdf>
- [2] Official CERN Website, "CERN — Accelerating Science". <https://home.cern/>
- [3] L. Evans and P. Bryant, "LHC Machine", J. Instrum., vol. 3, S08001, 2008. <https://iopscience.iop.org/article/10.1088/1748-0221/3/08/S08001>
- [4] T. Taylor and D. Treille, "The Large Electron Positron Collider (LEP): Probing the Standard Model", World Scientific, 2017. https://cds.cern.ch/record/2312570/files/9789814749145_0007.pdf
- [5] ATLAS Public Website, CERN, "The ATLAS Experiment". <https://atlas.cern/Discover/Detector>
- [6] CMS Official Website, CERN, "The CMS Experiment". <https://cms.cern/detector>
- [7] CERN Science Experiments Portal, CERN, "The ALICE Experiment". <https://home.cern/science/experiments/alice>

- [8] CERN Science Experiments Portal, CERN, "The LHCb Experiment". <https://home.cern/science/experiments/lhcb>
- [9] S. Giani et al., "Upgrade of the TOTEM T2 Telescope, Technical Design Report", CERN-LHCC-2019-007; TOTEM-TDR-004. <https://cds.cern.ch/record/2677468>
- [10] CERN Science Experiments Portal, CERN, "The LHCf experiment uses particles thrown forward by LHC collisions to simulate cosmic rays". <https://home.cern/science/experiments/lhcf>
- [11] CERN Science Experiments Portal, CERN, "The MoEDAL Experiment". <https://home.cern/science/experiments/moedal-mapp>
- [12] FASER Official Website, CERN, "FASER: The ForwArd Search Experiment". <https://faser.web.cern.ch/about-the-experiment>

Chapter 2

The ATLAS Experiment

2.0.1 The ATLAS Detector

ATLAS, or A Toroidal LHC ApparatuS, is one of the big particle physics experiments at CERN's Large Hadron Collider (LHC). Located in an underground cavern in the Swiss part of CERN, the ATLAS detector is the largest detector ever constructed for a particle collider. Cylindrical in shape, it measures 46 m in length, about 25 m in diameter, and weighs approximately 7000 tonnes. Designed to explore fundamental questions about the Universe, ATLAS investigates the basic forces that have shaped our cosmos since the beginning of time and that may determine its fate. Potential discoveries include evidence for extra dimensions in space, the unification of fundamental forces, and insights into dark matter. The detector uses a right-handed coordinate system, with the interaction point (IP) as its origin, where the beam direction defines the z-axis. The x-axis points from the IP to the center of the LHC ring, while the y-axis points upward, slightly tilted from the vertical. ATLAS is divided into two sides,

A-side and C-side, reflecting positive and negative z -values. In cylindrical coordinates, the azimuthal angle ϕ is measured around the beam axis from $-\pi$ to $+\pi$, while the radial component measures distance from the beam line. The pseudorapidity is defined as $\eta = -\ln(\tan \frac{\theta}{2})$, which is related to the polar angle in the relativistic limit. The ATLAS collaboration brings together over 3000 scientists from 182 institutions across 38 countries to advance our understanding of particle physics through high-energy proton collisions produced by the LHC.

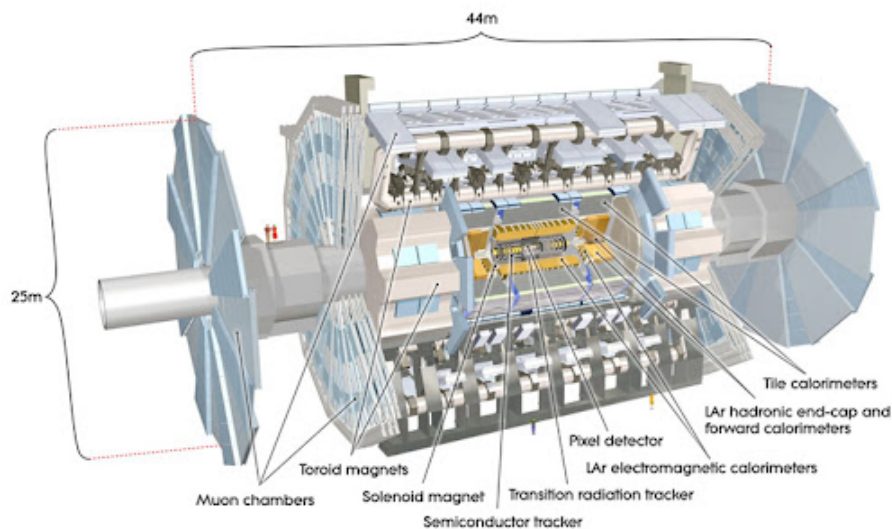


Figure 2.1: An illustration of the ATLAS Magnet System.

The main ATLAS subsystems are:

- Magnet System
- Inner Detector
- Calorimeters
- Muon Spectrometer

- Trigger and Data Acquisition System (TDAQ)

2.0.2 The Magnet system

Charged particles produced in proton–proton collisions would travel in straight lines in the absence of magnetic fields. By bending their trajectories with strong magnetic fields, ATLAS can measure their momentum and determine their charge. This is done using two different types of superconducting magnet systems[1] – solenoidal and toroidal. These impressive systems are cooled to about 4.5 K (-268°C) in order to provide the necessary strong magnetic fields. The main sections of the magnet system are: Central Solenoid Magnet, Barrel Toroid and End-cap Toroids.

- Central Solenoid Magnet: the ATLAS solenoid surrounds the inner detector at the core of the experiment. This powerful magnet is 5.8 m long, 2.56 m in diameter and weighs over 5 tonnes. It provides a 2 T magnetic field in just 4.5 cm thickness. This is achieved by embedding over 9 km of niobium-titanium superconductor wires into strengthened, pure aluminum strips, thus minimizing possible interactions between the magnet and the particles being studied.
- Toroid Magnet: the ATLAS toroids use a series of eight coils to provide a magnetic field of up to 3.5 T, used to measure the momentum of muons. There are three toroid magnets in ATLAS: two at the ends of the experiment, and one massive toroid surrounding the center of the experiment. At 25.3 m in length, the central toroid is the largest toroidal magnet ever constructed. It is unique in particle physics and an iconic element of ATLAS. It uses over 56 km

of superconducting wire and weighs about 830 tonnes. The end-cap toroids extend the magnetic field to particles leaving the detector close to the beam pipe. Each end-cap is 10.7 m in diameter and weighs 240 tonnes.

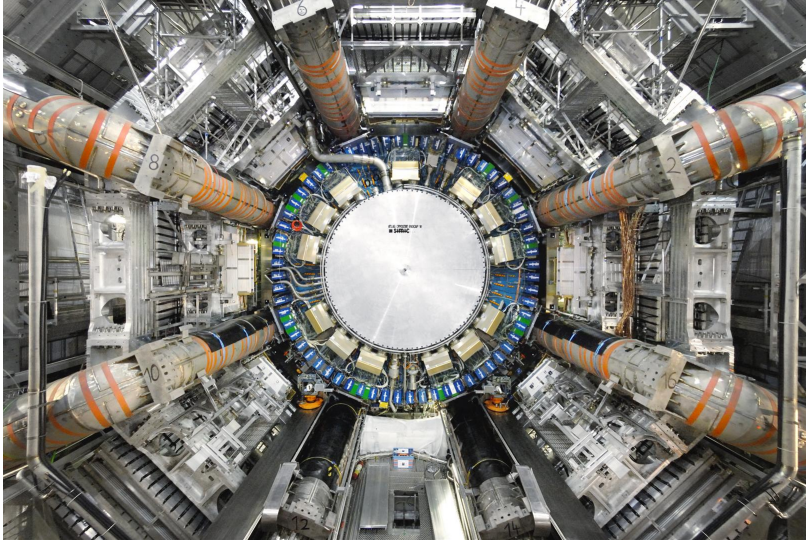


Figure 2.2: The ATLAS Magnets

2.0.3 The Inner Detector

The Inner Detector (ID)[2] is the first part of ATLAS to detect the decay products of the collisions. It is very compact and highly sensitive. The Inner Detector (ID) at the core of the ATLAS experiment provides precise tracking of charged particles across a pseudorapidity range of $|\eta| \leq 2.5$. Encased within a 7-meter-long, 1.15-meter-radius cylindrical solenoid generating a 2 T magnetic field, the ID comprises three main sub-detectors: the Pixel Detector, the Semiconductor Tracker (SCT), and the Transition Radiation Tracker (TRT). Together, these components combine high-resolution inner sensors with outer detectors, ensuring accurate

trajectory tracking within the solenoid.

The Pixel Detector, positioned closest to the beamline, features three silicon pixel layers in the barrel and three disks on each end-cap, with its innermost layer located just 50.5 mm from the interaction point (IP). To address radiation-related challenges and improve impact parameter resolution, an additional Insertable B-Layer (IBL) was introduced during LS1, reducing the distance from the beam axis to 33.25 mm.

Following the Pixel Detector, the SCT includes four silicon micro-strip layers in the barrel and nine disks per end-cap, crucial for measuring transverse momentum by capturing four track points per particle. On the outermost edge, the TRT consists of 50 layers of gaseous straw tubes, offering data points at 36 locations per track and enhancing electron identification through photon transition radiation detection. The ID's arrangement in concentric cylinders around the beamline in the barrel and perpendicular trays in the end-caps allows accurate momentum, origin, and energy measurements based on the curvature of particle orbits. This layered design of high-resolution detectors allows the ID to effectively operate under nominal and upgraded luminosity conditions.

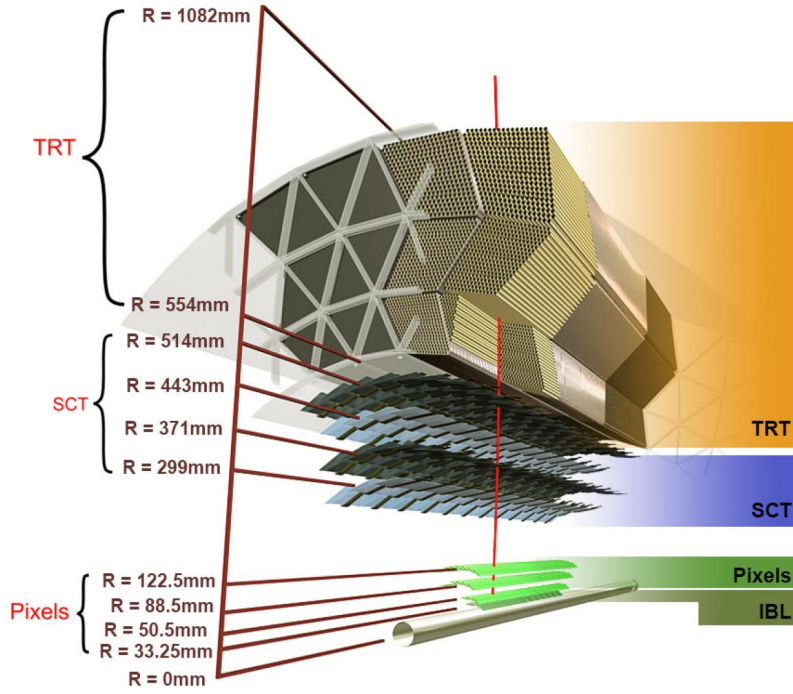


Figure 2.3: The ATLAS Inner Detector

2.0.4 The ATLAS Calorimeters

The ATLAS Calorimeters, as shown in Figure 2.4, include both Electromagnetic and Hadronic Calorimeters, each with barrel and endcap components. Positioned outside the Inner Detector and Solenoid Magnet, their primary function is to absorb the energy of most particles produced by collisions, compelling them to deposit all of their energy within the detector material. Designed with complete ϕ -symmetry and comprehensive coverage along the beam axis, the ATLAS Calorimeters use a range of sampling detectors, with the barrel region covering $|\eta| < 1.5$ and the endcap region spanning $1.4 < |\eta| < 3.2$.

Calorimeters measure the energy a particle loses as it passes through by

using layered materials. High-density “passive” layers like lead alternate with “active” materials, such as liquid argon or solid lead-glass, to absorb and detect particles’ energy. Electromagnetic calorimeters are optimized for electrons and photons, while hadronic calorimeters measure the energy of hadrons—particles containing quarks, such as protons and neutrons. These calorimeters are effective at stopping most known particles, except for muons and neutrinos.

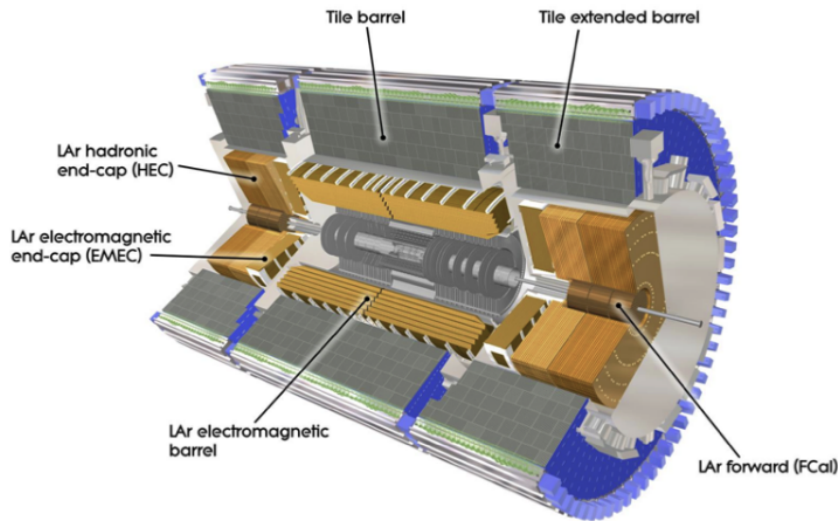


Figure 2.4: The ATLAS Calorimeters

The components of the ATLAS calorimetry system are: the Liquid Argon (LAr) Calorimeter and the Tile Hadronic Calorimeter.

- Tile Hadronic Calorimeter[3]: It includes a central barrel composed of 64 wedges, each measuring 5.6 m in length and weighing 20000 kg, along with two extended barrels, each also containing 64 wedges, each wedge being 2.6 m long and weighing 9600 kg. Altogether, this adds up to a total of 500,000 plastic scintillator tiles.

- Liquid Argon (LAr)[4] Calorimeter: It features a 6.4-meter-long barrel with a thickness of 53 cm and 110,000 channels, operating with Liquid Argon at -183°C . The LAr endcap includes the forward calorimeter as well as Electromagnetic (EM) and hadronic endcaps. Each EM endcap has a thickness of 0.632 m and a radius of 2.077 m. The hadronic endcaps consist of two wheels with thicknesses of 0.8 m and 1.0 m, both with a radius of 2.09 m. The forward calorimeter comprises three modules, each with a radius of 0.455 m and a thickness of 0.450 m.

2.0.5 Trigger and Data Acquisition System (TDAQ)

ATLAS is engineered to record up to 1.7 billion proton–proton collisions per second, resulting in a raw detector data rate on the order of terabytes per second. Since only a small fraction of these collisions contains features relevant for physics analyses, an efficient online selection system is required. The Trigger and Data Acquisition system (TDAQ) [5] is responsible for reducing this overwhelming data flow to a manageable rate while preserving the events of highest physics interest.

The first-level hardware trigger, built using custom electronics mounted directly on the detector, processes reduced-granularity information from the calorimeters and the muon spectrometer. It reaches a decision within a latency of about $2.5\ \mu\text{s}$, during which the full-resolution detector data are stored in front-end buffers. Accepted events are forwarded to the High-Level Trigger (HLT) at a maximum rate of approximately 100 kHz.

The High-Level Trigger is implemented entirely in software and runs on

a large computing farm consisting of several thousand CPU cores. Unlike the hardware trigger, the HLT has access to full detector information and performs refined event reconstruction, with typical processing times ranging from tens to hundreds of milliseconds per event. This stage further reduces the event rate to about 1 kHz, selecting only the most promising events for permanent storage and offline physics analysis.

2.0.6 The Muon Spectrometer

The Muon Spectrometer[6][7][8] forms the outer part of the ATLAS detector and is designed to detect charged particles exiting the barrel and end-cap calorimeters and to measure their momentum in the pseudorapidity range $|\eta| < 2.7$. It is also designed to trigger on these particles in the region $|\eta| < 2.4$. The ATLAS Muon Spectrometer (MS in the following) is designed to provide a standalone measurement of the muon momentum with an uncertainty in the transverse momentum varying from 3% at 10 GeV/c. to about 10% at 1 TeV, and to provide a trigger for muons with varying transverse momentum thresholds down to a few GeV/c. The muon momentum is determined by measuring the track curvature in a toroidal magnetic field. The muon trajectory is always normal to the main component of the magnetic field so that the transverse momentum resolution is roughly independent of η over the whole acceptance. The magnetic field is provided by three toroids, one in the “barrel” ($|\eta| < 1.1$) and one for each “end-cap” ($1.1 < |\eta| < 2.7$), with a field integral between 2 and 8 Tm. The muon curvature is measured by means of three precision chamber stations positioned along its trajectory. In order to

meet the required precision each muon station should provide a measurement on the muon trajectory with an accuracy of $50\text{ }\mu\text{m}$. In Fig. 2.5 a schematic view of the muon spectrometer is given.

The muon spectrometer consists of two sub-detectors for precision measurement :

- Monitored Drift Tubes (MDT)
- New Small Wheel (NSW) , that replaced Cathode Strip Chambers (CSCs)

And two sub-detectors for triggering :

- Resistive Plate Chambers (RPC)
- Thin Gap Chambers (TGC)

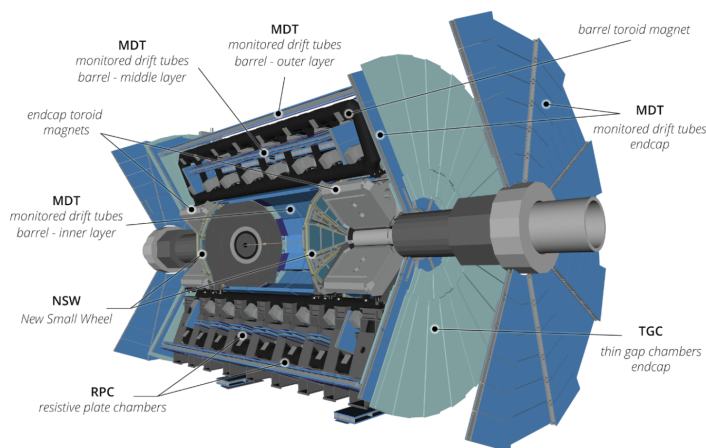


Figure 2.5: The ATLAS Muon Spectrometer

2.0.6.1 The Resistive plate chambers: RPCs

In the barrel region of ATLAS, the RPC (Resistive Plate Chamber) system is responsible for generating the trigger signals. RPCs are parallel-plate gas detectors designed to provide particle timing measurements with a precision of 1 ns, meeting the stringent requirements of the ATLAS trigger system. These chambers operate using a multi-component gas mixture consisting of $\text{C}_2\text{H}_2\text{F}_2 + 4.5\% \text{C}_4\text{H}_{10} + 0.3\% \text{SF}_6$. Additionally, they enable fast and coarse track measurements, which can be correlated with precision detector data to identify muon tracks. The detector includes three layers of RPC chambers in each end-cap, covering the pseudorapidity range $|\eta| > 1.05$.

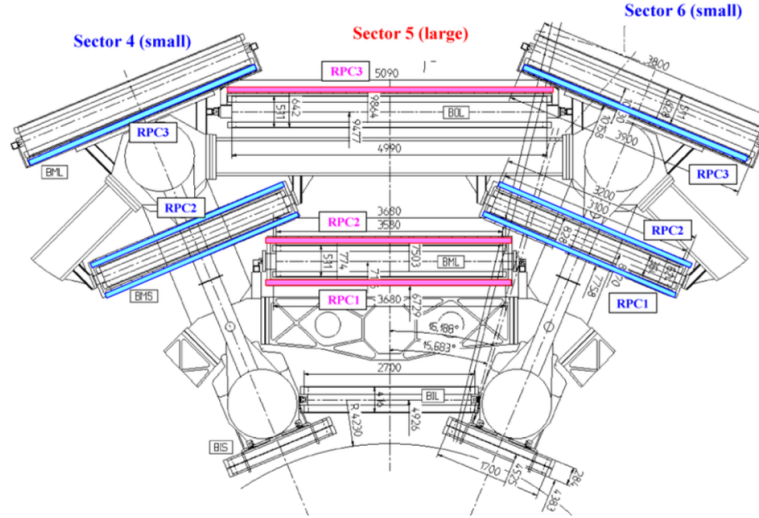


Figure 2.6: The Mechanical structure of an RPC chamber

2.0.6.2 The Thin Gap Chambers (TGCs): TGCs

In the end-cap region ($1.05 < \eta < 2.4$), the Thin Gap Chambers (TGC) provide the trigger information. The trigger system fulfills three key functions: identifying bunch crossings, establishing precise p_T thresholds, and offering a complementary azimuthal coordinate measurement in the bending (radial) direction, in addition to the MDT chambers. This fast trigger technology delivers track data within tens of nanoseconds following a particle's passage. Based on the operating principles of multiwire proportional chambers, TGCs feature anode wires encased between two FR4 cathode layers—graphite-coated on the interior and copper-clad on the exterior—and two layers of copper pick-up strips oriented perpendicular to the wires. They operate in a high-intensity electric field of approximately 3.2 kV and use a highly quenching gas mixture of $\text{CO}_2 + 45\% \text{ n-pentane (C}_5\text{H}_{12})$. TGCs offer excellent time resolution and high rate capability. Their spatial resolution is primarily defined by the granularity of the readout channels, which measure both track coordinates: one in the bending plane (η , through wire groups) and one in the non-bending plane (ϕ , through radial strips). Additionally, they provide a sharp momentum cut-off for triggering muons.

2.0.6.3 The Cathode Strip Chambers: CSCs

The complete CSC system (that currently is not included in the muon spectrometer) includes two disks, one on each end-cap side of the ATLAS detector, with each disk containing 8 small and 8 large trapezoidal

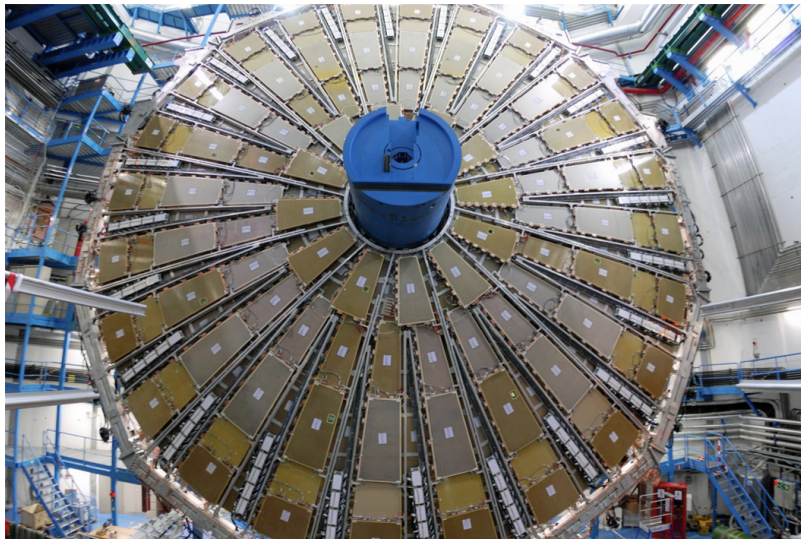


Figure 2.7: The Thin Gap Chambers

chambers, each made up of 4 layers. The CSCs are multi-wire proportional chambers with cathode planes divided into strips in perpendicular directions, allowing for both precision and transverse coordinate measurements. A gas mixture of $\text{Ar} + 20\% \text{CO}_2$ is used as the active medium within the detector. Instead of detecting signals directly from the wires, the track position is determined by interpolating the charges induced on adjacent cathode strips.

2.0.6.4 The Monitored Drift Tubes: MDTs

The design consideration with the strongest impact on the design of the ATLAS muon spectrometer is the requirement for stand-alone measurement capability. This safeguards against any unanticipated background and ensures a good discovery potential in the presence of unexpected event topologies due to unknown physics at the TeV scale. To accomplish a good momentum measurement even at low momenta, this requirement

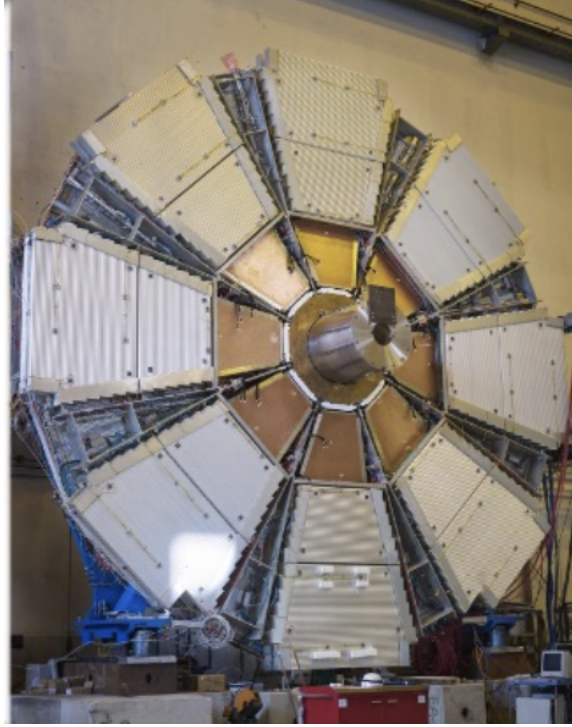


Figure 2.8: The Cathode Strip Chambers

leads to the choice of an air- core magnet system, which however puts high demands on the muon chamber system due to unavoidable field inhomogeneities and the relatively low fields in such systems. The open structure of the barrel toroid allows for the reconstruction of the muon momenta from a measurement of the sagitta in three muon stations in front, in the center and behind the magnetic field in the range $\eta < 1.4$. In the forward station the muon momenta are obtained from a point-angle measurement with one point in front and two points behind the endcap toroid cryostats. To achieve the required momentum resolution at high momenta (the sagitta for a 1 TeV muon is about $500\text{ }\mu\text{m}$) two requirements have to be fulfilled: the muon chambers have to provide a position measurement accuracy of about $50\text{ }\mu\text{m}$ per station and the alignment of the three stations with respect to each other has to be known to about $30\text{ }\mu\text{m}$. To achieve the first goal a system of high pressure (3

bar absolute) proportional drift tubes - monitored drift tubes - has been chosen. An MDT chamber consists of six layers of drift tubes, arranged such that three layers of closely-packed tubes (multilayers) are mounted on each side of a support structure. The two multilayers and the support structure form a chamber.

The muon precision system is dominated by the Monitored Drift Tubes (MDT), which covers 99.5% of the total area of the precision detectors. These detectors are positioned in the barrel (B) and end-cap (E) regions and are organized within the inner (I), middle (M), and outer (O) stations, segmented across 16 small (S) and 36 large (L) sectors in an alternating arrangement. MDTs are designated based on their specific locations. They provide precise track coordinate measurements across nearly the entire pseudorapidity range, up to $\eta < 2.7$, with the exception of the innermost end-cap layer, where coverage extends only up to $\eta < 2.0$. Each MDT is an aluminum cylindrical drift tube with a 29.97 mm diameter, pressurized and each of them filled with a non-flammable gas mixture of Ar+7% CO₂ and a trace of water vapor at 3 bar.

2.0.7 Atlas Phase-I Upgrades

In preparation for the coming years of LHC running at higher luminosity, two upgrade projects of the ATLAS Muon Spectrometer have been developed: the New Small Wheel project, improving the trigger in the end-cap regions, and the BIS78 project.

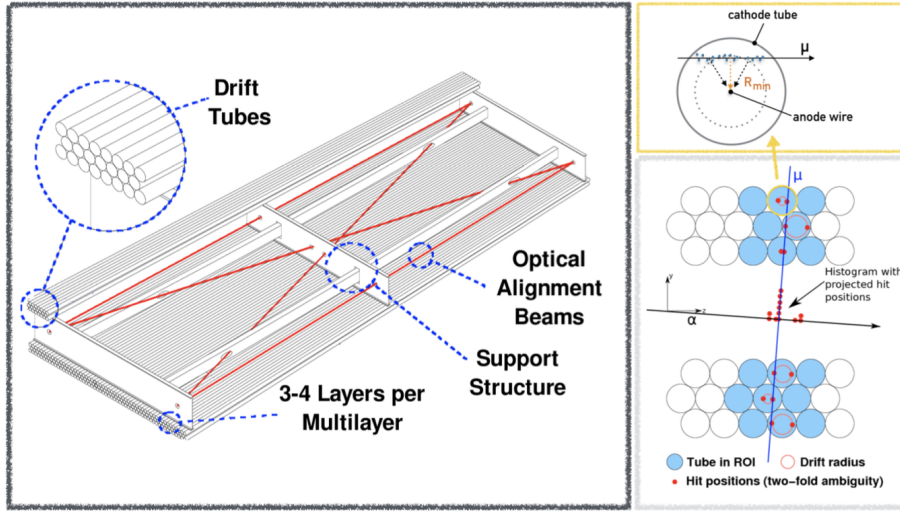


Figure 2.9: The Monitored Drift Tubes

2.0.8 The BIS78 Project

The Monitored Drift Tubes (MDTs) are high-precision drift chambers that form a crucial part of the ATLAS muon spectrometer. They are specifically designed to provide exceptional spatial resolution and efficient tracking, regardless of the track angle. Throughout the LHC and ATLAS experiment, these detectors have consistently demonstrated their capability to deliver accurate tracking over large areas.

The primary goal of upgrading the ATLAS muon spectrometer is to enhance muon trigger efficiency, improve the precision of muon momentum measurements, and increase the rate capability of the muon system in high-background regions during the High-Luminosity LHC (HL-LHC) runs. To achieve these improvements, the proposed upgrade incorporates small-diameter (15 mm) Muon Drift Tube, sMDT chamber technology.

This new detector design significantly enhances rate capability—by approximately an order of magnitude—while also allowing the installation of additional triplet Resistive Plate Chambers (RPCs) in the barrel inner layer of the muon system.



Figure 2.10: The BIS78A chambers as they are positioned into the ATLAS MS

A pilot project[9][10][11] for this barrel inner layer upgrade began during the 2019 LHC shutdown. As part of this effort, the Max-Planck-Institut für Physik in Munich constructed 16 sMDT chambers, each covering an area of approximately 2.5 m^2 . To ensure reliable performance in the experiment, these detectors undergo rigorous testing both at the production site and upon delivery to CERN. Once installed in the ATLAS muon spectrometer, the muon stations undergo further testing and commissioning using cosmic rays. This project serves as a pilot for the complete replacement of the existing 96 BIS1-6 MDT chambers during the LS3 period with the combined sMDT+RPC muon modules, which will have a similar design.

The sMDT detectors are composed of two multilayers of high-pressure drift tubes, with each multilayer consisting of four densely packed tube

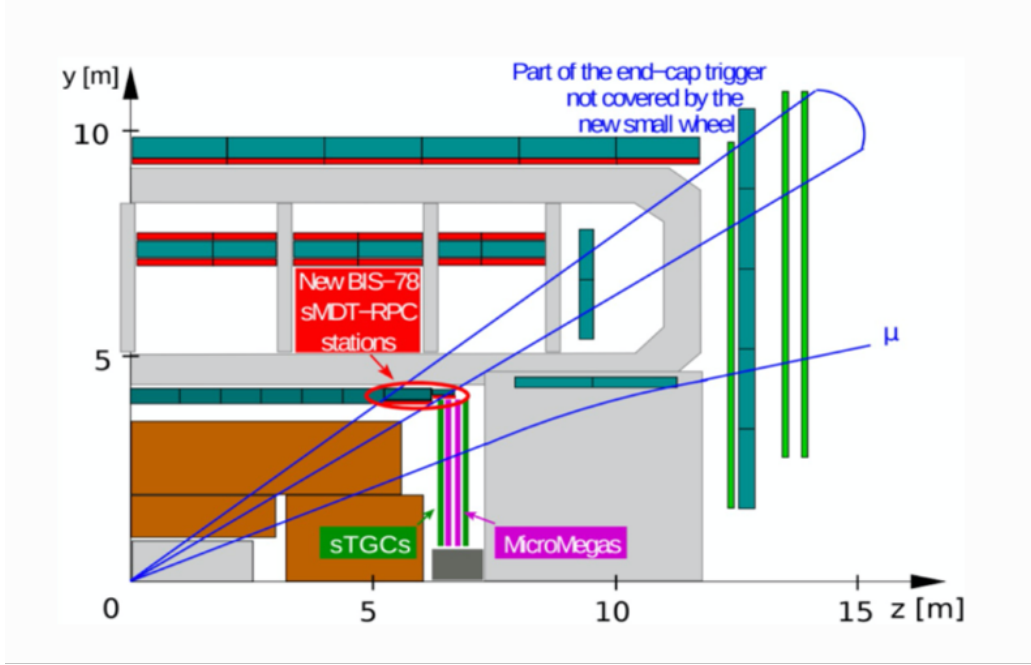


Figure 2.11: The BIS78A chambers as they are positioned into the ATLAS MS.

layers mounted on an aluminum support frame. The chamber sizes range from approximately 2.67 m^2 to 3.04 m^2 , while the tube lengths vary between 1009 mm and 1669 mm. For detector control data, the BIS78 sMDT chambers are equipped with 12 temperature sensors distributed across the multilayers and the support structure. Typically, eight platforms are mounted on the top surface of the detector, including four Axial-Prism platforms, two CCC platforms, and two B-field platforms. Additionally, each detector features an in-plane alignment system designed to monitor deformations such as sag and torsion. This system comprises two image sensors, four lenses, and either two or four masks. For the 16 A/C-side BIS78 sMDT detectors, the chamber-to-chamber alignment system and B-field components will be repurposed from the previous MDT detectors.

Moreover, the newly installed chambers will serve along with the existing

BIS7 and BIS8 chambers into several fields. Highlighting the main ones, the sMDT:

- can reduce the chamber thickness with minimal loss of resolution.
- are permitting the insertion of RPC trigger chambers which add crucial trigger acceptance.
- have 8 times lower background detector occupancy.
- have 4 times shorter electronics dead time.

Properties	Current MDT	New sMDT
Tube diameter	30 mm	15 mm
Operating gas mixture	Ar:CO ₂ (93:7)	Ar:CO ₂ (93:7)
Operating Pressure	3 bar	3 bar
Operating HV working point	3070 V	2730 V
Gas gain	2×10^4	2×10^4
Maximum drift time	~ 720 ns	~ 175 ns
Single tube space resolution	83 ± 2 μ m	106 ± 2 μ m

Figure 2.12: General characteristics and properties of the BIS78A chambers.

After the commissioning campaign, the sMDT chamber is then integrated with its two triplet RPC trigger detectors to form a so-called final muon station. Currently the sMDT have been installed at Side A of the ATLAS detector, as depicted in Fig. 2.14, while their installation on side C will follow closely. Focus of this work is the incorporation of the newly installed chambers into the MDTs. In order to fulfill these tasks, several projects had to be modified accordingly.

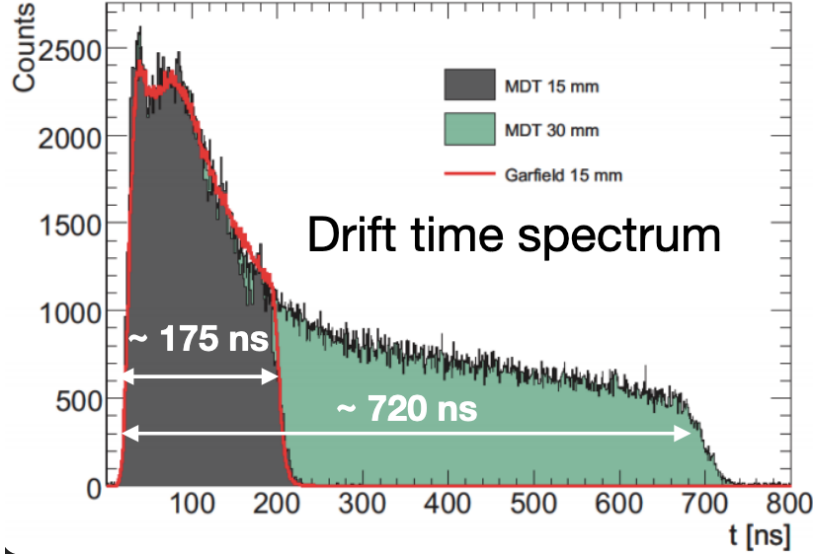


Figure 2.13: The drift time spectrum of the BIS78A chambers.

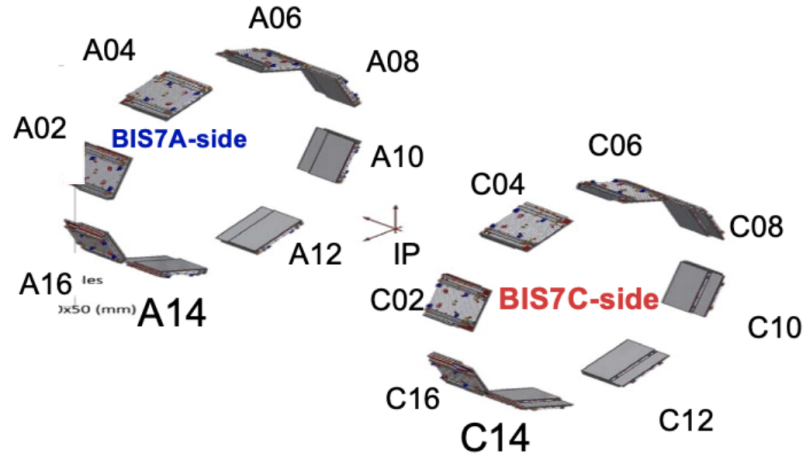


Figure 2.14: The position of the BIS78A chambers into the MS at the UX15 cavern

2.0.9 Micromegas Detectors

The resistive-strip Micromegas chambers[12], introduced as part of the New Small Wheel upgrade of ATLAS, constitute the principal tracking

technology in this system. Their design offers excellent spatial resolution ($\sigma < 100\ \mu\text{m}$), high detection efficiency even under intense background conditions, and very good two-track separation. These characteristics make Micromegas well suited for rejecting spurious signals such as delta electrons while maintaining reliable muon detection. The fine segmentation of the readout strips, combined with their fast timing response, allows the Micromegas system to complement and back up the trigger functionality of the small-strip Thin Gap Chambers (sTGC).

Each Micromegas chamber consists of a stainless-steel mesh that divides the gas volume into two regions: the **drift gap** and the **amplification gap**. The drift gap, typically 5 mm wide, is where charged particles ionize the gas, producing primary electrons. A drift field of about 600 V/cm guides these electrons toward the micromesh. The amplification gap is significantly thinner, about $128\ \mu\text{m}$, and operates with a stronger electric field (45 kV/cm). In this region, the primary electrons undergo avalanche multiplication, producing a strong signal that is collected on segmented anode strips with a pitch of roughly $450\ \mu\text{m}$. This configuration ensures good timing resolution, with electron drift times up to 100 ns and amplification pulses lasting only fractions of a nanosecond. The combination of a short electron pulse and a somewhat longer ion pulse (up to 200 ns) provides a clear and robust readout signal.

To ensure stable operation under high particle flux, Micromegas detectors employ a **resistive-strip technology**[13]. A thin resistive layer is placed above the copper readout strips and separated by a narrow insulator. This layer protects against electrical discharges, localizing potential sparks and preventing direct damage to the readout electronics. In practice, this approach reduces the probability of breakdowns, allowing the detectors

to function at higher gas gains while minimizing the risk of extended downtime.

The gas mixture used in Micromegas is based on $\text{Ar}+5\% \text{CO}_2+2\% \text{iC}_4\text{H}_{10}$, with CO_2 and iC_4H_{10} acting as quenchers. This baseline composition was extensively tested and adopted for Run-3.

In summary, the Micromegas detectors combine high spatial and timing precision with robustness against discharges, making them a crucial component of the ATLAS muon spectrometer upgrade. Their design addresses the challenges posed by high background rates and ensures reliable performance in the demanding environment of the Large Hadron Collider.

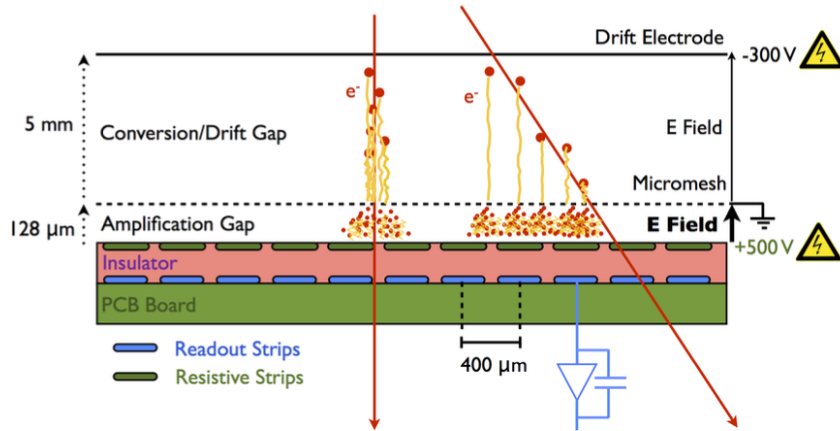


Figure 2.15: Micromegas Detector Structure

2.1 STG Detectors

The sTGC[14] are gaseous detectors composed of gold-plated tungsten wires, along with copper strips and pads. The wires, which have a diameter of $50\text{ }\mu\text{m}$, operate under an applied potential of approximately 2.9 kV . They are arranged with a pitch of 1.8 mm and are positioned between two cathode planes made of a graphite-epoxy composite, each located 1.4 mm away from the wires. These cathode planes typically exhibit a surface resistivity ranging between $100 - 200\text{ k}\Omega/\text{sq}$. On the outer sides of the cathodes, precision strips—placed perpendicular to the wires—and pads function as readout electrodes. The strips, which have a pitch of (significantly smaller than those in the current ATLAS TGC), enhance the angular resolution. In contrast, the pads, with a considerably larger pitch of around 80 mm , help identify muon tracks that approximately align with the interaction point by employing a 3-out-of-4 coincidence method. Additionally, they define a region of interest where the strips and wires are read out. The chamber is filled with a gas mixture consisting of $\text{CO}_2 + 45\%$ n-pentane (C_5H_{12}), which achieves an electron drift velocity of approximately $3\text{ cm}/\mu\text{s}$ under an electric field strength of 2.9 kV/cm .

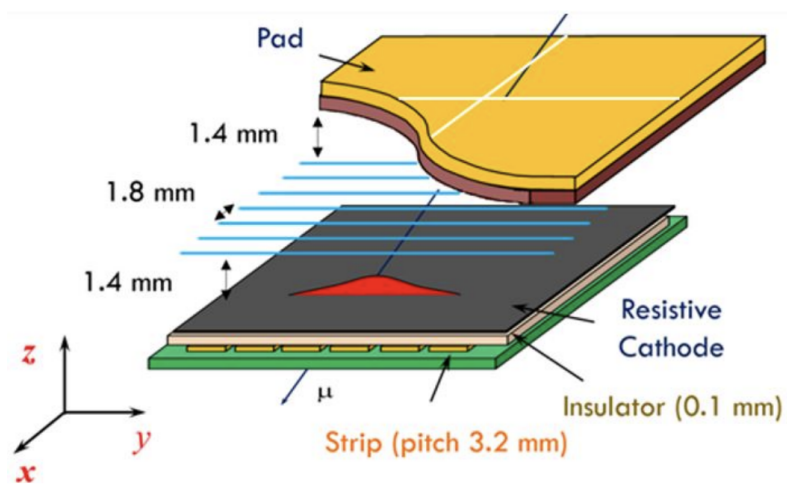


Figure 2.16: The sTGC Detector Structure

Bibliography

- [1] ATLAS Collaboration, "Magnet System Technical Design Report", ATLAS Technical Design Report, CERN, CERN-LHCC-97-018; ATLAS-TDR-6. <https://cds.cern.ch/record/338080/files/SC00000799.pdf>
- [2] ATLAS Collaboration, "The ATLAS Inner Detector commissioning and calibration", Eur. Phys. J. C, vol. 70, pp. 787–821, 2010. <https://cds.cern.ch/record/1262789/files/EurPhysJC.3FBE7E53d01.pdf>
- [3] A. Valero et al., "The ATLAS Tile Calorimeter", ATL-TILECAL-PROC-2015-002, CERN, 2015. <https://cds.cern.ch/record/2004868/files/ATL-TILECAL-PROC-2015-002.pdf>
- [4] ATLAS Collaboration, "ATLAS LAr Calorimeter Performance in LHC Run-2", ATL-LARG-PROC-2020-001, CERN, 2020. <https://cds.cern.ch/record/2707741/files/ATL-LARG-PROC-2020-001.pdf>
- [5] ATLAS HLT/DAQ/DCS Group, "ATLAS High-Level Trigger, Data Acquisition and Controls", ATLAS TDR-016. <https://atlas.cern/Discover/Detector/Trigger-DAQ>

- [6] L. Pontecorvo, "The ATLAS Muon Spectrometer", ATLAS Internal Note SN-ATLAS-2003-030, CERN, 2003. <https://cds.cern.ch/record/676896/files/sn-atlas-2003-030.pdf>
- [7] ATLAS Collaboration, "The ATLAS Muon Spectrometer Technical Design Report", ATLAS TDR 10, CERN, 1997. <https://cds.cern.ch/record/331068>
- [8] ATLAS Public Website, "Muon Spectrometer", CERN. <https://atlas.cern/Discover/Detector/Muon-Spectrometer>
- [9] ATLAS Collaboration, "The BIS78 Resistive Plate Chambers upgrade of the ATLAS Muon Spectrometer for the LHC Run-3", ATL-MUON-PROC-2020-017, CERN, 2020. <https://cds.cern.ch/record/2715711>
- [10] ATLAS Collaboration, "Commissioning of the BIS78 pilot project of the Phase-I upgrade of the ATLAS muon spectrometer", ATL-MUON-PROC-2021-002, CERN, 2021. <https://cds.cern.ch/record/2781390>
- [11] F. Pastore et al., "BIS78: a pilot project for Phase-II ATLAS RPC and beyond", J. Instrum., vol. 15, C05005, 2020. <https://inspirehep.net/literature/1829194>
- [12] Y. Giomataris et al., "MICROMEGAS: A High granularity position sensitive gaseous detector for high particle flux environments", Nucl. Instrum. Meth. A, vol. 376, pp. 29–35, 1996. <https://inspirehep.net/literature/404072>
- [13] T. Alexopoulos et al., "A spark-resistant bulk-micromegas chamber for high-rate applications", Nucl. Instrum. Meth. A, vol. 640,

pp. 110–118, 2011. <https://www.sciencedirect.com/science/article/abs/pii/S0168900211005869>

[14] ATLAS News Updates, "Detectors for a new era of ATLAS physics", CERN, 2021. <https://atlas.cern/updates/news/NSW-complete>

Chapter 3

The Development of the Detector Control System of the Muon Subdetectors of ATLAS Experiment

ATLAS is the largest experiment at the Large Hadron Collider (LHC), designed to study proton-proton and heavy ion collisions. To ensure coherent and safe operation, a Detector Control System (DCS)[1][2] has been implemented to oversee the control, configuration, and monitoring of all sub-detector systems within the experimental infrastructure. The primary role of the DCS is to ensure the stable and safe operation of the detector. This chapter begins by outlining the fundamental principles and infrastructure of the ATLAS DCS. It then details the development and modifications of the DCS for three muon sub-detectors: first, the existing Monitored Drift Tubes (MDTs), focusing on Phase-I developments and preparations for Phase-II; second, the two new detector technologies of the New Small Wheel (NSW), namely the Micromegas (MMG) and Small-strip Thin Gap Chambers (STG). The DCS work encompasses the

system's development, its installation at Point-1 of ATLAS, and its integration into the detector. This chapter also provides an overview of the software, hardware interfaces and capabilities, user interfaces, as well as the testing and commissioning of the entire system

3.1 The ATLAS Detector Control System

The Detector Control System (DCS) of ATLAS was developed and implemented as part of the Joint Controls Project (JCOP) [3], a collaboration between CERN's controls group and the DCS teams of the LHC experiments. This initiative established standards for both DCS hardware and software, along with implementation guidelines applicable to JCOP in general and ATLAS specifically. The Front-End (FE) equipment comprises specialized electronics and related services, such as power supplies and cooling systems. For the DCS Back-End (BE), the industrial Supervisory Control and Data Acquisition (SCADA) software WinCC OA serves as the foundation. Built on top of WinCC OA, the JCOP Framework streamlines the integration of standard hardware devices and the development of consistent control applications. The BE is structured into three layers (see Fig. 3.1): process control for subsystems, a dedicated control station for each sub-detector enabling independent operation, and global stations that host service applications and operator interfaces. The DCS enables equipment supervision using operator commands, reads, processes and archives the operational parameters of the detector, allows for error recognition and handling, manages the communication with external control systems, and provides a synchronization mechanism with the physics data acquisition system.

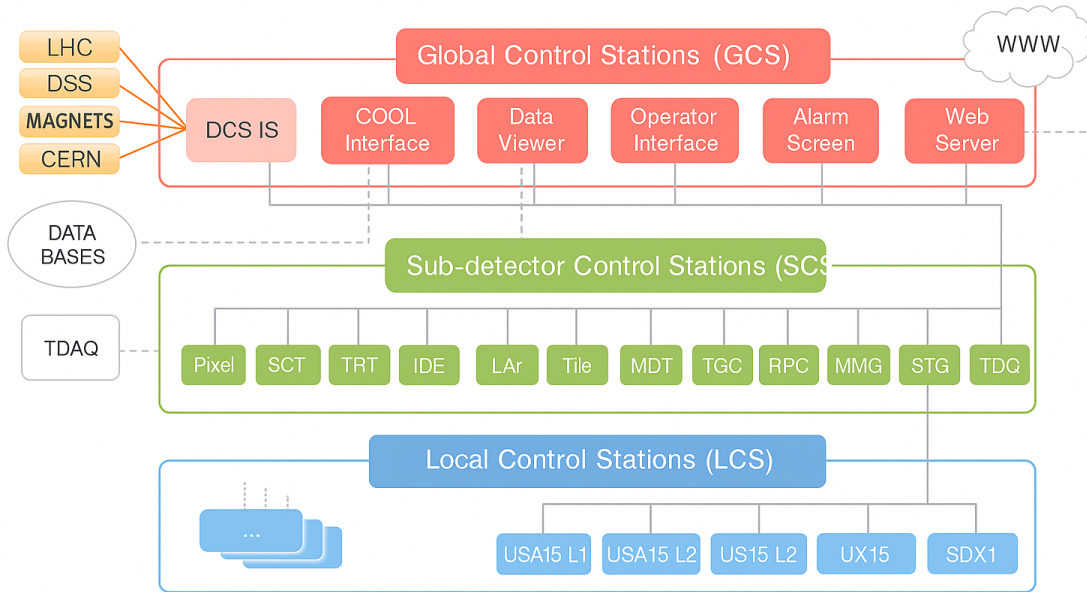


Figure 3.1: The basic architecture of ATLAS Detector Control System.

3.1.1 The DCS Building Blocks

The DCS Building Blocks are divided into 2 categories : the Back-End and the Front-End[4].

The DCS Back-End (BE) is built upon the industrial Supervisory Control and Data Acquisition (SCADA) software, WinCC OA. The JCOP Framework, operating on top of WinCC OA, enables seamless integration of standard hardware devices and facilitates the development of unified control applications. The BE is organized into three layers: the process control of subsystems, a dedicated control station for each sub-detector ensuring stand-alone operation, and global stations that include service applications and operator interfaces :

- DCS Control Station PC: The hardware platform for the BE system consists of industrial, rack-mounted server machines. There are two distinct standard machine types: one designed for applications that require strong I/O capabilities, and another for processing-heavy applications with I/O through Ethernet connectivity. Both models are equipped with redundant, hot-swappable power supplies and disk shadowing.
- WinCC OA: The SCADA package WinCC OA (rebranded as SIMATIC WinCC OA) serves as the primary framework for BE applications. Four key concepts of WinCC OA make it ideal for large-scale control system implementations:
 - Generic control process templates can be utilized based on the specific application type, minimizing unnecessary overhead.
 - Each WinCC OA application employs a local database to store control parameters, ensuring synchronized access across all connected processes. Data processing is event-driven, with selected DCS parameters archived to an external Oracle database for persistence.
 - Various control systems can be linked via LAN to create a Distributed System, enabling scalable remote data access and event notifications.
 - A generic Application Programming Interface (API) allows for further extension of control application functionalities.
- Front-end Interface Software: To connect the front-end devices with WinCC OA, the industry-standard OPC was selected. Both commercial equipment manufacturers and developers of custom devices provide the OPC servers, for which WinCC OA offers an OPC

client. A dedicated CANopen OPC server was developed for the ELMB CAN bus readout and control. For device types where OPC could not be used due to maintenance or platform limitations, custom readout applications were integrated with WinCC OA using the CERN standard middleware, DIM. PLCs are connected to WinCC OA via Mod-Bus.

- The JCOP Finite State Machine (FSM) offers a generic, platform-independent, and object-oriented implementation of a state machine toolkit designed for highly distributed environments, which is integrated with a WinCC OA control application. The attributes of an FSM object instance are stored persistently within the corresponding WinCC OA application database. This enables the archiving of FSM states and transitions, as well as the integration of FSM functionality into WinCC OA user interfaces.

The DCS Front-End (FE) equipment was designed to meet essential criteria such as cost-efficiency, low power consumption, and high I/O channel density. For system interconnections, the CAN industrial field-bus and the CANopen protocol were utilized where applicable. Additionally, the electronics in the detector cavern were engineered to support remote firmware updates, be resistant to magnetic fields, and endure the radiation exposure anticipated during the experiment's duration.

- The Embedded Local Monitoring Board (ELMB) is an affordable, custom-built I/O concentrator designed as a universal solution for connecting custom systems to the DCS. Measuring $50 \times 67 \text{ mm}^2$, the ELMB is equipped with an 8-bit, 4 MHz microcontroller, 64 analog

channels, 32 digital channels, and a CAN bus interface. It is resistant to strong magnetic fields and can withstand radiation doses up to 50 Gy. Additionally, the ELMB can be integrated into custom designs and features modular, remotely extendable firmware supporting a general-purpose CANopen I/O application. Over 10,000 ELMBs are currently deployed across all LHC experiments, with more than 5,000 used within the ATLAS experiment alone.

- Standardized Commercial Equipment: The VME, which is the industry standard, is utilized to enclose the electronics. Monitoring systems are implemented across all crates to track temperature, general status, power, and reset functions. The detector components are powered by various types of industrial power supplies, which include voltage and current control, over-voltage/current protection, and thermal monitoring.

3.2 The WinCC OA Framework

"WinCC OA"[5] is the abbreviation for "SIMATIC WinCC Open Architecture", a software package designed for the use in automation technology. The main application area is the operation and control of technical plants using VDU workstations with full graphical capability.

This application requires the possibility to transfer conditions and commands to the process and its control equipment. The user uses the mouse, the keyboard and other input devices interactively with an immediately displayed response on the screen. Alerting in case of critical conditions or exceeding of a threshold as well as historical archiving of data for later

presentation and interpretation also belongs to the core functions.

3.2.1 Process interface

The process interface modules, known as drivers (D) in WinCC OA, represent the lowest level of a WinCC OA system. These specialized programs facilitate communication with the control and field levels. Given the variety of communication methods used with PLCs and remote control nodes, multiple drivers are available.

The choice of WinCC OA driver depends on the specific PLC or communication bus in use. Simply put, a driver acts as a module that translates a specific protocol into WinCC OA's internal communication format. It retrieves real-time states, measured values, or counter readings from the field and transmits commands and set values to subordinate control systems. "Control" refers to all types of basic automation equipment, such as PLCs, DDCs, and telecontrol systems.

3.2.2 Project Administrator panel

The PA is responsible for the management of all the projects in the corresponding computer. Also various information for the projects is monitored like name, port number, distributed control, project creation utility, project start/stop etc. From PA one can start the Project Console and log viewer.

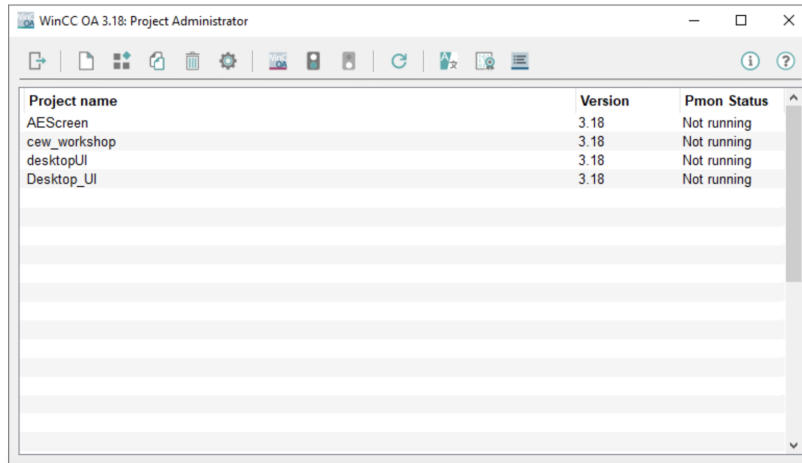


Figure 3.2: Project Administrator panel

3.2.3 Console

The console panel visualizes the state of the project and the state of the managers via easy symbolism. The manager configuration can be changed easily (changed restricted at run time). Since the console panel serves for visualization and controlling of the Pmon it can be closed anytime although the project is running. Furthermore, you can switch between several projects (projects may have different statuses) by just selecting a project. The Console lists all the managers and their configuration, but also hosts various settings and configuration file editor for each project.

3.2.4 Log Viewer

Log viewer is a very helpful tool that opens automatically with the Console. It shows State and error messages during the project start as well as errors of the running project. The Log Viewer can also be opened via the appropriate button in the console panel. If the Log Viewer is opened

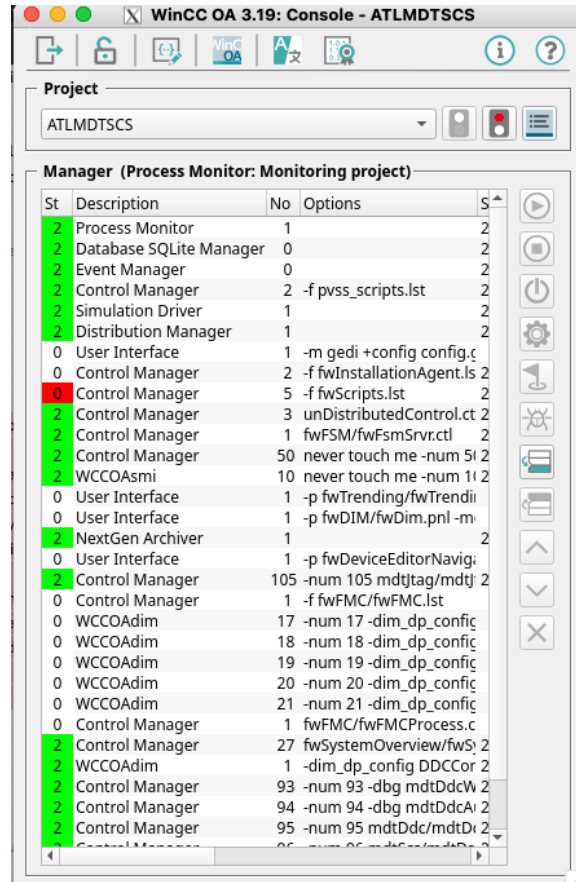


Figure 3.3: WinCC OA Console

via the console it is also closed together with the console.

3.2.5 Event Manager

In WinCC OA, the central processing unit is called the Event Manager (EV). This component maintains an up-to-date image of all process variables in memory. Any other functional unit (manager) that needs data retrieves it from the Event Manager's process image rather than communicating directly with a control system.

When an operator issues a command, it is initially recorded as a value

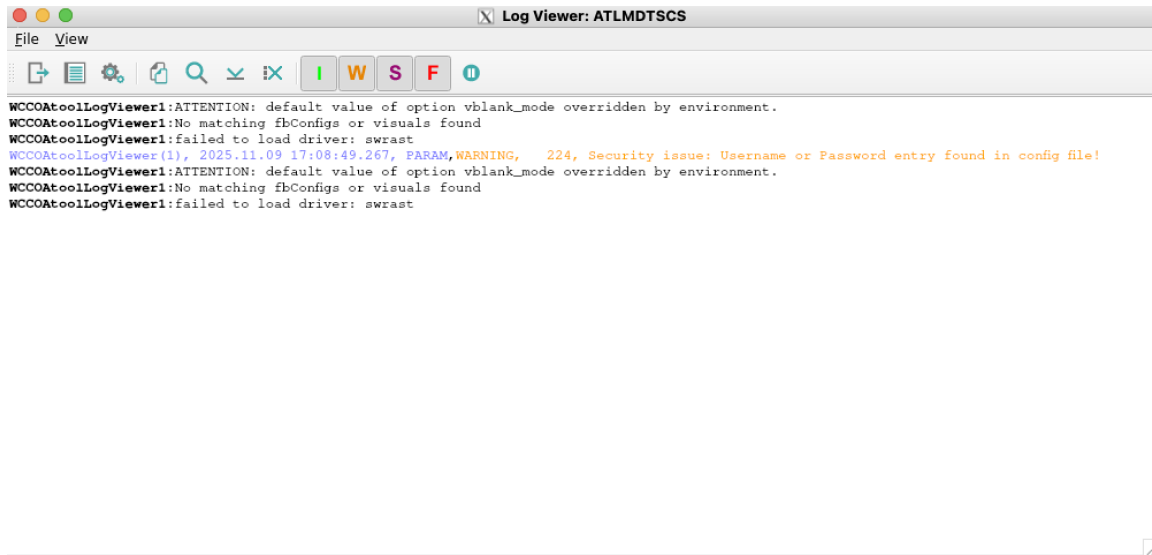


Figure 3.4: WinCC OA log viewer

change in the Event Manager’s process image. The responsible manager then automatically forwards this change to the appropriate target device, such as a PLC.

Acting as the communication hub of WinCC OA, the Event Manager serves as a central data distributor. Additionally, it handles alerts and can independently execute various calculation functions.

3.2.6 Database Manager

In WinCC OA, the Data Manager (DM) supports the Event Manager by serving as the interface to the database. It manages the application’s configuration data stored in the database and archives historical data, such as value changes and alerts. When historical data is queried, the Data Manager executes these queries, rather than the database itself. The process of archiving in WinCC OA involves storing and retrieving

information generated during process control or visualization, including values and messages resulting from value changes. This data is stored in Value Archives (VA), with each archive managed by a separate archiving process. Each archive consists of a series of chronologically ordered archive files.

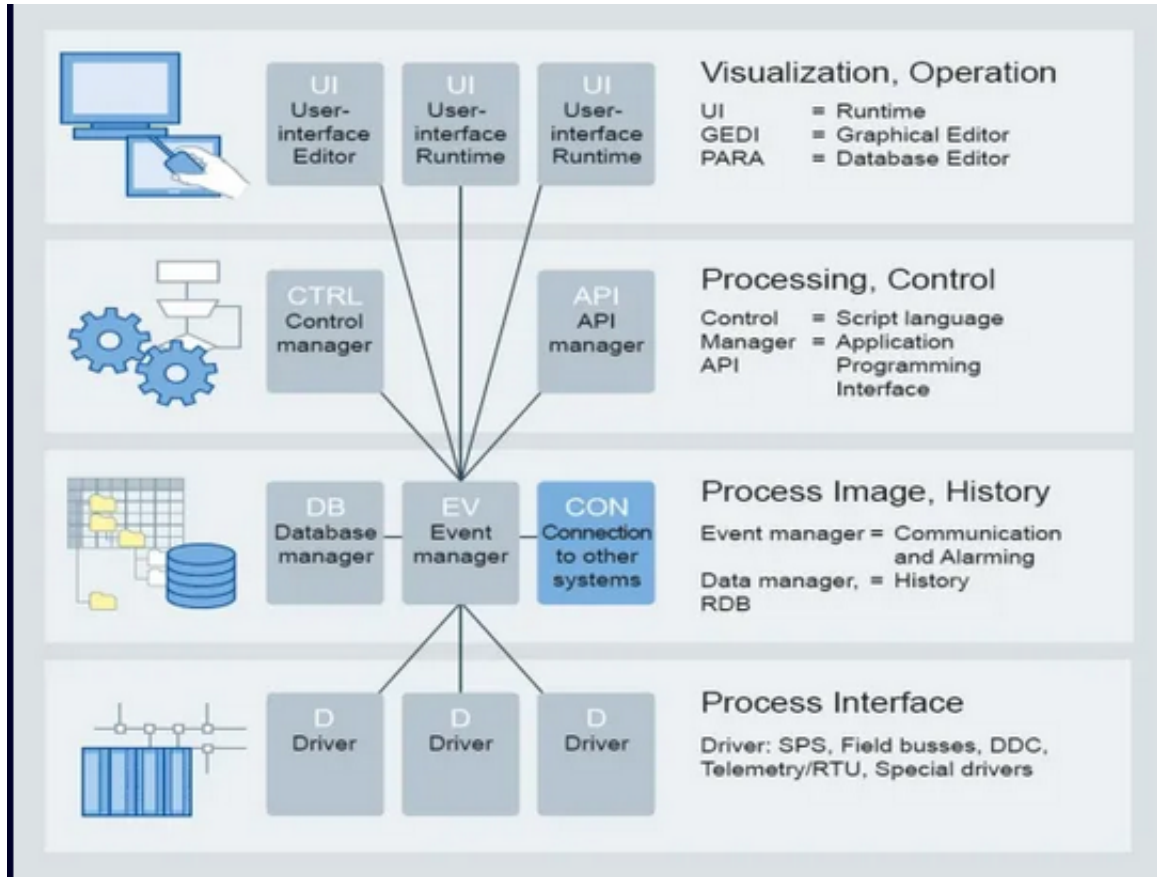


Figure 3.5: The WinCC OA architecture

3.2.7 Control Manager

Control is a robust scripting language within WinCC OA, designed for flexibility and efficiency. Its syntax closely mirrors ANSI-C, featuring

some simplified modifications, and supports advanced procedural programming with multi threading capabilities, allowing parallel processing managed by the system. Developers can utilize Control to create scripts that respond to various events, facilitating dynamic control and visualization tasks. Scripts written in Control are interpreted directly, eliminating the need for compilation. This feature streamlines the development process, enabling rapid deployment and testing of functionalities. Control provides a comprehensive standard library equipped with functions tailored for control and visualization applications, enhancing its utility for complex automation tasks. Beyond its role in user interfaces, Control scripts can operate independently as standalone processes, such as the CONTROL manager. This versatility allows for a wide range of applications, from user interface design to backend data processing, all within the WinCC OA environment.

3.2.8 Archive Managers

Allow users to archive data for later retrieval and examination. Configuration options are available for selecting which data to store.

3.2.9 API Managers

The WinCC OA Application Programming Interface (API) is a C++ class library that enables software developers to extend the system's functionality by implementing custom features as independent additional managers. This allows for the integration of specialized systems such as forecasting modules, simulation tools, planning utilities, or proprietary databases.

3.2.10 The WinCC OA User Interface

The User Interface Manager (UI) serves as the primary interaction point for users. It includes various components such as the Graphics Editor (GEDI), the database editor (PARA), and the general user interface of the application (Module VISION). Within the UI, users can view values, execute commands, and track alarms. Additionally, trends and reports are typically integrated into the interface.

In WinCC OA, user interaction is entirely separate from background processing. The UI functions purely as a visual representation of the current process image or historical data.

3.2.11 The Graphics Editor (GEDI)

GEDI is a powerful tool for creating and editing panels, offering a range of features for designing and configuring graphical objects. These objects can represent entire systems or simple operational screens. Within GEDI, users can design and configure graphic elements, linking them to "data points" defined in the PARA module (refer to PARA module basics). The VISION module provides a runtime display of these panels. WinCC OA enables users to develop customized panels through its dedicated User Interface Manager, known as GEDI (Graphical Editor). Within GEDI (Fig. 3.6), users can design tailored user interfaces, referred to as panels. The flexible, object-oriented framework of WinCC OA allows users to integrate various elements such as buttons, tables, text fields, and lists into their panels. Additionally, these objects can be manipulated using scripts,

granting developers the ability to define processes like initialization, button click actions, closure behavior, and other custom functionalities as needed.

Figure 3.6: The Graphics Editor (GEDI) of WinCC OA

3.2.12 The PARA module of WinCC OA

The fundamental structure of WinCC OA is built around Data Points (DPs), which represent logical devices or system entities within the control system. A Data Point is not a single value, but rather a container that groups together all relevant information needed to monitor and control a device. Each DP follows a predefined structure known as a Data Point Type (DPT), which acts as a template defining the components and attributes the DP must contain.

A Data Point expands into multiple Data Point Elements (DPEs). Each DPE corresponds to a specific attribute of the device, such as a measured

value, a configuration parameter, or a status flag. For example, a temperature sensor DP may contain DPEs representing the current temperature reading, alarm thresholds, hardware status, and calibration parameters. This hierarchical structure is conceptually similar to a struct in C programming, where a single structured object contains multiple typed fields.

WinCC OA stores and manages all DP and DPE values internally, ensuring consistency, continuous updates, and archiving when required. Furthermore, each DPE can be configured with data-specific behaviors, such as datatype assignments, alert conditions, trending settings, and history logging. This modular approach allows developers to create flexible and reusable control system objects that can be easily adapted to different devices and project requirements.

3.2.13 The WinCC OA Alarm Screen

The alarm screen is a panel used in ATLAS DCS, along the main FSM one, in order to show at each moment which alarms are active or need attention as shown in Fig. 3.8. These alarms are triggered in response to malfunctions in one or multiple hardware or software components, with severity categorizations ranging from WARNING to ERROR and FATAL. The Alarm Screen user interface includes features that enable filtering based on various attributes, such as the related system, description, severity, and time. It also allows users to query the alarm history of a specific system while incorporating all these filtering options. The alarm system plays a vital role in enabling shifters to quickly detect potential issues and ensuring experts can respond efficiently during routine

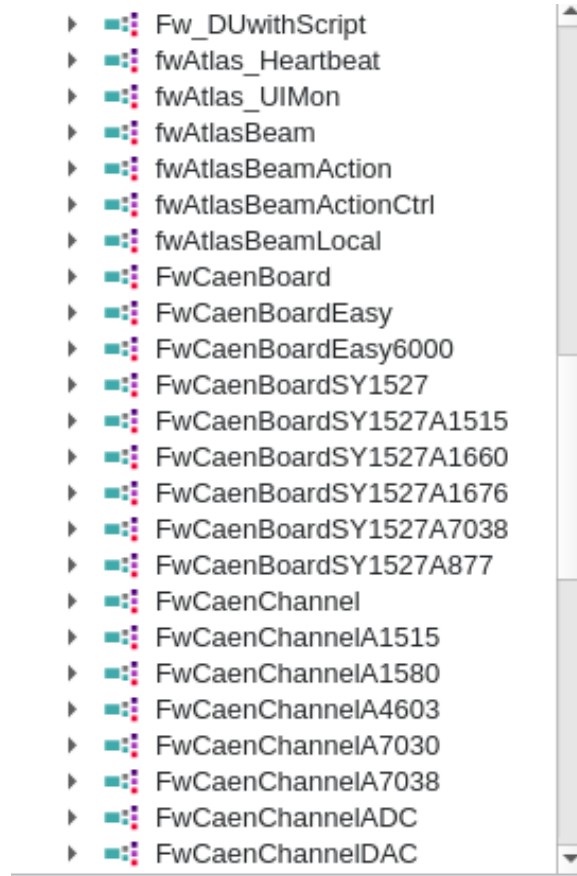


Figure 3.7: The PARA module of WinCC OA

operations. It provides shifters with real-time awareness of potential issues while offering a comprehensive history and filtering capabilities that support experts in conducting detailed analyses and investigations. The Alarm Screen remains a key component in the suite of tools that enhance the robustness and reliability of the ATLAS DCS.

3.2.14 The JOint Control Project Framework

The JCOP[6] Framework (FW) simplifies the development of experiment control systems by providing standardized guidelines, a unified look and

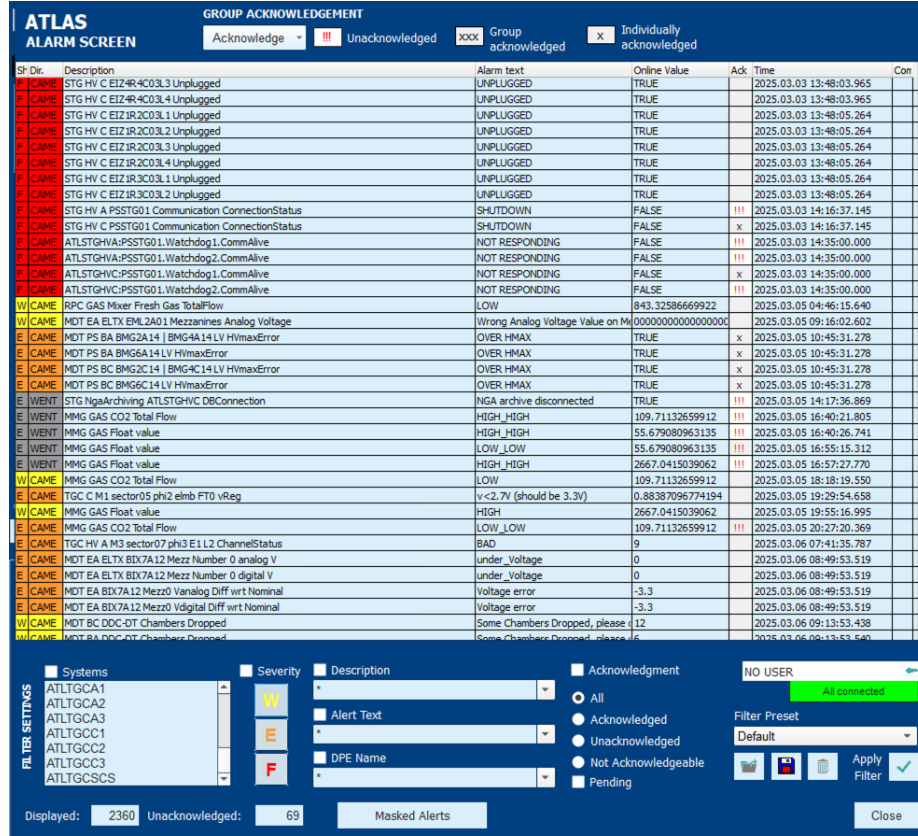


Figure 3.8: The WinCC OA alarm Screen

feel, and functionality tailored to High-Energy Physics (HEP) environments, particularly at the LHC. Instead of developing solutions from scratch, developers can reuse and integrate pre-tested components, promoting consistency and reducing development effort across multiple experiments.

FW extends the capabilities of WinCC OA by incorporating additional tools required for large-scale, hierarchical control. Notably, FW includes a Finite State Machine (FSM) toolkit based on SMI++, which enables the definition of structured operational states (e.g., OFF, STANDBY, READY, ERROR) and standardized state transitions across subsystems. This FSM functionality is not part of the core WinCC OA product but

is provided as a CERN-specific extension to address the coordination and supervision needs of complex detector systems. Additionally, FW integrates HEP-specific communication protocols, such as CERN's DIP and DIM, ensuring interoperability between distributed components.

By combining SCADA tools with these specialized toolkits, FW provides a homogeneous, high-level abstraction layer that minimizes the need for deep expertise in each individual component. Developers benefit from advanced HEP-oriented features while retaining access to underlying WinCC OA capabilities for customized or standalone implementations. An example of the JCOP Framework installation panel is shown in Fig. 3.9.

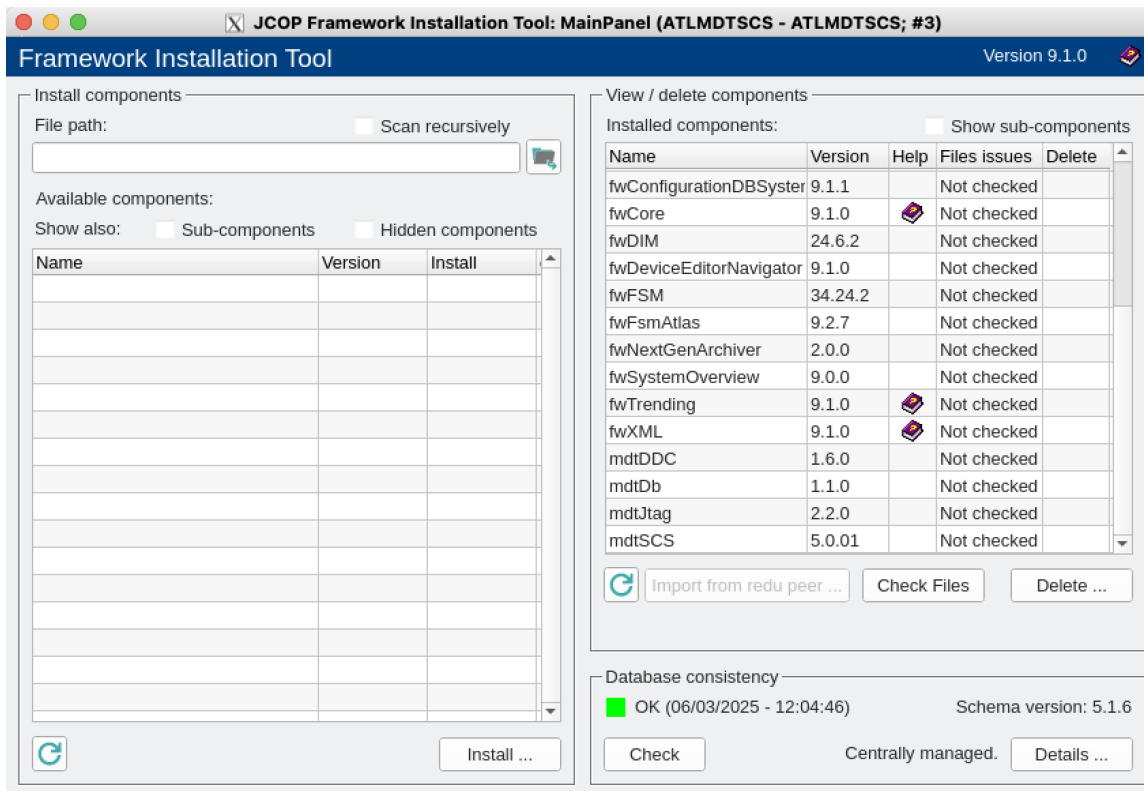


Figure 3.9: The Installation panel of JCOP Components

3.2.15 The WinCC OA Communication Protocols

3.2.15.1 The OPC UA Servers

The acronym OPC stands for "OLE (Object Linking and Embedding) for Process Control." The OPC Server is the foundation of OPC communication, functioning as software that adheres to the OPC standard and provides standardized interfaces to external systems. Internally, it integrates the proprietary communication protocol specific to the manufacturer's control system. Various entities develop and supply OPC Servers, with the core concept being that hardware manufacturers provide an OPC Server for their systems, enabling standardized access. These servers can be distributed as standalone software or embedded directly into devices or machine controllers. The DCS work described below utilizes OPC UA Servers, primarily to establish communication between projects involving power supplies and temperature monitoring. OPC-UA is an open-source protocol for machine-to-machine communication, developed by the OPC Foundation. It is widely adopted across research fields and industries for integrating diverse hardware systems. Based on a server-client model, OPC-UA facilitates seamless interoperability. In the context of the ATLAS experiment, WinCC OA will serve as the OPC client, linking control stations and interfacing with the OPC-UA server, which, in turn, communicates with the on-detector readout electronics.

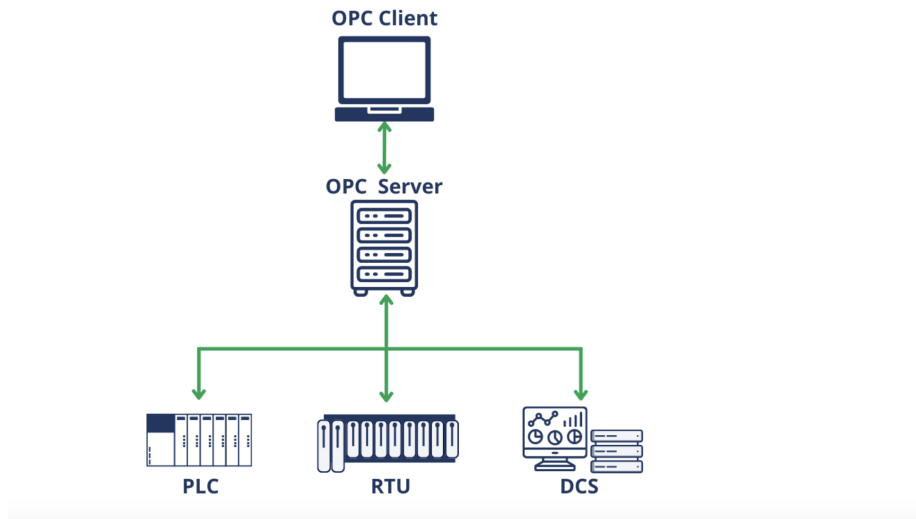


Figure 3.10: The OPC Communication Chain

3.2.15.2 The Distributed Information Management System

DIM[7] (Distributed Information Management System) is a portable, lightweight package for information publishing, data transfer, and inter-process communication. Based on the client/server paradigm, DIM operates through "named services," where servers provide data to clients. Clients request services once at startup, after which updates are automatically pushed by the server at set intervals or when conditions change. The client updating mechanism can be of two types, either by executing a callback routine or by updating a client buffer with the new set of data, or both. In fact this last type works as if the clients maintain a copy of the server's data in cache, the cache coherence being assured by the server. In order to allow for transparency (i.e, a client does not need to know where a server is running) as well as to allow for easy recovery from crashes and migration of servers, a name server was introduced. Servers "publish" their services by registering them with the name server (normally once, at startup). Clients "subscribe" to services by asking the name

server which server provides the service and then contacting the server directly, providing the type of service and the type of update as parameters. The name server keeps an up-to-date directory of all the servers and services available in the system. The Fig. 3.11 shows how DIM components (Servers, Clients and the Name Server) interact. Whenever one of the processes (a server or even the name server) in the system crashes or dies all processes connected to it will be notified and will reconnect as soon as it comes back to life. This feature not only allows for an easy recovery, it also allows for the easy migration of a server from one machine to another (by stopping it in the first machine and starting it in the second one), and so for the possibility of balancing the machine load of the different workstations.

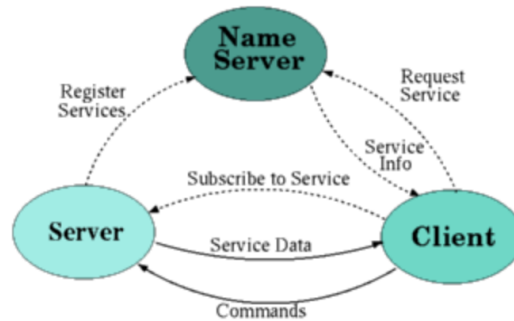


Figure 3.11: The Distributed Information Management System

3.2.15.3 The Data Interchange Protocol

The Data Interchange Protocol (DIP) is a communication system designed for exchanging small amounts of soft real-time data between loosely connected, heterogeneous systems. These systems do not require extremely low latency. The exchanged data is typically summarized rather than detailed low-level parameters—for example, the overall status of a

cooling plant rather than the specific position of a valve. In this Thesis the DIP was used for copy mechanisms on the Gas System of MDTs and the MUON Cooling Plants.

3.3 The Finite State Machine

A finite-state machine (FSM)[8] is a mathematical model of computation used to design both computer programs and sequential logic circuits. It is conceived as an abstract machine that can be in one of a finite number of states. The machine is in only one state at a time; the state it is in at any given time is called the current state. It can change from one state to another when initiated by a triggering event or condition; this is called a transition. A particular FSM is defined by a list of its states, and the triggering condition for each transition. Summarizing, the principle task of the DCS is to enable the coherent and safe operation of the detector by continuously monitoring its operational parameters and its overall state.

Each FSM node has a unique name based on the subsystem name and its functionality following the ATLAS DCS conventions and its state and status is defined by a corresponding internal DP. The FSM object type, that defines the basic functionality of the node and its sub-elements, depends on the element's functional purpose and position in the DCS architecture hierarchy. Three different object categories can be defined through the JCOP FSM toolkit :

- The Control Units (CU)
- The Logical Units (LU)

- The Device Units (DU)

3.3.1 Control Unit

Control Units are logical decision units. They can take decisions and act on their children (i.e. send them "Commands") based on their "States". Any Control Unit and the associated sub-tree can be a self-contained entity. The logic behaviour of a Control Unit is expressed in terms of Finite State Machines. State transitions can be triggered by:

- Command Reception (either from its parent or from an operator)
- State changes of its children

State transitions cause the evaluation of logical conditions and possibly "Commands" to be sent to the children. This mechanism can be used to propagate actions down the tree, to automate operations and to recover from error situations.

3.3.2 Device Unit

Device Units implement the interface with the lower level components (Hardware or Software). They are always a tree "leaf" (i.e. they have no children). They do not implement logic behaviour. They receive:

- "Commands" and act on the device
- device data and translate it into a "State".

3.3.3 Logical Unit

The Logical Units (LU) occupy a higher hierarchy level integrating several DUs (children) and their states/statuses are calculated on the base of their children via combination of boolean expressions. They can be used at the bottom levels of a tree (just like DUs) or can contain children like the CUs but in that case they cannot run in stand-alone.

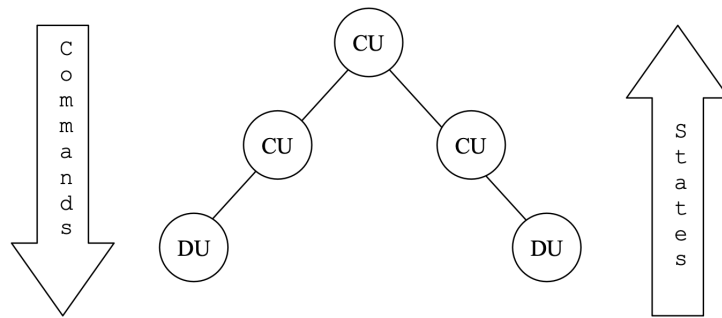


Figure 3.12: The FSM hierarchy with control units and device units

3.3.4 FSM States

In the ATLAS DCS, units are organized in a tree-like hierarchy. The top node represents the global state, while the lower levels consist of detector subsystems, followed by sub-groups, and so on. State changes are managed in a bottom-up manner, meaning that when a node's state changes, the update is propagated to all parent nodes. Conversely, control commands operate in a top-down fashion—when a user triggers a command on a node, it is passed down to all applicable child nodes. The most common states in the ATLAS DCS FSM include READY, STANDBY,

NOT READY, SHUTDOWN, TRANSITION, and UNKNOWN. This standardized set of states and commands is used across ATLAS to enhance the user experience in the control room.

- A state represents the operational mode of the system. For instance, when all detectors are powered ON, the system displays the state as ON. If the high voltage is in the process of ramping up, the message RAMPING or TRANSITION appears. Additional states include OFF, UNKNOWN, UNPLUGGED, and STANDBY. These state definitions can vary depending on the sub-detector, hardware, or specific technology used.
- Status describes how well the node is working while being in the current state. The status definitions are unique and identical across all ATLAS systems, with values either OK, WARNING, ERROR or FATAL, depending on the severity of the problem. In the panels the status and state of each lower level DU is also included.

A snapshot of the usual form of an FSM can be seen with the MDT System in the Fig. 3.13. The main overview panel with one picture will give a clear representation of the State and Status of the system. There is a colour code for the barrel and end-cap detectors with small banners describing it. In this panel the main points of interest are the High Voltage, Low Voltage and Electronics of the system. Usually most of the systems, during off Beam periods, are in STANBY which represents a slightly lower value of the High Voltage than the nominal. This is done in order to prevent unwanted discharges in the detector, which could come from high energy stray beam protons during beam stabilisation.

This main panel as well gives information about the Data Acquisition (DAQ) parameters of the system and the state as well.

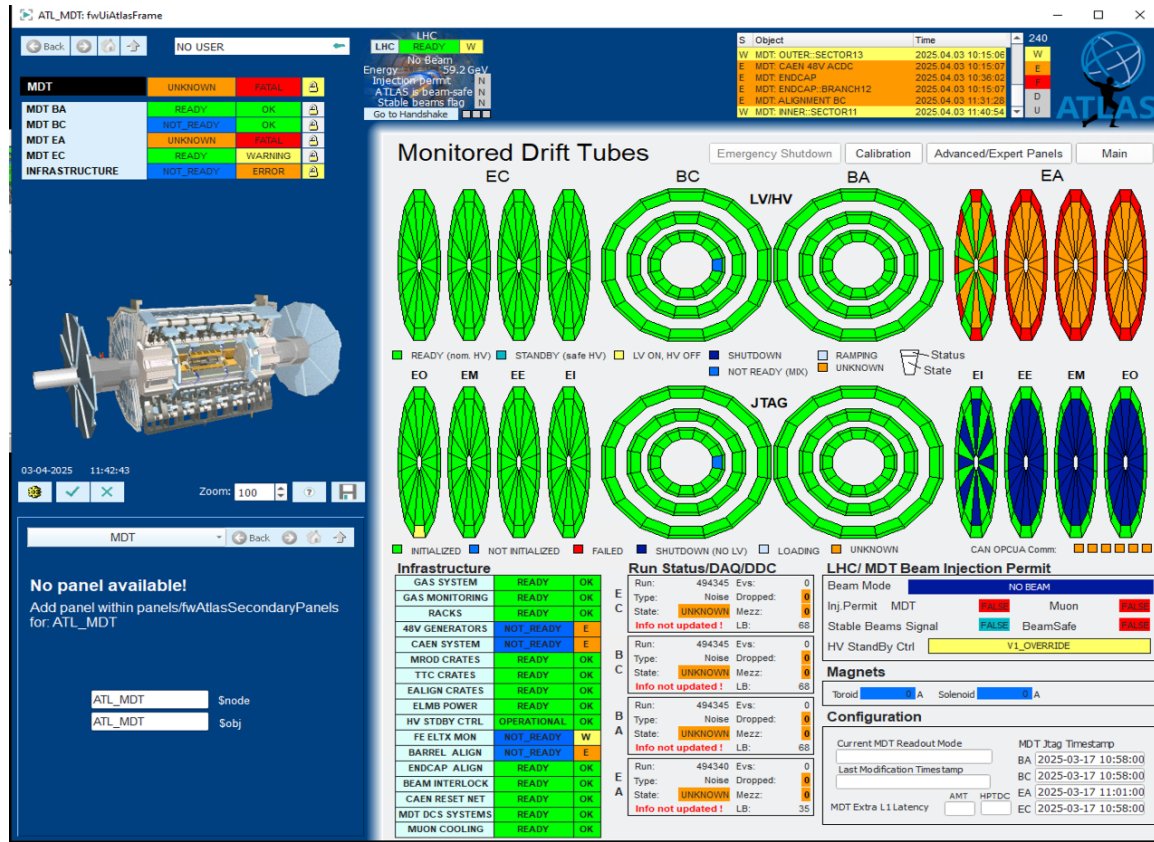


Figure 3.13: The Distributed Information Management System

The infrastructure nodes Fig. 3.14 helps with the observation and control of the Gas System, Power Supplies, ELMB, cooling system and Beam Injection System.

The next chapters will give more information about the DCS structure of the system.

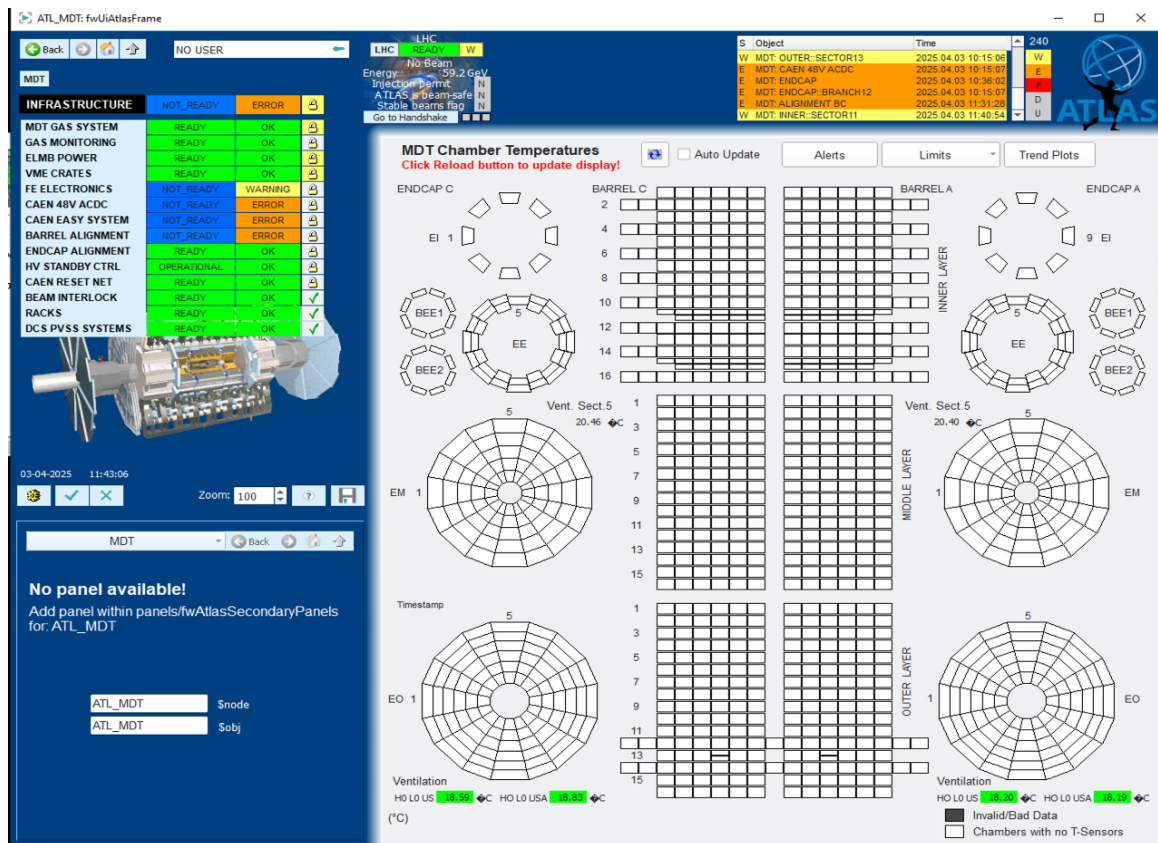


Figure 3.14: The MDT Infrastructure FSM Tree

3.4 The Muon Cooling Station

During LS2 some improvements were decided on the Muon Cooling System and integrated to DCS too. The first change was the publication of the values with the help of DIP and not for MODBUD[9] as before. The values in the form of data points are copied with the help of a control manager from a project of common infrastructure of central DCS (ATLGCSIS3).

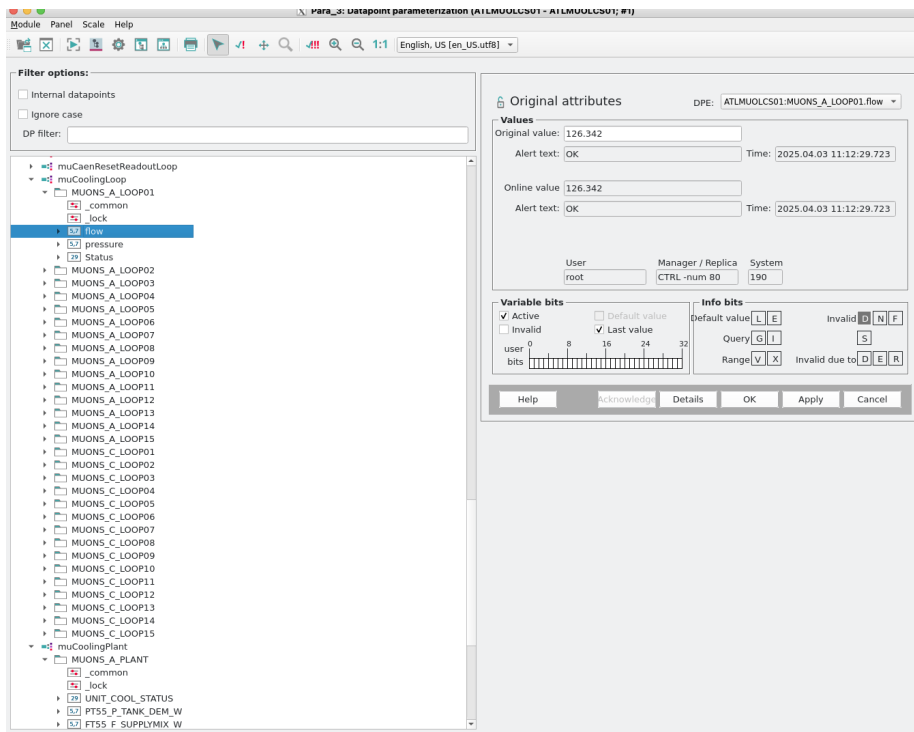


Figure 3.15: The New Datapoints structure of Muon Cooling

Two new datapoints were implemented as basic structure of the new system (Fig 3.15), that replace the previous that were created from an old deprecated JCOP Component. One is for the cooling loops(15 per side) and one for the cooling plant (one per side of the detector). The new DPs have 3 special configs parameters:

- a float value for flow
- a float value for pressure
- an integer value for status, that it translated to the state the specific cooling loop is like on, off, locked.

As next step the control manager is checking the communication between the distributed systems (muon cooling and supervisor pc of common infrastructure). If the communication cannot be established the copy mechanism cannot work.

After the creation of the new DPs (Data Points), which represent the structured objects containing the values and status of each cooling loop and cooling plant, and after establishing the communication, some updates were performed on the specific Service Panels to create alarms, descriptions and FSM structure automatically, as shown in Fig. 3.16.

The low level base of the FSM was built with the creation of the DUs based on the data points above : The muCoolingLoopDU and the muCoolingPlantDU. On Fig. 3.17 a more analytical structure of the DUs with the corresponding states can be viewed.

The DUs were created with the ATLAS FSM logic. A library is controlling their behavior (state/status). The FSM States connect with specific bits that every one of them cause the state to change (ON,OFF, etc). The status depends on the existence of the alarms of the DPs above. Every time the values are above or below the specific limits (Fig. 3.18), the status changes as well (OK,WARNING,ERROR,FATAL).

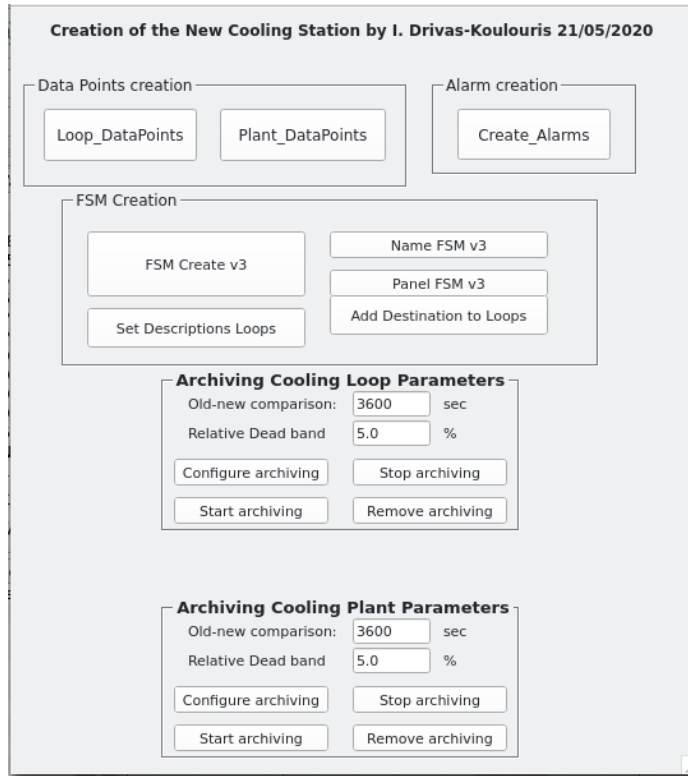


Figure 3.16: he service panel for the creation of Muon Cooling system

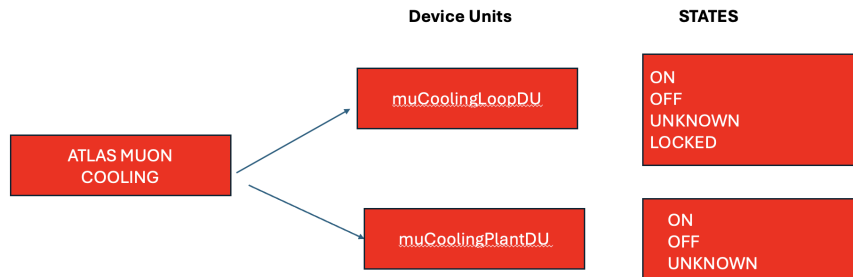


Figure 3.17: The DU structure of Muon Cooling FSM

The main FSM panels show a general view from outside with all the loops and their important information like flow, pressure and status (Fig. 3.19). If you navigate inside you can find some more specific information for every loop like the sub-detector they belong (Fig. 3.20).



Figure 3.18: The Alarm limits of Muon Cooling

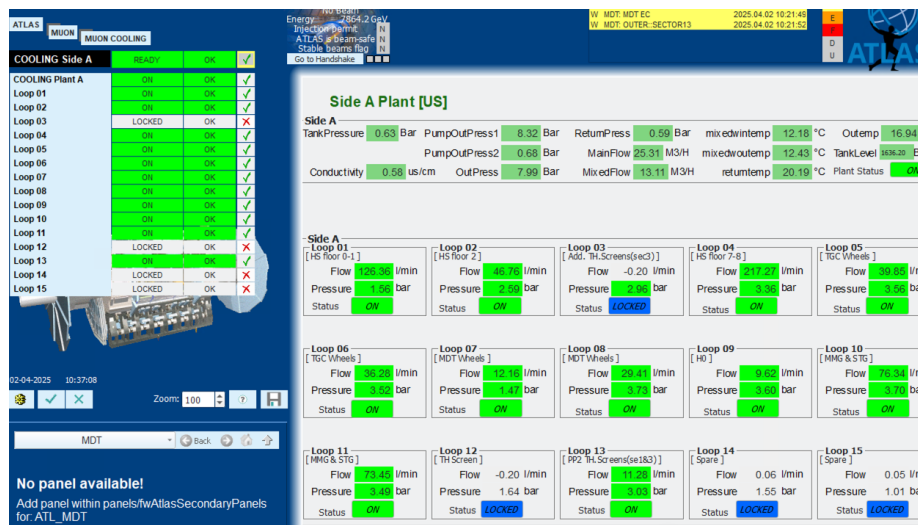


Figure 3.19: The Main FSM Panel of Muon Cooling



Figure 3.20: The Main FSM Panel that gives information for every loop

3.5 The High Voltage Power Systems

The developments on the DCS System for the NSW HV[11] will be discussed in this section.

Both the sTGC and Micromegas (MM) detector technologies used in the NSW operate under high voltage conditions. The sTGC detectors function with a single high positive voltage of 2800 V, with an expected maximum current of approximately 100 μA , even under the most intense luminosity scenarios. To account for safety considerations, a factor of five is applied [10], requiring the HV power system to deliver at least 500 μA and support voltages up to 3200 V. For effective monitoring and leakage detection, a current resolution of 0.1 μA and a voltage resolution of 0.5 V are recommended.

For the Micromegas detectors, the high voltage system must supply +570 V for the amplification gap and -300 V for the drift gap. Thus, a system capable of delivering up to $\pm 1000\text{ V}$ is considered suitable. As only the amplification gap needs to handle significant currents, the system should provide up to 10 μA (including a fivefold safety margin) for this gap, while just 1 μA is sufficient for the drift gap. Monitoring requirements suggest a current resolution of 2 nA and a voltage resolution of 0.5 V.

Table 3.1 summarizes the high voltage specifications for both sTGC and Micromegas detectors.

For the ATLAS New Small Wheel (NSW), the high voltage (HV) power supplies are provided by CAEN. The primary HV unit is the CAEN

HV Parameters	Value for sTGC	Value for MM
Max.output voltage (V)	+3200	+1000,−1000
Max.output current (μA)	500	10,1
Voltage resolution (V)	0.5	0.5
Current resolution (μA)	0.1	0.002

Table 3.1

The requirements of the high voltage power supply in sTGC and MM detectors [10].

SY4527 mainframe, which delivers HV directly to the HV boards of the Micromegas detectors. In the case of the sTGC detectors, the HV is routed from the mainframe to the HV boards via CAEN’s EASY 3000 crates[12], which are managed by A1676 branch controllers[13]. Detailed descriptions of the HV connections between the mainframe and the read-out channels of both the MM and sTGC detectors can be found in Section 3.5.1.

To ensure reliable operation, the ATLAS experiment employs a centralized Detector Control System (DCS) that monitors the status of various subsystems and facilitates inter-system communication. All DCS applications in ATLAS are built on SIMATIC WinCC Open Architecture (WinCC-OA), a Supervisory Control and Data Acquisition (SCADA) platform developed by Siemens. The HV components of the NSW are managed by a dedicated HV DCS, which interfaces with the NSW DCS and transmits status information to the central ATLAS DCS. Each control system uses its own naming convention to uniquely identify detector components and power units.

3.5.1 High Voltage Mapping

Maximizing phase space coverage in the recorded data is a key goal of the ATLAS physics program. In the New Small Wheels (NSWs), this is accomplished through a meticulously planned high voltage (HV) connection scheme. This scheme defines how HV is distributed from the power supplies to the readout channels of the sTGC and Micromegas detectors installed in the NSW sectors. The design ensures that any HV failure leads to only minimal data loss, thereby maintaining the broadest possible phase space coverage. Moreover, the connection strategy is tailored to make optimal use of available resources. The same HV mapping scheme is applied to both detector wheels, as outlined below.

3.5.1.1 sTGC

In the sTGC wedges, each radial segment within a layer is powered by its own dedicated high voltage (HV) channel. As a result, powering an entire wheel—comprising $16 \text{ sectors} \times 2 \text{ wedges} \times 4 \text{ layers} \times 4 \text{ radial segments}$ —requires a total of 512 HV channels. This demand is met using CAEN’s A3535[14] and A3540[15] HV boards. The A3535 model provides 32 channels, each capable of delivering up to 3.2 kV and 0.5 mA, in accordance with the HV specifications listed in Table 3.1.

The R1 segment, located closest to the beam pipe, experiences the highest particle flux and has occasionally drawn currents exceeding the 0.5 mA limit. To address this, A3540 boards, each offering 12 channels rated for up to 4 kV and 1 mA, are used specifically to power the R1 segments.

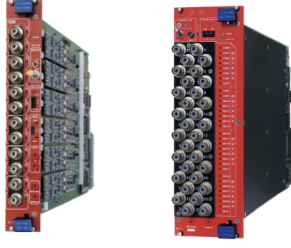


Figure 3.21: CAEN's A3540 (left) and A3535 (right) boards used in the high voltage connections for sTGC are shown.

Fig. 3.21 presents images of the CAEN A3535 and A3540 boards.

3.5.1.2 The NSW Mapping scheme

The A3535 boards supply HV in R2, R3, and R4 segments layer-wise in all the sectors. The channels are first connected to the R2 segment, and after supplying R2 in all four layers, the connections proceed to R3 until the 32 channels of each board are connected. In simple terms, the connection follows the pattern: $R2A01_L1 \rightarrow R2A01_L2 \rightarrow R2A01_L3 \rightarrow R2A01_L4 \rightarrow \mathbf{R3A01_L1} \rightarrow R3A01_L2 \dots \rightarrow R4A01_L4 \rightarrow \mathbf{R2A02_L1} \dots$. In this configuration, if one A3535 board fails, R2-R4 segments are affected in only three sTGC wedges of an entire wheel.

NSW-A		NSW-C	
Crate	Boards	Crate	Boards
Lower in Y.26-24.X1	$3 \times \text{A3540}$	Lower in Y.62-24.X1	$3 \times \text{A3540}$
	$3 \times \text{A3535}$		$3 \times \text{A3535}$
Upper in Y.26-24.X1	$3 \times \text{A3540}$	Upper in Y.62-24.X1	$3 \times \text{A3540}$
	$3 \times \text{A3535}$		$3 \times \text{A3535}$
Lower in Y.29-24.X1	$3 \times \text{A3540}$	Lower in Y.58-23.X0	$3 \times \text{A3540}$
	$3 \times \text{A3535}$		$3 \times \text{A3535}$
Upper in Y.29-24.X1	$3 \times \text{A3540}$	Upper in Y.58-23.X0	$3 \times \text{A3540}$
	$3 \times \text{A3535}$		$3 \times \text{A3535}$

Table 3.2

The arrangement of crate and HV boards for sTGC detectors in the cavern for NSW-A (left) and NSW-C (right). Every crate houses three A3540 and three A3535 boards. The crates are located in electronic racks in UX15. "Upper" and "Lower" refer to their positions in the rack, shown in Figure 3.22.

The A3540 boards supply HV in the R1 segment layer-wise in all the sectors similar to the A3535 board. After all the four layers are filled, the connection proceeds to the next sector, as $\text{R1A01_L1} \rightarrow \text{R1A01_L2} \rightarrow \text{R1A01_L3} \rightarrow \text{R1A01_L4} \rightarrow \mathbf{R1A02_L1} \dots$. With this arrangement, if one A3540 board fails, the R1 segment in only three sTGC wedges of an entire wheel is affected. It has to be noted that the A3535 and the A3540 boards supply HV to the two wedges interchangeably based on the cable length and available channels, which is not discussed here explicitly.

As mentioned earlier, the high voltage source that supplies power to the boards is the SY4527 mainframe. The mainframe is installed in USA15,

the service cavern, whereas the HV boards are located in UX15, the experimental cavern. The mainframe houses four branch controllers (two for each wheel), which distribute power to eight EASY 3000 crates (four crates per wheel), built to operate in a magnetic field and a radioactive environment of UX15. The crates accommodate the HV boards and are situated in dedicated ATLAS electronic racks in the cavern. NSW-A occupies the racks Y.26-24.X1 and Y.29-24.X1 whereas NSW-C occupies Y.62-24.X1 and Y.58-23.X0. The branch controllers in USA15 are connected to the crates in UX15 with cables of length ~ 120 m. In total, to supply high voltage to the sTGC detectors in one NSW, ATLAS employs 2 branch controllers, 4 crates, 12 A3535 boards, and 12 A3540 boards. The crate and board arrangement in the cavern is tabulated in Table 3.2 and illustrated pictorially in Fig. 3.22. Two CAEN 48V generators completing the hardware scheme. These new type of generators are handled directly by the branch controllers. They supply the "service" and the "power" lines of the CAEN easy chain circuitry. At this point is worth mentioning that a special customade component developed, the splitter board. The necessity of such tool emerged from the initial configuration of the CAEN hardware chain, with only 2 branch controllers. This specific setup introduced several issues, communication glitches, delayed response on commands, actions, the monitoring of the devices and also on to the archiving. Thus, another 2 branch controllers have been installed in order to share the data load. The incorporation of these new branch controllers along with their proper connections is performed via the splitter board as shown in Fig. 3.27.

The two A1676 branch controllers are inserted into the S4527 mainframe. The branch controller distributes the power from the generators to the crates, which house the A3540 and the A3535 HV boards. The mainframe

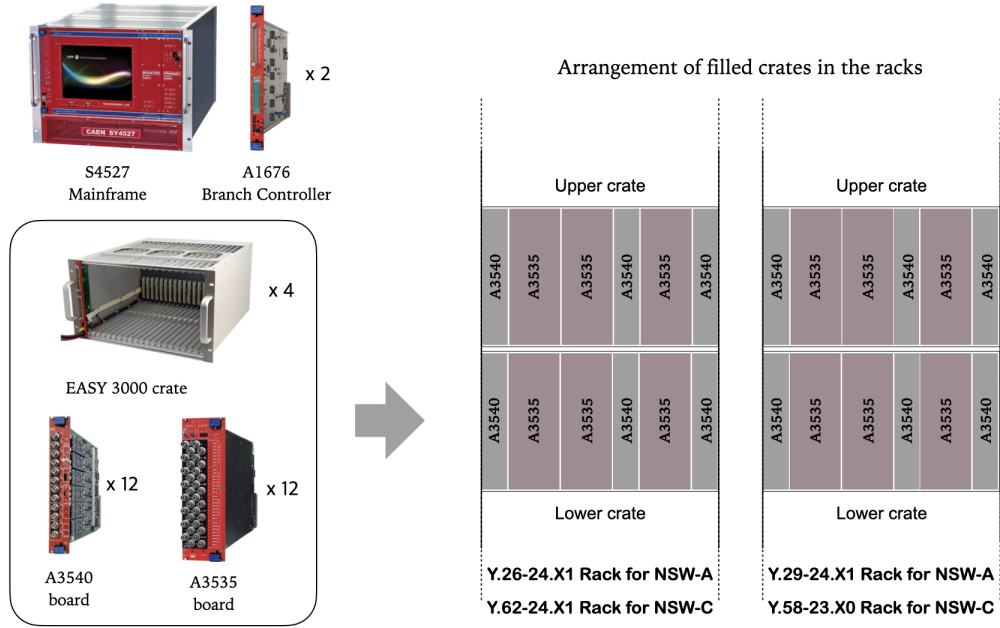


Figure 3.22: Arrangement of HV units for sTGC in the cavern. A graphical illustration of the arrangement of HV units for sTGC in the cavern is presented. The HV supplies (left) and arrangement of the HV boards in the crates (right) are shown.

and the branch controller are situated in USA15, whereas the crates and the HV boards are located in UX15. The branch controller in USA15 is connected to the crates in UX15 with the help of lengthy cables. Each crate hosts three boards, each of A3540 and A3535. A crate consists of 20 slots, and each A3540 board occupies two slots, and each A3535 board occupies four slots in the crate, leaving two slots free per crate. The HV boards are accommodated by four crates, arranged one on top of the other, named Upper and Lower, in two adjacent racks in the UX15 cavern.

The boards are inserted directly into the three mainframes, arranged one on top of the other in the US15 racks. Each mainframe consists of 16 slots, and the first mainframe accommodates 16 A7038AP boards (each occupying one slot in the mainframe). The second and the third

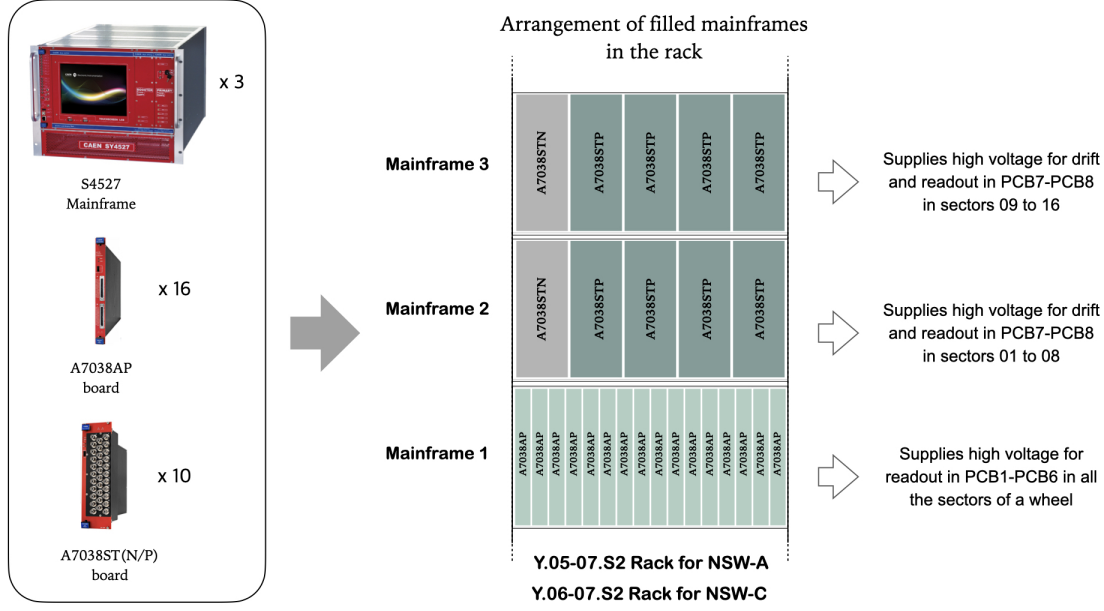


Figure 3.23: Arrangement of HV units for micromegas in the cavern. A graphical illustration of the arrangement of HV units for micromegas in the cavern is presented. The HV supplies (left) and arrangement of the HV boards in the mainframes (right) are shown.

mainframes each hold one A7038STN and four A7038STP boards. The A7038ST boards occupy three slots in the mainframe, thus leaving one slot free each in Mainframe 2 and Mainframe 3.

3.5.1.3 Micromegas

A micromegas detector operates with high voltages of two different polarities: a negative high voltage for the drift gap and a positive high voltage to amplify the signal for readout. The high voltage for drift is supplied to each radial segment, and all four layers of the segment share the voltage. Altogether, 64 HV channels are required to provide drift voltage in one wheel (16 sectors \times 2 wedges \times 2 radial segments). In the case of high voltage for readout, lowest HV unit is an HV channel supplied per radial

segment similar to sTGC according to the initial NSW design proposal. But in early 2020, it was decided to increase the HV granularity by providing high voltage to every PCB within a radial segment rather than to every radial segment. Therefore, to supply readout HV to one wheel ($16 \text{ sectors} \times 2 \text{ wedges} \times 4 \text{ layers} \times 8 \text{ PCBs}$), 1024 HV channels are required.



Figure 3.24: CAEN’s A7038AP (left) and A7038ST(N/P) (right) boards used in the high voltage connections for MM are shown.

The HV needs of micromegas are fulfilled by CAEN’s A7038ST(N/P) and A7038AP boards[16], shown in Fig. 3.24, both supplying 1 kV and 100 μA (10 times better than the requirements). The A7038ST boards consist of 32 channels, and they come in two different polarities: A7038STN for negative and A7038STP for positive. The A7038AP board (purchased following the increased HV granularity needs) consists of 48 channels and provides only positive voltage.

3.5.1.4 Mapping scheme

The channels in A7038STN board are connected such that each board supplies the radial segments of both the wedges sector-wise as $R1A01 \rightarrow R2A01 \rightarrow R1A02 \rightarrow R2A02 \rightarrow R1A03 \dots$. Therefore, only two such boards are required to provide the 64 HV channels for drift in one wheel.

For the readout HV, each HV channel is connected to the PCBs radially and supplies all layers before proceeding to the next sector. An example for the connection scheme is $R1A01_L1_PCB1 \rightarrow R1A01_L1_PCB2 \rightarrow R1A01_L1_PCB3 \rightarrow R1A01_L1_PCB4 \rightarrow R1A01_L1_PCB5 \rightarrow R2A01_L1_PCB6^1 \rightarrow R2A01_L1_PCB7 \rightarrow R2A01_L1_PCB8 \dots$. The HV connection scheme for MM readout channels is slightly more complicated than that for sTGC due to the large number of channels involved. The channels are assigned such that all the A7038AP boards are fully used first, and then the remaining supplies are provided by the A7038STP boards. Similar to sTGC, the HV power source for micromegas is also the SY4527 mainframe. But unlike sTGC, the HV supply for Micromegas is not operated based on the daisy chained CAEN Easy system. Instead, the HV boards are inserted directly into the mainframes, situated in the US15 service cavern². Each wheel utilizes three mainframes, and the HV boards each mainframe houses are tabulated in Table 3.3. In total, to supply high voltage to the MM detectors in one NSW, ATLAS employs 3 mainframes, 16 A7038AP boards, 8 A7038STP boards, and 2 A7038STN boards. The mainframes are located in the Y.05-07.S2 rack for NSW-A and the Y.06-07.S2 rack for NSW-C. A summary of the mainframe and board arrangement in the cavern is recorded in Table 3.3 and illustrated graphically in Fig. 3.23.

It is worth mentioning, that the HV connections from the rack to the MM and the sTGC detectors mounted on the NSW sectors are not made by a single stretch of cables. Instead, a complex network of six sets (three sets for each detector technology) of cables with different lengths are involved.

¹PCBs 6–8 belong to the R2 segment

²For sTGCs, crates that are built to function in a magnetic field and a radioactive environment are used because the HV boards are operated from the racks in the experimental cavern. As the HV boards for micromegas are located in the service cavern of US15, crates are not necessary.

Mainframe	Boards
Mainframe 1 in Y.(05/06)-07.S2	$16 \times \text{A7038AP}$
Mainframe 2 in Y.(05/06)-07.S2	$4 \times \text{A7038STP}$ $1 \times \text{A7038STN}$
Mainframe 3 in Y.(05/06)-07.S2	$4 \times \text{A7038STP}$ $1 \times \text{A7038STN}$

Table 3.3

The arrangement of mainframe and HV boards for Micromegas in the cavern is tabulated. The three mainframes are located in the respective racks in US15. Mainframe 1 hosts 16 A7038AP boards, whereas the other two mainframes house one A7038STN and four A7038STP boards each.

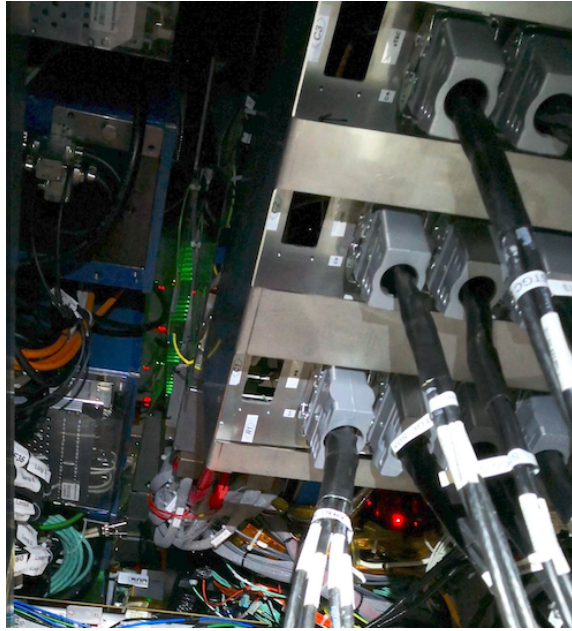


Figure 3.25: The MMG patch panel at the ATLAS UX15 Cavern.

Fig. 3.26 shows a schematic of the cable connections from the rack to the detector chambers. The current in the HV cables is conducted through copper wires that are surrounded by a protective film wrapped in an insulating sheath. The technical specifications of the different cable sets

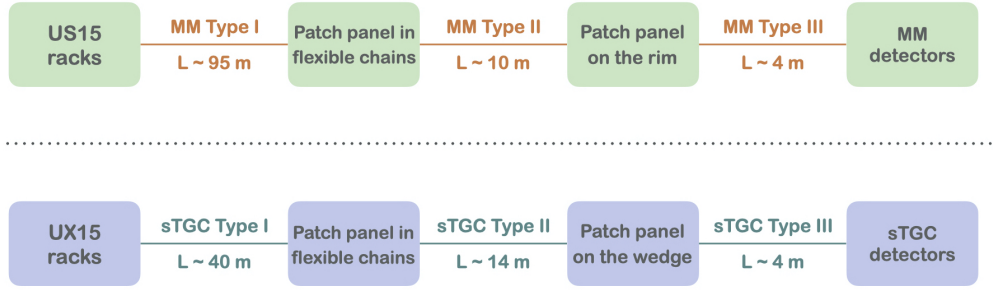
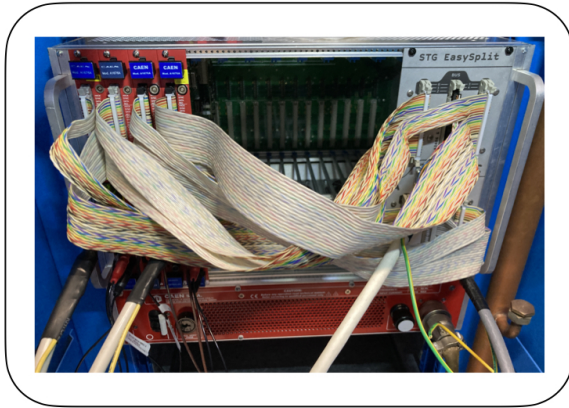


Figure 3.26: A schematic of the high voltage cable connections from the racks to the detectors is shown for micromegas (top) and for sTGC (bottom).

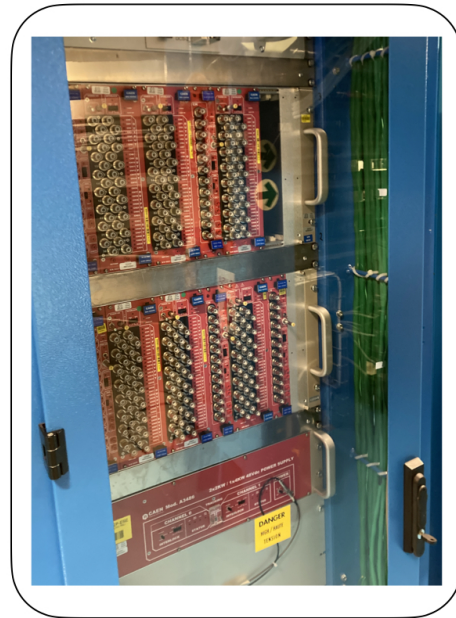
are beyond the scope of this note and are not described. More information can be found in [17, 18, 19, 20, 21].

For MMG, nearly 95 m long Type I cables are used to connect the HV boards in the US15 racks up to the patch panels as shown in Figure 3.25 located in the flexible chains in sector 9 of the NSW. From the flexible chains, Type II cables with 10 m are routed to the HV patch panel located in an accessible place on the outer rim of the wheel. The HV connection for drift and readout is then furnished by ~ 4 m long Type III cables. In the case of sTGC, Type I cables have a length of ~ 40 m and extend from the HV boards in the UX15 rack to the patch panel in the flexible chains of sector 09, similar to MM. Type II cables stretching over ~ 14 m continue the connections to the patch panel on the detector wedge and finally 4 m long Type III cables complete the supply to the sTGC detectors.

On account of the lengthy cables involved and complex cable connections, the images of the HV units and racks at different stages of HV connections are shown in Fig. 3.27. For simplicity, not all the stages of HV connection are shown for sTGC and MM.



SY4527 mainframe for sTGC with
4 A1676 branch controllers and
the STG Easy Split Board for
NSW-A and NSW-C



A single sTGC rack with
filled crates along with the
power generator before any
cabling is made



MM racks for NSW-A (right)
and NSW-C (left) after the
cabling is complete

Figure 3.27: The HV units and racks at different stages of HV connections are shown.

3.6 NSW Caen Easy System DCS

The CAEN EASY system is a modular system of LV and HV power supplies developed by CAEN for the LHC experiments; are grouped into two main categories, the radiation-sensitive parts, and the radiation hard parts. Among its core features are the remote control, the scalability, the compatibility with operation under strong magnetic fields, and radiation harsh environments like the ATLAS cavern (UX15).

The MMG HV system consists of three mainframes per side and the HV boards are installed directly onto them. The main difference between them is that the third mainframe is fully equipped with 16 A7038AP boards serving in such a way all 16 sectors, 4 layers, and the first 5 PCBs (8 in total per layer). The other mainframes follow the same “mapping” scheme, where 4 A7038STP HV boards supply the remaining 3 PCBs. The system is completed by two boards of type A7038STN, which supplies the voltages of the drift panels. The FSM tree consists of three nodes dedicated to each mainframe. The graphical user interface (panel), as illustrated in Fig. 3.28, monitors the vitals (fan speed, status, V1/V0 set flag, etc.) of each mainframe along with the visualisation of the installed board and their main status parameters.

The STG HV system architecture consists of a mainframe, two branch controllers and four crates per side. The branch controllers handles the chain along with the generators. The HV boards are installed in the CAEN Easy Crates and located in the UX15, in a unified format in order to regulate the power consumption per crate. There are two different types of boards, the A3540P and the A3535P serving the 16 STG sectors.

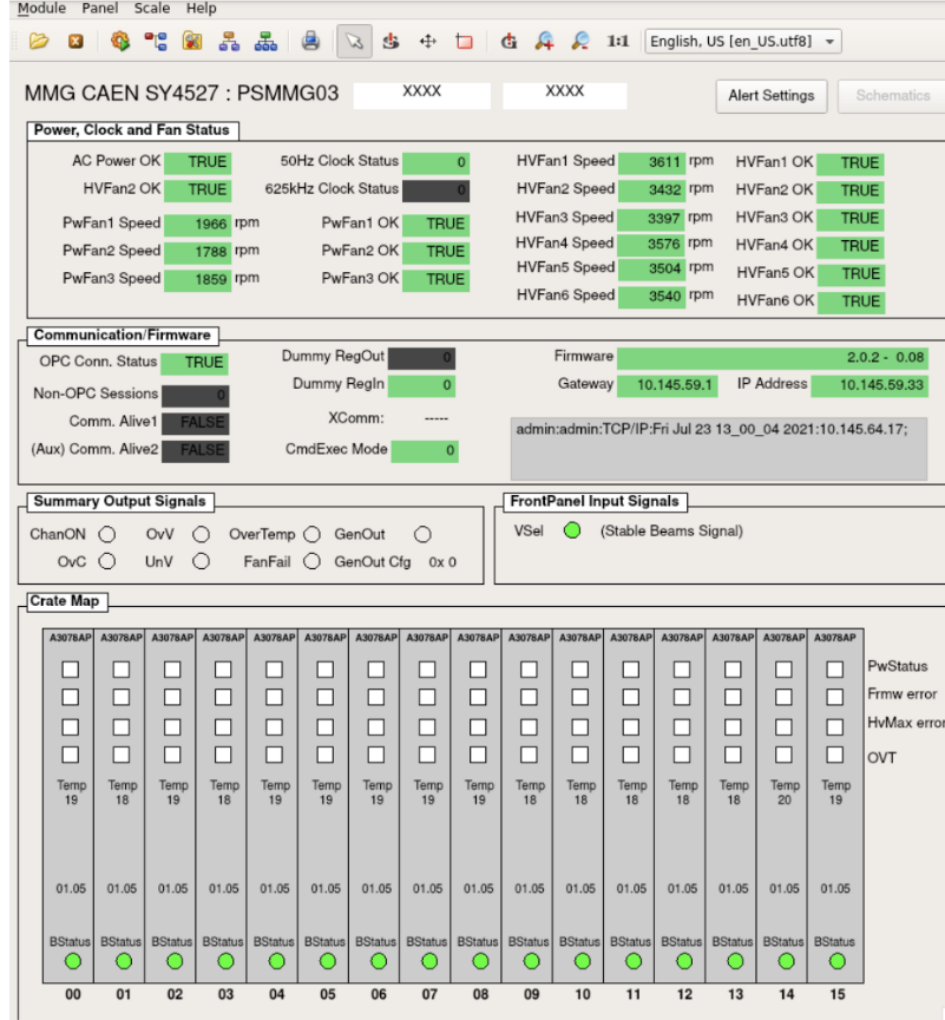


Figure 3.28: Main FSM MMG panel for the Mainframes

There are 4 parts per layer, where the former serves the innermost part of the detector while the other type the rest. The FSM is divided in three nodes :

- one for the mainframe with the main panel similarly to the MMG Tree, but branch controllers' information instead of boards as shown in Fig. 3.28.
- one node branch controllers.

- one node for the crates including also the FSM branch controllers for the HV boards, as shown in Fig. 3.29.



Figure 3.29: On the left is Main FSM STG panel for the Mainframes. On the right the Main FSM panel for STG crates.

3.7 NSW (STG) Caen 48 V Generators

The 48 V generators are used for the STG Sub-detector using the pre-existing muon logic. The crates and boards are supplied with an external DC power of 48 V generated by separate AC-DC converters. The system consists of two generators per side of detector. Each generator has two channels. The 48 V Service generator[22] is responsible for the control of the easy chain circuitry, distributing the power to the easy crate controllers. The 48 V power generator[23] on the other hand is responsible for the output power of the modules up to the channels' level.

Left Fig. 3.30 depicts the associated to the generators rack. Each generator is represented by a rectangle which holds the details about the current,

voltage and temperature of every channel. The panel also provides information about the branch controllers and the main logical parameters of the channels as well as supplementary information concerning the connected branch controllers and the generators channels, alongside with a visual representation of the associated to these generators' chambers. The user/expert can select a variety of monitoring controls to perform, from highlighting the associated to the generator chambers, up to configuring low level elements such as the alert handling. The main STG generators FSM include all these panels, which are associated with the respective nodes. By clicking the state of the nodes, the user can turn on/off the corresponding generators' channels, allowing in such way the control of all or part of the connected hardware.

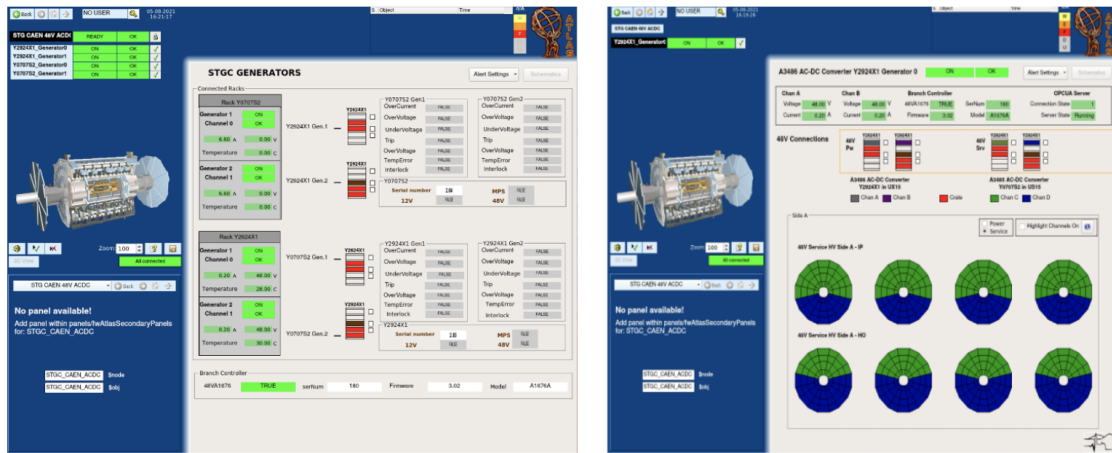


Figure 3.30: On the left is Main FSM STG panel for the Mainframes. On the right the Main FSM panel for STG crates.

3.8 NSW Reset Network

The CAEN Reset Network was implemented to provide a remote reset during periods without or limited access during beam mode were an actual incident might arise or a clean restart is needed to establish a glitch on power or even communication level. Similarly to the legacy systems, the NSW is using the same logic via the Agilent circuitry [24]. Due to the limitation of the lines in such module, the NSW took some lines from the legacy systems, one from the retired Cathode Strip Chambers (CSC) system, one from the Monitored Drift Tubes (MDT) and one line from the Resistive Plate Chambers (RPC). Multiplexing of some signals was performed in order to include all the hardware of the NSW for both technologies and both board types (LV and HV). A cable is connected for each branch controller to the Agilent module at USA15, where the presence or absence of the 50 Ohm resistor is emulated by a DCS controllable piece of electronics. The Reset Network allows to perform a simultaneous reset of the CAEN mainframes and the branch controllers individually. The MMG FSM has only the mainframe node, shown in Fig. 3.31, where with the “one click” mechanism the expert can reset all the associated to this line mainframes. Unfortunately, due to the limited numbers of lines in the Agilent module, this action will affect all the mainframes of the MMG system for both sides, and thus the expert has to be very careful, communicating to all the affected systems such action in advance.

Similarly to the MMG, the STG reset network has been developed. The possibility of resetting the mainframes of the STG or individually the

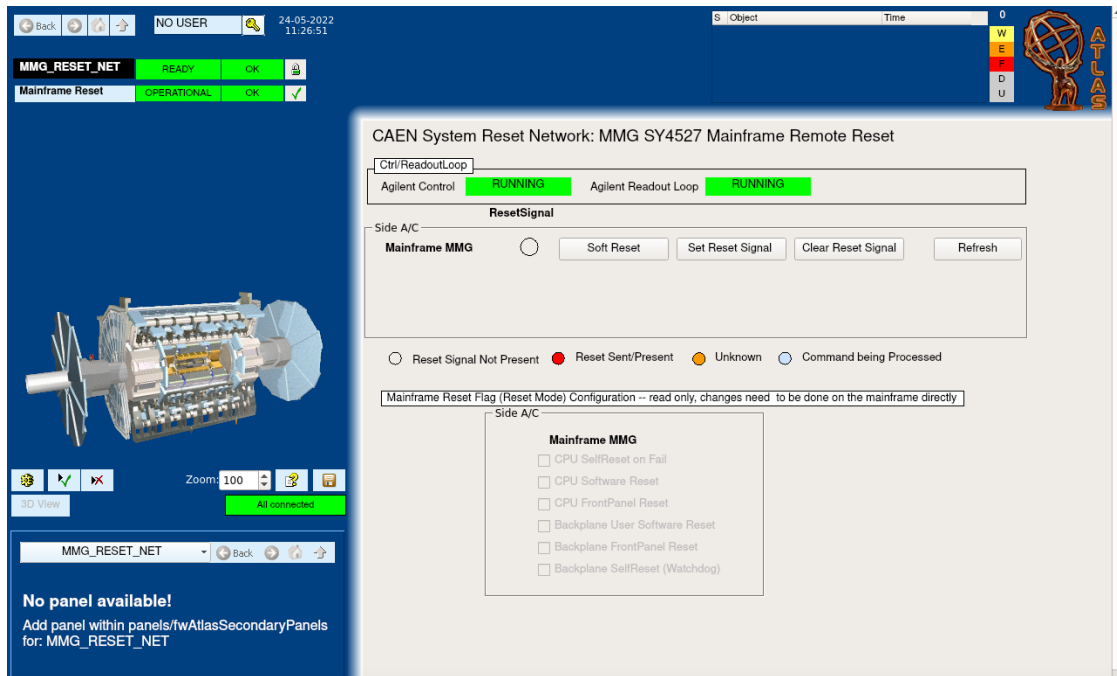


Figure 3.31: Main panel for MMG Reset Network FSM.

branch controllers is available. However, the mechanism to independently reset a crate is under development. The FSM of the STG follows explicitly the hardware structure, consisting of two nodes, one for the branch controllers and one for the mainframes as depicted in Fig. 3.33 and 3.63, respectively. By right clicking the branch controller object element (green circle) the user can perform the following actions:

- ENABLE DCS CTRL - Enables reset functionality for this line.
- DISABLE DCS CTRL - Disables reset functionality for this line.
- RESET - Perform the reset for the connected branch controller.
- GET STATUS - Reread the status of the line.
- CANCEL - Abort doing anything on this line.

Agilent channel	DCS DPs @ MUOLCS01	Latest Connections
Chan01	MUO BIS BISInterface MDT/CSC ForceMode	MDT FORCE (bistable)
Chan02	MUO BIS BISInterface RPC ForceMode	RPC FORCE (bistable)
Chan03	MUO BIS BISInterface TGC ForceMode	TGC FORCE (bistable)
Chan04	MUO BIS BISInterface MDT/CSC StableBeams Signal	MDT BYPASS to LHC (bistable)
Chan05	MUO BIS BISInterface RPC StableBeams Signal	RPC BYPASS to LHC (bistable)
Chan06	MUO BIS BISInterface TGC StableBeams Signal	TGC BYPASS to LHC (bistable)
Chan07	MUO BIS BISInterface BISPermit1, MDT	INJECTION PERMIT 1 MDT (bistable)
Chan08	MUO BIS BISInterface BISPermit2, RPC	INJECTION VETO 2 RPC (bistable)
Chan09	MUO BIS BISInterface BISPermit3, TGC	INJECTION PERMIT 3 TGC (bistable)
Chan10	MUO BIS BISInterface BISPermit4, CSC	INJECTION PERMIT 4 NSW (bistable)
Chan11	MDT CAENReset Mainframe1 Reset	MDT MAINFRAME RESET (both lines) (monostable)
Chan12	MDT CAENReset Mainframe2 Reset	NSW BYPASS TO LHC (bistable)
Chan13	x	RPC MAINFRAME RESET H1/H2 (monostable)
Chan14	x	NSW US MAINFRAME RESET (monostable)
Chan15	x	RPC MAINFRAME RESET L1/L2 (monostable)
Chan16	x	NSW USA MAINFRAME RESET (monostable)
Chan17	TGC CAENReset Mainframe SideA Reset	TGC MAINFRAME RESET A (monostable)
Chan18	TGC CAENReset Mainframe SideC Reset	TGC MAINFRAME RESET C (monostable)
Chan19	x	NSW FORCE (bistable)
Chan20	x	ISEL RPC (monostable)

Figure 3.32: The Agilent lines of Reset Network of the Muon Systems

The STG mainframe Reset panel connects the STG HV with the STG and MMG LV and can be operated by the following actions :

- **Soft Reset:** Reset signal to the mainframe's front-panel reset input is shorter than 1 second, equivalent to shortly depressing the front-panel reset button. A soft reset acts on parts of the mainframe only,

as defined in the "Reset Flag" configuration. A soft reset is used to reboot the mainframe CPU without affecting the back plane, i.e. without turning any EASY boards nor any LV/HV channels off.

- **Hard Reset:** This is a full reset, which will turn off all boards and channels controlled of the mainframe. A hard reset occurs if the reset signal is longer than 3 seconds in duration or equivalently, if the reset button is pressed for more than 3 seconds.

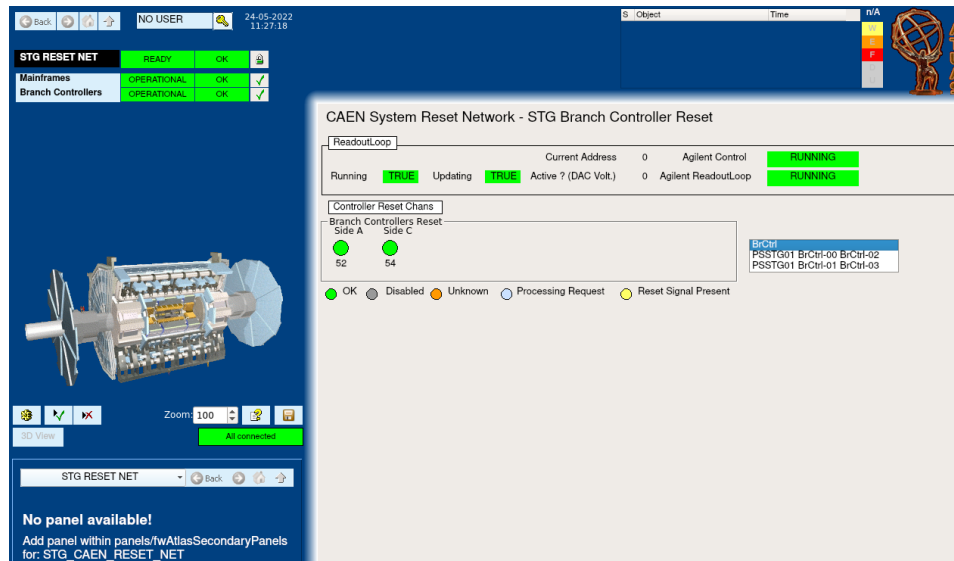


Figure 3.33: Main panel for STG Reset Network FSM, for controlling the branches.

The NSW Reset Tree has been tested succesfully validating at the same time the mapping of all the NSW Agilent lines between the mainframes and branches of both HV and LV of the systems.

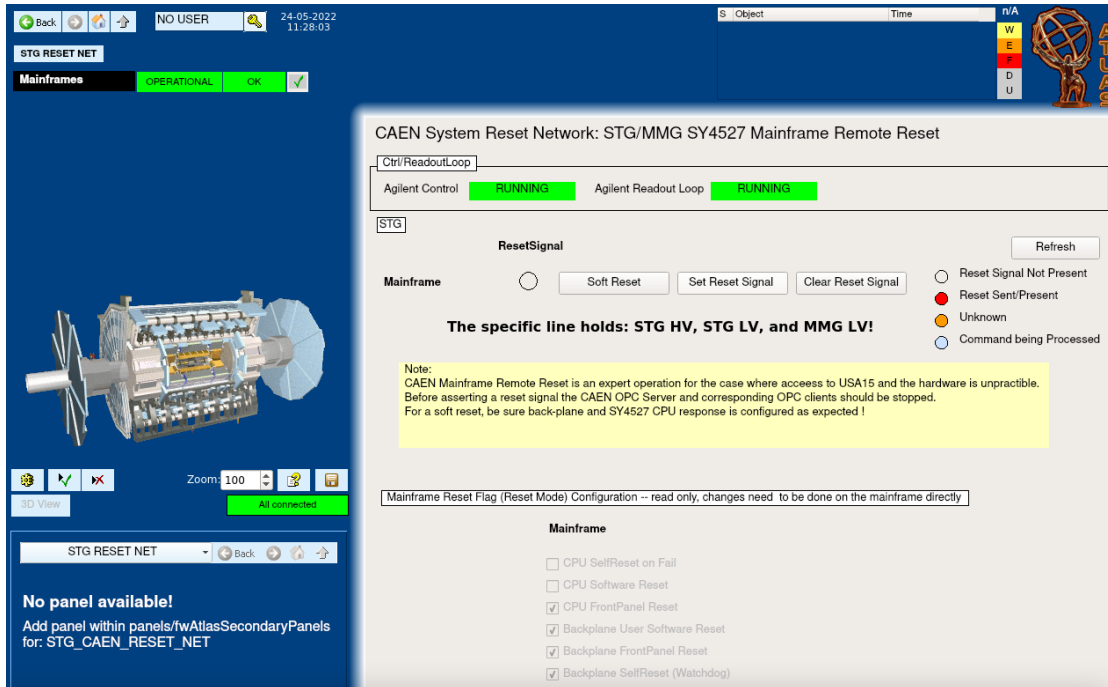


Figure 3.34: Main panel for STG Reset Network FSM, for controlling the Mainframes.

3.9 MM HV Validation Test

Before the installation of HV boards at the ATLAS US15 area, a validation test[25] had to be performed. The purpose of the test was to check if the boards can operate under specific conditions meeting all the requirements showing a stable behavior. The boards under-test had to go successfully through the following procedure :

- all channels are turned ON for 10 minutes.
- all odd channels are turned OFF while the even ones are kept ON for 30 minutes.
- all even channels are turned OFF while the odd ones are kept ON

for 30 minutes.

- all channels are turned OFF for 2 hours.
- all channels are turned ON for 40 minutes.
- all the channels are turned off and the test is finished.

In order to realise such test, a dedicated setup has been built at the BB5 laboratory at CERN as shown in Fig. 3.35. The setup consists of a DCS Project for the validation test and an OPC-UA server responsible for the communication between the DCS project and the mainframe.

In order to have representative system CAEN SY4527 mainframe[26] has been used. To complete the assembly of the test-stand two DB connectors and a load that works as a resistor have been utilised; terminating the circuitry and allowing the boards to be turned on. Due to the limited number of loads, 4 cables and two loads have been used, validating in such case two boards per test cycle.

DCS-wise a project has been developed for the monitoring and the validation of the HV boards along with their parameters. On the low level structure two data points types (DPTs) were created Fig. 3.36, one for the boards (A7037AP-MODULES) and one for the channels (A7037AP-CHANNELS). Each of these DPTs contain the most important DP elements (DPes) such as the monitoring current (iMon), and voltage (vMon) and the maximum allowed voltage that the channels can operate (Vmax-SoftValue), the trip limit, the trip time and much more.

The next step was the creation of a panel dedicated to monitor the under-test board as shown in Fig. 3.37. The panel contains information for the

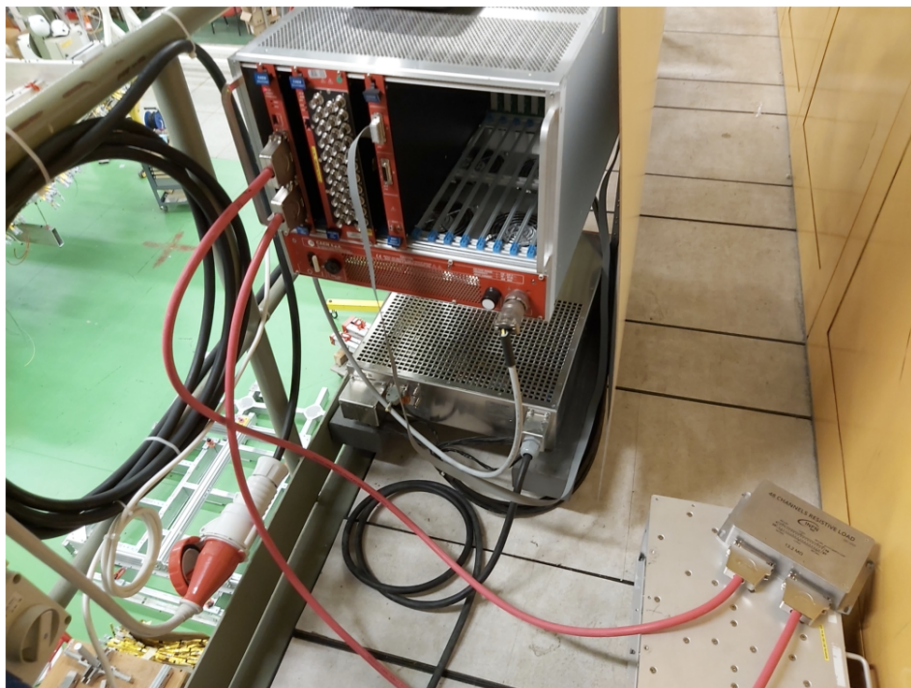


Figure 3.35: Test setup at BB5 laboratory.

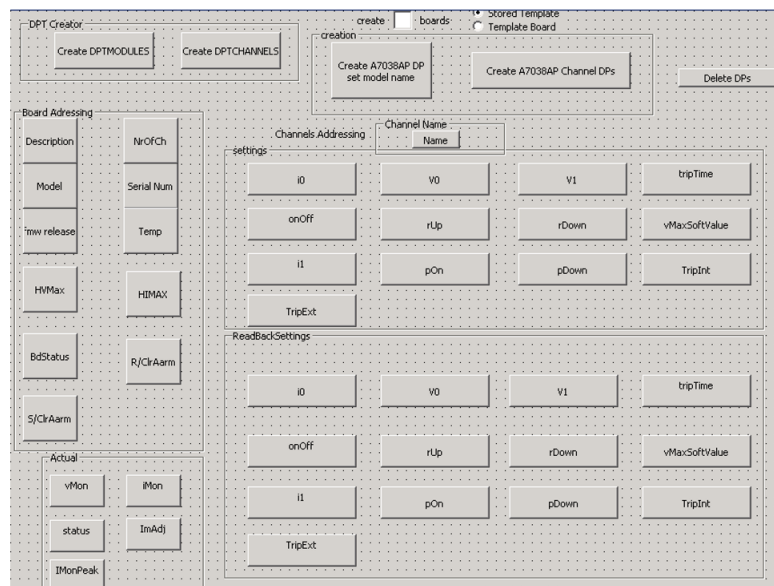


Figure 3.36: Data points and low level structure of the test parameters

serial number of the board (board id), the status of each of the channels and a button to facilitate the start and the stop of the test at any time.

Additionally, the panel offers the possibility to modify the duration of some of the previous steps : The duration can be adjusted based on the user's needs between 4 and 16 hours.

Figure 3.37: Main test visualization panel.

At the end of the test a .txt file is exported and can be analysed by using the ROOT framework. The validation parameters of highest interest are shown in Fig. 3.38 and are the monitoring voltage and the current for different time-lapses. During the tests there were only some minor issues on some of the boards due to connection problems between the OPC UA Server and the mainframe. In the end all the boards (36) were tested successfully and 32 of them were installed at the ATLAS US15.

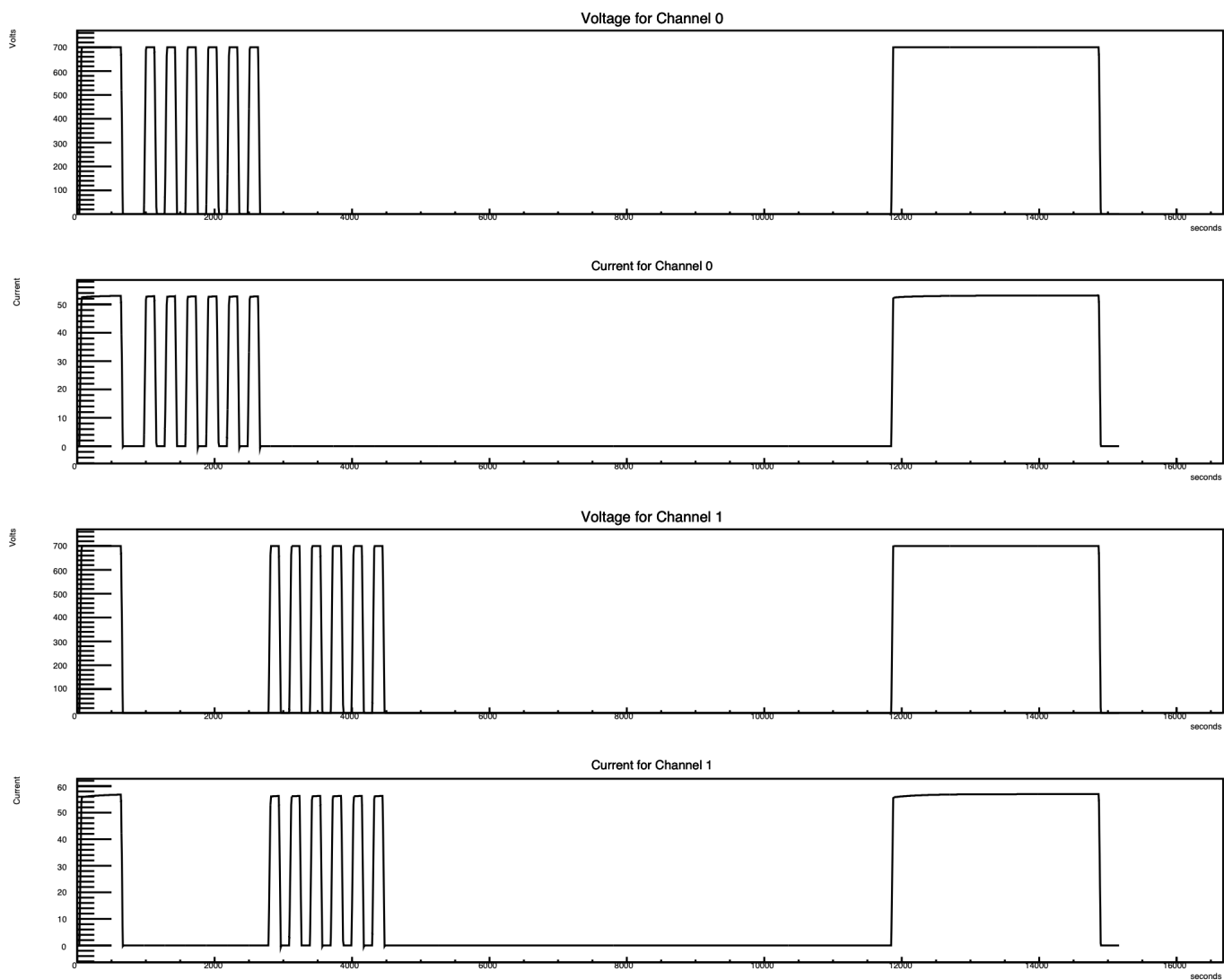


Figure 3.38: Monitoring Voltage (V) and Current (μA) of the boards, during a cycle.

3.10 HV Operation Panel

One of the upcoming tasks for the New Small Wheel (NSW) is the implementation of a dedicated operation panel for both of its sub-detectors, based on the MDT logic framework.

The Micromegas (MMG) HV Operation Panel offers an overview of the number of channels and their corresponding Power Supply (PS) Finite State Machine (FSM) states. A key feature is a navigable list of specific channels, enhanced with a filter function, allowing users to directly access FSM channels by right-clicking nodes in the list.

Additional features include:

- Trip limit data display alongside real-time current monitoring per channel.
- A newly added Beam Info section.
- A status plot showing the number of channels in each FSM state: ON, OFF, or DISABLED.

These FSM states are archived and accessible via the Detector Data Viewer (DDV), with daily updates managed by the system administrator. The displayed values represent averages over time but can be adjusted as needed. This panel design and functionality have also been extended to the sTGC subsystem.

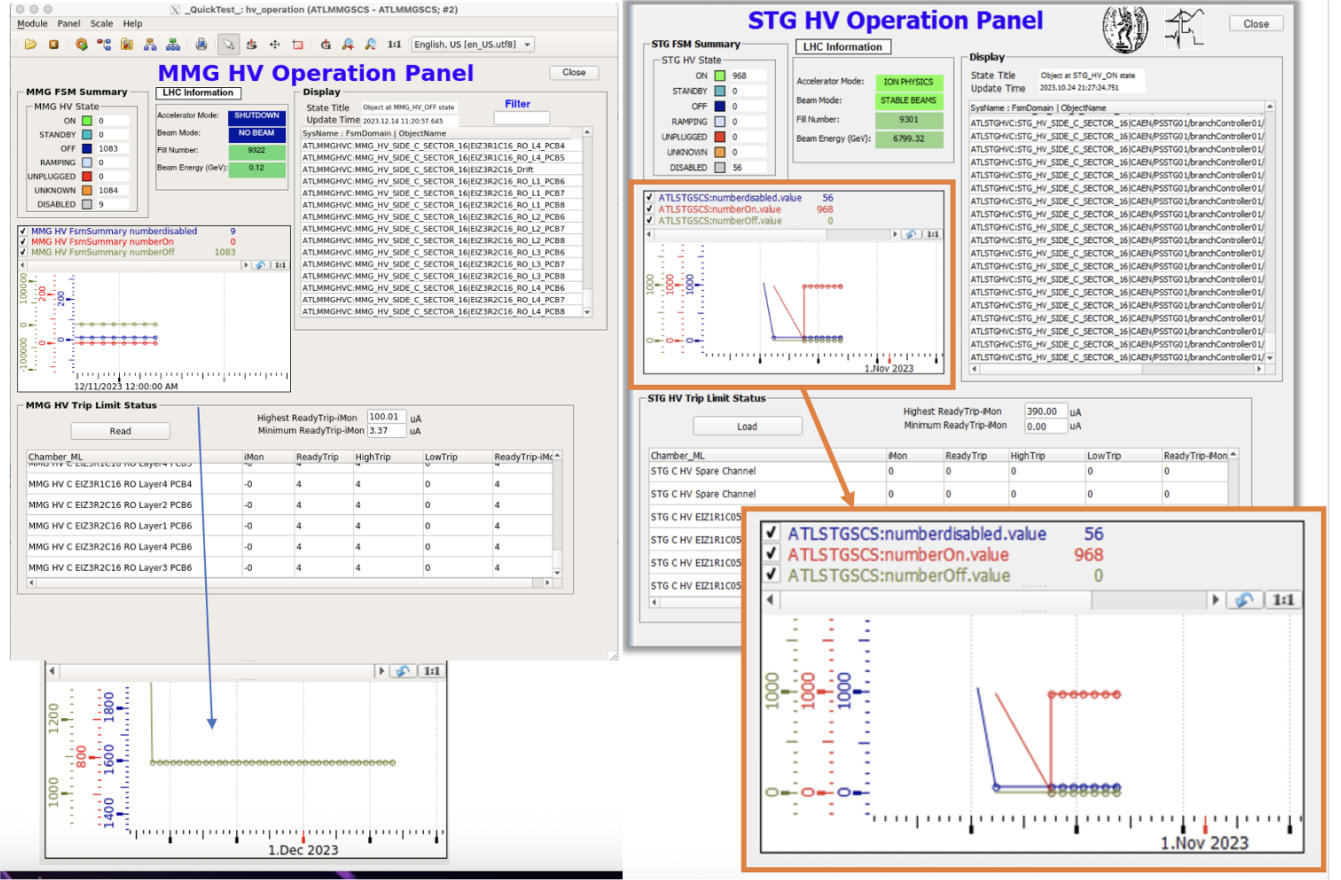


Figure 3.39: The NSW Operation panels

3.11 BIS78 DCS Project

In this part we focus on the creation of the DCS Project for the new sMDT BIS7 Chambers. This project has been developed for the side A of the detector, when on the same time the old BIS7 chamber are still install on the Side C. With the same tools this can be extend to side C as well.

The DCS Setup[27][28] is split in many sub-projects like : the Power

Supply, JTAG/Electronics, Gas, P2C and advanced panels that are important during the operation.

3.11.1 BIS78A DCS Power Supply

The Power Supply (PS) of the MDT [29] is consisted of two projects, the Barrel and the Endcap. Both projects facilitate the work of both the experts and the shifters, by providing continues monitoring and control of the system, in terms of High (HV) and Low Voltages (LV). chambers are exceptional; they belong to the EndCap project and are located on the even Sectors of the Inner Partition.

In order to supply the newly installed BIS78A chambers, additional HV boards and LV have been considered. Due to the high granularity of the legacy MDT system, the HV channels have been supplied from the existing boards while the LV requirements introduced several limitations. Thus, the addition of a new LV board was a necessity. Fig. 3.40 depicts the CAEN LV A3025B board at UX15 rack Y6004X1.

Each hardware installation should be also addressed accordingly by establishing the connection into the DCS project. In order to achieve that, the following DCS procedure is used:

- creation of 2 types of xml files, one for mainframe and another one for the project itself, as it shown in Fig. 3.41.
- update of the branch controller mapping with the aforementioned binary file.

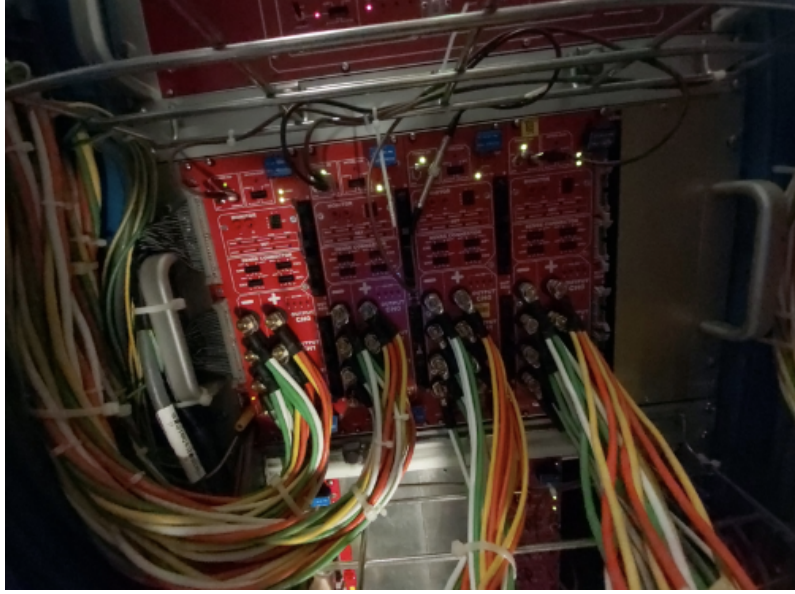


Figure 3.40: The crate at rack Y6004X1, hosts the LV boards, that supply the front-end electronics of the chambers.

- creation of the hardware tree on the Device Editor and Navigator (DE&N) tool.

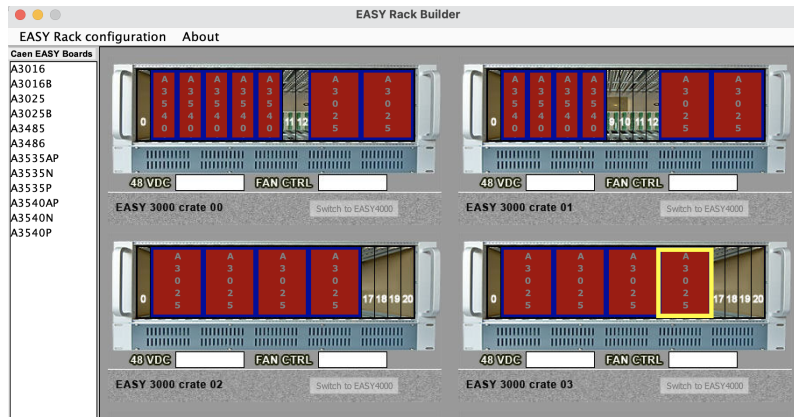


Figure 3.41: A typical RackBuilder file contains all the necessary information of the hardware mapping.

Special attention was given also to the low level structure of the project concerning data points, alarms, archive and mapping ,as shown in Fig. 3.42.

The reason for such unconventional approach stems from the nature of the hardware. The Barrel Power Supply project (PS2) is connected with the specific mainframe and the boards, while on the other hand the PS3 project handles the channels and the BIS7A chambers.

On DE&N the new board (4-2-13) and her channels have been created in both Power Supply projects. The archive and the alarm handling have been configured via dedicated panels (mdtPsTools) for both boards and channels. Once the desired chamber, connected to the board serving the BIS7A02/06/12/16, is selected the descriptions and the mapping is applied.

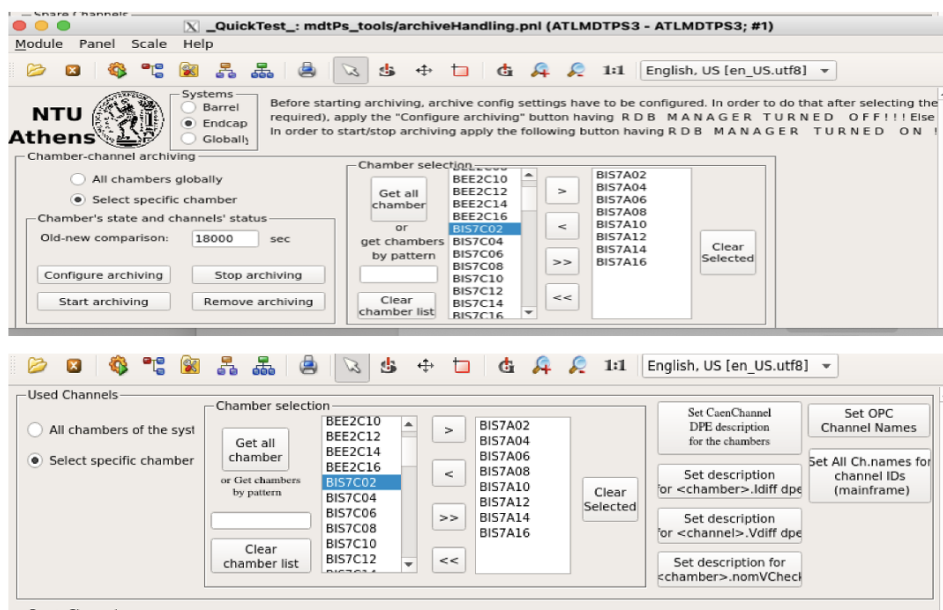


Figure 3.42: Advanced expert panels facilitating the configuration and the handling of all the vital parameters (mapping, archive, alarm, description). Typical examples can be seen for the archive handling (top), and the description handling (bottom).

Lastly, a lot of modifications have been made on the main Finite State Machine panels. A typical example is depicted in Fig. 3.43. It is worth mentioning here, the creation of a new panel for the shared LV channels,

located in the main channel panel. The panel facilitates the monitoring of all the vitals of the shared channels as shown in Fig. 3.43.

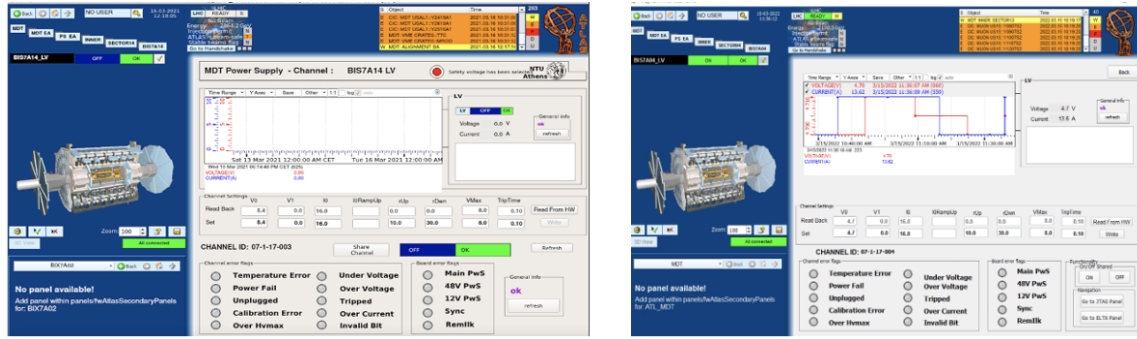


Figure 3.43: On the left the main channel panel have been modified to include all the shared channels wherever applicable. On the right, the associated for the shared LV channel panel.

The correct and smooth operation of the BIS78A chambers is handled by a sophisticated front-end electronics chain (CSM, Mezzanines, etc.). In order to acquire the detector signals and cope with the multiplexed serial data the BIS78A chambers are equipped with two CSMs. The dedicated front-end electronics protocol, namely the Joint Test Action Group (JTAG), is responsible for the configuration of the electronics, while the ELTX system is responsible for their monitoring. Both projects had to be modified accordingly.

3.11.2 BIS78A DCS JTAG/ELTX Project

The installation of these new chambers also involves their integration on the JTAG [30] and the ELTX Project. The JTAG architecture and protocol in general allows the access of the device registers for both writing and reading. Data is shifted in and out of devices along a serial path

connecting all the devices in a JTAG chain. In the MDTs, the JTAG is used to load the configurable parameters to the on-chamber electronics, both the TDCs and ASDs on each mezzanine card as well as to a chamber's CSM. The JTAG interface to the CSM, TDC and ASD devices is operated by the chamber's MDM (ELMB)[31] via a number of its digital I/Os and dedicated MDM firmware implementing the JTAG protocol. It is the job of DCS to retrieve the configuration parameters for each chamber from the MDT configuration DB, encode and assemble the data into a JTAG data bitstring, prepare the appropriate JTAG instruction bitstring and upload these strings to the electronics via the CAN-bus. To send the data over the CAN-bus, the CANopen protocol is used, whereby the strings are split into shorter segments which are sent sequentially, waiting for a confirmation reply at each step. Some of the JTAG data return bitstrings are read back from the MDM over the CAN-bus. They are then decoded, and the information on the results and/or the success of the various steps in the initialization sequence is extracted, which is subsequently processed by the DCS.

The new sMDT Chambers have 2 CSMs where each one of them controls a specific number of mezzanines cards and several other parameters like the temperature and the magnetic field.

For those two types of the CSMs it was decided to create two new Data Points to both JTAG (MDM4) and front-end electronics monitoring projects (ELTX). For the naming, the convention of BIX7 and BIY7 has been used, to reflecting in such way the two CSMs of the chamber. This has been done in order to introduce correctly the newly used schema of the two CSMs to the COOL DB since the existing folders of the BIS78 chambers will be abandoned JTAG-wise.

On MDM4 the new Datapoints BIX/Y7 were created on Elmb Barrel DPT, with their corresponding MDM paramerers, as well as on the ELTX project the new DPs ATL_MDT_ELTX-BI(X/Y)7 on MDT_ELTX_Chamber DPT.

Afterwards some of the main MDT libraries and scripts (mdtJtagUtil.ctl, mdtUtil.ctl, mdtJtagService.ctl) and the ELTX copy manager (num 20) were modified to take consideration the new naming scheme and to establish the connection with the Power Supply project. Lastly, the modification of the main FSM panels as shown in Fig. 3.44, Fig. 3.45 has been done. Fig. A.1 shows the information has been queried from the MDT Configuration DataBase (see Appendix A). The panel provides information about the Mezzanines' temperature, analog and Digital Voltage, along with the associated parent CSM.

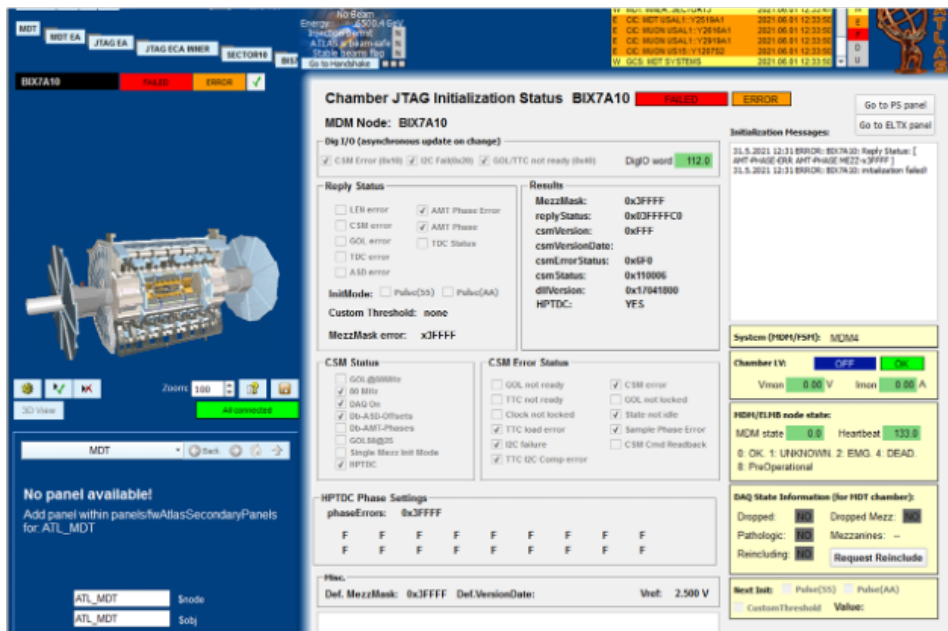


Figure 3.44: The main FSM panel of the JTAG along with all the main configuration parameters.

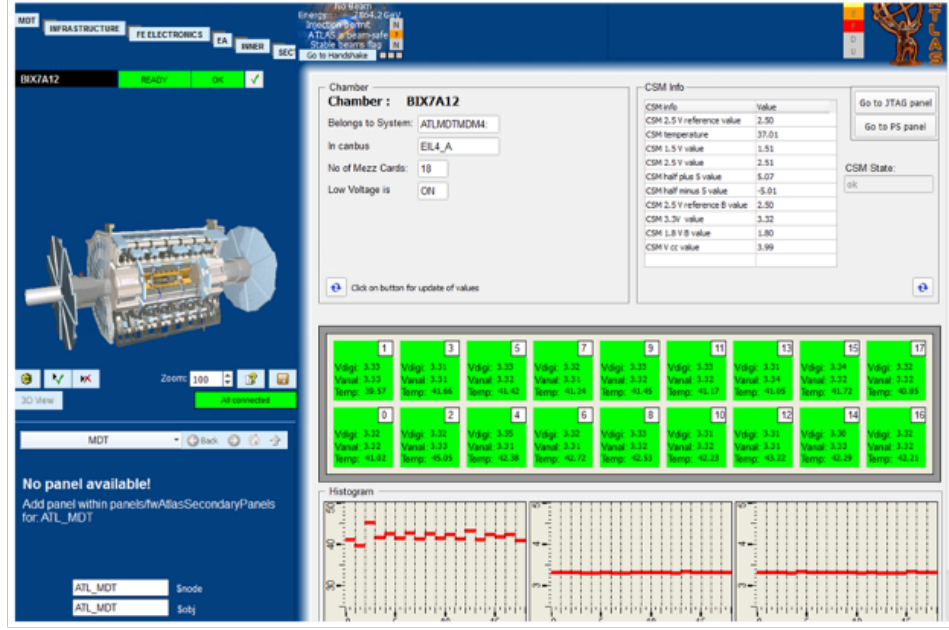


Figure 3.45: The main FSM panel of the ELTX along with all the main configuration parameters.

3.11.3 BIS78A DCS GAS Project

In the context of the BIS78A integration another core component needed to be modified was the MDT GAS project. The majority of the adjustments focused on the low level structure of the project, where all the basic information (volume, pressure, etc.) is stored. Initially, all the BIS8A chambers have been removed from the “chamber lists”, leaving space for new entries. In parallel, the mapping between the newly introduced chambers, the service lines and the associated racks have been updated accordingly. All these modifications performed also on the database side, reflecting in such way the complexity of the system. All the changes performed on the low level of the project have to be reflected on the

Graphical User Interface (GUI), namely the panels. Thus, the corresponding patches have been applied and a typical example can be seen in Figure 3.46.

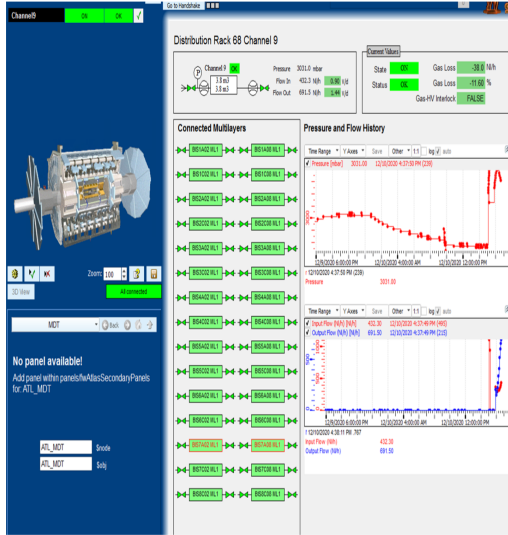


Figure 3.46: The main FSM panel of the GAS project along with all the gas parameters. Chambers have been grouped based on the associated gas line.

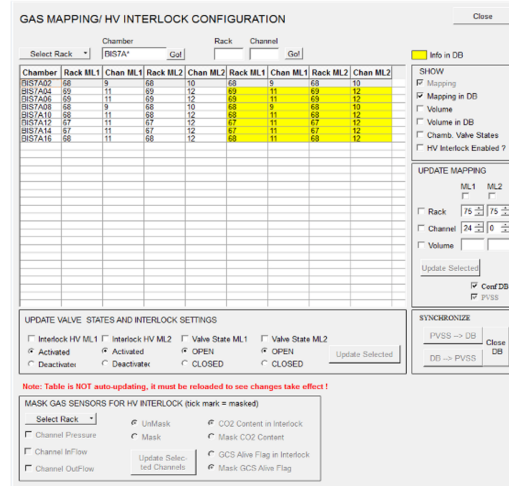


Figure 3.47: The Advanced Expert panel for the mapping and the HV interlock handling. A direct synchronisation with the ConfDB is established during the start up of the panel.

Fig. 3.47 depicts the changes in the GAS project for the BIS78A chambers. The table holds all the chambers along with their basic information of the associated gas channels for both multilayers. The specific panel facilitates the work of experts, providing a direct connection from the database to the system and vice-versa. If changes NEED to be applied in advance they can be downloaded from the DB or can be uploaded from it accordingly. Moreover, the handling of the main gas system components, like valves, and interlocks can be performed, revealing the direct connection to the PS system.

3.11.4 BIS78A DCS P2C Project

The Pvss2Cool project [30][32], in short P2C, connects the DCS archived parameters to the COOL database. The COOL database contains all the necessary information concerning the offline Data Quality and Athena, such as the high and low voltage values, the JTAG data, and their associated FSM states. This information is stored in folders that have been created in the database according to the CentralDCS conventions, as depicted in Fig. 3.48, giving the developer access to the full range of the database tools.

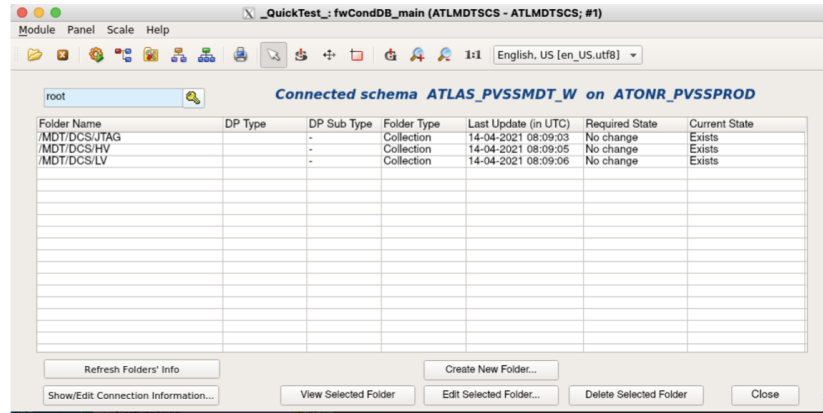


Figure 3.48: The main Conditional DB panel. The main MDT folders (HV,LV,JTAG) can be seen and selected for editing and viewing.

This intervention was divided in 3 parts. First the removal of the deprecated BIS8A Chambers from all the DB's folders (HV, LV, JTAG) has been performed. The second part was on the pre-existing chambers on the Power Supply side. The HV folder remains untouched. In the LV folder, a new mapping is going to be used, thus the changes have to be transferred into the DB as well. The last part concerns the JTAG folder, where sixteen new types of folders/channels have been created for the

new BIX/BIY7 Chambers of side A. The corresponding Data Points Elements (DPE) for each one of these chambers were created, according to the pre-existing chambers, as depicted in Figure 3.49.

#	Field Name	Type	Deadband	Timeout (s)
1	iMon_ML1	float	0	0
2	v0set_ML1	float	0	0
3	v1set_ML1	float	0	0
4	chanErrorFlag_ML1	bool	0	0
5	iOffset_ML1	float	0	0
6	IScale_ML1	float	0	0
7	iMon_ML2	float	0	0
8	v0set_ML2	float	0	0
9	v1set_ML2	float	0	0
10	chanErrorFlag_ML2	bool	0	0
11	iOffset_ML2	float	0	0
12	IScale_ML2	float	0	0
13	fsmCurrentState_ML1	string	0	0
14	fsmCurrentState_ML2	string	0	0

#	Field Name	Type	Deadband	Timeout (s)
1	configName	string		0
2	threshold	int		0
3	initModeSet	int		0
4	csmStatus	int		0
5	csmErrorStatus	int		0
6	amtPhaseErrors	int		0
7	fsmCurrentState_JTAG	string		0

#	Field Name	Type	Deadband	Timeout (s)
1	v0set_LV	float		0
2	fsmCurrentState_LV	string		0

Figure 3.49: Parameters and configs inside CoolDB channels

3.11.5 DAQ to DCS Communication

Next part of the BIS78A project was the connection between the DAQ and the DCS (DDC) [32]. The BIS78A chambers have been included into the main chamber DAQ-DCS lists in order to be used from all the dedicated to this project panels, like the DAQ Status panel shown in Fig. 3.50, or the Dropped Recovery panel shown in Fig. 3.53. Additionally, the basic scripts, the libraries and the copy mechanisms have been updated accordingly. Before digging into the changes, the “how to” of the DDC mechanism is briefly presented.

The information on chambers included in a run, either in the ATLAS partition or a standalone one, is written to the MDT Configuration database by the DAQ at the CONFIGURE stage when starting a new run. It is retrieved by the DAQ-Run Status Panel on opening the panel and when a change in run number, i.e. a new run start, is detected. If a run is ongoing, the information displayed is in all cases consistent with the actual situation while if no run is ongoing, the situation shown is the configuration of the previous run.

“Dropped” related information for chambers included in the run is sent from the DAQ to the DCS through the DAQ-to-DCS communication. This information is only available while the partition is up and the MDT RCD applications that handle and collect the dropped data on the DAQ side are running. If this information is not up-to-date, a NOT UPDATING status will be displayed for the corresponding partition in the run status summary box.

The Dropped Recovery panel gives the list of the dropped chambers and it is also responsible for stopless recovery. The automatic stopless recovery follows a standard procedure. First the DAQ provides to DCS the list of the dropped chambers. Then the DCS sends the command to re-initialise those chambers and if the re-initialisation is successful they are re-included into the DAQ.

On PARA some new datapoint elements have been created into the mdt-DDCchamber DPT, as they are depicted in Fig. 3.51. These new type of chambers contain information related to the slot, crate, channel and tower associated to those chambers, and it is displayed on the dropped Recovery panel. Likewise the lists of the mdtDDCMrod DPT now holds the new

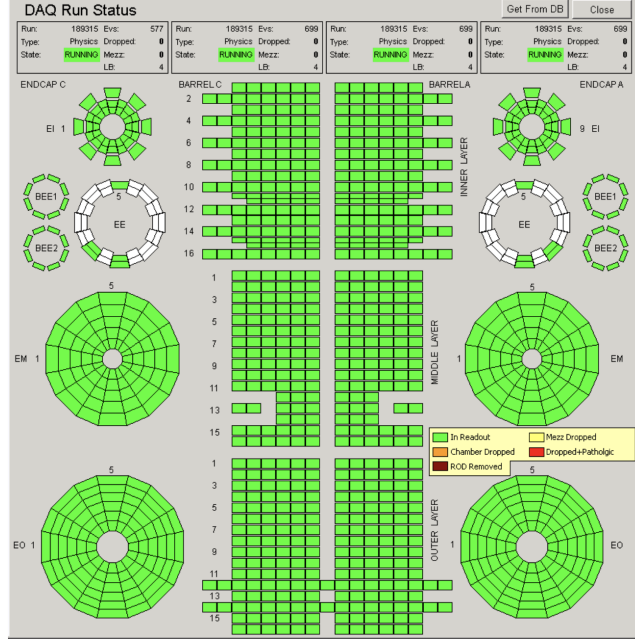


Figure 3.50: DAQ Run Status Panel

DPs as they are depicted in Fig. 3.52. The preceding BIS7A and BIS8A chambers have been removed. Complementary DPTs like the mdtDD-CDroppedRecovery have been utilized for the recovery of the chambers and displayed by the Dropped Recovery panel. They provide supplementary to the main ones information, like sections, requests, DDC2DAQ, Trigger, including also the status of the related elements.

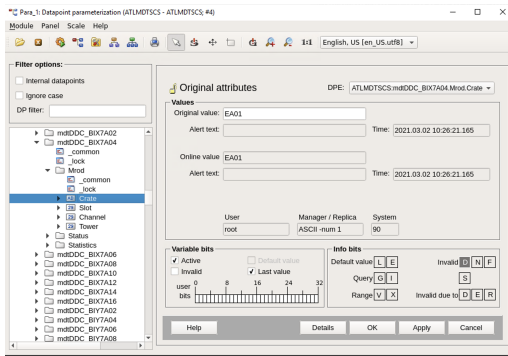


Figure 3.51: mdtDDC-chamber DPT

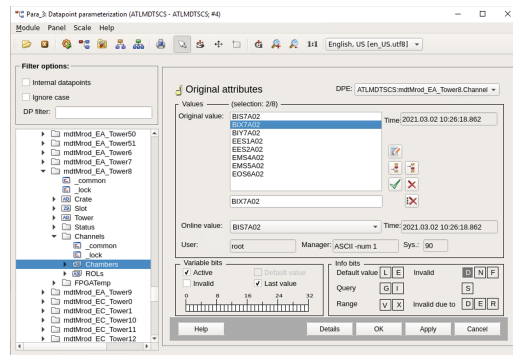


Figure 3.52: mdtDD-CMrod DPT

Changes had to be introduced also into the main MDT libraries (mdtUtil.ctl, mdtRodUtil.ctl,mdtJtagUtil), where the BI(X/Y)7 has been included, replacing in such way the obsolete BIS8A chambers.

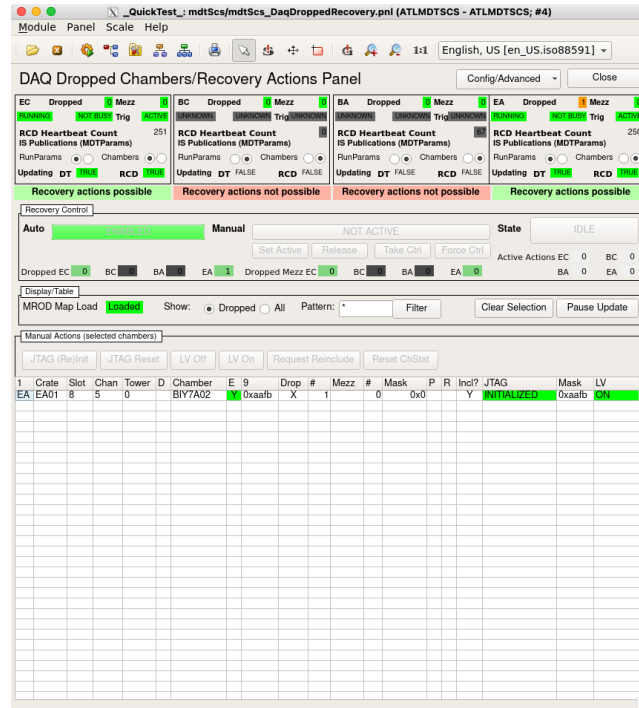


Figure 3.53: Dropped Recovery panel

Finally, three of the main control managers have been modified. Firstly, the mdtDdcRecovery.ctl (num 95), which is responsible for the Dropped Recovery mechanism, and provides all the necessary information from the Conditional Database (CondDB). Secondly, the mdtDdcAutoRecovery.ctl (num 94) which is responsible for the recovery of a Dropped mezzanine or a chamber's entry, and as its name implies, by handling automatically their main information (Status, trigger, mode, configuration). Lastly, the mdtDdcWatchdog.ctl completes the picture of the automatic recovery mechanism of the system, by checking regularly the smooth operation between the two systems (DAQ-to-bus).

3.11.6 Advanced Panels

The last part of the BIS78A project was the modification of the “Advanced Experts”. Several modifications were performed on both the panels and their associated libraries, such as the mdtUtil.ctl.

The MDM Node Browser expert panel, as shown in Fig. 3.54, provides an overview of the JTAG initial state, along with several parameters related to its configuration, such as the DigIO, the StatusWord, the Mezzanine Mask, wrapped with the timestamp of the last initialisation. The main part of the panel is occupied by a table displaying the information for the selected chambers, while additional parameters can be enabled afterward by selecting the respective checkbox.

The screenshot shows a software window titled "QuickTest : mdtJtag/mdtJtag_MdmNodeBrowser.pnl (ATLMDTSCS - ATLMDTSCS; #6)". It contains a table with columns: Sys, MDM, State, Bus, Port, Jtag State, 10, DigIO, StatusWord, MezzMask, DropMask, InitMode, and Thresh. The table lists several MDM4 nodes (BIX7A02 to BIX7A16) with their respective states (OK, NOT_INITIALIZED, or ERROR) and JTAG status (TTC/GO or ERROR).

Sys	MDM	State	Bus	Port	Jtag State	10	DigIO	StatusWord	MezzMask	DropMask	InitMode	Thresh
MDM4	BIX7A02	OK	EIL4_A	3	NOT_INITIALIZED	OK	0x70 TTC/GO	0x110006	0x3fff	0x0	0	from
MDM4	BIX7A04	OK	EIL4_A	3	NOT_INITIALIZED	OK	0x70 TTC/GO	0x110006	0x3fff	0x0	0	from
MDM4	BIX7A06	OK	EIL4_A	3	NOT_INITIALIZED	OK	0x70 TTC/GO	0x110006	0x3fff	0x0	0	from
MDM4	BIX7A08	OK	EIL4_A	3	INITIALIZED	OK	0x0	0x110007	0x3fff	0x0	0	from
MDM4	BIX7A10	OK	EIL4_A	3	NOT_INITIALIZED	OK	0x70 TTC/GO	0x110006	0x3fff	0x0	0	from
MDM4	BIX7A12	OK	EIL4_A	3	NOT_INITIALIZED	ERROR	0x70 TTC/GO	0x0	0x0	0x0	0	from
MDM4	BIX7A14	OK	EIL4_A	3	NOT_INITIALIZED	OK	0x70 TTC/GO	0x0	0x0	0x0	0	from
MDM4	BIX7A16	OK	EIL4_A	3	NOT_INITIALIZED	ERROR	0x70 TTC/GO	0x0	0x0	0x0	0	from

Figure 3.54: The mdmNodeBrowser Panel

By inserting the information for the BIX/BIY chambers on the main MDT library we were able to modify the main FSM Colormaps. Such action ensures the display of the status of the electronics, the JTAG , the Gas and the Temperatures of the chambers, as they illustrated in Fig. 3.55.



Figure 3.55: MDT ELTX and Temperature Colormap

3.12 The group Operation sMDT chambers panel

Lastly another addition on the sMDT Project is the creation of all sMDT chambers, the new BIS7 and the old BMG as well. The BMG[34],[33] are Twelve sMDT chambers, covering the acceptance gaps have been installed in the feet of the ATLAS detector in the 2016/17 winter shutdown of the LHC, at the middle layer of the barrel part of the muon spectrometer. The BMGs consist of 54 drift tubes of 15 mm diameter and a length of 1129 mm per layer, mounted on a spacer frame which provides high support against deformations, ($>20 \mu\text{m}$) without the need of an optical in-plane alignment system.

This new advanced panel give the lists for all sMDT chambers chambers. It provides a lot of help to experts with information like the mapping of those chambers and what channel they correspond to.. It also helps

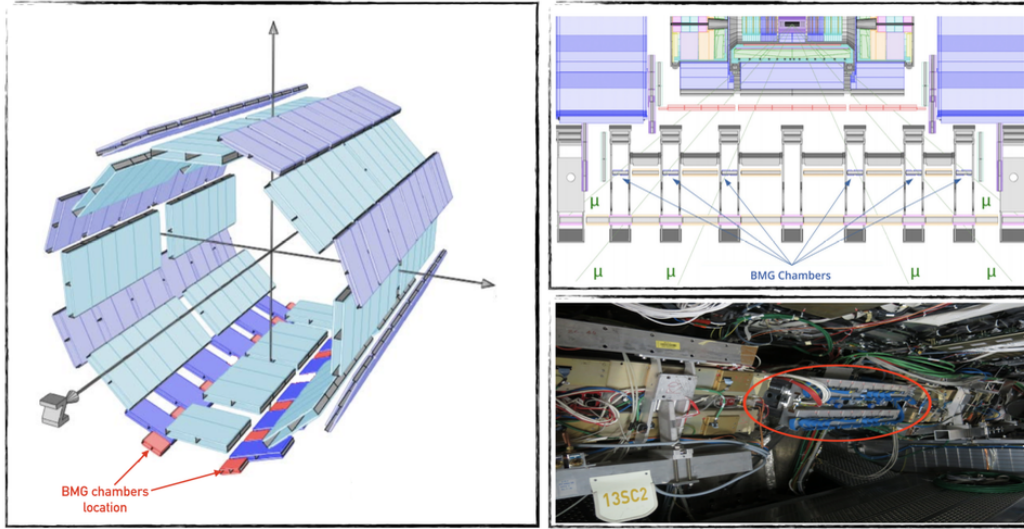


Figure 3.56: The BMG chambers installed in the feet of the ATLAS detector, at the middle layer of the barrel

the FSM Operation of this chamber for example the action to disable or enable an FSM Node or the (re)initialization of this chamber.

3.13 The MDT Small Wheel Removal

The decommissioning of the SW [35] started with the removal of all the High (HV) and Low Voltage (LV) boards from the associated crates of the racks Y2624X1 and Y6224X1 for both sides A and C. These have been accompanied by the removal of the cables from the relevant chambers along with the dedicated service and power generators lines. The EIL1/2 and EIS1/2 chambers were de-commissioned from ATLAS Cavern, while the EIL4 and BEE chambers remained untouched. The main conflict of such action was the shared hardware in term of crates and boards between the EIL1/2 and EIS1/2 and the EIL4 and BEE chambers. Hence, a

select channels

List of BIS78

List of BMG

Group Operations/Actions for BIS78 Chambers

Switch On

Switch Off

Enable PS FSM node

JTAG (Re)Init BIS78

Set Disable Flg

Clear Disable Flg

Disable PS FSM node

JTAG (Re)Init BMG

Channels

The table is by default not auto-updating; press Refresh to update the shown status.

☐ auto-update

Clear Selection

Refresh

Clear

Mainframe	BrCtrl	Crate	Board	Chan	Type	Chamber(s)	ML	Disabl.	Interl.	StatusWord	State	FSM State
PSMDT02	4	2	13	2	LV	BIS7A02 BIX7A02					1 ON	ON
PSMDT02	4	2	13	1	LV	BIS7A16 BIX7A16					1 ON	ON
PSMDT02	7	1	17	5	LV	BIS7A04 BIX7A04					1 ON	ON
PSMDT02	3	0	17	5	LV	BIS7A10 BIX7A10					1 ON	ON
PSMDT02	4	2	13	3	LV	BIS7A06 BIX7A06					1 ON	ON
PSMDT02	3	0	17	3	LV	BIS7A08 BIX7A08					1 ON	ON
PSMDT02	7	1	17	3	LV	BIS7A14 BIX7A14					1 ON	ON
PSMDT02	4	2	13	0	LV	BIS7A12 BIX7A12					1 ON	ON
PSMDT02	4	2	1	3	LV	BIY7A02 BIY7A16					1 ON	
PSMDT02	3	0	17	4	LV	BIY7A08 BIY7A10					1 ON	
PSMDT02	7	1	17	4	LV	BIY7A04 BIY7A14					1 ON	
PSMDT02	4	2	5	3	LV	BIY7A06 BIY7A12					1 ON	
PSMDT02	4	2	9	0	LV	BMG2A14 BMG4A14					1 ON	ON
PSMDT02	0	2	9	0	LV	BMG2A12 BMG4A12					1 ON	ON
PSMDT02	4	2	9	2	LV	BMG2C14 BMG4C14					1 ON	ON
PSMDT02	0	2	9	2	LV	BMG2C12 BMG4C12					1 ON	ON
PSMDT02	4	2	9	1	LV	BMG6A14					1 ON	ON

BIS7 on the table means BIX7

Figure 3.57: the sMDT Operational Panel

re-allocation of the channels was a necessity in order to save the space reserved for the newly introduced New Small Wheel (NSW) system and specifically for the hardware supplying the HV of the sTGC chambers.

Firstly, the remaining voltage cables replugged on to the existing boards, and then the boards have been re-allocated into the remaining crates for the MDT system. This resulted to the introduction of new multiplexed mapping containing different type of LV boards on the same crate. A complication reflected directly to the DCS system. Fig. 3.59 depicts the

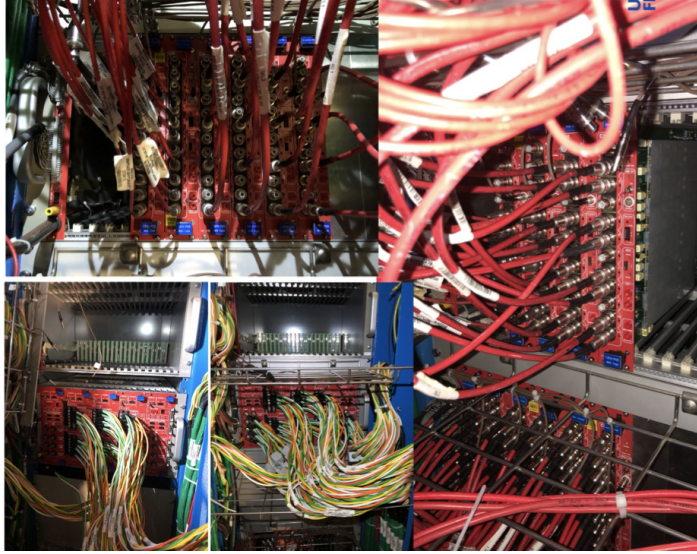


Figure 3.58: SW electronics decommissioning on both sides of ATLAS.

new mapping of the remaining chambers.

12-1-5		12-1-7		12-1-9		12-1-11	
Spare	0	Spare	0	Spare	0	Spare	0
Spare	1	Spare	1	EIL4A09	ML1	EIL4A09	ML2
Spare	2	Spare	2	EIL4A01	2	EIL4A01	2
Spare	3	Spare	3	Spare	3	Spare	3
BEE1A02	ML1	BEE2A02	ML1	EIL4A11	ML1	EIL4A11	ML2
BEE1A04	ML1	BEE2A04	ML1	EIL4A03	ML1	EIL4A03	ML2
BEE1A06	ML1	BEE2A06	ML1	Spare	6	Spare	6
BEE1A08	ML1	BEE2A08	ML1	EIL4A13	ML1	EIL4A13	ML2
BEE1A10	ML1	BEE2A10	ML1	EIL4A05	ML1	EIL4A05	ML2
BEE1A12	ML1	BEE2A12	ML1	Spare	9	Spare	9
BEE1A14	ML1	BEE2A14	ML1	EIL4A15	ML1	EIL4A15	ML2
BEE1A16	ML1	BEE2A16	ML1	EIL4A07	ML1	EIL4A07	ML2

Figure 3.59: New mapping provided for the new scheme

3.13.1 MDT High Voltage project

The ATLMDTPS3 is the project responsible for the monitoring and the control of the HV board supplying the MDT chambers on the Endcap A and C side. The modification of the ATLMDTPS3 project for the removal of the SW is described here and the changes can be divided into two parts.

Firstly, the datapoints (DP) in the project have been modified. The DP associated to each EIS/L1,2 of datapoint type (DPT) Fw_DUWithScript have been deleted from the system. In addition, the EIS/L1,2 chambers' name have been removed from the DP list of DPT Chamber_List. These changes remove the EIS/L1,2 information on the secondary panels in the project and on the table in the main panel associated to the Endcap Inner node. In addition, these modifications are changing the FSM nodes associated to each EIS/L1,2 chamber.

The second part was the adjustment of the two FSM main panels associated to the Endcap and Endcap Inner nodes, which are implemented in the panels ATL_MDTPS_EX and ATL_MDTPS_EX_LAYER, respectively. The State and Status for each EIS/L1,2 chamber were removed from these two panels. For this, the Scopelib of each of these two panels is modified. The FSM main panels associated to the partition (A and C side) node, the inner node and one sector of the inner node after the changes are shown in Fig. 3.62(a), Fig. 3.62(b) and Fig. 3.62(c), respectively. It is evident that the system "dynamic" structure facilitates such work, whose DPT, DP and DPEs are directly associated with a graphical representation element on the panel.

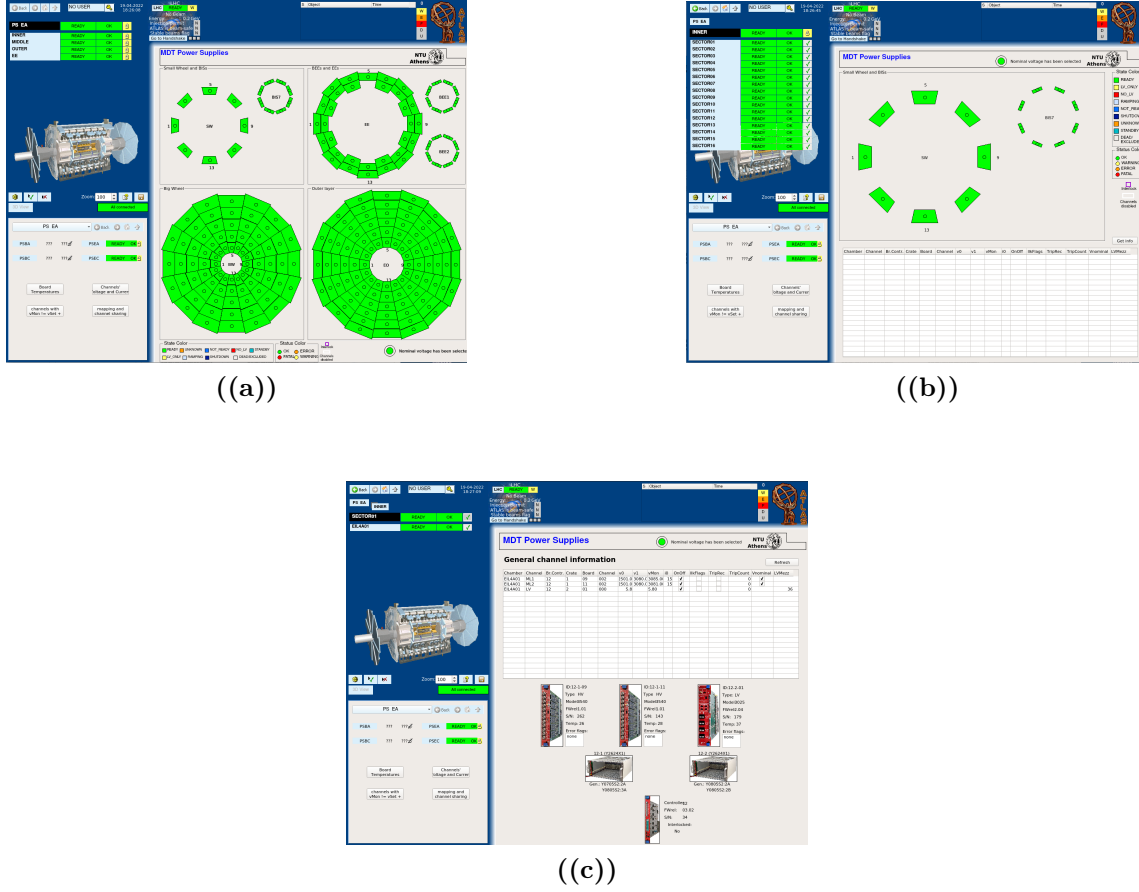


Figure 3.60: The FSM main panels of the ATLMDTPS3 project after the removal of the SW. (a) Main panel associated with the partition node. (b) Main panel associated with the inner layer node. (c) Main panel associated with a sector node.

3.13.2 MDT MDM project

The monitoring and the control of the MDT-DCS-Module (MDM) [31] system on the Endcap A and C side are implemented in the ATLMDT-MDM4 project. Similar to the previous system, the removal of the SW consists of the modification of panels and DPs. For this project only one FSM main panel, named MDT_JTAG_PARTITION_ENDCAP, is changed so that the State and Status of the EIS/L1,2 chambers are being

removed. Fig. 3.61 depicts the panel after the removal of the SW. In addition, the DPs associated to each EIS/L1,2 chambers of DPT ElmbEndcap have been deleted from the system.

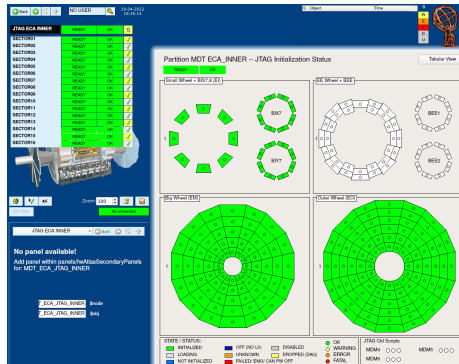


Figure 3.61: The FSM main panel associated to the partition node of the ATLMDTMDM4 project after the removal of the SW. It is evident on the top left the missing even sectors.

3.13.3 MDT ELTX project

The ATLMDTELTX project is used to monitor and operate the frontend electronics [31][36] of the MDT system on the Endcap A and C side, as well as on the Barrel A and C side. It constantly monitors the parameters of the mezzanines and the Chamber Service Module (CSM) chips. For the removal of the SW, the intervention consists of the modification of graphical user interface (GUI) and the PARA of the project related to the Endcap projects. For the former, two FSM panels, namely ATL_MDT_ELTX_Partition and ATL_MDT_ELTX_Layer, were modified such that the information about the SW chambers will be removed. For the latter, the EIS/L1,2 chambers' name were removed from the DP MDT_CHAMBERS. Fig. 3.62 depicts the main panel associated to the partition, the inner layer and one sector of the inner layer nodes after the intervention, respectively.

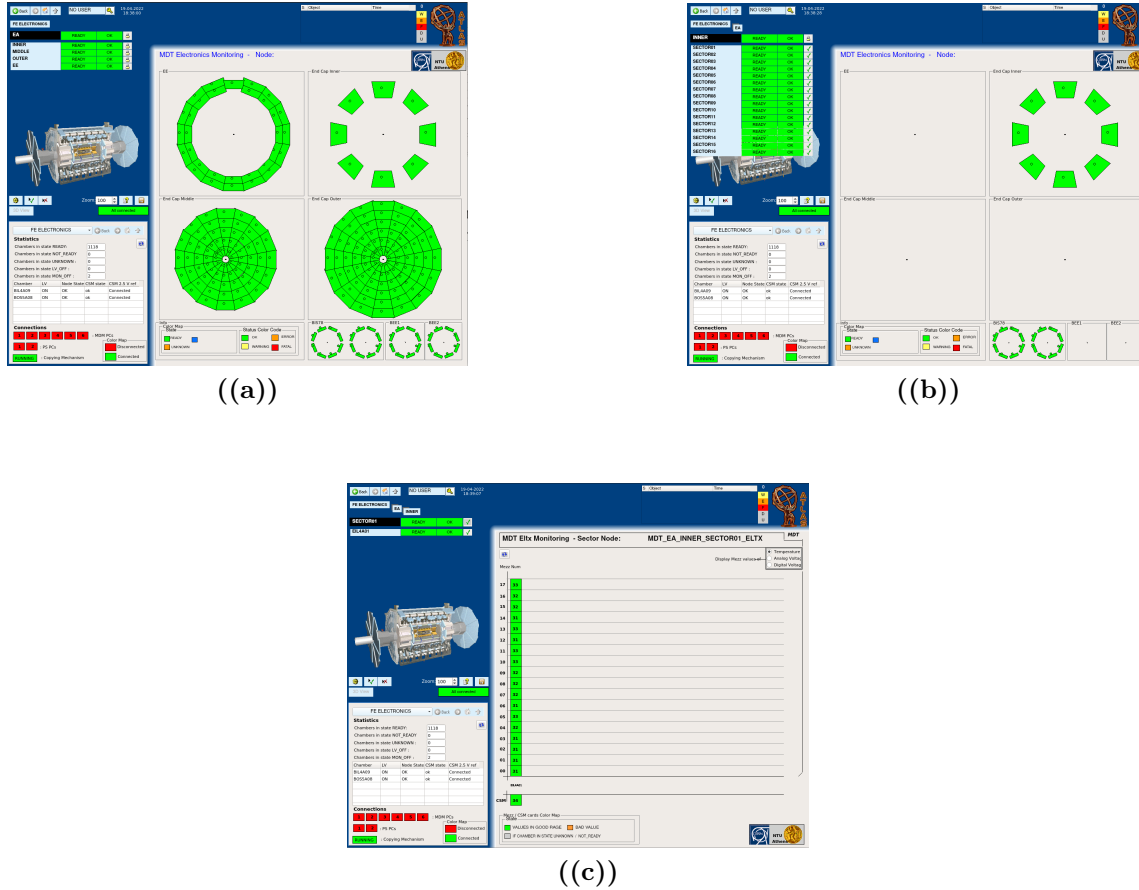


Figure 3.62: The FSM main panels of the ATLMDTELTX project after the removal of the SW. Figure (a) shows the main panel associated to the partition node, figure (b) shows the main panel associated to the inner layer node and figure (c) shows the main panel associated to one sector node.

3.13.4 EI DCS P2C Project

This intervention was divided in 3 parts and follow the same logic with BIS78. First the removal of the obsolete EIL1/2 and EIS1/2 Chambers from all the condDB's folders (HV, LV, JTAG)[37] has been performed. The second part was the pre-existing chambers on the Power Supply side, where the HV part remained untouched. However, the LV folder needs to be modified, since a new mapping is going to be used for both

#	Field Name	Type	Deadband	Timeout (s)
1	iMon_ML1	float		0
2	v0set_ML1	float		0
3	v1set_ML1	float		0
4	chanErrorFlag_ML1	bool		0
5	iOffset_ML1	float		0
6	iScale_ML1	float		0
7	iMon_ML2	float		0
8	v0set_ML2	float		0
9	v1set_ML2	float		0
10	chanErrorFlag_ML2	bool		0
11	iOffset_ML2	float		0
12	iScale_ML2	float		0
13	fsmCurrentState_ML1	string		0
14	fsmCurrentState_ML2	string		0

#	Field Name	Type	Deadband	Timeout (s)
1	configName	string		0
2	threshold	int		0
3	initModeSet	int		0
4	csmStatus	int		0
5	csmErrorStatus	int		0
6	amtPhaseErrors	int		0
7	fsmCurrentState_JTAG	string		0

#	Field Name	Type	Deadband	Timeout (s)
1	v0set_LV	float		0
2	fsmCurrentState_LV	string		0

Figure 3.64: Parameters and configs inside ConditionDB collection folder. On the left, the folder's payload where the main configs declared. This defines the amount of data per channel pushed into the CondDB. The middle area is the channel definition where the expert can add or import via file new channels or to edit existing ones. Last, the rightmost part holds the mapping of each selected channels.

accordingly. All these modifications performed also on the MDT configuration database side [38], reflecting in such way the complexity of the system. All the changes performed on the low level of the project have to be reflected on the Graphical User Interface (GUI), namely the panels. Thus, the corresponding patches have been applied and a typical example can be seen in Fig. 3.65.

Fig. 3.66 depicts the changes in the GAS project for the EI chambers. The table holds all the chambers along with their basic information of the associated gas channels for both multilayers. The specific panel facilitates the work of experts, providing a direct connection from the database to the system and vice-versa. If changes have been applied in advance either into the database or the system, they can be downloaded or uploaded accordingly. Moreover, the handling of the main gas system components,

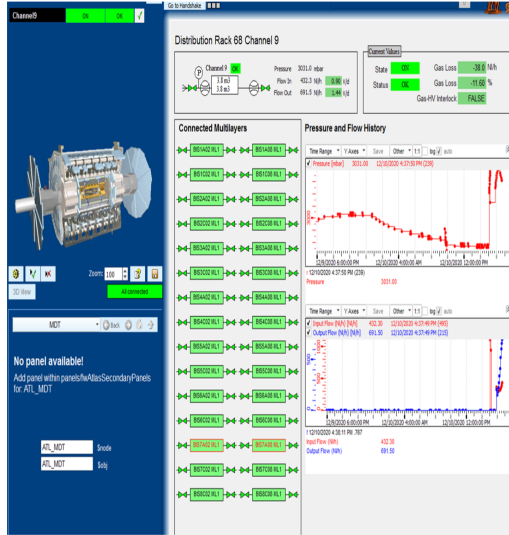


Figure 3.65: The main FSM panel of the GAS project along with all the gas parameters. Chambers have been grouped based on the associated gas line.

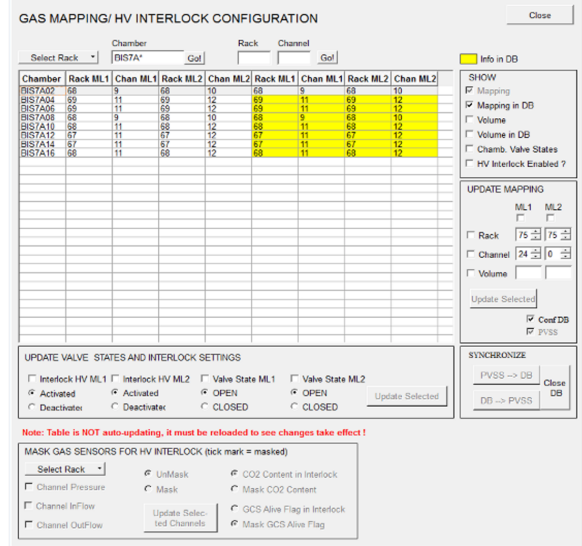


Figure 3.66: The Advanced Expert panel for the mapping and the hv interlock handling. A direct synchronisation with the ConfDB is established during the start up of the panel.

like valves, and interlocks can be performed, revealing the direct connection to the PS system.

3.14 MDT DSS Revival

The task of identifying critical safety threats, such as fires, smoke, or the presence of flammable gases that pose risks to human life, is entrusted to the CERN Safety Alarm Monitoring (CSAM) system. Positioned between CSAM and the experimental infrastructure, the Detector Safety System (DSS) plays a key role in safeguarding equipment during abnormal or hazardous conditions.

The DSS automatically initiates safe, non-destructive shutdown procedures without requiring immediate operator input. However, human involvement remains essential for diagnosing faults, implementing corrective actions, and restoring normal system operation. Notably, the DSS does not autonomously restart any equipment; reactivation is exclusively performed by authorized personnel.

DSS operations are independent of the experiment's current activity phase. Whether during data acquisition, maintenance, or other tasks, the DSS maintains a consistent focus on equipment protection, delivering uniform safety coverage across all modes of operation.

The DSS is organized into three main functional elements:

- **Sensors:** Continuously survey the environment to detect anomalies or hazardous conditions.
- **Alarms:** Triggered by programmable logic in response to sensor data.
- **Actions:** Automatically performed to bring systems into a safe state when alarms are activated.

The system architecture consists of two core components:

- **Front-End (FE):** Interfaces directly with sensors, handles alarm generation, and manages actuators in response to detected anomalies.
- **Back-End (BE):** Provides user interfaces for configuring the FE,

monitoring the system, and managing alarm resets and safety actions.

Communication between the BE and the Detector Control System (DCS) is facilitated via Ethernet using CERN's proprietary Data Interchange Protocol (DIP). This link enables the transmission of alarms and safety actions to the DCS, which then relays the information to the relevant sub-detector systems to initiate coordinated shutdown procedures. Furthermore, DSS alarm and status data are integrated into the global ATLAS alarm and status overview managed by the DCS.

Designed for autonomous functionality, the DSS operates independently and does not rely on software inputs from external systems, ensuring high reliability and operational integrity.

For the MDT DCS, a dedicated interface panel (Fig. 3.67) has been developed. This panel manages DSS data points (DPs) and their essential configurations, such as alarm thresholds, descriptions, and associated actions. It also includes a control manager and supports the duplication of DPs for integration into the central DCS project.

Afterwards the DSS panel has been setup, holding all the system's alarms. For the MDT case we focus more on alerts part. The actions are included on Power Supply scripts, so in case of emergency, the actions take part automatically.

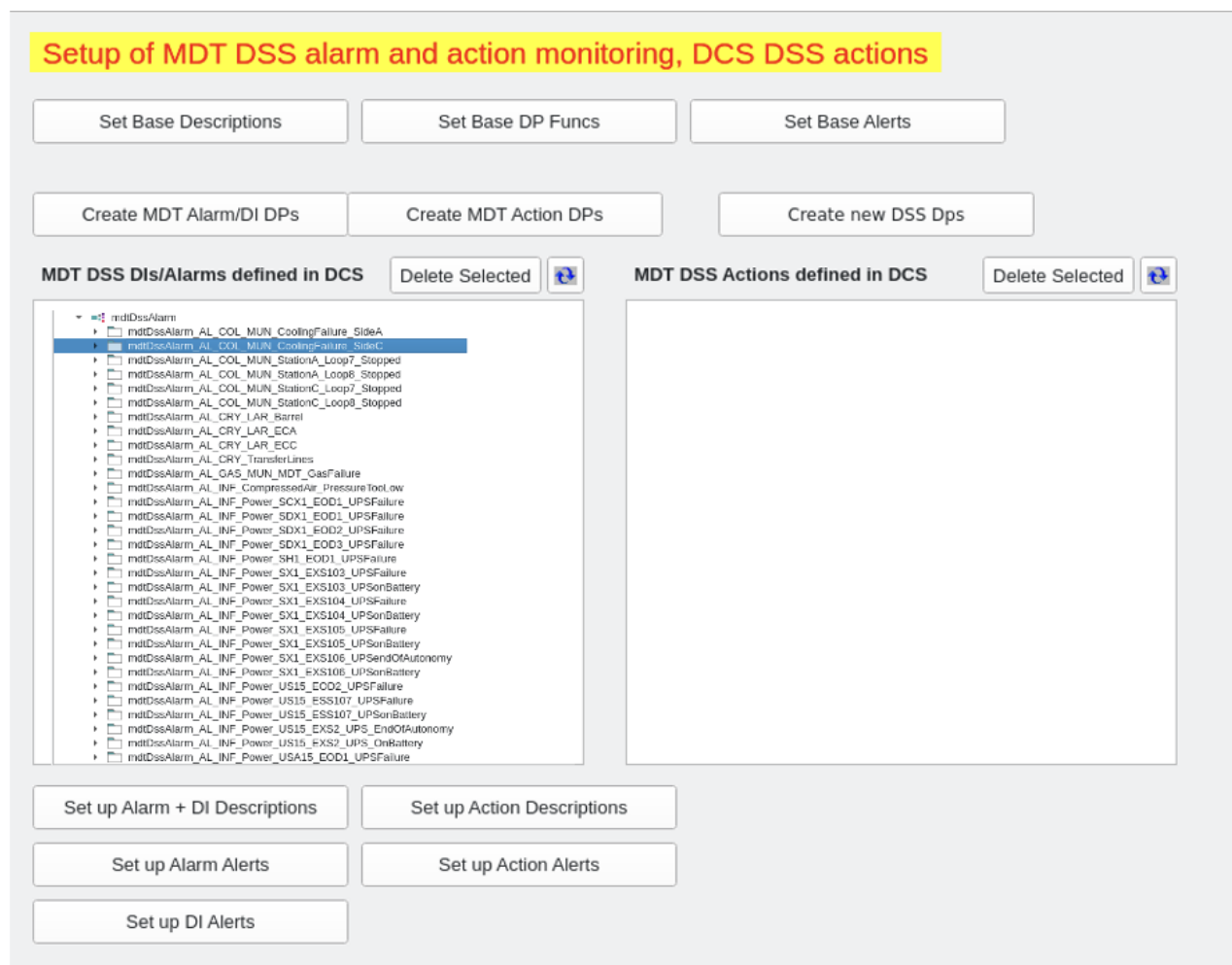


Figure 3.67: A service panel has been created for the restoration of the MDT DSS System.

3.15 MDT GAS Developments

The main role of a detector gas system is to combine different gas components in accurate ratios and supply the resulting mixture to the detector chambers. To streamline construction and maintenance, these systems are designed using standardized functional modules that share common characteristics. Common modules include a gas mixer, pre-distribution

DSS Alarms and Dig. Inputs -- MDT DCS Action Configuration

Action Inhibit

False

DCS Alert

Dectivate

Activate

sort by Name

sort by Alarm (show DI with Alarm)

Close

Note: Only DSS items known also to MDT DCS are shown !

DSS Alarm/Digital Input	Active?	Quality	Alert?	Associated DCS Action(s)	Delay	Confirm	Enabled	Triggered
AL COL MUN CoolingFailure SideA		Good	✓		0			
AL COL MUN CoolingFailure SideC		Good	✓		0			
AL COL MUN StationA Loop7 Stopped		Good	✓		0			
AL COL MUN StationA Loop8 Stopped		Good	✓		0			
AL COL MUN StationC Loop7 Stopped		Good	✓		0			
AL COL MUN StationC Loop8 Stopped		Good	✓		0			
AL CRY LAR Barrel		Good	✓		0			
AL CRY LAR ECA		Good	✓		0			
AL CRY LAR ECC		Good	✓		0			
AL CRY TransferLines		Good	✓		0			
AL GAS MUN MDT GasFailure		Good	✓		0			
AL INF CompressedAir PressureTooLow		Good	✓		0			
AL INF Power SCX1 EOD1 UPSFailure		Good	✓		0			
AL INF Power SDX1 EOD1 UPSFailure		Good	✓		0			
AL INF Power SDX1 EOD2 UPSFailure		Good	✓		0			
AL INF Power SDX1 EOD3 UPSFailure		Good	✓		0			
AL INF Power SH1 EOD1 UPSFailure		Good	✓		0			
AL INF Power SX1 EXS103 UPSFailure		Good	✓		0			
AL INF Power SX1 EXS103 UPSonBattery		Good	✓		0			
AL INF Power SX1 EXS104 UPSFailure		Good	✓		0			
AL INF Power SX1 EXS104 UPSonBattery		Good	✓		0			
AL INF Power SX1 EXS105 UPSFailure		Good	✓		0			
AL INF Power SX1 EXS105 UPSonBattery		Good	✓		0			
AL INF Power SX1 EXS106 UPSendOfAuto		Good	✓		0			
AL INF Power SX1 EXS106 UPSonBattery		Good	✓		0			
AL INF Power US15 EOD2 UPSFailure		Good	✓		0			
AL INF Power US15 ESS107 UPSFailure		Good	✓		0			
AL INF Power US15 ESS107 UPSonBattery		Good	✓		0			
AL INF Power US15 EXS2 UPS EndOfAuto	✓	Good	✓		0			
AL INF Power US15 EXS2 UPS OnBattery	✓	Good	✓		0			
AL INF Power USA15 EOD10 48VFailure		Good	✓		0			
AL INF Power USA15 EOD10 UPSFailure		Good	✓		0			
AL INF Power USA15 EOD1 UPSFailure		Good	✓		0			
AL INF Power USA15 EOD2 UPSFailure		Good	✓		0			
AL INF Power USA15 EOD3 UPSFailure		Good	✓		0			
AL INF Power USA15 EOD4 UPSFailure		Good	✓		0			
AL INF Power USA15 EOD5 UPSFailure		Good	✓		0			
AL INF Power USA15 EOD6 UPSFailure		Good	✓		0			
AL INF Power USA15 EOD7 UPSFailure		Good	✓		0			
AL INF Power USA15 EOD8 UPSFailure		Good	✓		0			
AL INF Power USA15 ESS01 UPSFailure		Good	✓		0			
AL INF Power USA15 ESS01 UPSonBattery		Good	✓		0			
AL INF Power USA15 ESS02 UPSFailure		Good	✓		0			

DCS Action Configuration (for selectec alarms/digital inputs)

DCS Action	Confirm After delay	Delay (secs)
------------	---------------------	--------------

Figure 3.68: The main DSS Expert panel with alarms and actions for the MDT System.

and distribution units, circulation pump, purifier, humidifier, membrane, liquefier, and analysis components, among others[39]. The MDT gas system will be described together with the control system developed to

173

oversee its physical parameters.

3.15.1 The Mixer Module

The gas mixture stability is perhaps the most basic requirement for good and stable long term operation of all detectors. The primary task of a mixer module is to provide the gas system and ultimately the detector with the suitable gas mixture for nominal operation. During particular phases, it might also be needed to supply different gases (for example for purging the detector when the standard gas mixture needs to be evacuated, like at the beginning of a long shutdown period) or standard mixture at very high flow (for example when the detector is going to be restarted after a long shutdown, filling mode).

The MDT detector's mixer module includes 2 separate lines, each supplying one of the gas components. The final gas mixture is combined in the mixer tube and subsequently delivered to the rest of the gas system. A detailed schematic of the setup is presented in Fig. 3.69.

All relevant parameters of the mixer module, such as pressures, flow rates, and mixing ratios, are continuously monitored. These values are used not only to trigger alarms or interlocks within the MDT gas system but also to assess the operational state and status of the mixer module. These functionalities are defined by the functional analysis requirements based on the specific needs of MDT and shown as well in the corresponding DCS Panel.



Figure 3.69: The main FSM panel Gas Panel for the Gas Mixer

Due to some issues with the Gas Mixer values some additional modifications were implemented on Gas Mixer in order to cover some specific cases.

First of all a new list of data points was created to give information for the fresh gas, fresh water and primary supply. And also some more parameters like the average temperature of every rack. All these parameters have been updated from the corresponding control manager by copying the data points from a Central DCS project (ATLCICIS2 Project). Some new panels were created in order to hold all this information. Fig. 3.70,3.71 are connected with navigation button from the Gas Mixer.

A datapoint has also been created that checks if the flow reported from the primary gas is smaller than the flow reported by the MDT mixer, in order to show an alarm on the alarm screen (Fig. 3.72).

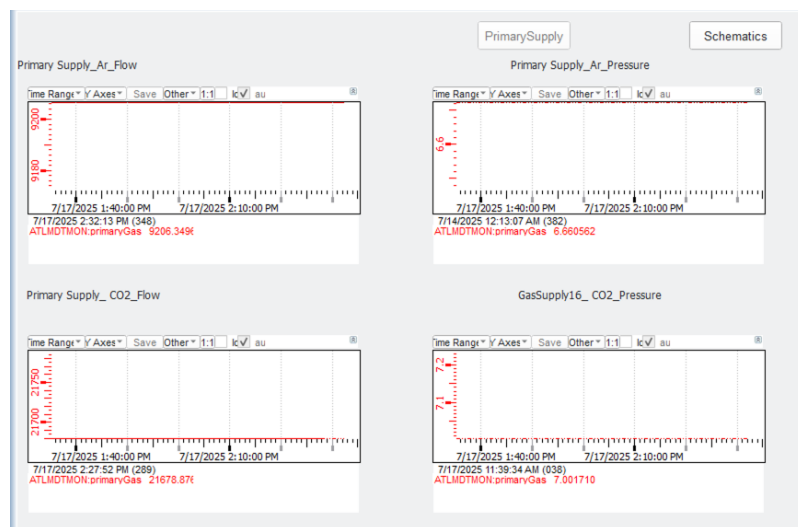


Figure 3.70: The FSM Panel of Primary Supply for the Gas Mixer

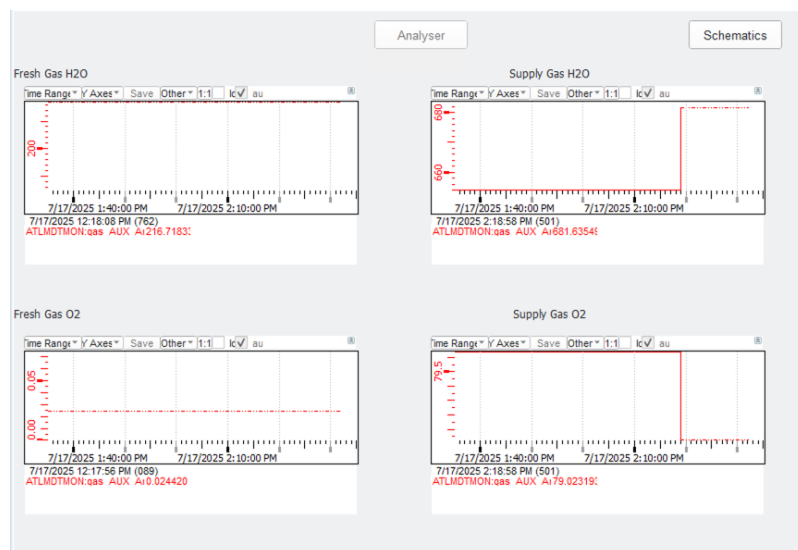


Figure 3.71: The FSM Panel of Analyser for the Gas Mixer

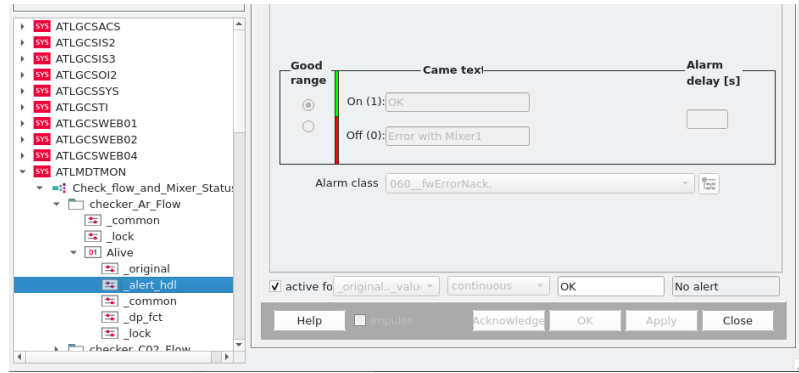


Figure 3.72: A datapoint that checks if the Gas Mixer has higher value than the primary gas

3.15.2 The Gas Humidifier

The purpose of the Humidifier[40] modules is to add the appropriate quantity of water to the process gas. On DCS we focus on the modifications of the panel and inclusion on the MDT Gas FSM. The panel gives information for many parameters :

- fresh humidity. "Fresh gas" means gas that hasn't passed through the detector yet, it's newly mixed or supplied from the bottles or gas mixers.
- mixed humidity. This refers to the humidity level in the recirculated (mixed) gas, which is a combination of Fresh gas (humidified, from the input), Returned gas (from the detectors, after passing through them), sometimes a purifier is involved before remixing.
- the water tank level
- evaporator temperature and pressure
- flow and pressure

All these parameters have been updated from the corresponding control manager by copying the data points from a Central DCS project(ATLCICIS2 Project).

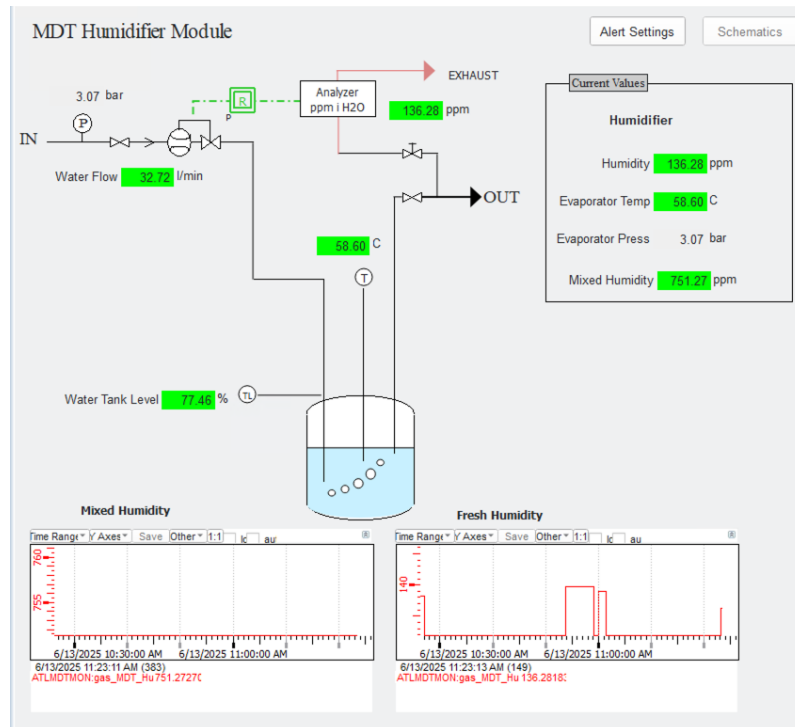


Figure 3.73: The main FSM panel for Gas Humidifier

3.15.3 The MDT Gas Pump

Some more DCS modification has been performed on the Gas Pump Panel. Fig. 3.74 portray now two pumps instead of one as the panel during Run-2 but also some more parameters like :

- the pump current
- pump speed

- motor temperature
- running time of the pumps
- and as before flow and pressure

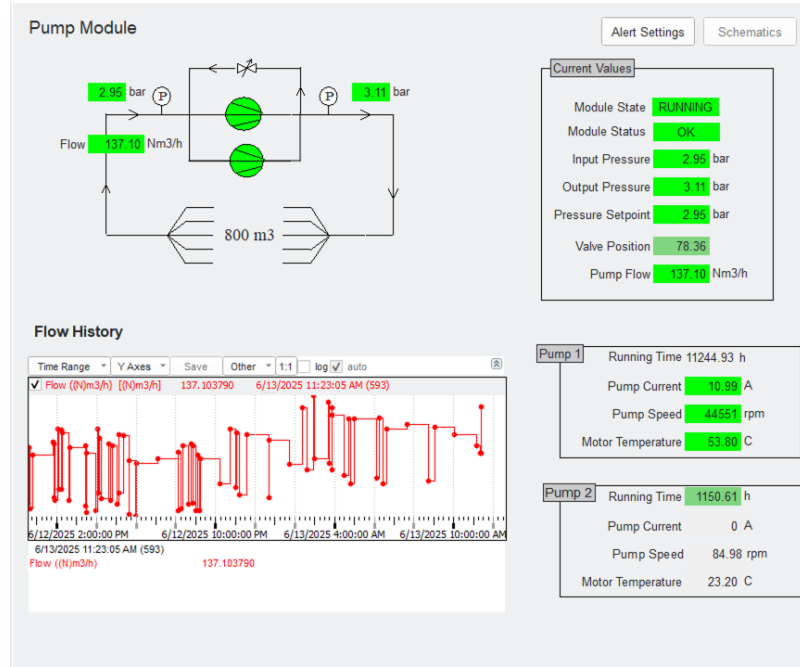


Figure 3.74: The main FSM panel for Gas Pumps

3.16 The MDT Endcap Alignment System

In the ATLAS spectrometer, all muon chambers are required to meet strict criteria regarding positioning accuracy, as well as spatial and momentum resolution, with uncertainties smaller than the intrinsic single-hit resolution. To achieve this precision, an alignment system was developed using alignment bars, along with optical, magnetic, and temperature sensors. This system establishes the relative positions of the chambers to each other and to the global ATLAS reference frame.

The end-cap alignment system[33] complements the muon alignment system and operates on the same fundamental principles as the barrel system. It utilizes either an LED light source with a coded mask or a pair of Brandeis CCD Angular Monitor (BCAM) laser diodes [42], which project through a lens system onto a Charge-Coupled Device (CCD) acting as a screen. The resulting image is captured by a camera, enabling the determination of the light source's position.

All components of the end-cap alignment system are monitored, controlled, and analyzed through the Long Wire Data Acquisition (LWDAQ) system [43]. The data output is processed via a dedicated software framework, which stores the results in an Oracle Database. Subsequently, the ARAMyS software [44] reads this data and reconstructs the alignment parameters of the full system, following a method similar to that used for the barrel. Fig. 3.75 (left) shows the layout of the muon end-cap alignment system, while the internal alignment of an MDT chamber is depicted on the right.

The constant monitoring of the End-cap Alignment system is essential in order to ensure the efficient and coherent operation of the full chain allowing also the immediate detection of possible errors. For this purpose a dedicated DCS[41] has been developed following the rules and conventions of the ATLAS DCS.

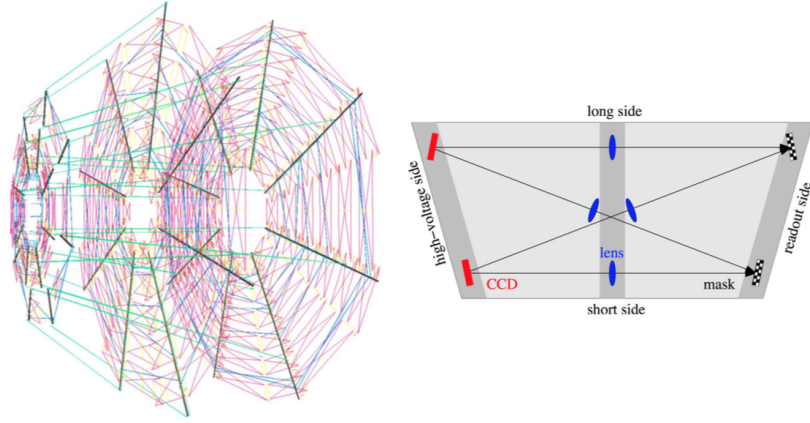


Figure 3.75: The layout of the end-cap alignment system. The various colored lines indicate the end-cap alignment sensor lines. With green are the polar BCAMs, blue the azimuthal BCAMs, orange the RASNIK proximity sensors, red the in-plane RASNIKs and in yellow the chamber temperature sensors. Right: Schematic representation of the in-plane RASNIK layout for an MDT chamber installed in the internal spacer frame.

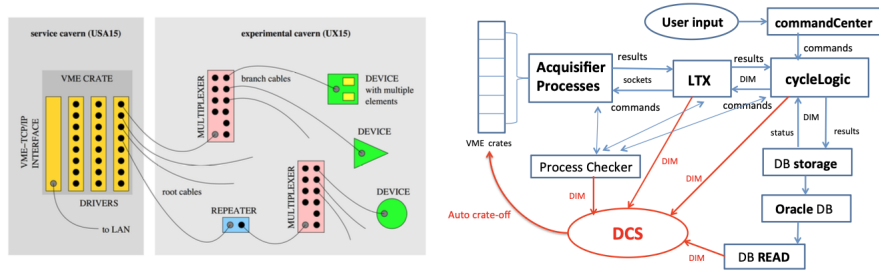


Figure 3.76: Left: Graphical representation of the LWDAQ system cabling scheme. A single LWDAQ device may be connected directly to the driver via a root cable or alternatively multiple devices can be connected through branch cables to the multiplexers. Right: A block diagram representing the flow of the End-cap Alignment data through the various processes and the DCS.

3.16.1 Process Heartbeat Monitoring

The status of each process is monitored using heartbeat DIM messages, which are emitted from within the process itself. Upon receiving a heartbeat, WinCC records a timestamp, enabling the measurement of the update frequency. In the End-cap Alignment system, the time interval between two updates is predefined by the respective alignment processes operating behind the DIM servers. A statistical analysis is applied to each process heartbeat to determine whether its update rate is within acceptable limits. The following processes are continuously monitored by the End-cap Alignment Detector Control System (DCS):

- Process Checker
- LTX
- CycleLogic
- Database Reading

3.16.1.1 Process Checker Monitoring

The Process Checker is a background program running within the End-cap Alignment system that communicates the operational status (running/not running) of key processes—such as cycleLogic, LTX, Java, and tcsh, via DIM. To ensure accurate process monitoring, the DCS cross-checks the heartbeat messages with the Process Checker’s output, allowing for rapid identification of irregularities.

3.16.1.2 CycleLogic Monitoring

The cycleLogic process acts as an intermediary between the LTX, user interface, DCS, and database. It controls the reading cycle of End-cap Alignment devices and transmits the data acquired by the LTX to the database. During operation, it publishes both the number of devices read and the number of readout errors to the DCS through DIM services.

There are two data streams: live readings, updated after each driver board is read, and final readings, compiled at the end of the full reading cycle. The length of each cycle is governed by a configurable time duration parameter. The total readings per device type are not only visualized by the DCS but also automatically validated at the end of the cycle for integrity against expected values.

3.16.1.3 Database Monitoring

A dedicated End-cap Alignment process accesses the online database to retrieve the latest entry related to the statistics of a complete reading cycle. This information is then sent to the DCS via DIM. Internal DCS scripts use this data to perform additional integrity checks by comparing the new entries to expected statistical values from the most recent complete cycle.

3.16.1.4 Crate Communication Monitoring

The communication with the VME crates is facilitated by the LWDAQ readout chain. In addition to reading device data, the system must verify the readiness and reliability of the hardware. Within the LTX process, a built-in mechanism pings each crate at fixed intervals to assess its operational state.

The resulting communication status is sent to the DCS through a dedicated DIM service. The DCS evaluates the health of the communication by monitoring the percentage of failed pings. To ensure reliability, the failure rate must remain below 5% over a statistically significant number of pings. This is calculated using a moving window that ends with the most recent ping from each crate. The tolerance level for failed pings and the size of the sample window are configurable.

3.16.1.5 Automatic Crate-Off Mechanism

The End-cap Alignment devices are powered via driver boards located in VME crates. As described previously, the readout sequence powers on one board at a time, reads all connected devices, and then powers off the board to ensure safety. Continuous power could lead to hardware damage, making automated shutdowns critical.

In rare instances, communication issues may interrupt the readout, leaving devices or boards powered on. To prevent potential damage, a watchdog mechanism within the DCS monitors system status and initiates a

shutdown if necessary.

The system considers the following conditions abnormal and triggers an automatic crate shutdown via a separate CAN communication path:

- Missing heartbeats from cycleLogic, LTX, or Process Checker.
- cycleLogic or LTX processes reported as not running by the Process Checker.
- At least one crate shows unhealthy communication (i.e., excessive failed pings).
- DIM and/or Ctrl Manager of the DCS project are not operational.

When any of these conditions are met, the system cannot guarantee proper monitoring and control, and therefore automatically powers down the affected crates to protect the hardware.

3.16.1.6 The EndCap Alignment DCS

All this information is summarized in the main MDT FSM using four nodes (Fig. 3.77). During Run-3, the primary focus was on restoring the EndCap Alignment system, in collaboration with alignment experts. Additionally, a mechanism was developed to notify experts of any issues, using both email and SMS alerts. This system was implemented with the help of two control managers (Fig. 3.78) that are continuously running. If an issue arises with any of the four nodes—for example, if one of the crates accidentally turns off—the expert is immediately informed of the

specific incident. This system proved highly beneficial during the start of Run-3 and has laid the groundwork for future improvements that are currently under discussion.

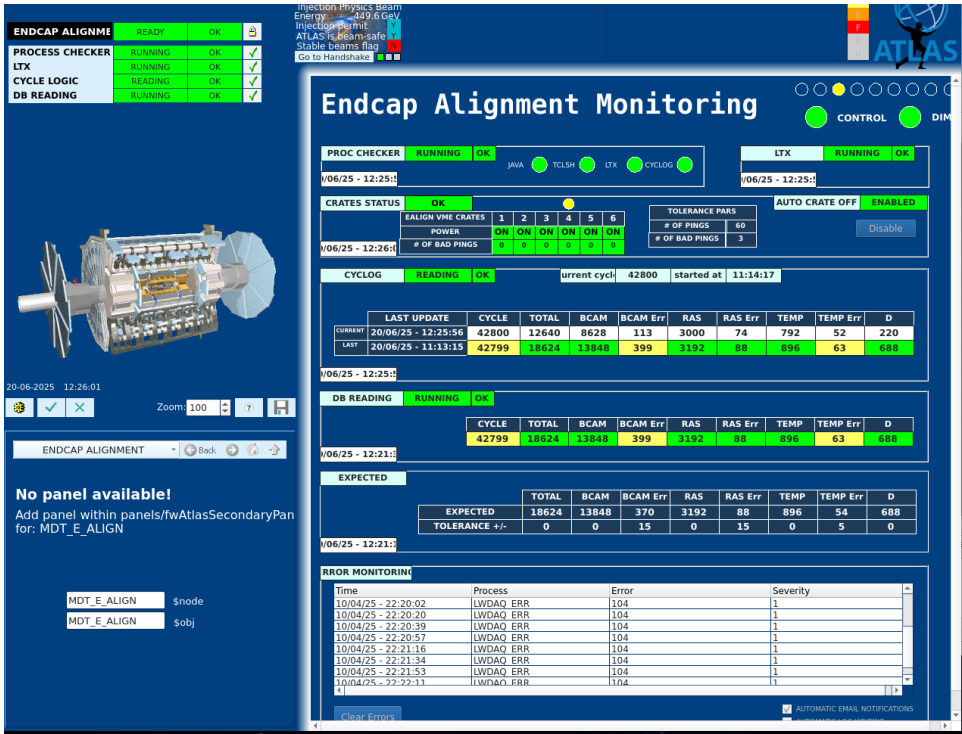


Figure 3.77: The MDT DCS Alignment

2	Control Manager	96	-num 96 mdtLwdaq/mdtLwdaqDimToTempDp.ctf	2025.03.18 15:57:00.7	68280	ah
0	User Interface	1	-p fwDIM/fwDim.pnl -menuBar -iconBar		-1	m
2	<WCCOAdim> in manager	93	-num 93 -dim_dns_node pcatmdtLwdaq01 -dim_dp_config LwdaqDimConfig	2024.12.11 11:12:22.2	70254	ah
2	Control Manager	97	-num 97 mdtLwdaq/mailmsms_alignment.ctf	2025.03.18 15:57:43.1	68721	ah

Figure 3.78: The control managers 93,97 that help the operation of the EndCap alignment DCS System.

Bibliography

- [1] A. Barriuso Poy, et al., "The detector control system of the ATLAS experiment", J. Instrum., vol. 3, P05006, 2008. <https://iopscience.iop.org/article/10.1088/1748-0221/3/05/P05006>
- [2] H.J. Burckhart, et al., "CERN The Common Infrastructure Control of the ATLAS experiment", Proc. Topical Workshop on Electronics for Particle Physics. <https://cds.cern.ch/record/1159528/files/p428.pdf>
- [3] O. Holme, et al., "The JCOP framework", Proc. ICALEPCS 2005, Conf. Proc. C051010:WE2.1-6O, 2005. <https://inspirehep.net/literature/699121>
- [4] S. Schlenker, et al., "THE ATLAS DETECTOR CONTROL SYSTEM", Proc. ICALEPCS2011, Grenoble, France. <https://accelconf.web.cern.ch/icalepcs2011/papers/mobaust02.pdf>
- [5] SIMATIC WinCC OA World. <https://www.winccoa.com/>
- [6] O. Holme, et al., "The JCOP Framework", Proc. ICALEPCS 2005, CERN. https://accelconf.web.cern.ch/ica05/proceedings/pdf/03_005.pdf

- [7] C. Gaspar, "DIM Distributed Information Management System", CERN. <https://dim.web.cern.ch/>
- [8] A. Barriuso Poy, S. Schlenker, "FSM Integration Guideline", DCS Documentation, CERN, 2016. https://web.pa.msu.edu/hep/atlas/l1calo/hub/reference/dcs/FSM_Integration_Guideline_v3p0_2016_02_01.pdf
- [9] O. Crespo-Lopez, J. Hugny, "Specification of control interface between Muons control cooling system ATLAS DCS", ATLAS Internal Doc., CERN, 2016.
- [10] ATLAS Collaboration, "New Small Wheel Technical Design Report", CERN-LHCC-2013-006; ATLAS-TDR-020. <https://cds.cern.ch/record/1552862>
- [11] I. Drivas-Koulouris *et al.*, "The DCS of the NSW High Voltage Infrastructure", ATL-MUON-INT-2024-006, CERN, 2022. <https://cds.cern.ch/record/2886706/files/ATL-MUON-INT-2024-006.pdf>
- [12] CAEN S.p.A., "EASY3000 Technical Information Manual", 2020. <https://www.caen.it/products/easy3000s/>
- [13] CAEN S.p.A., "A1676A Branch Controllers User Manual", 2020. <https://www.caen.it/products/a1676a/>
- [14] CAEN S.p.A., "A3535 HV Board Manual", May 2012. <https://www.caen.it/products/a3535/>
- [15] CAEN S.p.A., "A3540 HV Board Manual", May 2012. <https://www.caen.it/products/a3540/>
- [16] CAEN S.p.A., "A7038 HV Board Manual", Feb. 2022. <https://www.caen.it/products/a7038/>

- [17] A. Lanza, et al., "NSW HV bundles type 1 Technical Specification", CERN, 2018. https://edms.cern.ch/ui/file/2021595/1/nsw-hv-bundles_type1_v1-1.pdf
- [18] A. Lanza, et al., "NSW HV bundles type 2 Technical Specification", CERN, 2018. https://edms.cern.ch/ui/file/2012865/1.0/nsw-hv-bundles_type2_v1.pdf
- [19] A. Lanza, et al., "NSW HV bundles type 3 MM SM1 Technical Specification", CERN, 2018. https://edms.cern.ch/ui/file/2012865/1.0/nsw-hv-bundles_type2_v1.pdf
- [20] A. Lanza, et al., "NSW HV bundles type 3 MM SM2 Technical Specification", CERN, 2018. https://edms.cern.ch/ui/file/2012850/2.0/nsw-hv-bundles_type3-sm2_v2.pdf
- [21] A. Lanza, et al., "NSW HV bundles type 3 LM1-LM2 Technical Specification", CERN, 2018. https://edms.cern.ch/ui/file/2012837/2.3/nsw-hv-bundles_type3-stgc-lm1-lm2_v2-3.pdf
- [22] CAEN S.p.A., "A3485 48 V Generator Manual". <https://www.caen.it/products/a3485/>
- [23] CAEN S.p.A., "A3486 48 V Generator Manual". <https://www.caen.it/products/a3486/>
- [24] Agilent Technologies, "34970 Data Acquisition Unit User Manual". <https://www.agilent.com>
- [25] I. Drivas-Koulouris, et al., "The NSW High Voltage Infrastructure", J. Phys.: Conf. Ser., 2022. <https://iopscience.iop.org/article/10.1088/1742-6596/2375/1/012010/meta>

- [26] CAEN S.p.A., "SY4527 Power Supply User Manual". <https://www.caen.it/products/sy4527/>
- [27] I. Drivas-Koulouris et al., "Implementation of the DCS System of the new MDT BIS78 Chambers for the upgrade of the muon system of the ATLAS Experiment", ATL-MUON-INT-2024-007, CERN, 2022. <https://cds.cern.ch/record/2886707/files/ATL-MUON-INT-2024-007.pdf>
- [28] I. Drivas-Koulouris et al., "Implementation of the DCS System for the validation of MM HV Boards and the DCS System of the new BIS78 Chambers for the upgrade of the muon system of the ATLAS Experiment", *J. Phys.: Conf. Ser.*, vol. 2105, 012027, 2021. <https://iopscience.iop.org/article/10.1088/1742-6596/2105/1/012027/pdf>
- [29] M. Barreta, "Power Supply for MDT Detector", CERN (internal). <https://cds.cern.ch/record/722102/files/p364.pdf>
- [30] E. Karentzos, "PhD. Thesis", NTUA, 2019. <http://cds.cern.ch/record/2683712/files/CERN-THESIS-2412019-094.pdf>
- [31] H. Boterenbrood, "MDT-DCS CANopen Module", CERN, 2008. https://270edms.cern.ch/ui/file/901204/1/MDT-DCS_CANopen_Module.pdf
- [32] V. Khomutnikov, "DDC User's Guide (UG v55)", CERN, 2015. <https://twiki.cern.ch/twiki/pub/Atlas/DcsDdc/DDCUGv55.pdf>
- [33] E. Karentzos, "PhD. Thesis", NTUA, 2019. <https://repository.cern/records/zrjrr-87z81>

- [34] E. Karentzos, et al., "The BMG Chambers Incorporation in the ATLAS Detector Control System", ATL-MUON-INT-2024-002, CERN, 2022. <https://cds.cern.ch/record/2886702/files/ATL-MUON-INT-2024-002.pdf>
- [35] I. Drivas-Koulouris, et al., "The Small Wheel (EI) Decommissioning: The Detector Control System (DCS) Approach", ATL-MUON-INT-2024-005, CERN, 2024. <https://cds.cern.ch/record/2886705?ln=en>
- [36] R. Hart, et al., Proc. ICALEPCS 2009, TUP079, 2009. <https://accelconf.web.cern.ch/icalepcs2009/papers/tup079.pdf>
- [37] E. Karentzos, V. Khomutnikov, ATL-MUON-INT-2024-004, CERN, 2024. <https://cds.cern.ch/record/2886704/files/ATL-MUON-INT-2024-004.pdf>
- [38] CERN Twiki: MDT and CSC Configuration DB. https://edms.cern.ch/ui/file/901204/1/MDT-DCS_CANopen_Module.pdf
- [39] R. Barillere, et al., "LHC GCS: A homogeneous approach for the control of the LHC experiments gas systems", Proc. ICALEPCS 2003. <https://inspirehep.net/literature/639756>
- [40] IT-CO Gas Working Group, "CERN Report", 2003. <https://cds.cern.ch/record/1070768/files/cer-002726467.pdf>
- [41] K. Ntekas, "Ph.D. Thesis", NTUA, 2016. <https://inspirehep.net/literature/1503893>
- [42] C. Amelung, et al., "Results from Tests of the Muon Endcap Alignment System in the H8 Beam Line 2002", ATL-MUON-2004-009, CERN. <https://cds.cern.ch/record/681419>

- [43] S. Aefsky, et al., "The Optical Alignment System of the ATLAS Muon Spectrometer Endcaps" J. Instrum., vol. 3, P11005, 2008. <https://iopscience.iop.org/article/10.1088/1748-0221/3/11/P11005>
- [44] C. Amelung, "ARAMyS – Alignment Reconstruction Software for the ATLAS Muon Spectrometer", Nucl. Phys. B Proc. Suppl., 172 (2007) 132-134. <https://cds.cern.ch/record/1067480?ln=en>

Chapter 4

Z boson mass measurement

The mass of the boson, is a fundamental parameter within the Standard Model. Its current world average, primarily determined by measurements from the four LEP experiments [1][2], is reported as $91.1876 \pm 0.0021 \text{ GeV}/c^2$, corresponding to a relative uncertainty of 2×10^{-5} .

This chapter focuses on the determination of the Z boson mass across three main categories. First, distributions of key parameters from Z boson decays into muon pairs are produced using the Histmaker framework. In the second part, the analysis concentrates on studying the sagitta bias affecting the Z boson. Finally, the third part explores fitting techniques aimed at improving the precision of the mass measurement.

4.1 The origin of weak bosons

In particle physics, the W and Z bosons are classified as vector bosons and are collectively known as the weak bosons, or more generally, intermediate

vector bosons. These elementary particles mediate the weak nuclear force. Their symbols are W^+ , W^- , and Z . The W^+ and W^- bosons carry positive and negative electric charges, respectively, and are each other's antiparticles. In contrast, the Z boson is electrically neutral and is its own antiparticle.

The Z boson mediates the electroweak *neutral current* interaction. In such processes, the participating particles exchange momentum and energy without changing their electric charge. Neutral current interactions occur both in elastic scattering, such as $\nu e^- \rightarrow \nu e^-$ where the outgoing electron can be detected, and in inelastic neutrino–nucleus interactions where the nuclear breakup products are observed.

Unlike the W^\pm bosons, which mediate charged current interactions and therefore involve the emission or absorption of charged leptons (e.g. $\nu_\mu \rightarrow \mu^-$), the Z boson does not change the identity or charge of the interacting particles. For example, in neutrino–electron elastic scattering mediated by Z exchange, the neutrino transfers part of its momentum to the electron, which recoils and can be detected.

Since the Z boson is its own antiparticle and carries no flavor or electric charge, it mediates neutral current interactions, where particles retain their identities while exchanging momentum or spin.

Z boson interactions with neutrinos are especially important, as they provide the only known mechanism for elastic neutrino scattering in matter. Such interactions are nearly as probable as inelastic interactions involving W bosons. The existence of weak neutral currents via Z boson exchange was confirmed in 1973 during a neutrino experiment using the Gargamelle

bubble chamber at CERN[3].

Unlike beta decay, detecting neutral current interactions involving particles other than neutrinos requires significant infrastructure, including high-energy accelerators and advanced detectors, due to the Z boson's large mass and photon-like behavior at high energies.

The discovery of the W and Z bosons was a milestone for CERN. In 1973, electroweak theory's prediction of neutral current interactions was validated when the Gargamelle experiment recorded neutrino events without visible charged leptons—evidence of Z boson-mediated interactions with nucleons.

However, the direct detection of W and Z bosons required a powerful accelerator. The Super Proton Synchrotron (SPS) met this need, and in January 1983 the W boson was conclusively observed by the UA1 and UA2 collaborations, led by Carlo Rubbia (UA1) and Pierre Darriulat (UA2)[4].

A crucial element that made these discoveries possible was the development of the stochastic cooling technique by Simon van der Meer, which enabled the accumulation of sufficiently intense antiproton beams in the SPS. Just a few months later, in May 1983, the Z boson was also detected.

For their pioneering contributions — Rubbia in the experimental discovery and van der Meer in the accelerator beam technology — both were awarded the Nobel Prize in Physics in 1984, a remarkably swift recognition by the Nobel Foundation[5].

Together with the photon (γ), the W^+ , W^- , and Z bosons form the quartet of gauge bosons governing the electroweak interaction. The Z boson typically decays into a fermion–antifermion pair.

4.2 ElectroWeak Fit

The Standard Model of particle physics (SM) represents certainly the biggest success of 20th century physics. Its validity over a very wide range of energies has been experimentally tested to unprecedented precision, showing a perfect agreement of theory and experiment. The use of electroweak corrections, combined with precision measurements is the main strategy used to evaluate the parameters of the model which are still unmeasured or which are measured with the poorest accuracy, such as the mass of the top, m_t , and of the higgs, m_H . Electroweak radiative corrections to physical observables are computable in perturbation theory and they depend quadratically on m_t and logarithmically on m_H .

The global electroweak fit combines all the information coming from many experiments into one single χ^2 fit, to obtain the best evaluation of all the parameters of the SM. The fit accepts as input the following measurements from LEP: the mass and width of the Z , the hadronic pole cross section of Z exchange, the Z leptonic branching ratio, the leptonic forward backward asymmetry ($A_{\text{FB}}^{0,\ell}$), the τ polarisation, the $q\bar{q}$ charge asymmetry, and the mass and width of the W boson (m_W, Γ_W). Other inputs come from the combination of SLD and LEP heavy flavour measurements: the ratios of b and c partial widths of the Z to its total hadronic width (R_b^0, R_c^0), the b and c forward backward asymmetries and

the coupling parameters A_b and A_c . The other measurements used are the coupling parameter A_ℓ from SLD, m_W , Γ_W and m_t from $\bar{p}p$ colliders, the measurements of Atomic Parity Violation (APV), $\sin^2 \theta_W$ from νN scattering and the contribution of light quarks to the photon vacuum polarization ($\Delta\alpha_{\text{had}}^{(5)}$) from low energy $e^+e^- \rightarrow q\bar{q}$.

The measurements of the Z boson properties including its mass m_Z , width Γ_Z , and pole cross section σ_0 — have been carried out by all LEP experiments (ALEPH, DELPHI, L3, and OPAL) as well as by the SLD collaboration at the Stanford Linear Collider (SLC). Figure 4.1 displays the measured values of the Z mass along with their uncertainties. In particular, Figure 4.1(a) shows the results from the four LEP experiments, while Figure 4.1(b) illustrates the progression of m_Z measurements over time, highlighting improvements in experimental techniques and technologies.

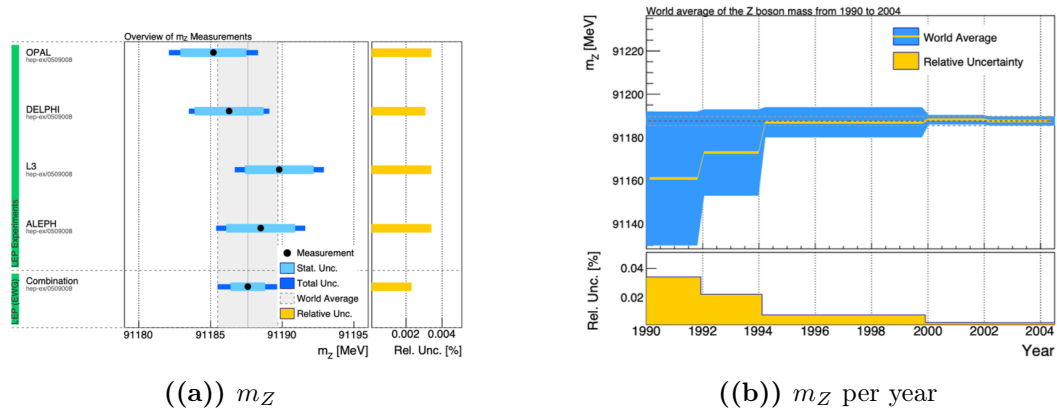


Figure 4.1: (a) Summary of measurements performed by the LEP collaborations (ALEPH, L3, DELPHI, and OPAL), along with their combined result. (b) Evolution of the world average value of and its associated uncertainties from 1990 to 2004.

The mass of the Z boson, measured as $m_Z = 91.1876 \pm 0.0021 \text{ GeV}/c^2$

according to PDG-2022 [6], is known with remarkable precision. However, performing this measurement again using ATLAS Run-2 data could provide valuable insights for studies involving the W boson and the higgs boson.

Fig. 4.2 illustrates the evolution of the W boson mass measurements, with the current value being $m_W = 80412 \pm 29 \pm 3 \text{ MeV}/c^2$. Similarly, Fig. 4.2 shows the progression of the higgs boson mass measurements, with the latest measurement at $m_H = 125.10 \pm 0.14 \text{ GeV}/c^2$.

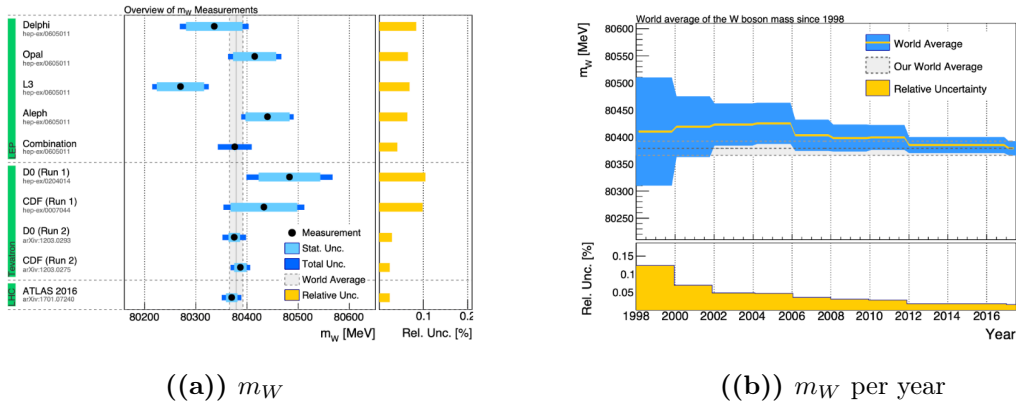


Figure 4.2: (a) Overview of the measurements of m_W by the LEP, Tevatron and LHC collaborations. (b) Overview of world average of m_W and its uncertainties versus Year from 1998 to 2016.

4.3 Motivation

A precise measurement of the Z boson mass is a cornerstone of the Standard Model. Its value, determined with very high precision at LEP, is strongly correlated with the beam energy calibration and with assumptions on detector performance specific to the LEP era. Re-measuring m_Z at the LHC provides an independent validation of the momentum scale

and alignment of the ATLAS detector under radically different experimental conditions and at significantly higher instantaneous luminosities.

Although the Z boson mass is already known with high precision, small deviations in its reconstructed value can indicate residual detector biases, particularly in the muon momentum scale, alignment uncertainties, and magnetic field modeling. These effects directly influence precision electroweak measurements, including the determination of the W boson mass and the Higgs boson mass from global electroweak fits.

The decay channel $Z \rightarrow \mu^+ \mu^-$ is especially suitable for such studies, as it offers a clean final state with excellent charge and momentum reconstruction, low background contamination, and large statistics across the full LHC Run-2 dataset. Therefore, the precise reconstruction of the dimuon invariant mass peak serves both as a physics observable of interest and as a high-accuracy probe of the detector calibration strategy.

4.4 Datasets and Monte Carlo Simulations

In this subsection a brief description of the Data and Simulated samples used in the Z mass precision measurement analysis will be made.

4.4.1 Datasets for Z Mass Analysis

The dataset analyzed in this study was recorded by the ATLAS detector during the 2015–2018 data-taking period, corresponding to proton–proton collisions at a center-of-mass energy of $\sqrt{s} = 13$ TeV. Only

events collected under stable beam conditions, with all relevant ATLAS magnets and detector subsystems operating nominally, are included in the analysis.

Event selection is based on a set of trigger algorithms, including single-muon triggers optimized for $Z \rightarrow \mu\mu$ decays, as well as dedicated dimuon triggers designed for the $J/\psi \rightarrow \mu\mu$ and $\Upsilon \rightarrow \mu\mu$ decay channels.

The single-muon trigger is configured to select events with a single muon, targeting the dimuon final state from Z boson decays. This trigger identifies such events by detecting a characteristic single-muon signature.

To efficiently capture J/ψ and Υ meson decays into muon pairs, a dedicated dimuon trigger is used. This trigger is specifically optimized to improve the selection of these lower-mass resonances.

After applying all trigger conditions and data quality criteria, the resulting dataset corresponds to an integrated luminosity of 139 fb^{-1} , with an average number of interactions per bunch crossing of $\langle \mu \rangle = 33.7$.

4.5 Monte Carlo Simulated Samples

Monte Carlo (MC) simulated samples of various particle decays and production processes were used in the analysis.

Samples of $Z \rightarrow \mu\mu$, $Z \rightarrow \tau\tau$, $W \rightarrow \mu\nu$, and $Z/\gamma \rightarrow \mu\mu$ events were generated using POWHEG-BOX v1 at next-to-leading order (NLO) in perturbative QCD, interfaced with PYTHIA 8.186 for parton showering

and hadronization. Final-state QED radiation effects were simulated using PHOTOS++. The Z boson samples were reweighted to reproduce the transverse momentum (p_T) and pseudorapidity (η) distributions observed in data.

Additional contributions from diboson processes (ZZ , WZ , WW) and top-quark pair production ($t\bar{t}$) were included. Diboson events were simulated with POWHEG-BOX v2 interfaced with PYTHIA 8.210, while $t\bar{t}$ events were generated using PYTHIA 8.230.

The ATLAS detector response was modeled using the GEANT4 simulation toolkit. The same reconstruction algorithms applied to collision data were used for the simulated events, enabling a consistent reconstruction of particle trajectories and properties. In addition, samples with intentionally misaligned detector geometries were employed to validate the robustness of the calibration procedures.

4.6 Muon Selections

Event selections are displayed in the Table 4.1.

Selections for Signal Region
Only two Muons
Muon Trigger matched
Muons Isolated
Opposite charge
Both $p_T^\mu > 25 \text{ GeV}/c$
Both $ \eta^\mu < 1.05$
$66 < m_{\mu\mu} < 116 \text{ GeV}/c^2$

Table 4.1
Selections on analysis data

The selection of dimuon events is a critical step in suppressing background contributions from processes involving multiple leptons in the final state, such as top-quark pair production ($t\bar{t}$) and diboson processes. Ensuring proper trigger matching and trigger pass criteria is essential for accurate event normalization, guaranteeing that the selected events correspond to the trigger conditions applied during data taking.

Muon isolation requirements are imposed to suppress backgrounds in which muons originate from jets or are produced in association with other particles. These isolation criteria enhance the purity of the selected sample by reducing contributions from non-prompt or secondary muons, particularly improving rejection of $t\bar{t}$ events.

Requiring opposite-charge muon pairs is fundamental, as the $Z \rightarrow \mu^+\mu^-$ decay inherently involves a muon and an anti-muon. A transverse momentum threshold of $p_T^\mu > 25$ GeV/c is applied to remove low-energy backgrounds and increase the selection efficiency for signal-like events. Furthermore, restricting the muon pseudorapidity to $|\eta| < 1.05$ ensures that only muons within the barrel region of the Inner Detector are selected, where the tracking resolution is highest.

Finally, selecting events with a dimuon invariant mass within the range $116 \text{ GeV}/c^2$ isolates the region dominated by the Z boson peak. At this stage, background contributions are highly suppressed, and the event yield is well described by the combination of signal and residual background processes.

4.7 Selection Criteria

In Fig. 4.3, 4.4 the signal and the all background are presented for all datasets of Run-2 together with the cuts. Cut flow histograms are normalized to the luminosity of the individual years. After the opposite sign selection, at the last three bins, there is good agreement between simulation and data. Background contributes significantly in the first bin ("No cut"). As the cut flow histogram progresses to the signal region the background becomes negligible. The mass selection is reducing the background to an percentage of $\approx 1\%$.

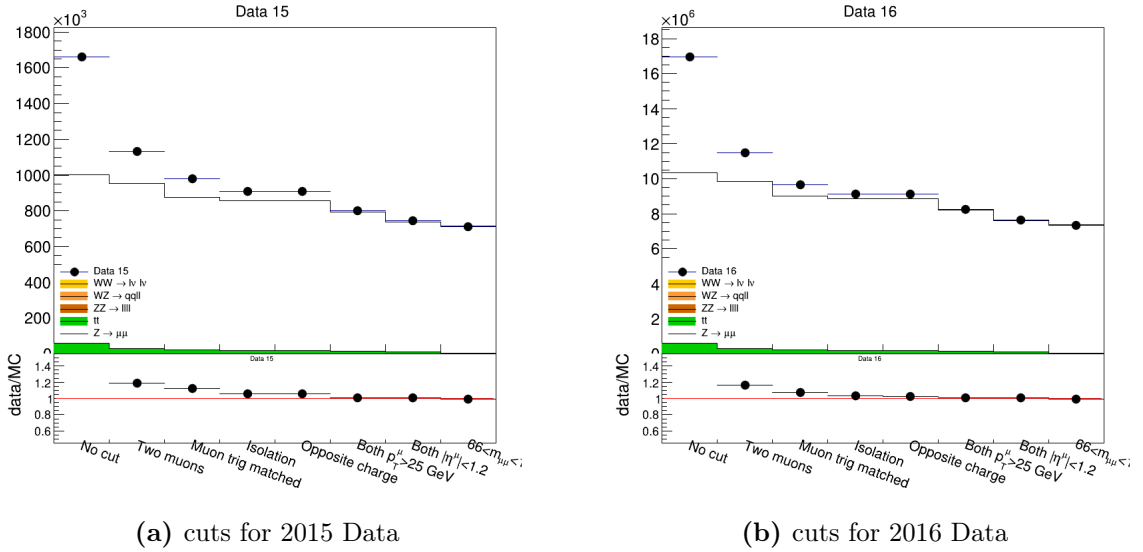


Figure 4.3: Cuts applied for Data of years 2015-16.

4.8 Histmaker Plots

In this section we are creating plots with the help of Histmaker framework. This framework use the corresponding normalized by luminosity datasets

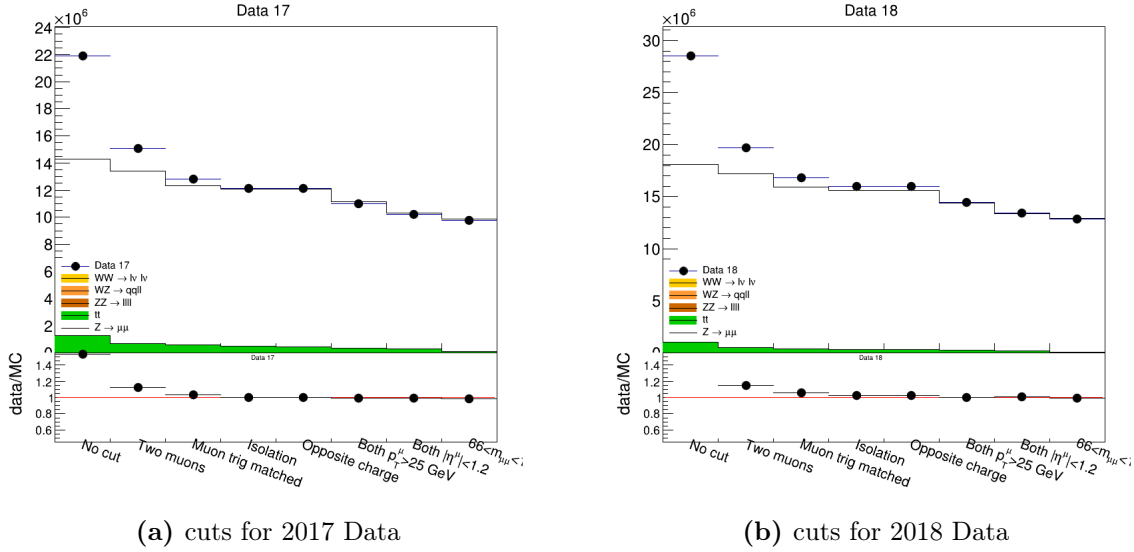


Figure 4.4: Cuts applied for Data of years 2017-18.

or the MC of the background and by applying the cuts from the previous section create the distributions we want.

Kinematic distributions play a crucial role in evaluating both the underlying physics processes and the accuracy of the measurement. Fig. 4.5- 4.10 display the transverse momentum (p_T) distributions of the leading muon, sub-leading muon, and di-muon system, respectively.

A clear trend is observed in the ratio plots, indicating increasing disagreement between data and simulation at higher p_T values. In particular, the leading muon distributions show a noticeable deviation starting around $p_T \approx 90$ GeV/c, consistently across all data-taking campaigns. Similarly, for the sub-leading muon, a mismatch becomes evident at approximately $p_T \approx 50$ GeV/c. The di-muon transverse momentum distributions also reveal significant discrepancies at $p_T^{\mu\mu} > 100$ GeV/c.

These discrepancies become more pronounced at higher transverse momentum values and are primarily attributed to the absence of higher-order corrections beyond Next-to-Leading Order (NLO), specifically the missing contributions from Next-to-Next-to-Leading Order (NNLO) QCD diagrams in the signal modeling. These corrections grow increasingly important with rising energy.

Fig. 4.11- 4.16 present the distributions of the leading muon pseudorapidity (η_μ) and di-muon rapidity ($Y_{\mu\mu}$), which are angular observables. These angle-related distributions are sensitive not only to the absence of higher-order corrections but also to potential mis-modeling of angular variables and imperfections in the detector geometry not accounted for during calibration. However, an excellent agreement between Monte Carlo simulations and data is observed for these angular distributions.

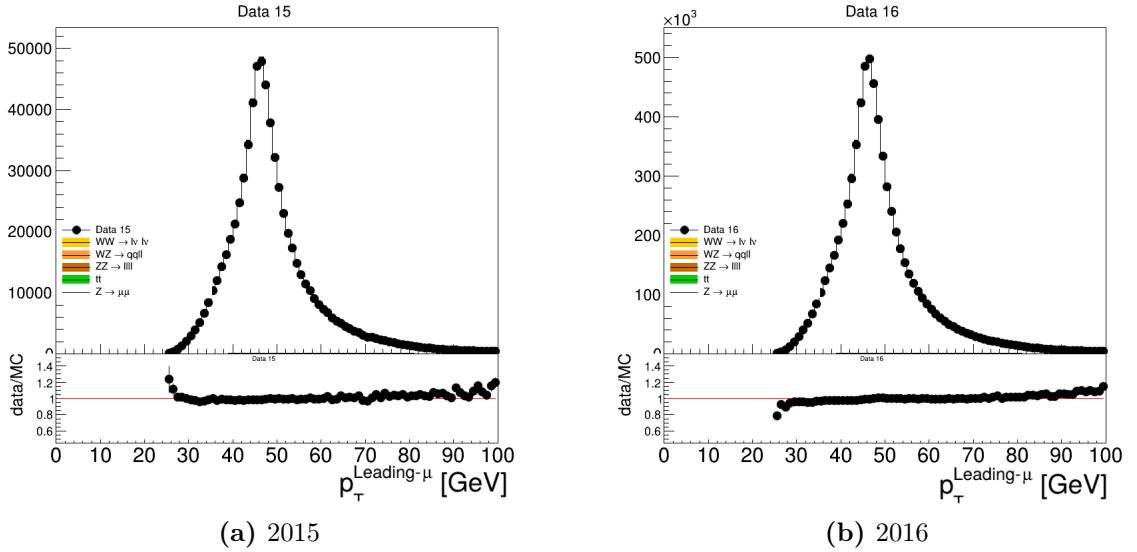
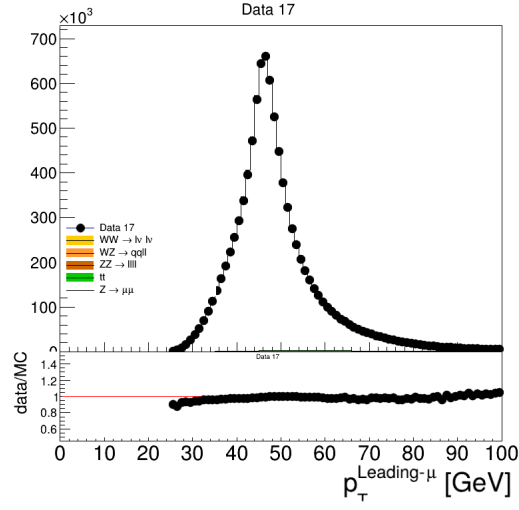
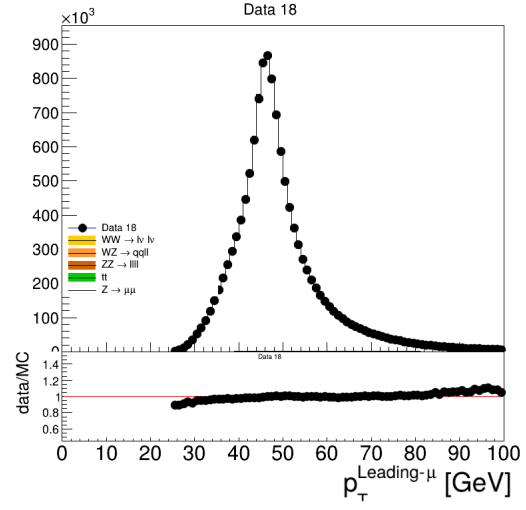


Figure 4.5: p_T of leading muon

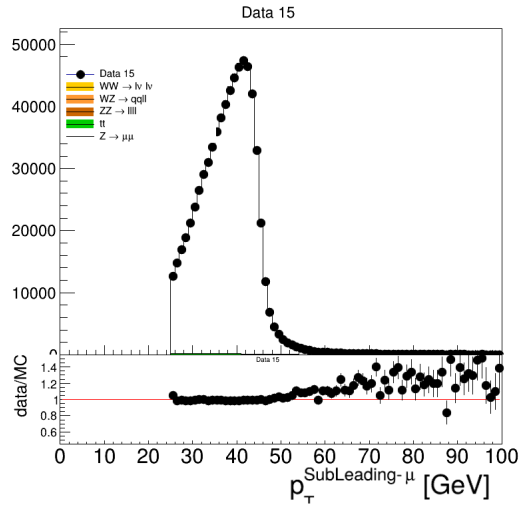


(a) 2017

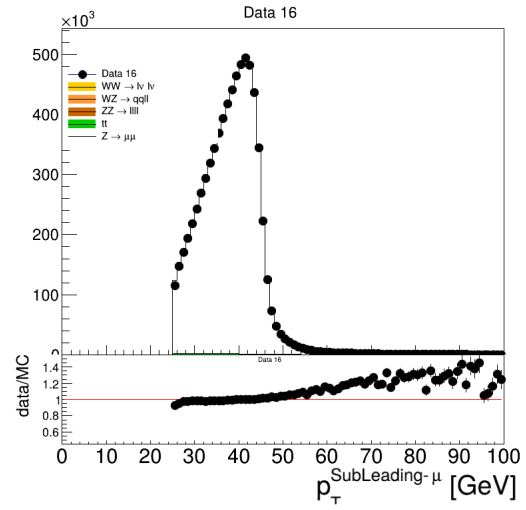


(b) 2018

Figure 4.6: p_T of leading muon



(a) 2015



(b) 2016

Figure 4.7: p_T of sub-leading muon

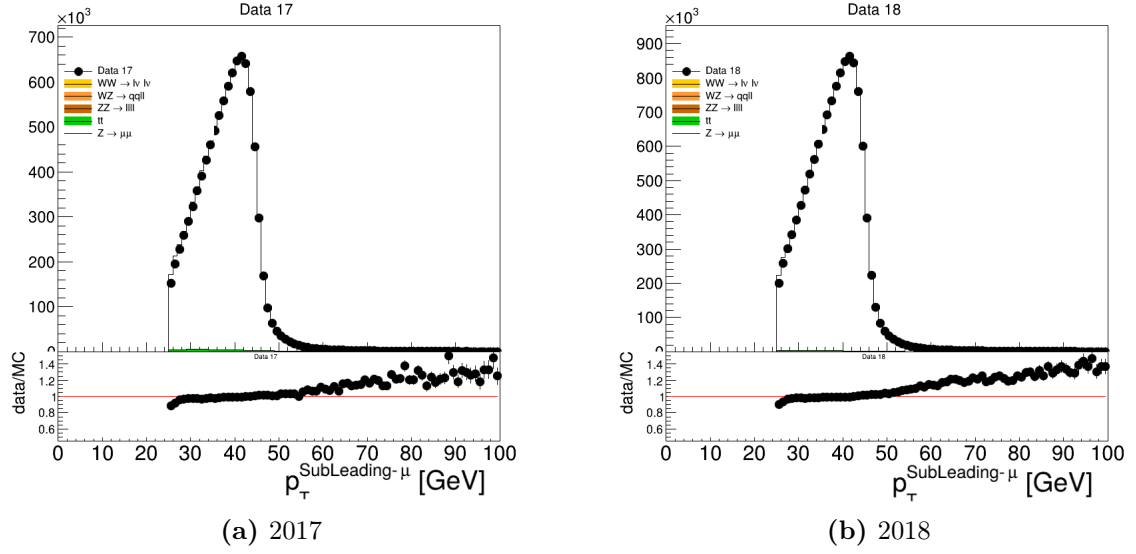


Figure 4.8: p_T of sub-leading muon

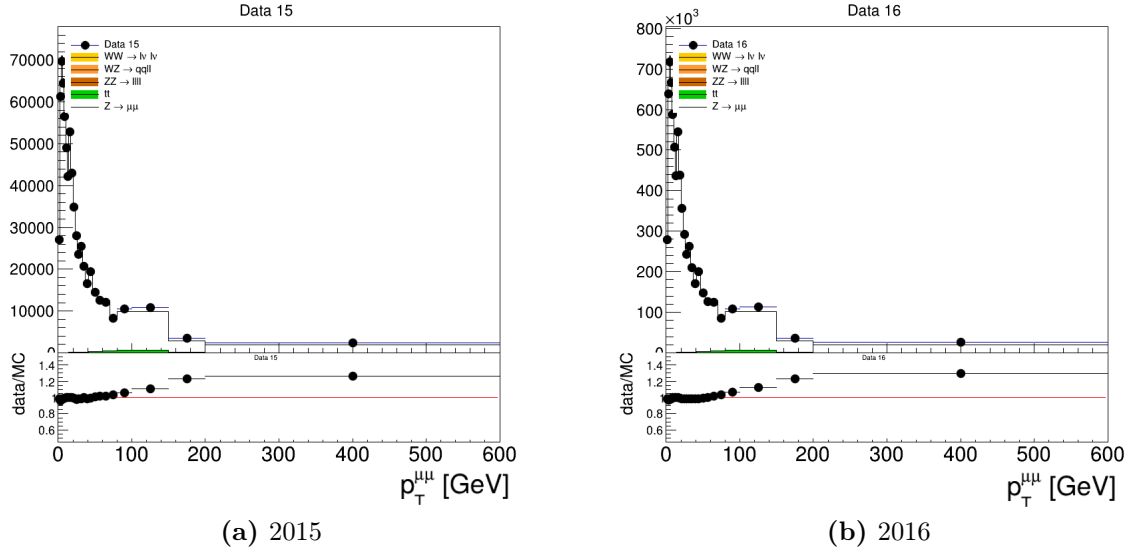
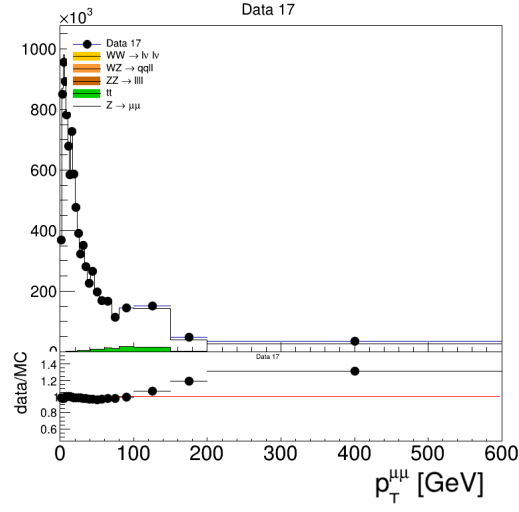
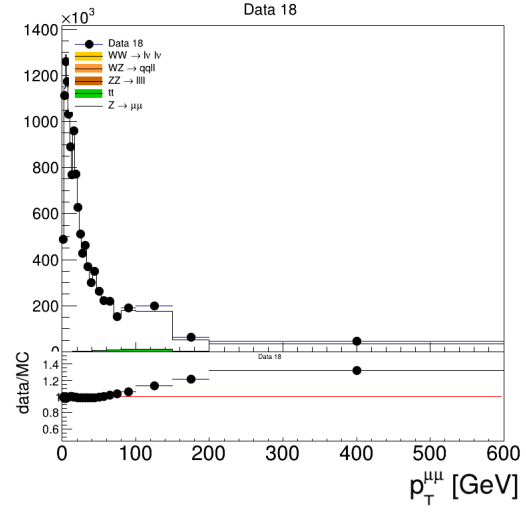


Figure 4.9: p_T for di-muon

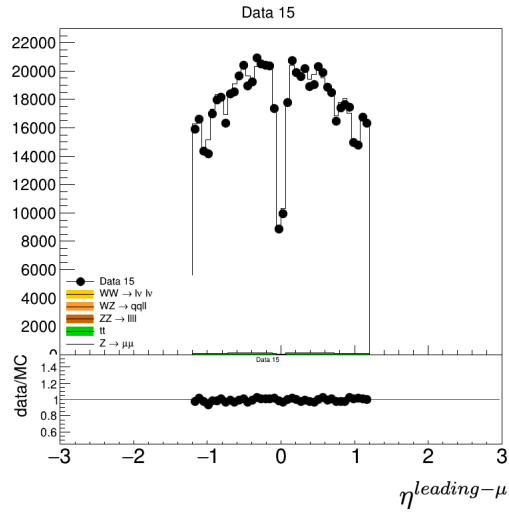


(a) 2017

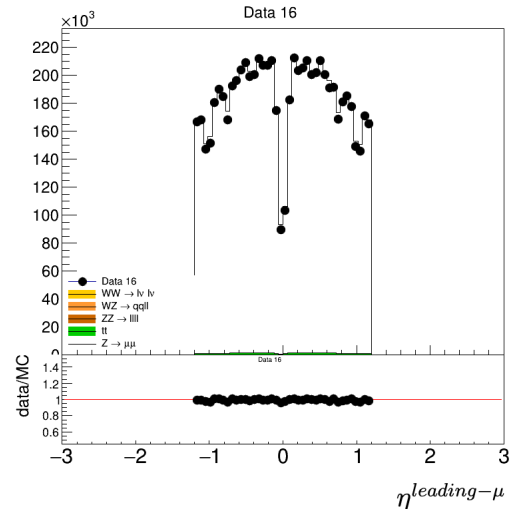


(b) 2018

Figure 4.10: p_T for di-muon

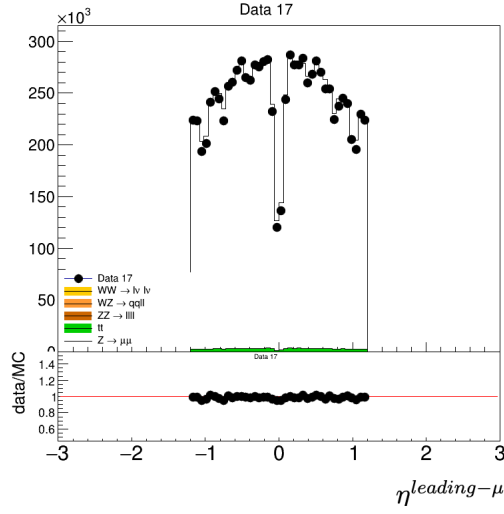


(a) 2015

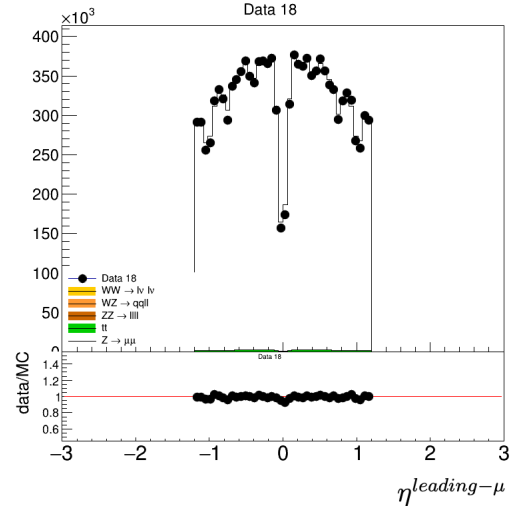


(b) 2016

Figure 4.11: η_μ leading muon

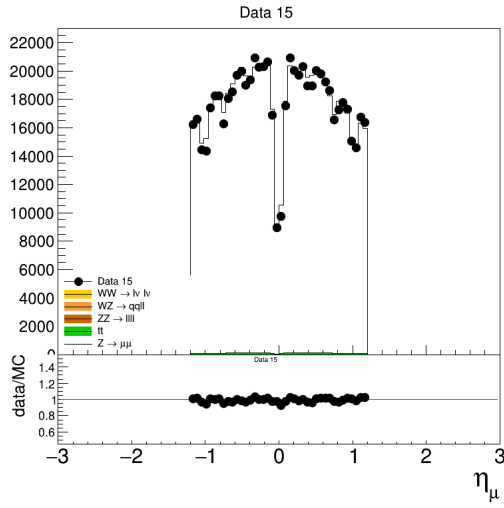


(a) 2017

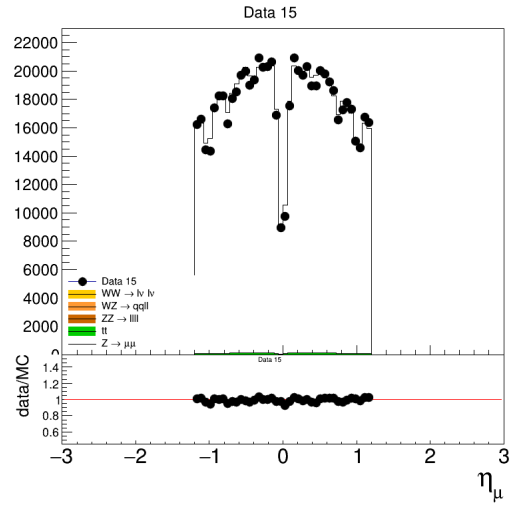


(b) 2018

Figure 4.12: η_μ of leading muon

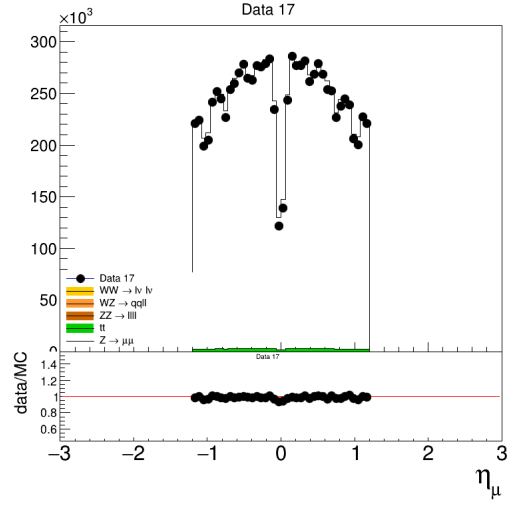


(a) 2015

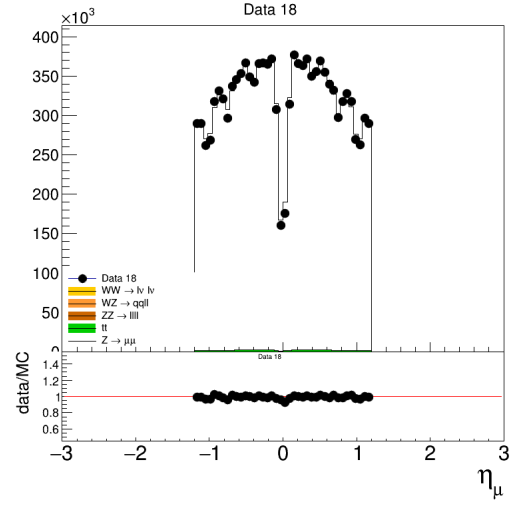


(b) 2016

Figure 4.13: η_μ of sub-leading muon

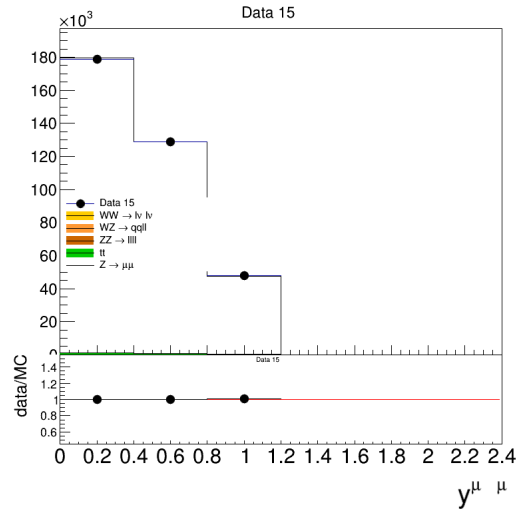


(a) 2017

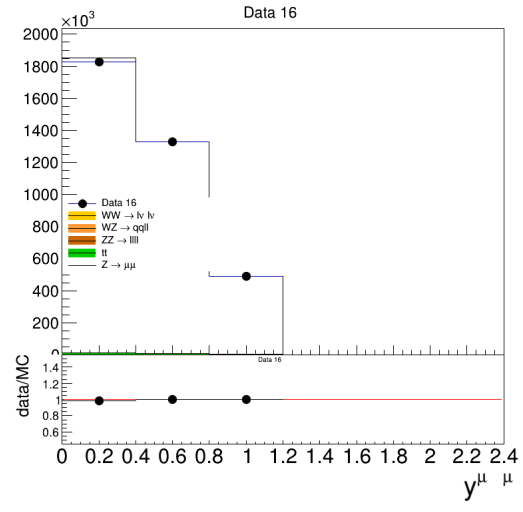


(b) 2018

Figure 4.14: η_μ of sub-leading muon



(a) 2015



(b) 2016

Figure 4.15: $Y_{\mu\mu}$ for two muons

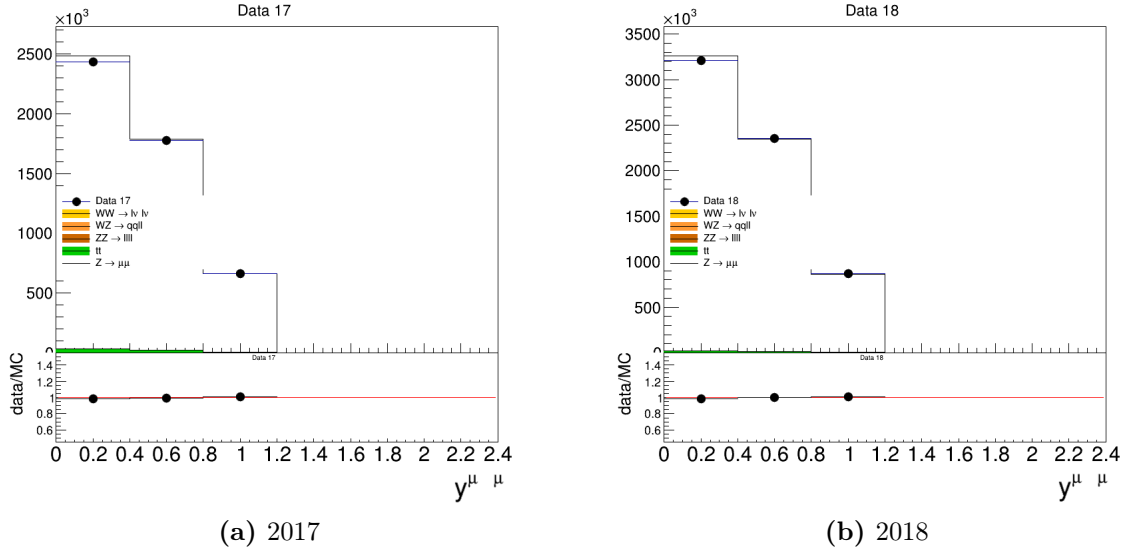


Figure 4.16: $Y_{\mu\mu}$ for two muons

4.9 Multijet background Estimation

In this part we are focusing on the distribution of the mass of Z boson with Histmaker. We run the framework for the whole sample (~ 100 million events), for the Data from 2015-18 and comparing them with the backgrounds.

By looking the Fig. 4.17- 4.18 we see that we have an agreement for the values around $90 \text{ GeV}/c^2$ for the mass as we expected.

As a next study we try to see the existence of same sign muons. Same-sign muon pairs (i.e., two muons with the same electric charge) are an interesting and relatively rare signature in particle physics. Unlike opposite-sign muon pairs, which commonly arise from standard processes such as the decay of neutral bosons ($Z \rightarrow \mu^+\mu^-$, $J/\psi \rightarrow \mu^+\mu^-$), same-sign muons

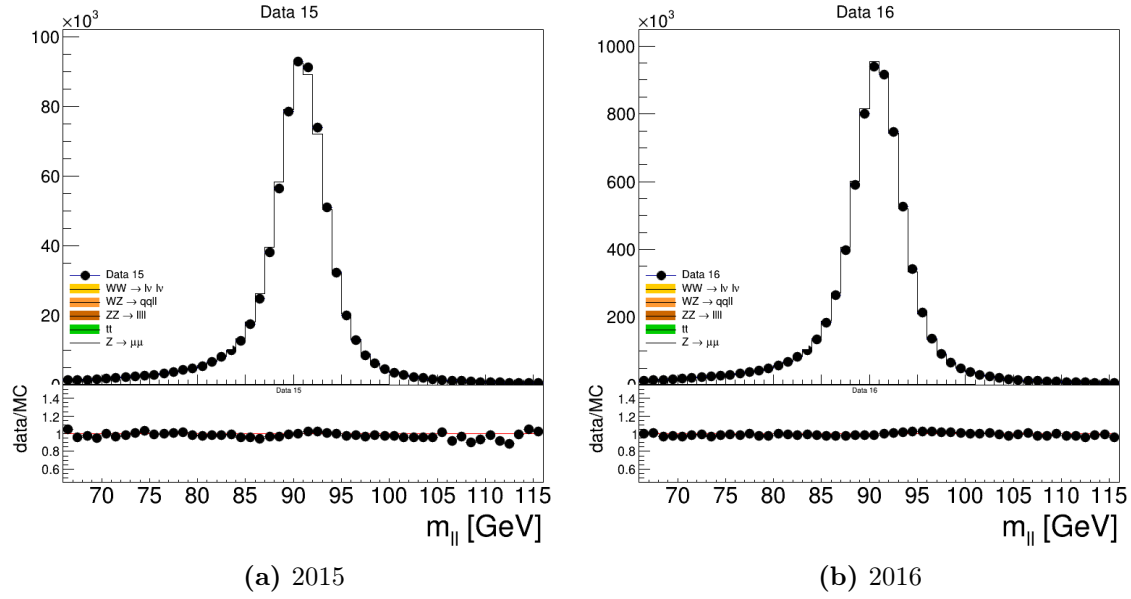


Figure 4.17: Z mass distributions for 2015 and 2016 data

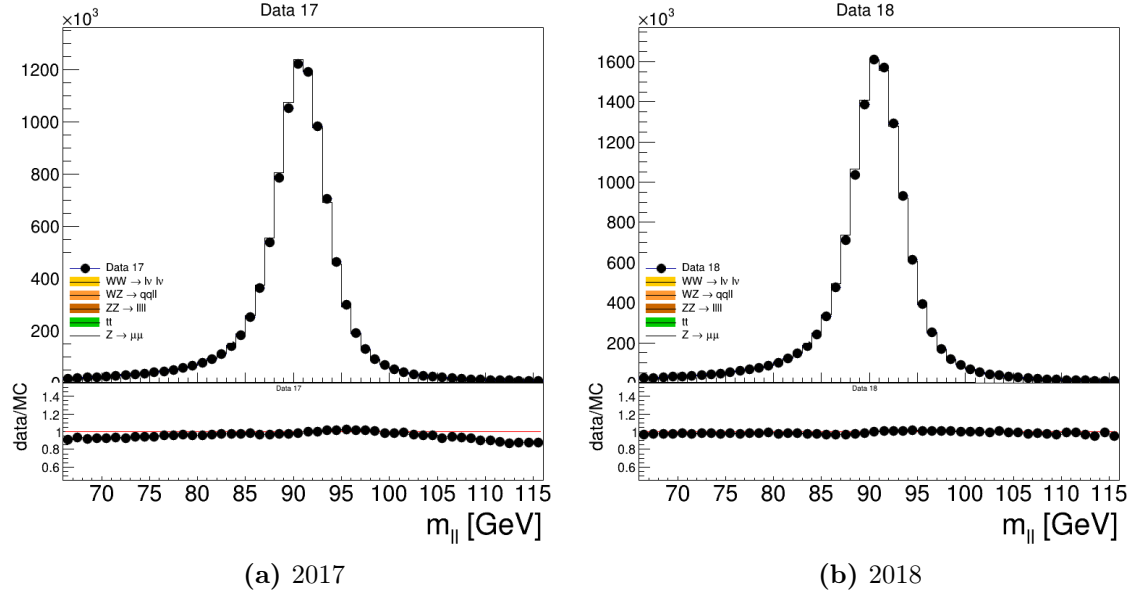


Figure 4.18: Z mass distributions for 2017 and 2018 data

can indicate muons in jets (heavy flavor decays)

In order to study this case, we modify the selection presented in the

previous paragraphs and use same sign muons. In Fig. 4.19 we can see the results.

By comparing the distributions of the same-sign muon pairs in data, we observe that the number of entries is very small. This confirms that the contribution from same-sign muons to our selected sample is negligible, as is the overall background, which is consistent with our expectations after the applied selection cuts.

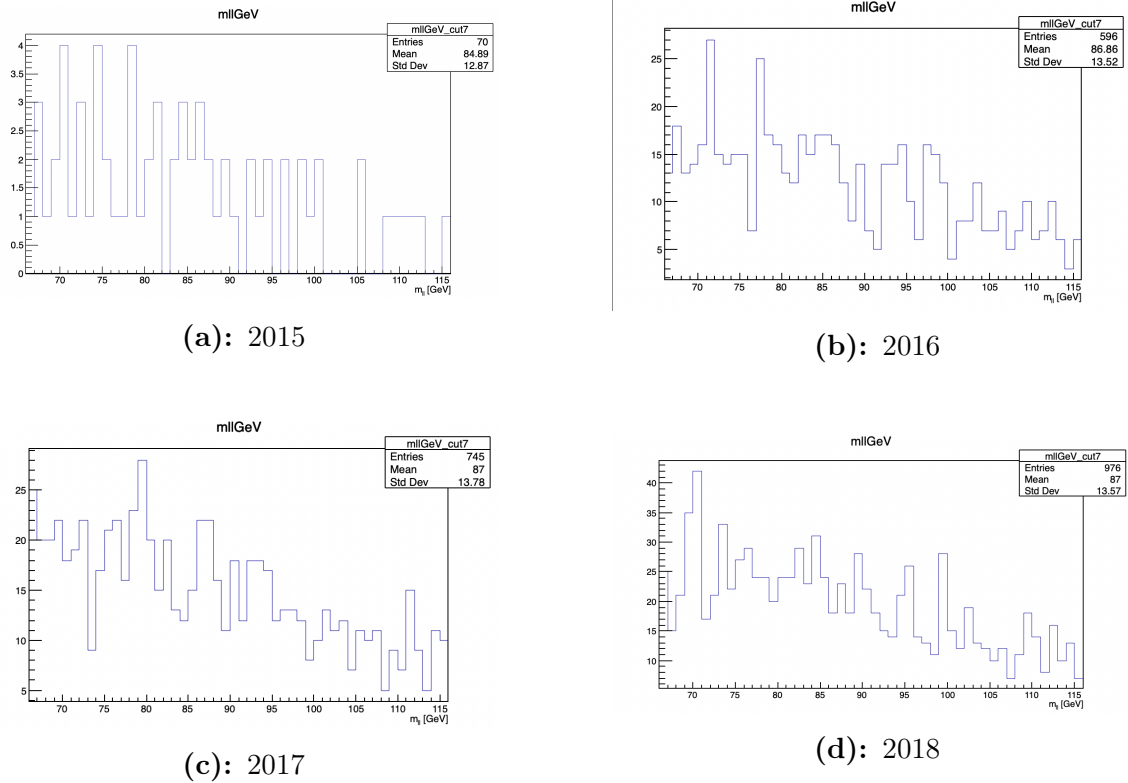


Figure 4.19: same sign muons on datasets 2015-18.

4.10 Radial Bias Analysis

In this section, we focus on the sagitta bias in relation to the Z boson mass, dividing the study into three parts. First, we investigate how the pseudomass distribution changes when a sagitta bias is artificially introduced. Second, we calculate the asymmetry between the two muons originating from the Z boson. Finally, we assess how background processes contribute to the observed Z mass asymmetry.

4.10.1 Distortions of the inner detector: sagitta bias

The weak modes in the Inner Detector alignment refer to specific geometric distortions that leave the track fit chi-square unchanged but introduce systematic biases in the reconstructed track parameters. In particular, sagitta bias results from distortions in the detector's bending plane, leading to differential effects on the curvature of tracks for positively and negatively charged particles, as shown in Fig. 4.20.

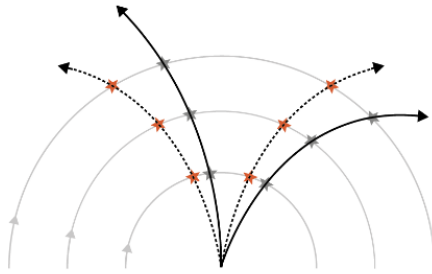


Figure 4.20: Schematic illustration of the sagitta bias in charged particle tracks, arising from geometrical deformations in the bending plane.

The charge-asymmetric deformation of the track curvature can be parametrized

as:

$$p' = p(1 + q p_T \delta_s)^{-1} \quad (4.1)$$

Here, p' denotes the reconstructed momentum of the track, while p and p_T represent the true total and transverse momenta, respectively. The variable q indicates the particle's electric charge sign, and δ_s represents the sagitta bias parameter. This parameter is common to all measured momenta and uniquely characterizes the geometric deformation of the detector.

Sagitta biases are corrected in the alignment campaigns by introducing constraints on the track parameters, as described in [7]. In the analysis of the Z boson mass, residual sagitta biases after the alignment campaigns are evaluated and corrected to enhance the precision of track momentum reconstruction.

4.10.2 The Pseudo-mass method

A data-driven approach, known as the *pseudomass*, is used to evaluate the sagitta bias in data using $Z \rightarrow \mu^+ \mu^-$ events. Originally introduced in [8], this method has been adopted by the LHCb Collaboration to improve the momentum reconstruction of high- p_T tracks [9].

The pseudomass method approximates the invariant mass of $Z \rightarrow \mu^+ \mu^-$ decays using the momentum of one muon and only the direction of the other. The pseudomass m^\pm is defined as:

$$m^\pm = \sqrt{m^2 \frac{p_T^\pm}{p_T^\mp}} \quad (4.2)$$

where m^2 is the invariant mass of the dimuon system, and p_T^\pm is the transverse momentum of the μ^\pm . By substituting the relativistic expression for m^2 , $m^2 = 2p^+p^-(1 - \cos \theta)$, where p^+ and p^- are the momenta of positive and negative muon, respectively, and θ the opening angle between them. The pseudomass can be rewritten as:

$$m^\pm = \sqrt{2p^+p^-(1 - \cos \theta) \frac{p_T^\pm}{p_T^\mp}}. \quad (4.3)$$

The pseudomass provides an estimate of the dimuon mass under the assumption that the system has zero momentum transverse to the bisector of the two lepton transverse momenta. This assumption is motivated by the fact that the majority of the $Z \rightarrow \mu^+\mu^-$ cross section at hadron colliders occurs in the region where $p_T(Z) < m(Z)$.

m^\pm is sensitive to the momentum of a single muon, enabling binning as function of muon η and ϕ . It serves as a robust observable to probe the global sagitta bias at the Z -boson peak, without direct sensitivity to the Z -boson mass.

Fig. 4.21- 4.24 shows the simulated pseudomass distribution for positive and negative muons. In the absence of a sagitta bias, the m^+ and m^- distributions are identical, peaking at the Z -boson mass. However, when a sagitta bias of $\delta_s = -0.1 \text{ TeV}^{-1}$ in our case, the pseudomass distributions shift in opposite directions for positive and negative muons.

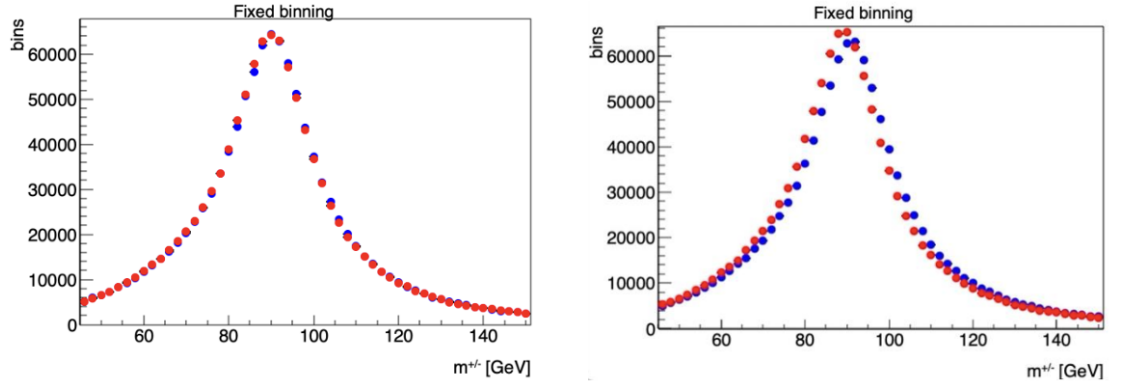


Figure 4.21: Z mass distribution for 2015 data. On the left is the distribution for sagitta bias $\delta_s = 0 \text{ TeV}^{-1}$ and on the right for $\delta_s = -0.1 \text{ TeV}^{-1}$.

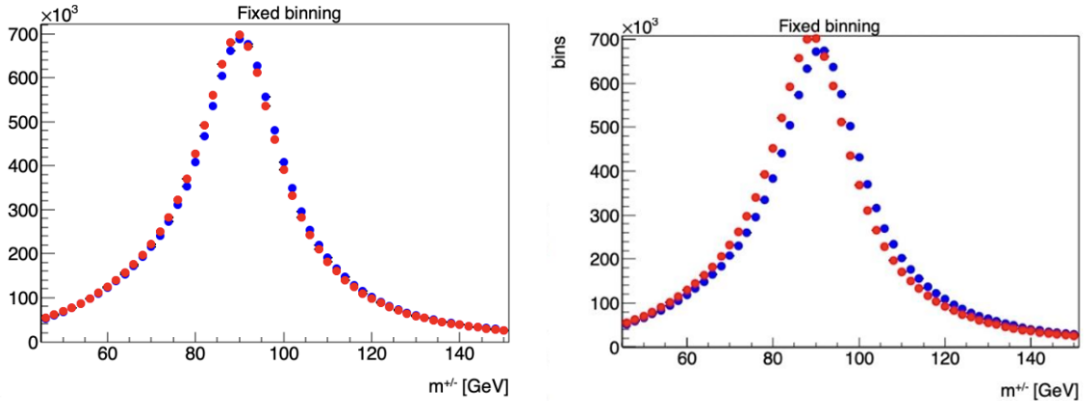


Figure 4.22: Z mass distribution for 2016 data. On the left is the distribution for sagitta bias $\delta_s = 0 \text{ TeV}^{-1}$ and on the right for $\delta_s = -0.1 \text{ TeV}^{-1}$.

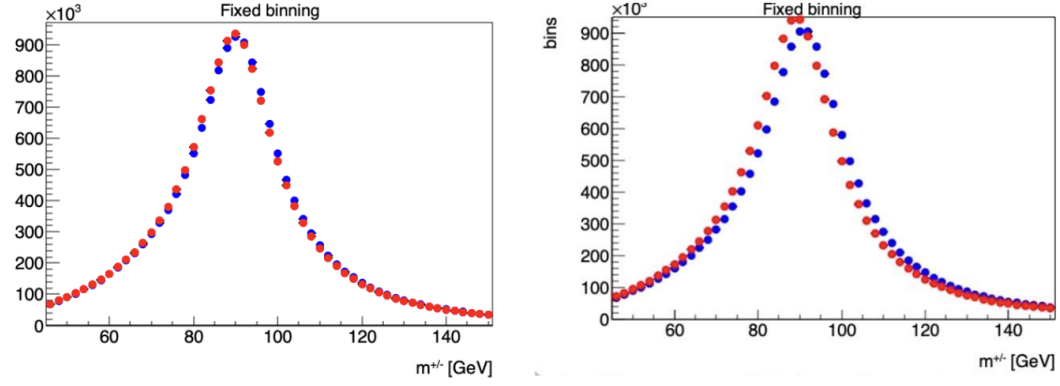


Figure 4.23: Z mass distribution for 2017 data. On the left is the distribution for sagitta bias $\delta_s = 0 \text{ TeV}^{-1}$ and on the right for $\delta_s = -0.1 \text{ TeV}^{-1}$.

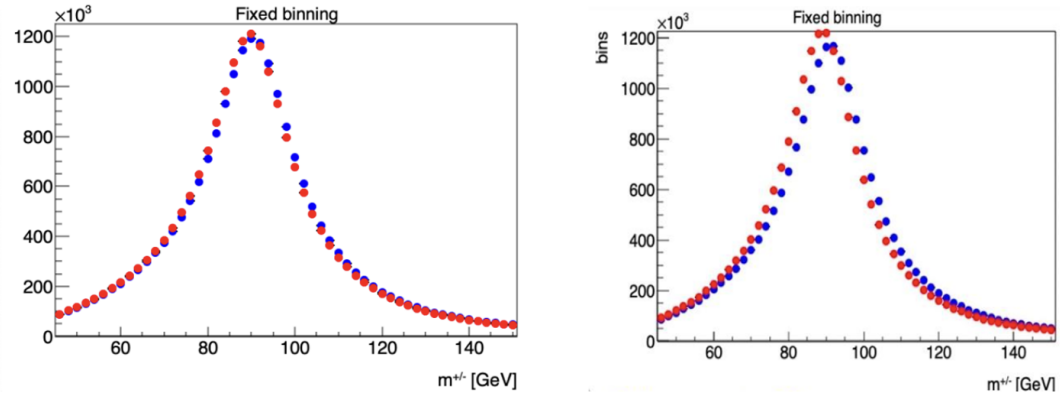


Figure 4.24: Z mass distribution for 2018 data. On the left is the distribution for sagitta bias $\delta_s = 0 \text{ TeV}^{-1}$ and on the right for $\delta_s = -0.1 \text{ TeV}^{-1}$.

The pseudomass asymmetry (A) is defined as:

$$A = \frac{m^+ - m^-}{m^+ + m^-} \quad (4.4)$$

where m^+ and m^- are the pseudomasses of positive and negative muons, respectively. As shown in Fig. 4.25, when the sagitta is perfectly reconstructed, the pseudomass asymmetry remains flat at 0. However, in the presence of a sagitta bias in the reconstructed track, the asymmetry exhibits a clear dependence on the pseudomass. This behavior allows the pseudomass asymmetry to serve as a robust quantifier of charge-dependent sagitta biases, making it a key tool in the Z boson mass measurement for determining sagitta bias in reconstructed data.

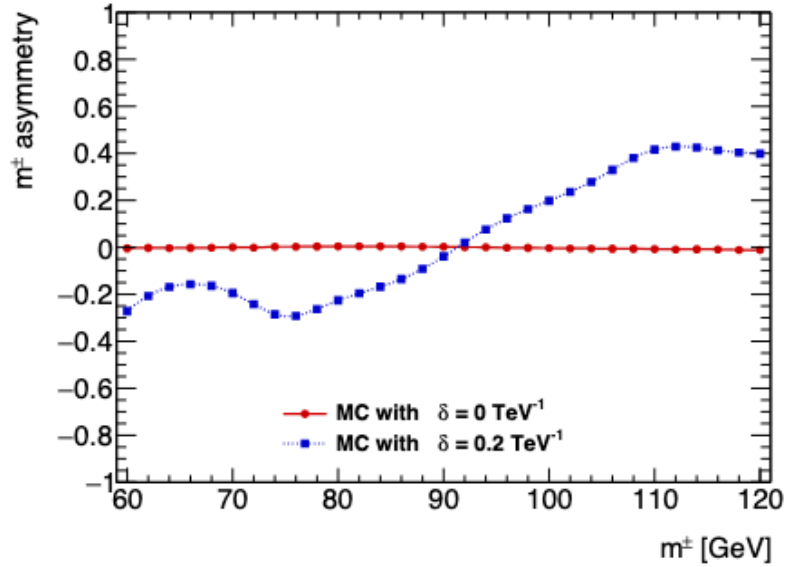


Figure 4.25: Pseudomass asymmetry distribution for simulated $Z \rightarrow \mu^+\mu^-$ events generated with Powheg, shown for the case without any sagitta bias (red) and after introducing a sagitta bias of $\delta_s = 0.2 \text{ TeV}^{-1}$ (blue).

Following Fig. 4.25 we calculate the sagitta for all the dataset of Run-2 (Fig. 4.26- 4.29). The sagitta has the distribution we expected. Ongoing

studies from the analysis group try to find the correct sagitta injector so the distribution to be close to flat at 0.

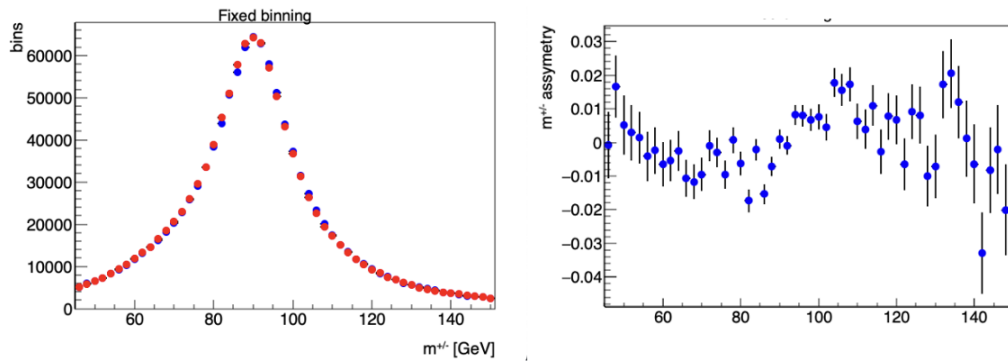


Figure 4.26: The Pseudomass distribution for 2015 data (left) and the pseudomass asymmetry (right).

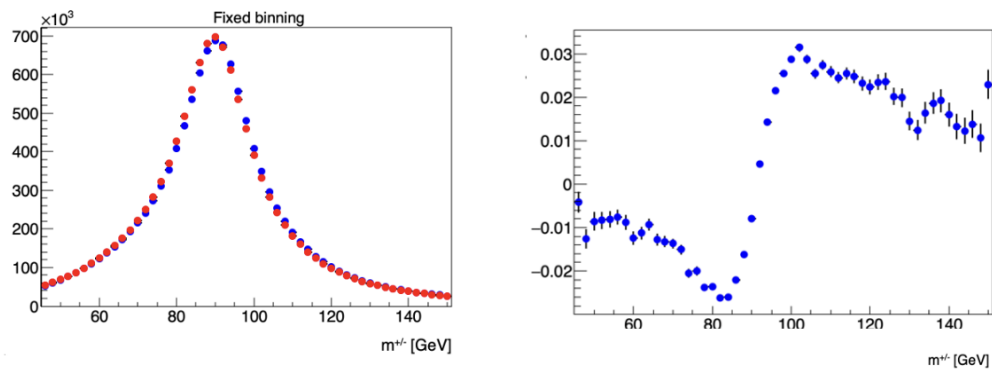


Figure 4.27: The Pseudomass distribution for 2016 data (left) and the pseudomass asymmetry (right).

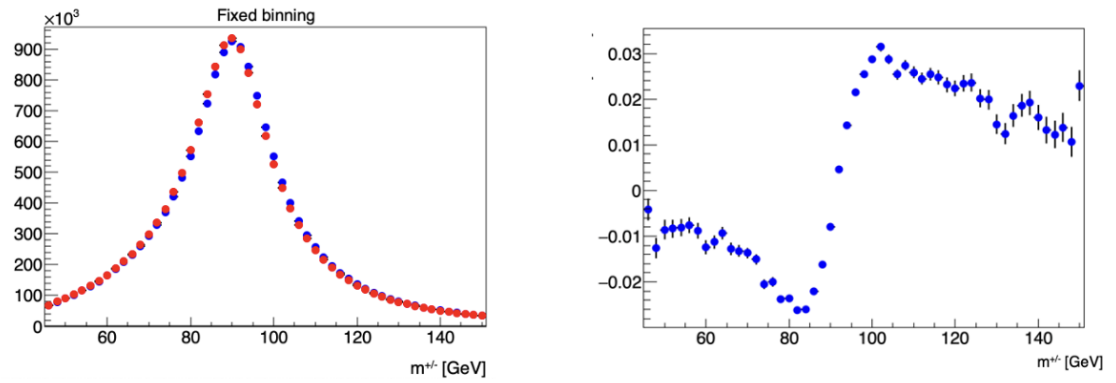


Figure 4.28: The Pseudomass distribution for 2017 data (left) and the pseudomass asymmetry (right).

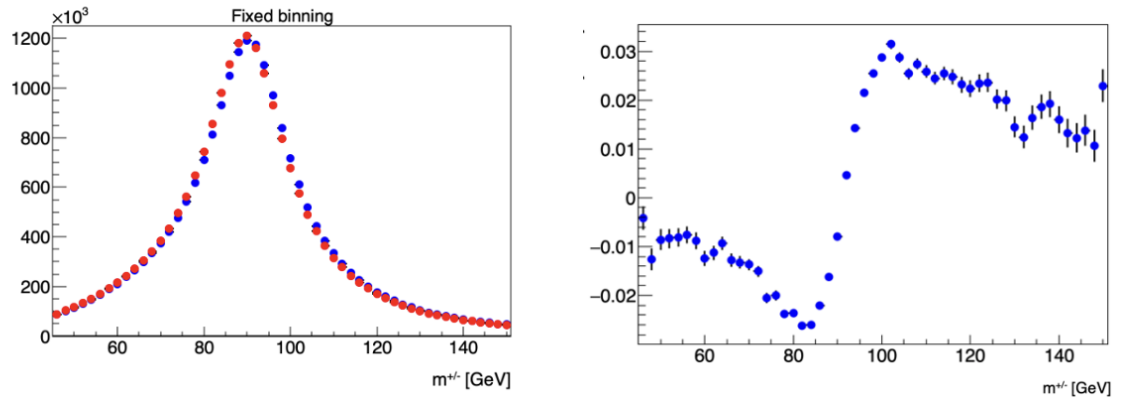


Figure 4.29: The Pseudomass distribution for 2018 data (left) and the pseudomass asymmetry (right).

4.10.3 Sagitta and background

In the final part of our study, we examine how the background influences the sagitta. The background distributions are normalized using the luminosity corresponding to each year, as summarized in Table 4.2.

Using these luminosities, we normalize the major background contributions: $t\bar{t}t\bar{t}$, $Z \rightarrow \tau\tau$, $Z \rightarrow \tau\tau$, and diboson ($WWWW$) processes. As shown in Fig. 4.30, these background distributions are significantly smaller compared to the data for each respective year. Furthermore, by incorporating the **Histmaker** plots from the previous chapter, we observe that the background contribution to the yearly data is minimal.

year	luminosity
2015	3.23 fb ⁻¹
2016	33.0 fb ⁻¹
2017	44.3 fb ⁻¹
2018	58.5 fb ⁻¹

Table 4.2
Luminosity per year for the entire Run-2

The plots below also show that, after subtracting the background processes from the data, the asymmetry in each year's distribution remains unchanged. This further confirms the minimal impact of background contributions on both the data and the observed asymmetry.

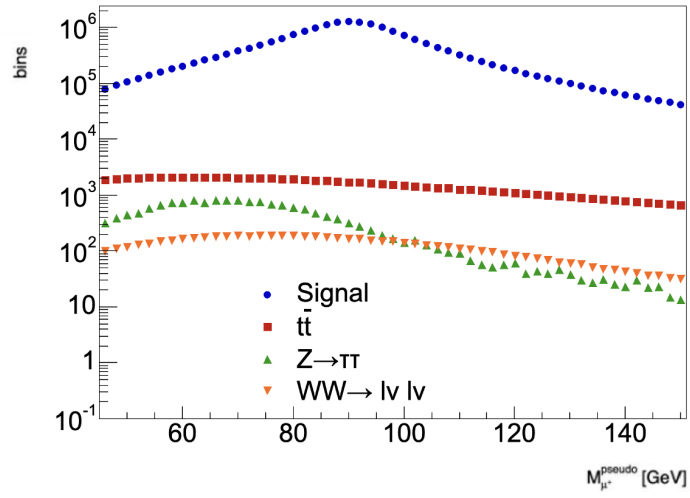


Figure 4.30: Normalized backgrounds and signal for year's 2018 luminosity.

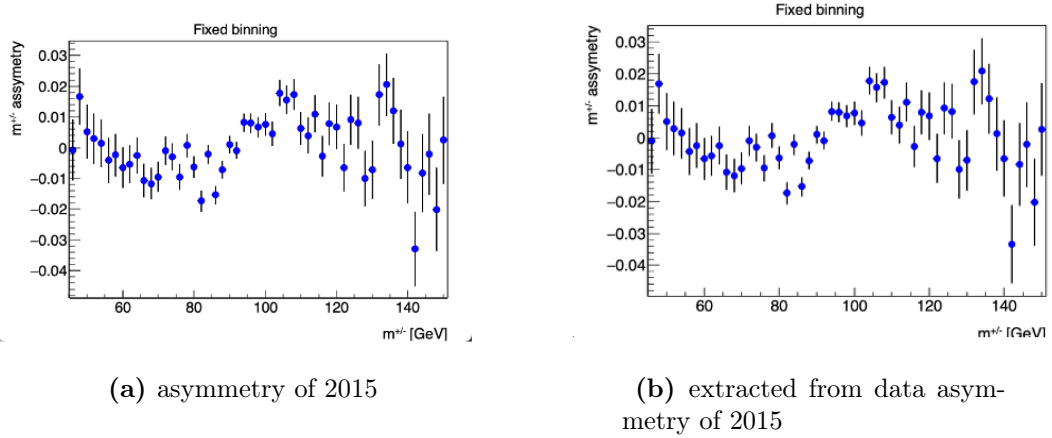
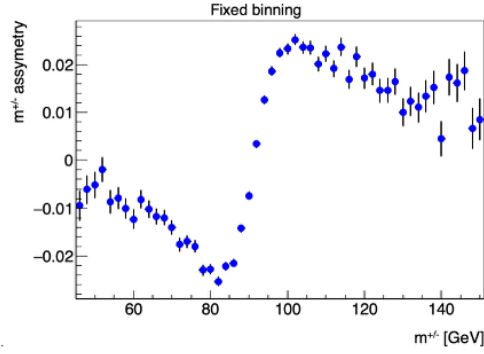
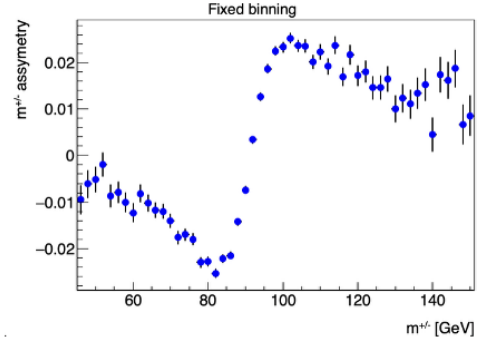


Figure 4.31: On the left is the initial asymmetry and on the right the sagitta from extracted backgrounds.

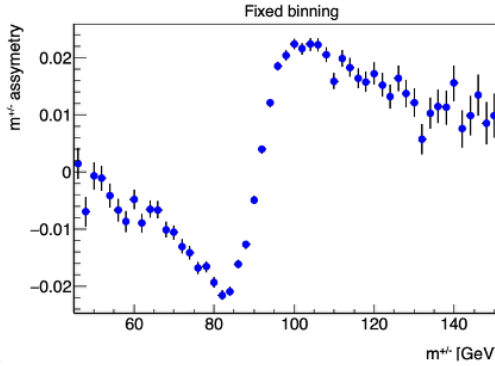


(a) asymmetry of 2016

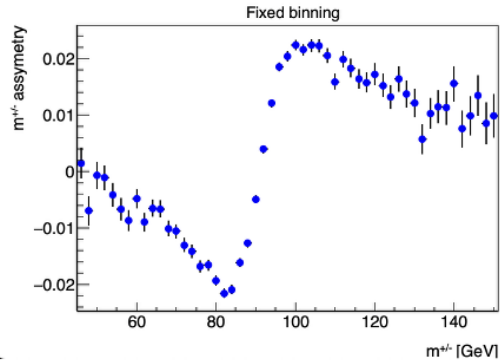


(b) extracted from data asymmetry of 2016

Figure 4.32: On the left is the initial asymmetry and on the right the sagitta from extracted backgrounds.

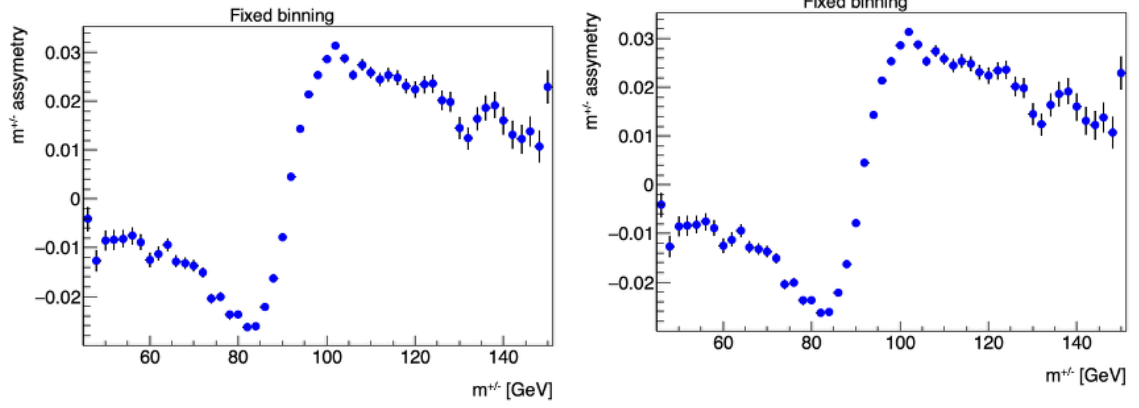


(a) asymmetry of 2017



(b) extracted from data asymmetry of 2017

Figure 4.33: On the left is the initial asymmetry and on the right the sagitta from extracted backgrounds.



(a) extracted from data asymmetry of 2018

(b) extracted from data asymmetry of 2018

Figure 4.34: On the left is the initial asymmetry and on the right the sagitta from extracted backgrounds.

4.11 Likelihood Fit

In this section we will talk about the likelihood fit that is going to be used for the next part.

In statistics, Maximum Likelihood Estimation (MLE) is a method of estimating the parameters of an assumed probability distribution, given some observed data. This is achieved by maximizing a likelihood function so that, under the assumed statistical model, the observed data is most probable. The point in the parameter space that maximizes the likelihood function is called the maximum likelihood estimate. The logic of maximum likelihood is both intuitive and flexible, and as such the method has become a dominant means of statistical inference.

We are focusing on two categories of parameters :

- Parameters of interest, that are determined by our fit. In our case this Parameter of Interest is the Z Mass .
- The nuisance parameters that in our case is the systematic uncertainties and in this thesis the systematics uncertainties from Luminosity.

By using prior information, profile likelihood fits can constrain systematic uncertainties. The total likelihood is structured as:

$$L_{\text{total}} = \mathcal{L}_{\text{phys}}(x_{\text{data}} \mid \mu, \hat{\theta}_t) \mathcal{L}_{\text{subs}}(\theta \mid \hat{\theta}, \sigma_{\theta})$$

where:

- $\mathcal{L}_{\text{phys}}(x_{\text{data}} \mid \mu, \hat{\theta})$ is the physical likelihood function, which depends on the observed data x_{data} , the parameter of interest μ , and the profiled nuisance parameters $\hat{\theta}$.
- $\mathcal{L}_{\text{subs}}(\theta \mid \hat{\theta}, \sigma_{\theta})$ is the subsidiary likelihood, which constrains the nuisance parameters θ using prior information (such as external measurements).

The nuisance parameters θ are constrained by a Gaussian distribution with known mean $\hat{\theta}$ and standard deviation σ_{θ} . This reflects the prior knowledge we have about these parameters.

The procedure is as follows:

1. **Profiling the Nuisance Parameters:** The nuisance parameters θ are *profiled* by maximizing the likelihood function for each fixed value of the parameter of interest, μ . This procedure involves determining the values of θ that best fit the data under the constraint of a constant μ . Formally, this is expressed as:

$$\hat{\theta}(\mu) = \arg \max_{\theta} \mathcal{L}(\mu, \theta)$$

where $\hat{\theta}(\mu)$ denotes the profiled nuisance parameters at a given μ .

2. **Estimating the Parameter of Interest:** After profiling the nuisance parameters, the next step is to determine the value of μ that maximizes the total likelihood function, using the profiled values of θ . This yields the best-fit estimate for μ :

$$\hat{\mu} = \arg \max_{\mu} \mathcal{L}(\mu, \hat{\theta}(\mu))$$

Here, the likelihood becomes a function of μ alone, with the dependence on θ absorbed through the profiling process.

4.12 TRexFitter

In this analysis, the likelihood fit is performed using the **TRexFitter** framework [10] [11]. **TRexFitter** constructs likelihood functions based on binned distributions (histograms) of observables, such as the invariant mass or transverse momentum. These templates are created for both signal and background processes.

For this work, the same datasets and background processes described in the **HistMaker** section are used. This part of the thesis focuses on the pre-fit and post-fit distributions produced by **TRexFitter**.

A Python script was developed to automate the setup. It takes as input the defined signal and background processes, along with nuisance parameters that account for systematic uncertainties. The script generates a configuration file used by **TRexFitter**, which specifies the model setup, input templates, and systematic uncertainties to be included in the fit.

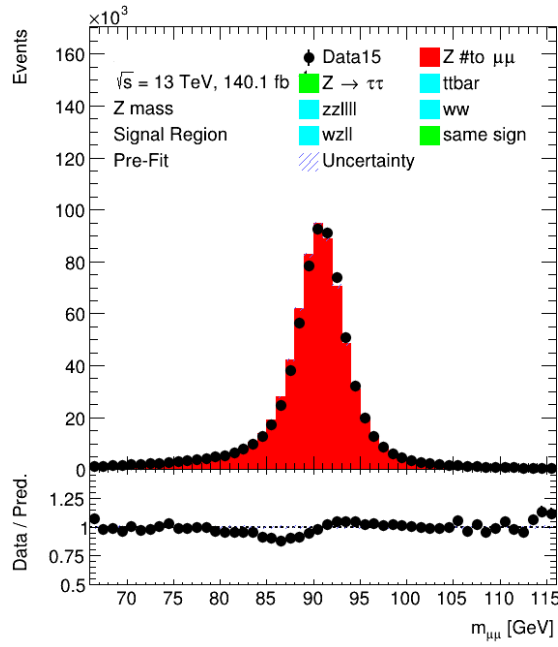
The analysis is performed in blinded mode, which means that an unknown offset is applied to the measured Z boson mass. This is controlled internally in the configuration via the flag:

MW_BLINDMASS: 1

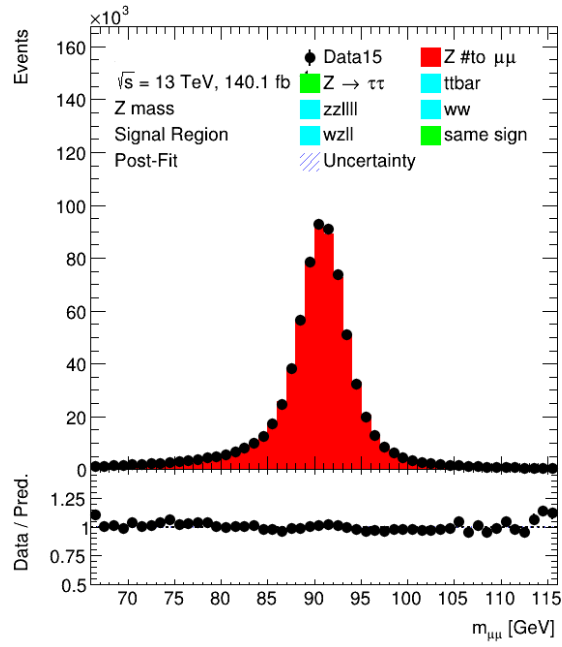
This ensures that the extracted mass values are shifted by an unknown constant, preventing any unintentional tuning of the model to match the expected result. Therefore, the absolute values obtained from the fit should not be interpreted as physical Z boson mass values, but rather serve for studying year-to-year variations and validating the fit setup.

As shown in Fig. 4.35- 4.39, the $m_{\mu\mu}$ distributions are displayed for the pre-fit (a) and post-fit (b) scenarios across all years of Run-2 (2015–2018), as well as for the combined dataset. In the pre-fit plots, a visible trend is observed, especially in the ratio panels, indicating deviations between the model and the data. After the fit is performed, the post-fit plots show that the ratio becomes nearly flat, demonstrating that the model provides a good description of the (blinded) data within the statistical uncertainties.

From the fitter, we also obtained an estimation of the Z boson mass, with an associated uncertainty for each year, as shown in the table below. Note that the central values listed in the table are blinded and include an unknown offset. Therefore, they should not be interpreted as the physical Z boson mass but are shown here for illustration and comparison across different years.



(a) 2015 pre-fit plot



(b) 2015 post-fit plot

Figure 4.35: Pre-fit (left) and post-fit (right) distributions for the 2015 dataset.

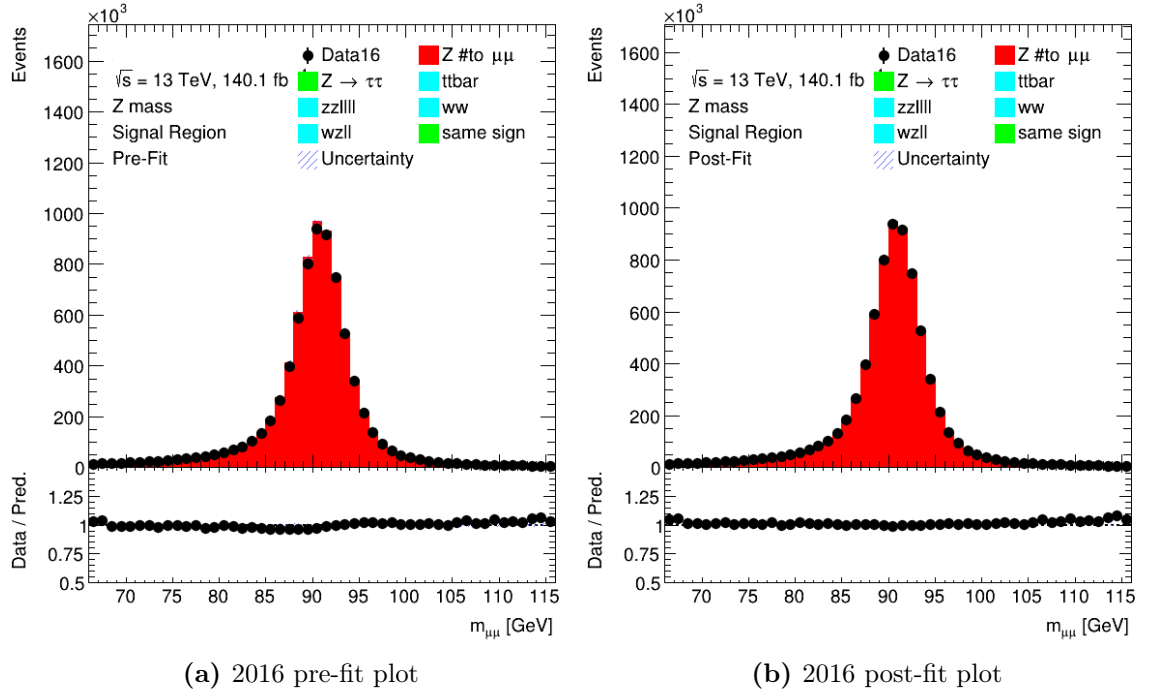
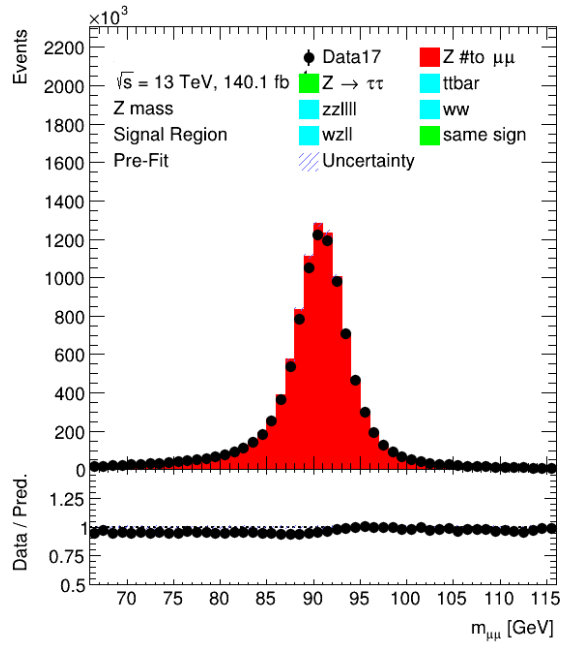
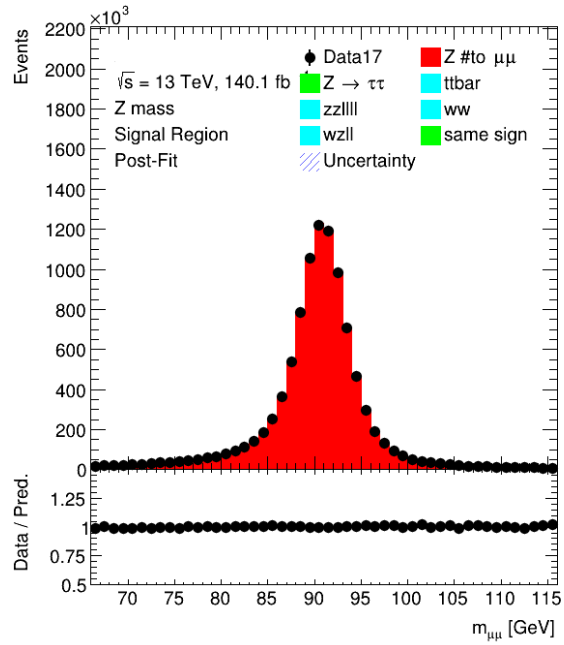


Figure 4.36: Pre-fit (left) and post-fit (right) distributions for the 2016 dataset.

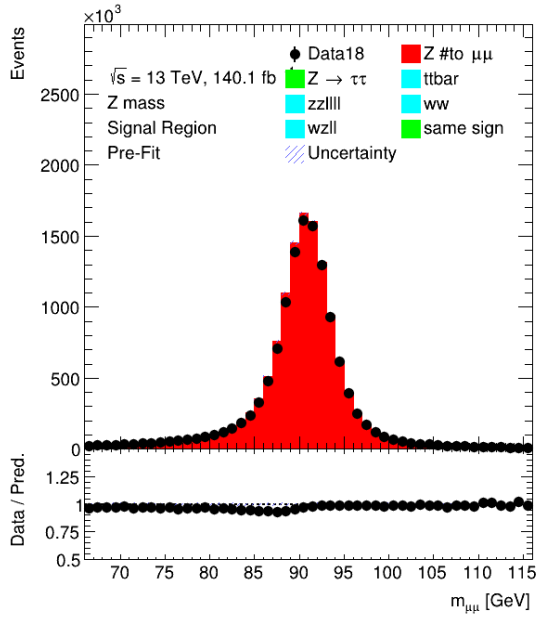


(a) 2017 pre-fit plot

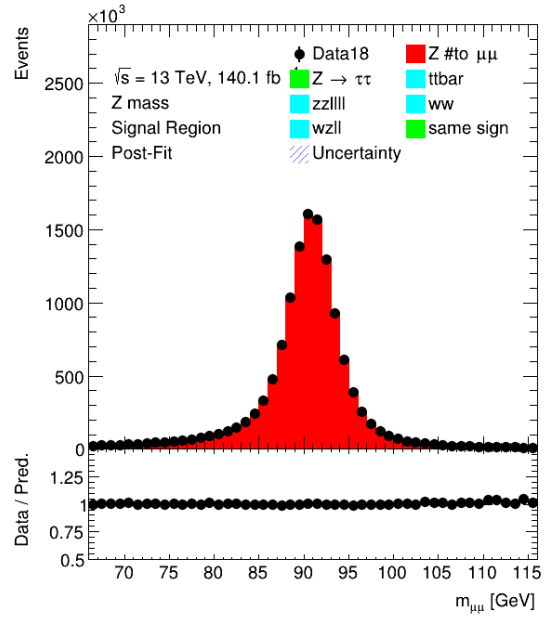


(b) 2017 post-fit plot

Figure 4.37: Pre-fit (left) and post-fit (right) distributions for the 2017 dataset.

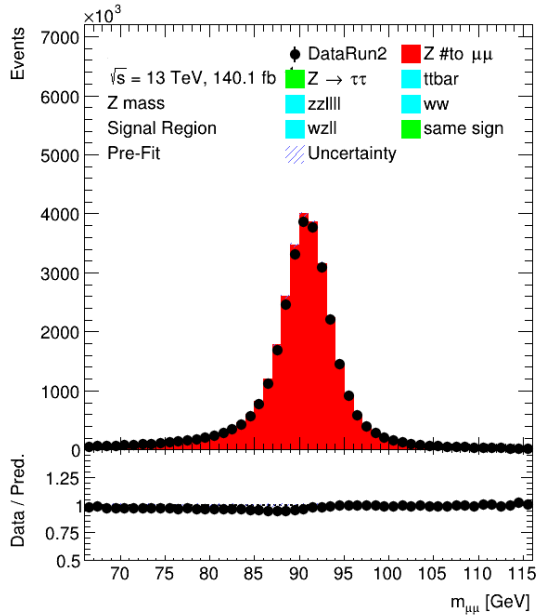


(a) 2018 pre-fit plot

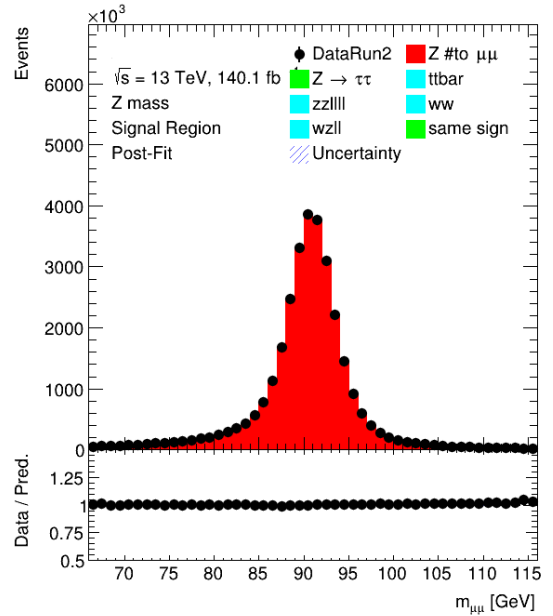


(b) 2018 post-fit plot

Figure 4.38: Pre-fit (left) and post-fit (right) distributions for the 2018 dataset.



(a) Pre-fit for all Run-2 data



(b) Post-fit for all Run-2 data

Figure 4.39: Pre-fit and post-fit plots for the full Run-2 dataset.

4.13 Trex Fit Results

In order to avoid biasing the analysis, the measurement of m_Z is blinded in the fit. This means that an unknown offset is applied to the measured value, and the true central value remains hidden. In our implementation, the central value lies within a blinded interval around the world-average Z mass, typically $M_Z^{\text{PDG}} \pm 50 \text{ MeV}/c^2$. As a result, the absolute values shown here cannot yet be compared directly to the PDG value. Instead, the focus of this work is on evaluating statistical uncertainties and investigating potential differences between data-taking years, which may point to systematic effects such as residual sagitta bias or modeling discrepancies.

In the current analysis, only a limited set of systematic uncertainties, mainly related to luminosity, has been included. Further work is planned to refine the fit and incorporate additional systematics, aiming for an accurate measurement of the Z mass consistent with the PDG value. The background contributions are found to be very small in all signal regions, as shown in the pre-fit and post-fit plots.

Summary

The analysis was performed using the full Run-2 pp collision dataset at $\sqrt{s} = 13 \text{ TeV}$. The final event selection required two isolated opposite-sign muons with $p_T > 25 \text{ GeV}$ and $|\eta| < 1.05$, ensuring that the muon momenta were measured in the central region of the Inner Detector, where the alignment and momentum resolution are optimal. The invariant mass

window $66 < m_{\mu\mu} < 116 \text{ GeV}$ was used to define the signal-dominated region.

Background validation was carried out using the same-sign muon control region. After the full selection, the background contribution was found to be negligible ($\sim 1\%$), confirming that the $Z \rightarrow \mu\mu$ channel provides a clean dataset suitable for precision calibration studies. The comparison of kinematic distributions between data and MC using the Histmaker framework showed overall good agreement, with small discrepancies at high p_T attributed to missing higher-order QCD corrections.

A dedicated study of the muon momentum scale was performed using the pseudo-mass technique, allowing the sagitta bias to be evaluated separately as a function of η and ϕ . The charge-dependent shifts observed in the pseudo-mass distributions were consistent with residual alignment effects. The derived correction factors were propagated into the statistical model.

The final measurement was performed with a binned likelihood fit using TRExFitter. Pre-fit distributions showed a visible mismatch between data and simulation in the peak region, while the post-fit distributions demonstrated a significant improvement, with the ratio Data/MC becoming flat within uncertainties. The mass and width of the Z boson remain blinded during the ongoing systematic uncertainty evaluation.

These results demonstrate that the implemented momentum calibration strategy is robust and that the $Z \rightarrow \mu\mu$ dataset is suitable for a precision measurement of m_Z in ATLAS, forming the foundation for the forthcoming unblinded result.

Bibliography

- [1] ALEPH, DELPHI, L3 and OPAL Collaborations, "Precise Determination of the Z Resonance Parameters at LEP: Zedometry", Eur. Phys. J. C, vol. 19, pp. 587–651, 2001. <https://arxiv.org/abs/hep-ex/0012018>
- [2] The LEP Collaborations, "Measurement of the Z resonance parameters at LEP", Eur. Phys. J. C, vol. 14, pp. 373–426, 2000. <https://link.springer.com/article/10.1007/s100520000319>
- [3] CERN Courier, "The discovery of the weak neutral currents", CERN Courier, 2009. <https://cerncourier.com/a/the-discovery-of-the-weak-neutral-currents/>
- [4] Luigi Di Lella, Carlo Rubbia, "The Discovery of the W and Z Particles", World Scientific Open Access, 2015. https://cds.cern.ch/record/2103277/files/9789814644150_0006.pdf?version=1
- [5] Nobel Prize Committee, "The Nobel Prize in Physics 1984", The Nobel Foundation, 1984. <https://www.nobelprize.org/prizes/physics/1984/summary/>
- [6] R. L. Workman, et al., "Review of Particle Physics", Prog. Theor. Exp. Phys., vol. 2022, no. 8, 083C01, 2022. <https://cds.cern.ch/record/2836514?ln=en>

- [7] ATLAS Collaboration, "Alignment of the ATLAS Inner Detector in Run-2", arXiv:2007.07624, 2020. <https://arxiv.org/abs/2007.07624>
- [8] ATLAS Collaboration, "A simple method to determine charge-dependent curvature biases...", arXiv:2101.05675, 2021. <https://arxiv.org/abs/2101.05675>
- [9] ATLAS Collaboration, "Curvature-bias corrections using a pseudomass method", J. Instrum., vol. 19, P03010, 2024. <https://iopscience.iop.org/article/10.1088/1748-0221/19/03/P03010>
- [10] CERN Software Documentation Portal, "Documentation for TRExFitter". <https://trexfitter-docs.web.cern.ch/trexfitter-docs/latest/>
- [11] ATLAS Software Tutorial, "ATLAS Software Documentation Portal". <https://atlassoftwaredocs.web.cern.ch/analysis-software/ASWTutorial/TutorialWeek/day4/>

Conclusion

In this work, two complementary objectives were achieved. The first was the development, integration and validation of the Detector Control System for the muon detectors of the ATLAS experiment and the second was the contribution to the precise measurement of the mass of the Z boson using Run-2 data.

Regarding the muon system upgrade and operations, significant contributions were made to the development and integration of Detector Control System (DCS) components across multiple detector technologies. A complete DCS framework was implemented for the BIS78 MDT chambers, including the re-design of the high-voltage (HV) power distribution, updated readout-to-channel mapping schemes, and full integration into the ATLAS Finite State Machine (FSM) architecture. User-oriented control panels and monitoring interfaces were developed to ensure safe and efficient chamber operation. Beyond the BIS78 project, contributions extended to the integration and operation of the New Small Wheel (NSW) Micromegas and sTGC HV system within the global ATLAS DCS infrastructure. In addition to upgrade activities, operational support was provided for the existing Muon Drift Tube (MDT) system through LS2 and Run-3. This involved detector development and maintenance in many tasks like the Muon Cooling System, the MDT Gas System and the End-Cap Alignment. Overall, these developments have strengthened the reliability, safety, and operational readiness of the ATLAS muon spectrometer control systems, ensuring sustained detector performance under the increased luminosity and trigger conditions of the High-Luminosity LHC era.

On the physics side, a full Run-2 analysis of the channel $Z \rightarrow \mu\mu$ was performed. Event selection and background suppression were implemented using the Histmaker framework, while the same-sign muon technique was used to validate residual background contributions. A dedicated study of the muon momentum scale was carried out through the sagitta bias correction using the pseudo-mass method, allowing the separation of alignment and magnetic field effects. Finally, a likelihood-based statistical model was constructed using TRExFitter, enabling pre-fit and post-fit comparisons and the inclusion of systematic uncertainties in a controlled way. The final Z mass result remains blinded, and further refinement is ongoing through the inclusion of additional systematic sources and year-by-year consistency checks.

Appendix A

MDT Configuration Database

The MDT Configuration database provides access to the data required for the configuration of the detector and the online software. This includes information pertaining to the DAQ, DCS, JTAG, power supply, calibration and alignment, as well as tube and mezzanine mappings for online monitoring and conditions data. Table 1 contains the information from the Configuration DB concerning the CANBUS parameters as they have been recorded in both ATONR and DEVDB1. For instance, Fig. A.1 shows the information for the BIX7A02, with S/N (serial number) C989 and node id 96, temperature (T) and magnetic field (B) sensors. Similarly Figure 24 displays all the connected mezzanine cards to BIX7A02 CSM, that they have been stored to the DB. Each rectangle holds the slot number of the mezzanine, along with the basic operational parameters (temperature, analog, digital, etc).

BIS78 ConfDB Information		
BIX7A02	mdm	C989
BIX7A02	node	96
BIX7A02	type	b
BIX7A02	mask_bsen	15
BIX7A02	mask_tsen	4095
BIX7A02	n_tsen	12
BIX7A02	csm_conn_mezz_mask	262143
BIX7A02	n_mezz	18
BIX7A02	csm_enable	262143

Table A.1

Information stored into the configuration database for the BIS78 chambers.

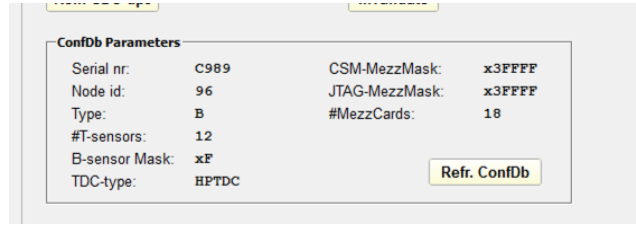


Figure A.1: MDM Browser details from MDT configuration database.

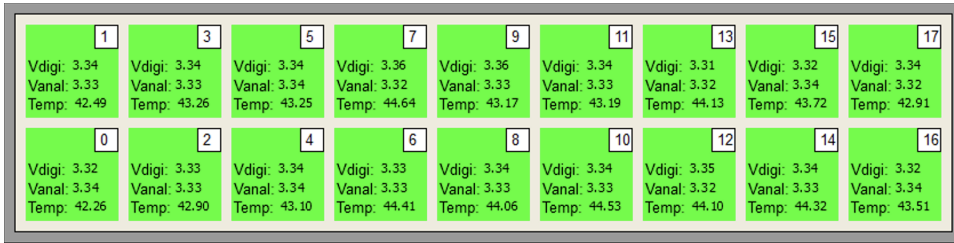


Figure A.2: Number of chamber Mezzs filled by MDT configuration database.

Glossary

AC	Alternating Current
ALICE	A Large Ion Collider Experiment
ALEPH	Apparatus for LEP pHysics
APV	Atomic Parity Violation
ARAMyS	Alignment Reconstruction Software for the ATLAS Muon Spectrometer
ASD	Amplifier-Shaper-Discriminator
ATLAS	A Toroidal LHC Apparatus
BC	bunch crossing
BCAM	Brandeis CCD Angular Monitor
BE	DCS Back-End
BIS	Barrel Inner Small
CCD	Charge-Coupled Device
CMS	Compact Muon Solenoid
CPU	Central Processing Unit
CSAM	CERN Safety Alarm Monitoring
CSCs	Cathode Strip Chambers
CSM	Chamber Service Module
CU	Control Unit
DC	Direct Current
DCS	Detector Control System
DDC	DAQ to DCS
DDV	Detector Data Viewer
DE&N	Device Editor and Navigator
DELPHI	DEtector with Lepton, Photon and Hadron Identification
DIM	Distributed Information Management system
DIP	Data Interchange Protocol

DM	Data Manager
DP	Data Point
DPE	Data Point Element
DPT	Data Point Type
DSS	Detector Safety System
DU	Device Unit
EV	Event Manager
FASER	ForwArd Search ExpeRiment
FE	Front-End
FP7	European Commission's Seventh Framework Programme
FSM	Finite State Machine
FW	Framework
GED	Graphical Editor
HEP	High Energy Physics
HL-LHC	High-Luminosity Large Hadron Collider
HV	High Voltage
IBL	Insertable B-Layer
ID	Inner Detector
IP	interaction point
JCOP	Joint Controls Project
JTAG	Joint Test Action Group
LAr	Liquid Argon
LEP	Large Electron-Positron accelerator
LHC	Large Hadron Collider
LHCb	LHC-beauty
LHCf	LHC-forward
LS	Long Shutdown
LU	Logical Unit

LV	Low Voltage
LWDAQ	Long Wire Data Acquisition
MC	Monte Carlo
MDM	MDT-DCS-Module
MDT	Monitored Drift Tubes
MLE	Maximum Likelihood Estimation
MM	MicroMegas
Micromegas	Micro-Mesh Gaseous Structure
MoEDAL	Monopole and Exotics Detector At the LHC
MS	Muon Spectrometer
NLO	Next-to-Leading Order
NNLO	Next-to-Next-to-Leading Order
NSW	New Small Wheel
OPAL	Omni-Purpose Apparatus for LEP
OPC	Open Platform Communications
PA	Project Administrator panel
PARA	Parameterization Environment
PCB	Printed Circuit Board
PDR	Preliminary Design Report
PLC	Programmable Logic Controller
PS	Power Supply
QCD	Quantum Chromodynamics
RPC	Resistive Plate Chambers
SCADA	Supervisory Control and Data Acquisition
SCT	Semiconductor Tracker
SMDT	small Monitored Drift Tubes
SM	Standard Model
SMI	State Management Interface

SND	Scattering and Neutrino Detector
STGC	Small Thin Gap Chambers
TDAQ	Trigger and Data Acquisition System
TDC	Time-to-Digital Converter
TDR	Technical Design Report
TGC	Thin Gap Chambers
TOTEM	Total Cross Section, Elastic Scattering and Diffraction Dissociation
TRT	Transition Radiation Tracker
UI	User Interface
USA15	Main ATLAS underground electronics cavern
US15	ATLAS underground service area
UX15	ATLAS underground experimental cavern
VDU	Visual Display Unit
VME	Versa Module Europa
WinCC OA	SIMATIC WinCC Open Architecture